UNIVERSITY OF SOUTHAMPTON

FACULTY OF NATURAL AND ENVIRONMENTAL SCIENCES

Chemistry

Volume 1 of 1

Soft-Templating of Nanostructured Materials for Thermoelectric Power Harvesting and Catalysis

by

Matthew Richard Burton

Thesis for the degree of

Doctor of Philosophy

June 2017

UNIVERSITY OF SOUTHAMPTON

ABSTRACT

FACULTY OF NATURAL AND ENVIRONMENTAL SCIENCES

Chemistry

Thesis for the degree of Doctor of Philosophy

SOFT-TEMPLATING OF NANOSTRUCTURED MATERIALS FOR THERMOELECTRIC POWER HARVESTING AND CATALYSIS

Matthew Richard Burton

The ever increasing demand for energy along with climate change has stimulated much research in the field of green energy technology. Thermoelectric generators are one form of green energy technology that generates electrical power from waste heat harvesting. Current fabrication techniques for thermoelectric materials are costly and the efficiency of materials is low. This work uses electrodeposition as a cheap fabrication that allows for control of a large number of variables to optimise materials.

In the literature the doping of bismuth tellurium selenide has shown improvements in thermoelectric performance. Bismuth telluride and bismuth tellurium selenide have been electrodeposited before, but the electrochemical doping of bismuth tellurium selenide has not received much interest in the literature. In Chapter 3 bismuth tellurium selenide was doped with Cu to higher levels than ever reported before, by the addition of $Cu(NO_3)_2$ into the electrolyte. The level of Cu doping was shown to be linear with increasing $Cu(NO_3)_2$ concentration in the electrolyte, as determined by EDX. Cu doping was shown to exponentially decay the electrical conductivity, whilst concentrations between 1.25 mM and 1.75 mM $Cu(NO_3)_2$ were shown to increase the magnitude of the Seebeck coefficient, from -55 $\mu V\ K^{-1}$ in the absence of Cu to a peak value of -390 $\mu V\ K^{-1}$ when using an electrolyte concentration of 1.50 mM $Cu(NO_3)_2$. Whilst a slight improvement in power factor was seen for one sample made with 1.50 mM $Cu(NO_3)_2$ present in the electrolyte, this was not reproducible and on average Cu doping was not shown to improve thermoelectric performance. The electrochemical doping of bismuth tellurium selenide with Ag is reported for the first time and was shown to be linear with increasing $Ag(NO_3)$ concentration in the electrolyte. The addition of 0.25 mM $Ag(NO_3)$ in the electrolyte was shown to lower electrical conductivity to 296 S cm^{-1} from 564 S cm^{-1} in the absence of $Ag(NO_3)$. Further addition of $Ag(NO_3)$

into the electrolyte was shown to not diminish the electrical conductivity further. Ag doping also diminished the magnitude of the Seebeck coefficient. The most striking observation was the use of a SMSE reference electrode instead of a SCE reference electrode yielded the greatest improvement in thermoelectric performance of bismuth tellurium selenide films, producing a power factor of 0.33 mW m^{-1} K^{-1}, compared to a value of 0.13 mW m^{-1} K^{-1} when using an SCE reference. The effect of different reference electrodes on the electrodeposition of bismuth telluride based materials has not been reported in the literature. The improvement in power factor is believed to be caused by the removal of Cl^- ions, which may have been causing a detrimental effect on the electrodeposition of bismuth tellurium selenide films for thermoelectric applications.

Reduced dimensionality offers a strategy for increasing the efficiency of thermoelectric materials primarily by lowering lattice thermal conductivity. In Chapter 4 a lyotropic liquid crystal is used for the first time to template bismuth telluride. The use of a phytantriol template during bismuth telluride electrodeposition was shown to produce a disordered nanostructure containing nanowires with diameters as low as 6 *nm*. Prior to this work the smallest bismuth telluride nanowires reported in the literature were 15 *nm*. The composition of these nanowires was controlled by altering the composition of the electrolyte. A Seebeck coefficient of -88 µV K^{-1} was measured. The films were seen to oxidise, with oxygen content of 60 atomic % measured by EDX. This oxidation resulted in a low electrical conductivity of 19 S cm^{-1} being measured.

Whilst bismuth telluride is the best performing room temperature thermoelectric material, the rarity and toxicity of tellurium restricts the commercial viability of thermoelectric generators manufactured with bismuth telluride. Sulphur is an earth abundant element that is considered non-toxic and like tellurium sulphur is a group 16 element. This makes bismuth sulphide a potential alternative to bismuth telluride. In Chapter 5 planar bismuth sulphide films were successfully electrodeposited at a potential of -0.4 V vs SCE form an electrolyte created using 100 mM $Bi(NO_3)_3$, 100 mM $Na_2S_2O_3$ and 200 mM EDTA in deionised water. A room temperature Seebeck coefficient of -29.8 µV K^{-1} was recorded. The use of a phytantriol template resulted in the production of a single diamond nanostructure with a lattice parameter of 139.6 (± 3.2) *Å*, as shown by SAXS and TEM. The electrodeposit was the first ever single diamond phytantriol templated semiconductor material. A lower Seebeck coefficient of -12.3 µV K^{-1} was recorded for the nanostructure.

Fuel cells are promising technologies for transport and portable power generation due their ability to continually generate electricity when supplied with fuel. Current fuel cells are electrocatalysed by expensive Pt based materials. Pd is a more earth abundant and cheaper

material with the potential to be used instead of Pt for the electrocatalyst in fuel cells. In Chapter 6 a phytantriol template was used for the first time to electrodeposit Pd with a high surface area per mass of 30.8 $m^2 g^{-1}$, and a high surface area per volume of 3.66×10^6 $cm^2 cm^{-3}$. The large surface area was due to a single diamond nanostructure being formed with a lattice parameter of 140.0 (± 4.6) *Å*, as determined by SAXS. This high surface area Pd nanostructure allowed for greater electrooxidation of methanol, ethanol and glycerol per gram of Pd when compared to Pd black and a film deposited in the absence of phytantriol.

Table of Contents

List of Tables

List of Figures

List of Accompanying Materials

M. R. Burton, S. J. Richardson, P. A. Staniec, N. J. Terrill, J. M. Elliott, A. M. Squires, N. M. White, I. S. Nandhakumar, “A novel route to nanostructured bismuth telluride films by electrodeposition”, Electrochemistry Communications, Volume 76, Pages 71-74, Year 2017.

DECLARATION OF AUTHORSHIP

I, Matthew Burton, declare that this thesis and the work presented in it are my own and has been generated by me as the result of my own original research.

Soft-Templating of Nanostructured Materials for Thermoelectric Power Harvesting and Catalysis...

.....

I confirm that:

1. This work was done wholly or mainly while in candidature for a research degree at this University;
2. Where any part of this thesis has previously been submitted for a degree or any other qualification at this University or any other institution, this has been clearly stated;
3. Where I have consulted the published work of others, this is always clearly attributed;
4. Where I have quoted from the work of others, the source is always given. With the exception of such quotations, this thesis is entirely my own work;
5. I have acknowledged all main sources of help;
6. Where the thesis is based on work done by myself jointly with others, I have made clear exactly what was done by others and what I have contributed myself;
7. [Delete as appropriate] None of this work has been published before submission [or] Parts of this work have been published as: [please list references below]:

Signed: .....

Date: 20/06/2017 .....

Acknowledgements

I would like to thank my supervisor, Dr. Iris Nandhakumar, who has provided countless support and guidance during my research. My co-supervisors Professor Neil White and Dr. Elena Koukharenko (School of Electronics and Computer Science) have also provided support by passing on their knowledge. I must acknowledge my funding sources, the Nation Physical Laboratory (NPL), the department of Chemistry and the School of Electronics and Computer Science. Diamond Light Source is also acknowledged for supporting this work by providing beam time. I would also like to recognise the Royal Society of Chemistry, the Institute of Physics and the International Thermoelectric Society for all providing funding which allowed me to present my work at the 35th International Conference on Thermoelectrics in Wuhan, China in May 2016.

Much appreciation must go to Dr. Adam Squires (University of Reading), his PhD student Samuel Richardson and Dr. Paul Staniec (Diamond Light Source), who have all provided countless hours of help during diamond trips and who have all taken a keen interest in this research. I would also like to acknowledge former members of the Nandhakumar group. Dr. Andrew Naylor is acknowledged for his detailed discussions at the beginning of the project. Dr. Chunhong Lei is acknowledged for his scientific discussions in the lab throughout his postdoctoral research. I would also like to acknowledge the project students I supervised, Alex Brett who enthusiastically helped investigate the effects of Ag doping Bismuth Tellurium Selenide and Anand Selvam who helped conduct research into Pd nanostructuring.

Dr. Eugen Stulz and his group must all be given praise for both providing small amounts of chemicals for this work, and for making the laboratory a pleasant place to be. In particular Dr. Gabriella Marth, Dr. Iwona Mammes, Dr. James Wood, Joanna Pursey and Lauren Sargisson are to be praised. Dr. Daniel Singleton, Dr. Owen Cox, Dr. Rachael Wilkinson and Dr. Warren Duffy all also need to be praised for their contribution to making my time during my research more enjoyable. Finally I would like to thank everyone in building 30 level 5 and building 29 level 6/7, who helped or took time to get to know me.

Definitions and Abbreviations

Symbols

PF – Power factor

S – Seebeck coefficient ($V\ K^{-1}$)

T – Temperature (*K*)

T_H – Temperature on the hot side (*K*)

T_C – Temperature on the cold side (*K*)

$\bar{T}$ – Average temperature of the hot and the cold surfaces

ZT – Dimensionless figure of merit

σ – Electrical conductivity ($S\ m^{-1}$)

η – Efficiency

ρ – Electrical resistivity ($\Omega\ m$)

κ – Thermal conductivity ($W\ m^{-1}\ K^{-1}$)

Abbreviations

AAM - Anodic Alumina Membranes

COD – Crystallography Open Database

CV – Cyclic Voltammetry/Voltammogram

EDX – Energy Dispersive X-Ray Spectroscopy

FTO - Fluorine doped Tin Oxide

HCPA - Hexachloroplatinic Acid

HIM – Helium Ion Microscopy

ICDD – International Centre for Diffraction Data

MA - Mechanical Alloying

SAXS – Small Angle X-Ray Scattering

SCE – Saturated Calomel Electrode

SEM – Scanning Electron Microscopy

SMSE – Saturated Mercury/Mercury Sulphate Electrode

SPS - Spark Plasma Sintering

SS - Stainless Steel

TEM – Transmission Electron Microscopy

XRD – X-Ray Diffraction

Chapter 1: Introduction

The ever growing pressure of global warming and the ever diminishing supply of fossil fuels, combined with safety concerns over nuclear fission are the main drivers for the need to develop renewable energy generation. Thermoelectric (TE) generators offer a root of renewable energy generation by exploiting temperature gradients generated by waste heat (e.g. from a vehicles exhaust [1]). Thermoelectric generators are solid state devices that require no maintenance, are highly reliable and have scalability. Thermoelectric generators can also be a reliable source of energy, unlike other renewable energy devices such as windmills and solar panels. This is because waste heat energy can be produced at a dependable rate, whereas sun and wind energy, for solar panels and windmills respectively, fluctuate with weather conditions.

1.1 Thermoelectric Generators

Semiconductor TE generators work by applying a temperature gradient across p-n junctions. A p-n junction forms where a p-type semiconductor and an n-type semiconductor meet. At the junction a region is formed called the depletion zone, this is where free electrons from the n-side and free holes from the p-side have crossed the p-n junction and upon meeting a free hole or free electron respectively, have fallen in energy. Consequently the depletion zone has no free holes or electrons, and any that do wander in are repelled by positive charges (from donor atoms) on the n-type side and negative charges (from acceptor atoms) on the p-type side respectively. This results in an energy barrier being present, blocking any charge flow across the barrier [2]. This is illustrated in Figure 1-1.

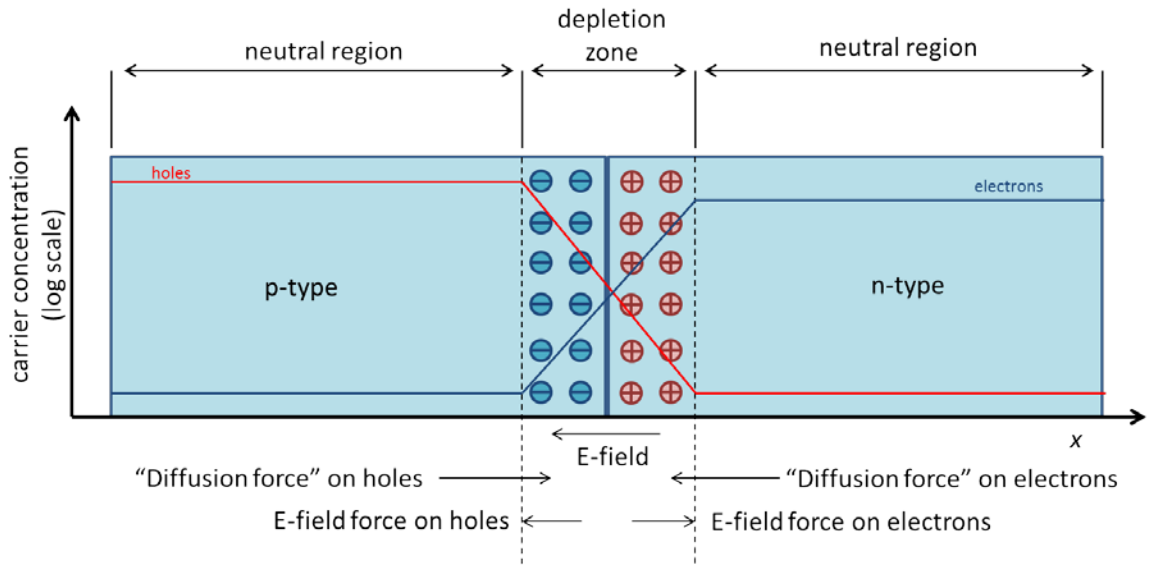

Figure 1-1 – Schematic diagram of a p-n junction, adapted from [3].

Applying a temperature gradient across a p-n junctions, causes diffusion of charge carriers (electrons or holes) through the semiconductors from the warmer side to the cooler side resulting in a voltage, or electrical current [4]. This is known as the Seebeck effect. It should be noted that charge carriers can carry charge as well as heat. TE generators can also be run in reverse, where the application of an electrical current can cause the formation of a temperature gradient [4]. This is called the Peltier effect. These two effects are illustrated in Figure 1-2.

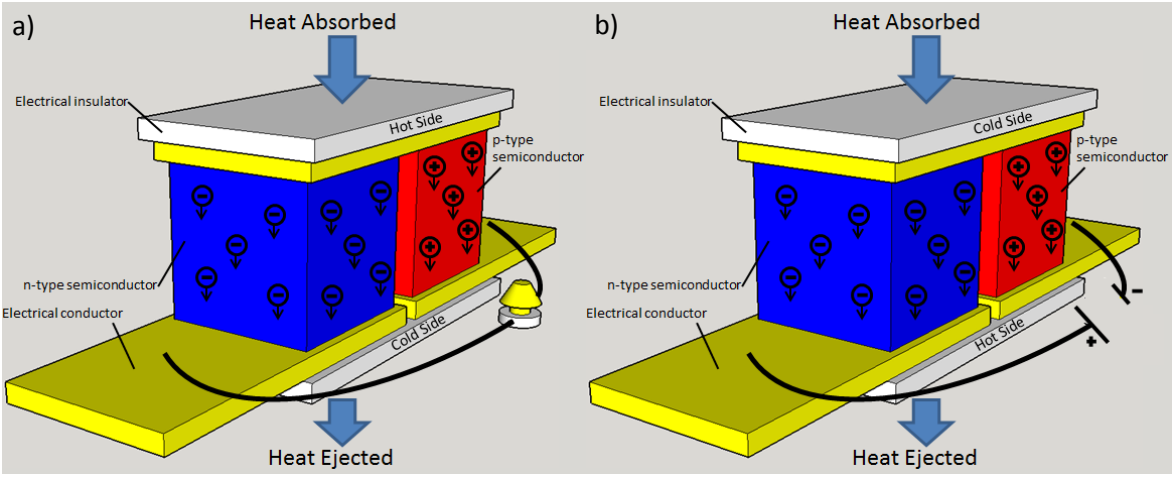

Figure 1-2 – Schematic diagram showing: a) the Seebeck effect and b) the Peltier effect in basic thermoelectric devices

In practice a single p-n junction, as shown in Figure 1-2, does not create a very useful device as a low voltage is generated. In order to produce more powerful devices, commercial thermoelectric devices consist of several p-n junctions aligned electrically in series, whilst thermally in parallel. This is demonstrated in Figure 1-3, which is a schematic diagram of a typical commercial device. This allows for a workable voltage to be created as the voltage is the sum of each of the individual p-n junctions.

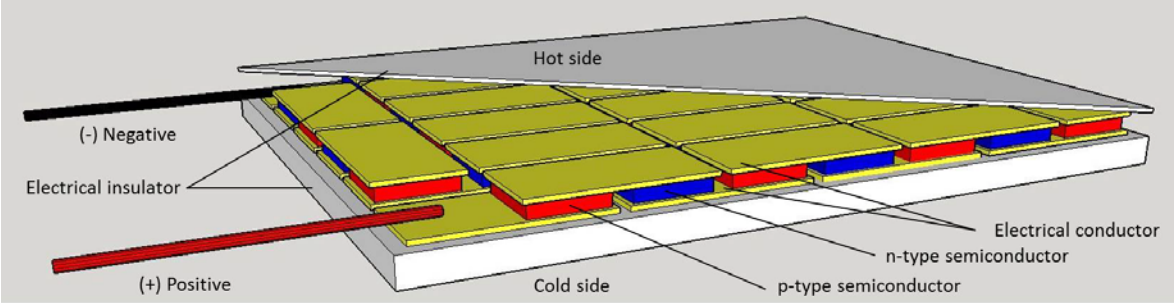

Figure 1-3 – Diagram of a commercial thermoelectric generator, with p-n junctions connected electrically in series but thermally in parallel.

1.1.1 Efficiency of Thermoelectric Generators

Thermoelectric devices are heat engines. A consequence of this being that the maximum potential efficiency is limited by the Carnot efficiency. The Carnot efficiency can be described as shown in Equation 1.1.

$$\eta = \frac{T_H - T_C}{T_H} \tag{1.1}$$

where η is the efficiency, T_H is the temperature on the hot side in Kelvin and T_C is the temperature on the cold side in Kelvin.

The efficiency must be considered in potential thermoelectric applications. A potential application of a thermoelectric generator is to capture waste heat energy from a car's exhaust. This would allow for a smaller alternator, or potentially the removal of the alternator completely. Both of these scenarios would improve the efficiency of the engine, with the removal of the alternator potentially leading to an increased efficiency of around 5% for an average car. The typical temperature of a car exhaust is around 800 *K* [5], with typical outdoor temperature being 300 *K.* The maximum efficiency based on Carnot in this scenario is 62.5%. Thermoelectric devices efficiencies, however, are further limited by the so called thermoelectric figure of merit *ZT* Equation 1.2.

ZT is a dimensionless figure of merit that allows for the direct comparison of the ability of thermoelectric materials to efficiently produce thermoelectric power. The higher a *ZT* value, the more efficient a material is at harvesting heat energy and converting it into usable electrical energy.

$$ZT = \frac{S^2\sigma}{\kappa}T \tag{1.2}$$

S is the Seebeck coefficient ($V\,K^{-1}$), σ is the electrical conductivity ($S\,m^{-1}$), κ is the thermal conductivity ($W\,m^{-1}\,K^{-1}$) and *T* is the absolute temperature (*K*) [4]. It is to be noted that κ (as shown in Equation 1.3) is the direct sum of the contributions from both the electronic thermal (κ_e) and lattice thermal (κ_L) contributions to the thermal conductivity which result from heat carrying charge carriers (electrons or holes) travelling through the crystal lattice and heat transporting phonons respectively [6].

$$\kappa = \kappa_e + \kappa_L \tag{1.3}$$

A thermoelectric device comprises of two materials, an n-type and a p-type. As a consequence, to work out theoretical maximum efficiency for a device a *ZT* value which encompasses the characteristics of both is required. This hybrid $Z\bar{T}$ value is calculated as shown in Equation 1.4.

$$Z\bar{T} = \frac{(S_p - S_n)^2 \bar{T}}{(\sqrt{\rho_n \kappa_n} + \sqrt{\rho_p \kappa_p})^2} \quad (1.4)$$

where $\bar{T}$ is the average of the hot and the cold surfaces, ρ is the electrical resistivity and subscripts *n* and *p* refer to n-type and p-type semiconductors respectively.

The theoretical maximum efficiency (η_{max}) of a p-n junction can be calculated by using Equation 1.5.

$$\eta_{max} = \frac{T_H - T_C}{T_H} \frac{\sqrt{1+Z\bar{T}} - 1}{\sqrt{1+Z\bar{T}} + \frac{T_C}{T_H}} \quad (1.5)$$

Using Equation 1.5 a realisation of how *ZT* values relate to efficiencies can be calculated. A plot of how various *ZT* values equate to different efficiencies at temperatures elevated from room temperature is shown in Figure 1-4.

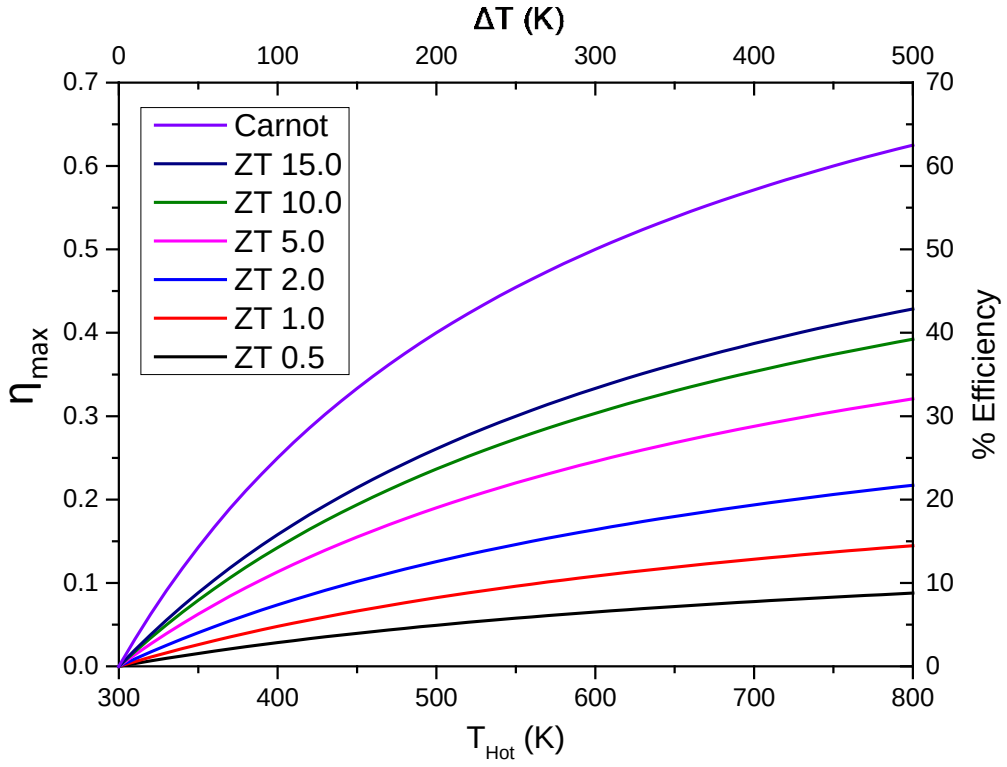

Figure 1-4 - Efficiency performance of thermoelectric materials with different *ZT* values and the maximum theoretical efficiency defined by the Carnot equation (Equation 1.1). 300 *K* and 800 *K* have been chosen as temperature limits as they represent a temperature difference seen in car exhausts [5].

The task for thermoelectric research is to increase *ZT* to allow the use of thermoelectric generators beyond the current niche application areas such as in space travel [7], [8], portable

device charging [9] and furniture heating [10], to more widespread applications such as in vehicles [11], steel works waste heat [12] and other proposed waste heat sources [13].

1.1.1.1 Power Factor

Whilst the figure of merit (*ZT*) is a measure of a material's efficiency, the power factor (*PF*) is also important in determining the usefulness of a material for thermoelectric applications. The power factor is shown in Equation 1.6.

$$PF = S^2\sigma \tag{1.6}$$

A high *PF* indicates that the material is able to harvest more energy in space restricted applications, although this energy may not be generated very efficiently. Therefore *PF* is often viewed as a more important figure when considering the viability of practical devices.

Often the *PF* is used as the only indicator of a materials thermoelectric performance in papers. This is because normally a thermal conductivity value would need to be measured as well to obtain a *ZT* value, which for thin films is rarely achievable.

1.2 Semiconductors

The Seebeck and Peltier effects, which allow thermoelectrics to function, were discovered in metals. Despite their lower electrical conductivities however, semiconductors are currently the preferred thermoelectric materials due to their ability to generate higher Seebeck voltages [7]. This can be seen in the fact that metallic thermocouples can typically generate voltages in the order of tens of microvolts per degree, whereas, thermoelectric semiconductors can generate voltages in the region of an order of a magnitude higher [7]. The maximum *ZT* typically occurs at carrier concentrations between 10^{19} and 10^{21} carriers cm^{-3}, which are found in heavily doped semiconductors [14]. This is illustrated in Figure 1-5 which is modelled from bismuth telluride data.

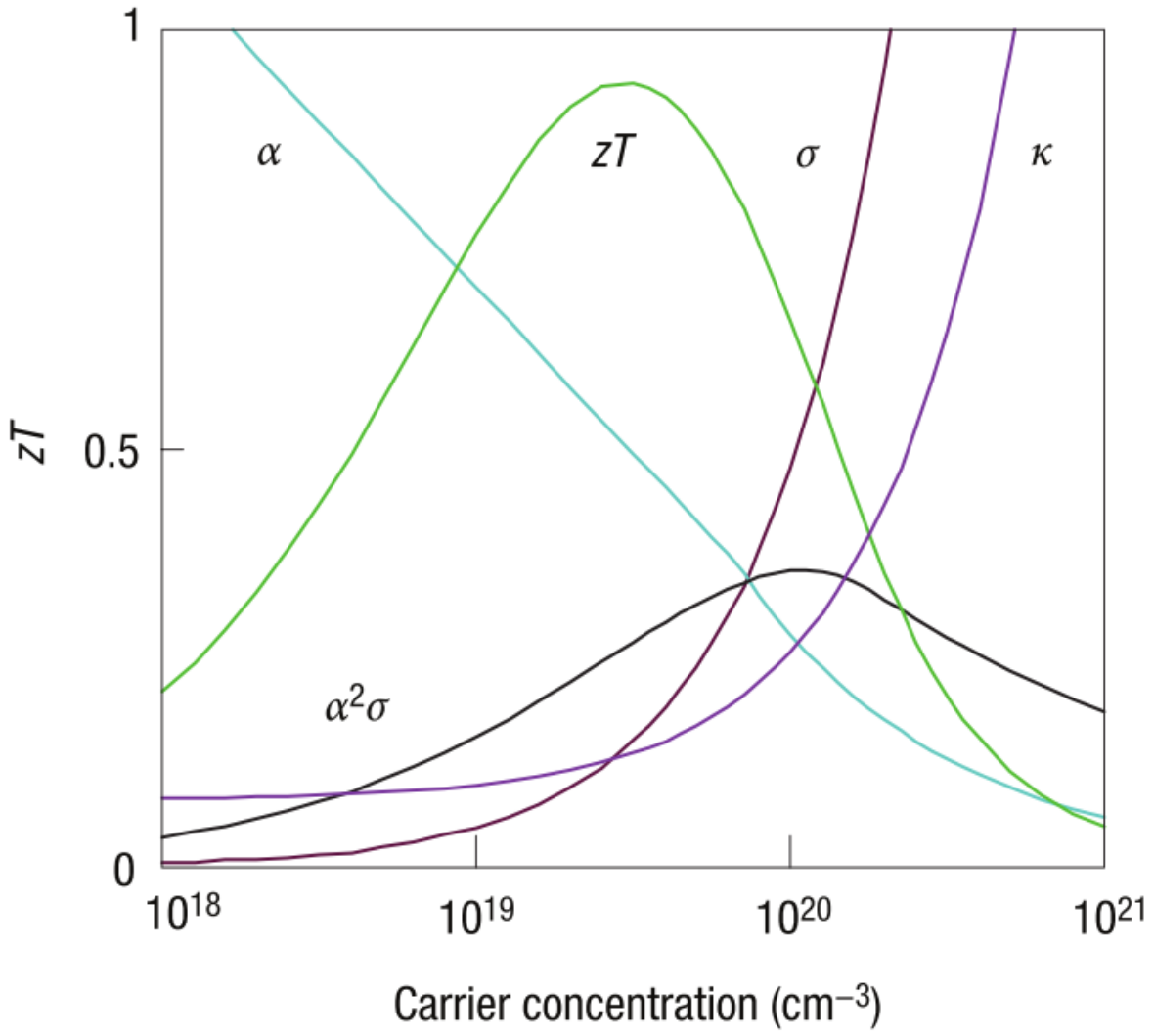

Figure 1-5 – Optimising *ZT* through carrier concentration tuning. Y axes: thermal conductivity (κ) from 0 to 10 $W\ m^{-1}\ K^{-1}$, Seebeck coefficient (S) from 0 to 500 $\mu V\ K^{-1}$ and electrical conductivity (σ) from 0 to 5000 $S\ cm^{-1}$. Trends shown were modelled from bismuth telluride based on empirical data in [15]. Reprinted by permission from Macmillan Publishers Ltd: Nature Materials [14], copyright 2008.

Molecular orbital theory describes the electronic structure of individual molecules, where the highest occupied molecular orbital (HOMO) and the lowest unoccupied molecular orbital (LUMO) are separated by the Fermi level [16]. For bulk materials, the molecular orbitals of the constituent atoms can be viewed as combined; band theory can be used to explain their electronic configuration [17]. This results in 2 bands, a valence band which contains the valence electrons of individual atoms and a conduction band [18]. In a conductor, these 2 bands overlap, allowing electrons to freely move from the valence band to the conduction band, allowing conduction. In an insulator, the valence band and the conductance band are separated by a large band gap (e.g. 5.5 *eV* for undoped diamond [19]), which prevents electrons travelling between the 2 bands. The electronic structure of a semiconductor lies between that of a conductor and an insulator, in that

there is a band gap like an insulator, but the band gap is sufficiently small (e.g. 1.11 *eV* for Si [19]) that electrons can make the jump across the band gap allowing conduction. However energy needs to be provided to make that jump. The energy can be provided by, for example, thermal energy or radiation [20]. These band features are shown in Figure 1-6.

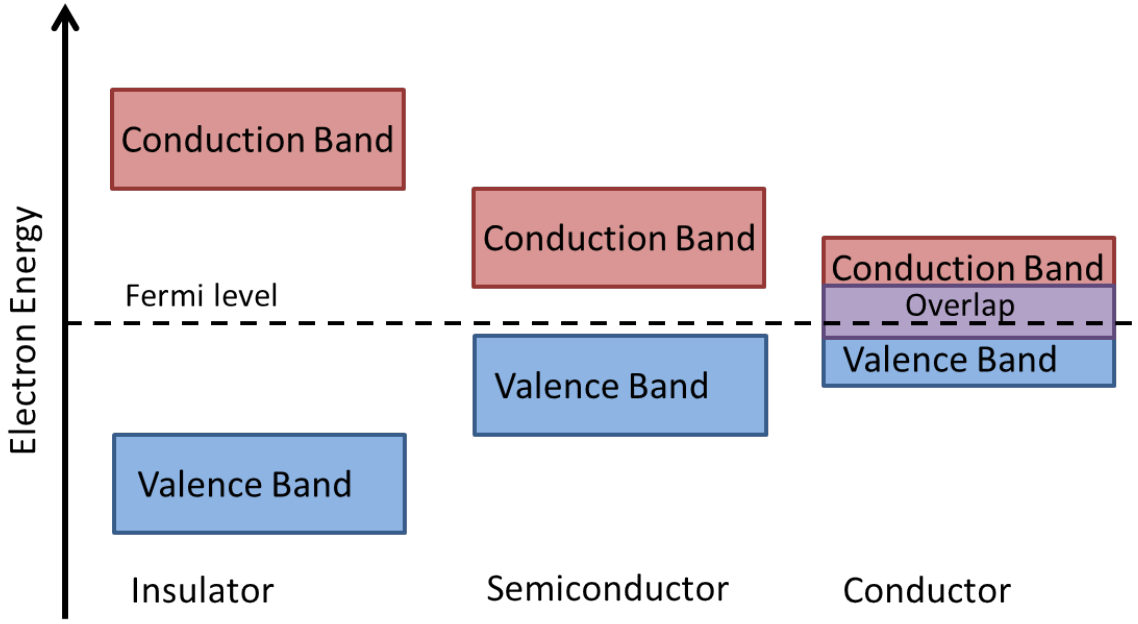

Figure 1-6 – The conductance of insulators, semiconductors and conductors explained by band theory.

In intrinsic semiconductors (e.g. Si and Ge), the Fermi level is fundamentally halfway between the conductance band and the covalence band and for conduction to happen electrons need to pass between the valence and the conductance bands. Doping of semiconductors (e.g. Ge doped Si) can create n- and p-type semiconductors where extra energy levels are added between the valence and conductance bands to allow for conduction to occur with less energy. In n-type materials these are extra electron energy levels added near the top of the band gap which can be easily excited into the conduction band. In p-type materials these are extra hole energy levels added near the bottom of the band gap which allow excitation of valence band electrons, leaving mobile holes in the valance band. A band diagram for these types of semiconductors is shown in Figure 1-7.

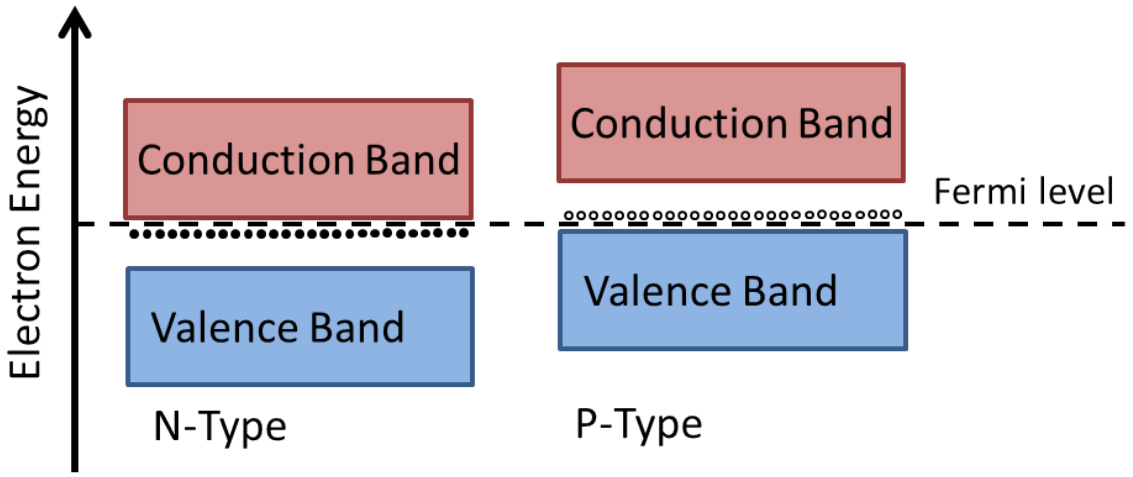

Figure 1-7 – N-Type and P-Type semiconductors explained by band theory, where filled circles represent extra electron energy levels and empty circles represent extra hole energy levels.

1.3 Thermoelectric Materials

Thermoelectric materials are typically classified by material structure and composition. Chalcogenide, clathrate, skutterdite, half-Heusler, silicide and oxides are some of the main classifications [21]. A summarisation of the highest currently reported measured *ZT* values of the main groups of thermoelectric materials is shown in Table 1-1.

Chalcogenides are chemical compounds containing one or more chalcogen (group 16) anion and one or more electropositive element. Typical thermoelectric examples include, Bi_2Te_3, Bi_2S_3 and PbTe. *ZT* values of up to 1.72 have been shown at room temperature for BiSbTe + Te dislocation arrays [22], whilst a *ZT* value of up to 2.3 has been shown for PbTe-PdS at 923 *K* [23].

Clathrates are inclusion compounds in which the guest molecule is in a cage formed by the host molecule or by a lattice of host molecules [24]. Typical thermoelectric examples include $Sr_8Ga_{16}Ge_{30}$, $Ba_8In_{16}Sn_{30}$, $Ba_8Ga_{16}Ge_{30}$ and $Ba_8Ga_{16}Si_{30}$ [25], which are reported to show *ZT* values of 0.5 at room temperature and up to 1.70 at 800 *K* [26]–[28].

Skutterdite is a cobalt arsenide mineral, with variable amounts of Ni and Fe substituting for Co with the general formula $(Co_{1-x-y}Ni_xFe_y)As_{2-3}$. *ZT* values of 0.2 have been shown at room temperature, whilst *ZT* values of 1.2 have been shown at 750 *K* [29].

Half-Heuslers are alloys consisting of three different element groups, two from transition metals and the third from a metal or metalloid group. Typical thermoelectric examples are MNiSn (M= Ti, Zr, Hf), which exhibit *ZT* values of 0.1 at room temperature and *ZT* values of 0.8 at 1000 *K* [30].

Silicides are compounds that contain Silicon. Typical thermoelectrics include Mg(Si, Sn), $MnSi_{1.7}$, CoSi, $Mg_2Si_{0.4}Sn_{0.6}$ and $CrSi_2$[31]. *ZT* values of 0.4 at room temperature and up to 1.1 at 900 *K* have been shown for $Mg_2Si_{0.4}Sn_{0.6}$ [32].

Oxides are compounds that contain oxygen. Typical thermoelectrics include ZnO, SnO_2, InO_3, $SrTiO_3$ and $CaMnO_3$ [33]. Al/Ga co-doped ZnO has been shown to have a *ZT* of 0.65 at 1273 *K* [34], currently substantial room temperature *ZT* values have only been theorised.

Table 1-1 – Summary of the highest currently reported measured *ZT* values of the main groups of thermoelectric materials.

Thermoelectric Material Type	*ZT* at 300 *K*	*ZT* at elevated temperature
Chalcogenides	1.72	2.3
Clathrates	0.5	1.7
Skutterdite	0.2	1.2
Half-Heusler	0.1	0.8
Silicides	0.4	1.1
Oxides	Unknown	0.65

Despite the innovation into several new thermoelectric materials, bismuth telluride and its related compounds are still considered to be the best room temperature thermoelectric materials and are the material of choice in commercial devices for room temperature applications (e.g. heated chairs [10]) [35]. These commercial devices are only being employed in very niche markets, such as portable device charging [9] and furniture heating [10], due to the low efficiency which is directly related to *ZT*, as show in Equation 1.5.

1.3.1 Nanostructuring

Bismuth telluride has shown to exhibit *ZT*s in the region of 1 at room temperature since the 1950s [36]. This was thought to be the highest efficiency achievable until the 1990s. In 1993 Dresselhaus theorised that a large increase in *ZT* could be achieved by quantum confinement, in either 2D (that occurs in quantum wells [37]) or 1D (that occurs in quantum wires [38]). Reduced dimensionality can lead to increases in *ZT* by three means. Reduced dimensionality can provide a

method for enhancing the density of states near the Fermi level (E_F), leading to an enhancement of the Seebeck coefficient (S). Reduced dimensionality can provide opportunities to increase the scattering of phonons due to additional boundaries in the lattice, thus lowering thermal conductivity (κ) by lowering the lattice thermal conductivity (κ_L). Reduced dimensionality can finally provide opportunities for increased carrier motilities at a given carrier concentration when quantum confinement conditions are satisfied, increasing the power factor ($S^2\sigma$). This gave a prediction that ZT values up to 14 could be achieved which led to rejuvenation in the field of thermoelectrics.

1.4 Fabrication Techniques

The quick fabrication of highly efficient, low cost thermoelectric materials is the key challenge in modern thermoelectrics [39]. There are several techniques used to fabricate thermoelectric materials, including thin film technologies (metal organic chemical vapour deposition [40], [41], molecular beam epitaxy [42], [43]), single crystal growth [44], and ball milling [45]. These techniques require high vacuum and elevated temperatures, which makes fabrication costly.

Electrodeposition offers a cheap and facile way of producing p- and n–type films of thermoelectric materials, as fabrication can be done at room temperature and atmospheric pressure [46]. Room temperature fabrication has the benefit of reducing thermal stress, whilst the absence of a vacuum reduces equipment costs. Electrodeposition allows the control of a large number of variables such as: deposition potential, electrolyte concentration (both the inert and electroactive species), pH of the electrolyte, temperature of the electrolyte, along with additives and impurities in the electrolyte. This large range of variables, gives an ability to produce films with different characteristics and the ability to produce high deposition rates [47], [48] allowing fast fabrication.

Electrodeposition techniques facilitate the doping of further electroactive species within the electrolyte solution, this in turn can broaden the variety of otherwise more simplistic films. As a result of this there is the potential to improve current electrodeposited thermoelectric materials. This is the research rational in Chapter 3.

Nanostructured materials can also lead to increases in thermoelectric performance (ZT). Templates can be added onto the working electrode within electrochemical cells, to produce nanostructured thermoelectric materials. Current examples of this include porous alumina [49], polyimide [50], [51] or polycarbonate [52]. The fabrication process of templates, typically anodizing aluminium, and the removal of the templates (if required), for example dissolution in NaOH, leads to time consuming steps in harsh conditions (e.g. alkaline) which can cause degradation of the electrodeposits. The use of a lyotropic liquid crystal (LLC) (1.5) as a template

instead, would be cheaper, quicker and allow for mild conditions to be used for the removal of the template (e.g water). Furthermore, LLCs can exhibit several different phases, such as lamellar, hexagonal and bicontinuous cubic [53], which means there is the potential for forming a variety of different nanostructures. These reasons are the research rational why lyotropic liquid crystals were used as templates in Chapter 4 and Chapter 5.

1.5 Lyotropic Liquid Crystals

Liquid crystals combine the flow properties of an ordinary liquid, with the anisotropic physical parameters generally only found for crystals (e.g. birefringence) [53]. Two main groups of liquid crystals exist, thermotropic and lyotropic [53]. This work will only focus on lyotropic liquid crystals; thermotropic liquid crystals will not be discussed further.

Lyotropic liquid crystal phases can be formed on the dissolution of amphiphilic molecules in a solvent. Amphiphilic molecules are bifunctional molecules that comprise a polar (hydrophilic) head group and a non-polar (hydrophobic) carbon tail. There are several different types of lyotropic liquid crystal phase structures, such as lamellar, hexagonal and bicontinuous cubic, each with a different extent of molecular ordering within the solvent matrix. Some of these phases are shown in Table 1-2. The concentration of the material in the solvent dictates the type of lyotropic liquid crystal phase that forms. It is however also possible to alter the type of lyotropic phase exhibited at each concentration by changing the temperature [53]. Different amphiphilic molecules will form different phases at different concentrations and temperatures.

Table 1-2 – a) Illustration of an amphiphilic molecule, b-f) type 1 and type 2 orientation and a selection of phases exhibited by lyotropic liquid crystal molecules

<table>
<tr><td rowspan="2"> 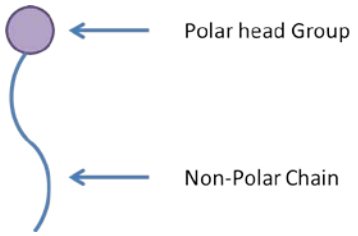
</td><td>i</td><td> 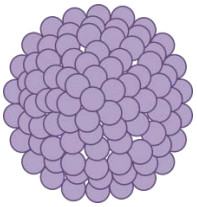 </td><td>i</td><td> 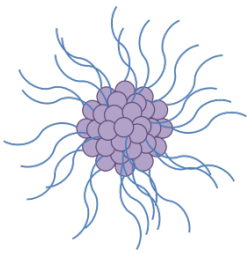 </td></tr>
<tr><td>ii</td><td> 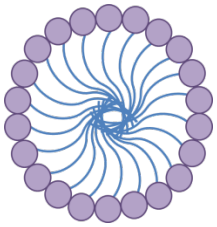 </td><td>ii</td><td> 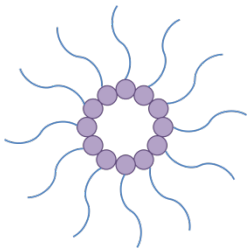 </td></tr>
<tr><td>a) Amphiphilic molecule</td><td colspan="2">b) i) Type 1 micellar
ii) Type 1 micellar cross-section</td><td colspan="2">c) i) Type 2 micellar
ii) Type 2 micellar cross-section</td></tr>
<tr><td> 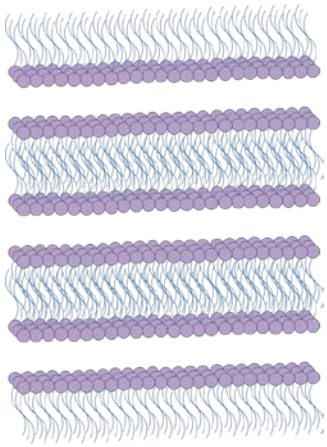 </td><td colspan="2"> 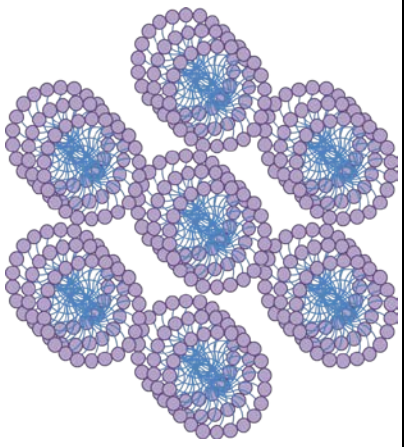 </td><td colspan="2"> 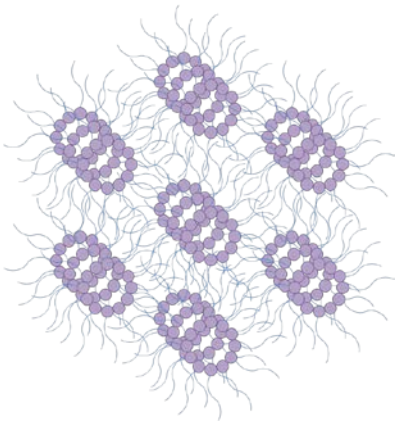 </td></tr>
<tr><td>d) Lamellar</td><td colspan="2">e) Type 1 hexagonal</td><td colspan="2">f) Type 2 hexagonal</td></tr>
</table>

When amphiphilic molecules are mixed with an aqueous electrolyte solution in the correct proportions the electrolyte acts as the solvent, causing the formation of a liquid crystal phase. This can give rise to water channels (as seen in Figure 1-8). Aqueous electrodeposition occurs in these water channels, causing the resulting electrodeposited species to have a nanostructure that is the same as the water channels [54]. This process is illustrated in Figure 1-8. For type 1 lyotropic liquid crystals (curved away from the solvent, Table 1-2b+e) this is the inverse of the lyotropic liquid crystal phase, for type 2 lyotropic liquid crystals (curved towards the solvent, Table 1-2c+f) this is the same as the lyotropic liquid crystal phase.

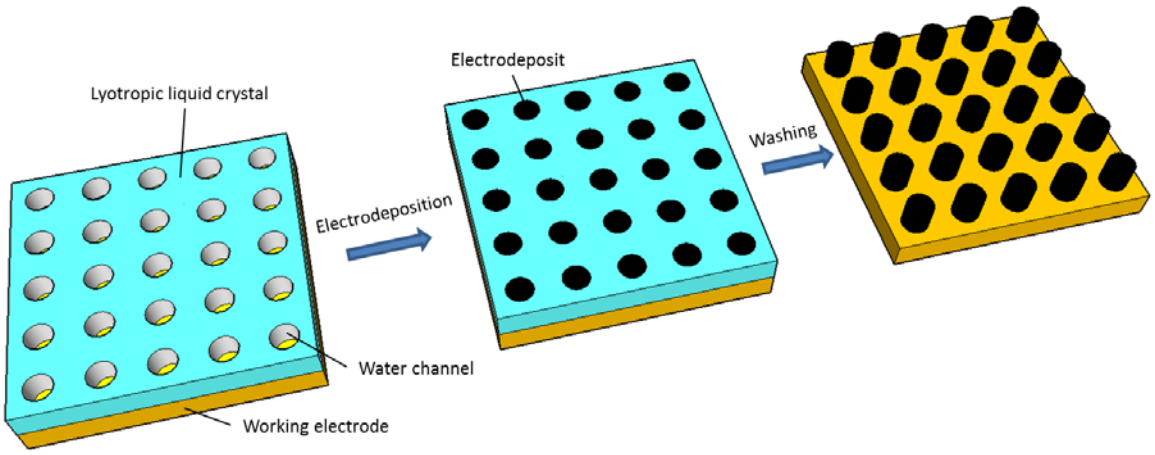

Figure 1-8 – Schematic diagram illustrating the principle of lyotropic liquid crystal templating during electrodeposition.

There are currently no examples of nanostructured bismuth telluride or bismuth sulphide being produced by electrodeposition through lyotropic liquid crystals. In fact, there is only one paper reporting use of any thermoelectric material (CdTe) [55], however, other nanostructured materials have been electrodeposited through lyotropic liquid crystals. These include metals (Pt, Sn, Co and Pd) [56]–[60], metal oxides (ZnO and Cu_2O) [61], semimetals (Se and Te) [62], [63], polymers (poly-(1,2-diaminobenzene)) [64], and bimetallic layered structures (Pd with Rh) [65].

1.6 Pd Nanostructuring

One of the materials that have been nanostructured previously using a lyotropic liquid crystal template is Pd [60]. This was achieved by electrodepositing through the type 1 hexagonal phase of the non-ionic surfactants $C_{16}EO_8$ (octaethyleneglycol monohexadecyl ether) and Brij®56. A follow up paper studied the potential application of the material in a gas sensor [66]. Nanostructured palladium however has a range of potential applications in electrochemical biosensors [67] and supercapacitors [68], [69] as well as gas sensors [66], [70], [71]. The largest area of interest is fuel cells [72]–[79]. Fuel cells are seen as a key new green technology with applications in transport and portable power generation. Currently fuel cells are electrocatalysed by platinum based materials, but the cost and limited supply of Pt makes this option far from ideal. Comparatively Pd has a three times higher abundance in the Earth's crust compared to Pt, 0.015 ppm by weight and 0.005 ppm by weight respectively [72].

There are currently no examples of nanostructured Pd being formed from a type 2 lyotropic liquid crystal phase. The usefulness of nanostructured Pd produced using a lyotropic liquid crystal phase has also not been studied for fuel cell applications.

Chapter 2: Experimental Methods

2.1 Materials

2.1.1 Electrodes

2.1.1.1 Working Electrodes

For cyclic voltammetry and surface area studies either a 2 *mm* gold electrode encapsulated in Kel-F (Teflon-like) support (CH101, CH Instruments, Inc.), or a 3 *mm* glassy carbon electrode encapsulated in glass was used. Prior to use the electrode was polished using 3 different grades of alumina powder on MicroCloth (Buehler 407218). The first grade of alumina used was 1.00 μm, the second 0.30 μm and the third 0.05 μm. Finally the electrode was polished on clean MicroCloth. The electrode was washed with deionised water after each polishing step.

For samples used for Helium Ion Microscopy (HIM), Scanning Electron Microscopy (SEM), Energy Dispersive X-ray spectroscopy (EDX), X-Ray Diffraction (XRD), Seebeck and Hall characterisations, gold (Au) on silicon (Si) wafer electrodes were used unless otherwise stated. These were prepared by taking 6 inch p-type (1 0 0) Si wafers and sputtering a 20 *nm* layer of titanium (Ti), followed by a 200 *nm* layer of Au on, using an AJA ATC-Orion 5 UHV with Load-Lock. The wafer was then cut into 1.5 *cm* × 1.5 *cm* sections using a diamond tipped pen, each of which would make a working electrode. The Au on Si wafer section was sonicated in isopropyl alcohol (IPA) for 10 minutes. Copper (Cu) tape was used to make an electrical contact and polyimide tape was used to define a 10 *mm* × 10 *mm* working electrode area.

Au DVDs (Delkin Devices) were used to prepare samples to take to SAXS facilities (see 2.3.6). The two plastic layers of the DVD were separated using mechanical force. The exposed gold layer disc was cut into 1.5 *cm* × 1.5 *cm* using scissors. Cu tape was used to make an electrical contact and polyimide tape was used to isolate a 10 *mm* × 10 *mm* working electrode area.

2.1.1.2 Reference Electrodes

Custom made saturated calomel electrodes (SCE) were used as a reference for every experiment, unless otherwise stated. The SCEs were prepared by the dropwise addition of Hg into the inner glass tube of the electrode, so that it made a contact with the Pt wire. On top of this a layer of mercury (I) chloride (Hg_2Cl_2) was added, followed by a layer of glass wool which had been soaked with saturated potassium chloride (KCl). The glass wool acted as a plug, preventing the Hg and

Hg_2Cl_2 layers from moving. The outer glass tube of the electrode, which had a porous glass frit at the bottom, was filled with saturated KCl solution. The inner glass tube of the electrode was then screwed into the outer glass tube of the electrode, forming the SCE reference electrode. The SCEs were then left for several days to equilibrate. The electrodes were tested against a commercial SCE and were only used if found to be stable and within ±5 *mV*. The SCEs were stored in a saturated KCl solution when not in use and potentials were regularly tested to ensure they had not drifted.

Saturated mercury/mercury sulphate electrodes (SMSE) were used as reference electrodes when electrolytes contained Ag. SMSEs were also used to perform cyclic voltammetry (CV) to calculate surface area. The SMSEs were prepared by the dropwise addition of Hg into the inner glass tube of the electrode, so that it made a contact with the Pt wire. On top of this a layer of mercury sulphate (Hg_2SO_4) was added, followed by a layer of glass wool which had been soaked with saturated K_2SO_4. The glass wool acted as a plug, preventing the Hg and Hg_2SO_4 layers from moving. The outer glass tube of the electrode, which had a porous glass frit at the bottom, was filled with saturated K_2SO_4 solution. The inner glass tube of the electrode was then screwed into the outer glass tube of the electrode, forming the SMSE reference electrode. The SMSEs were then left for several days to equilibrate. The electrodes were tested against a commercial SCE and were only used if found to be within +444±5 *mV* of the standard. The SMSEs were stored in a saturated K_2SO_4 solution when not in use and potentials were regularly tested to ensure the voltage had not drifted.

2.1.1.3 Counter Electrodes

All counter electrodes used were platinum (Pt) gauze electrodes, which had a much larger surface area than the working electrode. This ensured electrochemistry was limited at the working electrode, rather than the counter electrode. Prior to use they were annealed in a clean blue flame, to remove any contaminants from the electrode.

2.1.2 Electrolytes

2.1.2.1 Bismuth Telluride and derivatives

Bismuth telluride and its ternary (bismuth tellurium selenide) and quaternary (Cu or Ag doped bismuth tellurium selenide) derivatives were prepared by dissolving the semimetal and metal precursors (see Table A-1 – Table A-8) in concentrated HNO_3. This was achieved by leaving them stirring overnight. Deionised water (Merck Millipore Milli-Q Gradient A10 Ultrapure water purification system, 18.2 *MΩ cm*) was then added to make the solutions up to the desired

concentration. After further stirring the solution was bubbled through with Argon for a minimum of 20 minutes, to remove dissolved oxygen. Doped bismuth tellurium selenide electrolytes with doping of less than 2.00 *mM* Cu doping or 1.00 *mM* Ag, were prepared by mixing undoped bismuth tellurium selenide electrolytes with doped bismuth tellurium selenide electrolytes of either Cu or Ag in the required ratios.

2.1.2.2 Bismuth Sulphide

Bismuth sulphide electrolytes were prepared by mixing the bismuth and sulphide precursors along with EDTA in dissolved water (Merck Millipore Milli-Q Gradient A10 Ultrapure water purification system, 18.2 *MΩ cm*) over night (Table A-9). The solution was then left to settle for 2 days to allow a formed black precipitate to settle. A clear electrolyte solution was then separated and bubbled through with Argon for a minimum of 20 minutes, to remove dissolved oxygen.

2.1.2.3 Palladium (Pd)

Palladium (Pd) electrolytes were prepared by adding the Pd precursor ($(NH_4)_2PdCl_4$) and NH_4Cl to concentrated stirring HCl and then immediately adding dissolved water (Merck Millipore Milli-Q Gradient A10 Ultrapure water purification system, 18.2 *MΩ cm*) at a rate of approximately 10 *mL* a minute (Table A-10). The solution was left stirring overnight to allow for full dissolution. After further stirring the solution was bubbled through with Argon for a minimum of 20 minutes, to remove dissolved oxygen.

The constituents of each electrolyte are shown in Table A-1 - Table A-10 in Appendix A.1.

2.2 Electrochemical Techniques

All electrochemical experiments were conducted using a 3 electrode setup. The reference electrode was placed as close as possible to the working electrode without touching the working electrode. Where possible the working and counter electrodes were placed parallel to each other. An example setup is shown in Figure 2-1, which contains a phytantriol coated working electrode.

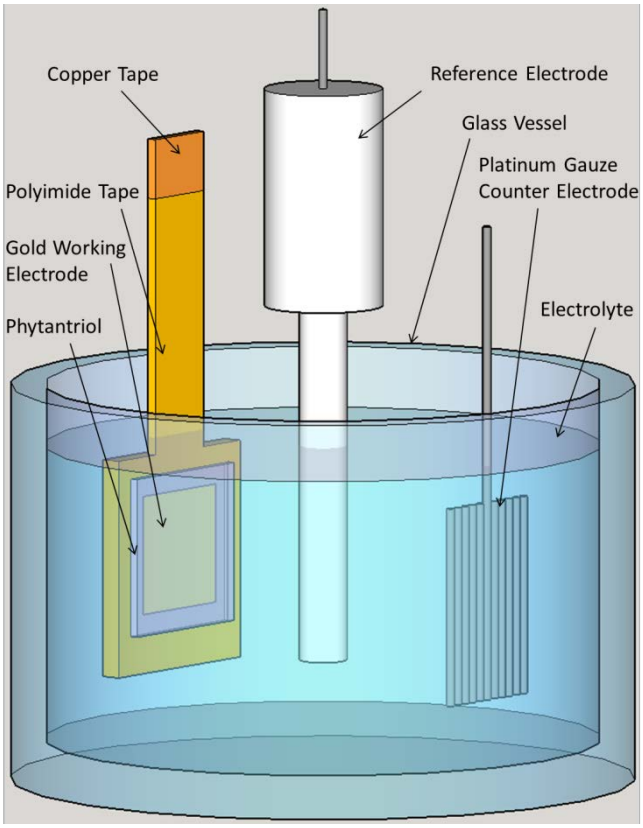

Figure 2-1 – An example of the electrochemical setup. Here the working electrode is made of Au on Si and the working electrode is coated in phytantriol.

2.2.1 Cyclic Voltammetry

Cyclic voltammetry (CV) was conducted using an AutoLab Lab PGSTAT30 potentiostat/galvanostat and the AutoLab General Purpose Electrochemical System (GPES) software. The working electrode was a gold disc or glassy carbon disc electrode (as described in 2.1.1.1), the counter electrode a Pt gauze electrode (2.1.1.3) and either a reference electrode of a SCE or a SMSE (2.1.1.2). Initially the potential was held at a potential where no reaction occurred for 5 *s*, after which the potential was swept cathodically until the onset of hydrogen evolution. At the onset of hydrogen evolution the potential was swept anodically until the onset of oxygen evolution, after which the potential was swept back to the initial potential (the potential time profile is shown in Figure 2-2a). A typical CV is shown in Figure 3-3.

2.2.2 Potentiostatic Electrodeposition

Potentiostatic electrodeposition (chronoampometry) was performed using an AutoLab Lab PGSTAT30 potentiostat/galvanostat and the AutoLab General Purpose Electrochemical System (GPES) software. For electrode choices see 2.1.1. The potential was initially held at a potential where no reaction occurs before stepping to a potential where deposition occurs (as shown in

Figure 2-2b), as determined by CV. This potential was held for a set period of time, at the end of which the cell was turned off.

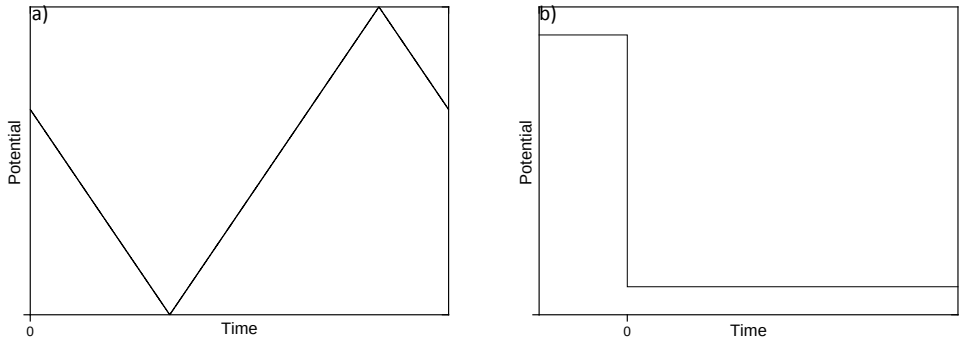

Figure 2-2 – Potential time profiles for a) Cyclic voltammetry and b) Potentiostatic electrodeposition

2.3 Analytical Techniques

2.3.1 Scanning Electron Microscopy (SEM)

A scanning electron microscope (SEM) (as shown in Figure 2-3) uses a finely focused beam of electrons produced by an electron gun which are scanned over a conducting sample. Images are formed by observing either directly backscattered electrons (electrons bouncing back immediately of the surface), or more commonly by observing secondary electrons (inelastically scattered electrons) which originate from within a few nanometres of the sample surface due to their low energy (<50 *eV*) [80]. For this work only secondary electrons have been observed.

When a sample is scanned an inelastic collision can occur, resulting in the outer atoms becoming ionised. A secondary electron current is formed when electrons escape from these ions on the surface into the vacuum of the microscope. This current is representative of only a very small outer layer of a sample; this allows an image of the surface to be formed in high resolution, yielding the ability to observe the morphology of the surface.

A Zeiss EVO LS25 ESEM was used to observe samples in this work. Accelerating voltages up to 15 *kV* were used with a secondary electron detector.

Samples were mounted as deposited, on either a 12 *mm* diameter aluminium SEM specimen stub with double sided adhesive carbon discs, or mounted using a 18 *mm* SEM clip specimen mount (Agar Scientific).

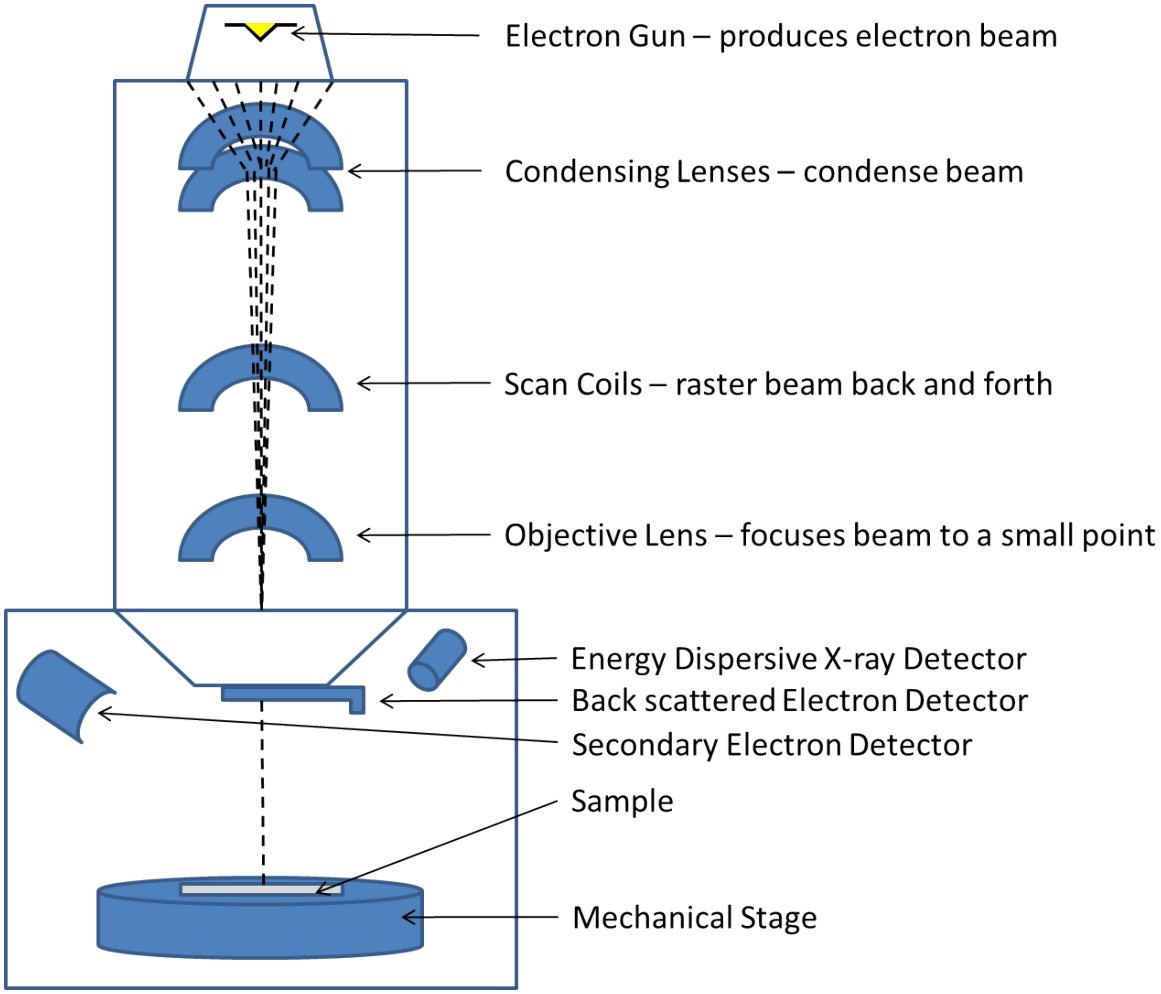

Figure 2-3 - Schematic diagram of a scanning electron microscope (SEM), showing a beam of electrons being finely focussed by the condensing lenses, moved by the coils and focused by the objective lens before hitting the sample. Various signals are consequently produced which can be detected by various detectors [81].

2.3.2 Energy Dispersive X-Ray Spectroscopy (EDX)

Energy dispersive x-ray spectroscopy (EDX) is a technique used to perform elemental analysis of samples. The technique uses an x-ray detector mounted inside a SEM chamber, which detects the characteristic x-ray patterns emitted by excited atoms. Each element emits x-rays of different wavelengths, which allows for the differentiation of elements [82].

An EDX spectrum consists of, white radiation (Bremsstrahlung) emitted from decelerating electrons when they are fired at a metal target [83] and discrete wavelengths emitted characteristically by elements. The characteristic emission (as shown in Figure 2-4) occurs after a core electron is displaced from an atom in the sample by the electron beam, this allows an electron from one of the higher energy shells to fill the vacancy, causing a photon emission that is

equal to the drop in energy of the electron. These photons are characteristic for each element and form the x-ray patterns that are detected by the EDX probe.

The Zeiss EVO LS25 ESEM incorporated an Oxford Instruments EDX detector which was used to analyse the composition of materials produced in this work. A bismuth telluride standard (Mirco-Analysis Consultants Ltd) was used as a reference.

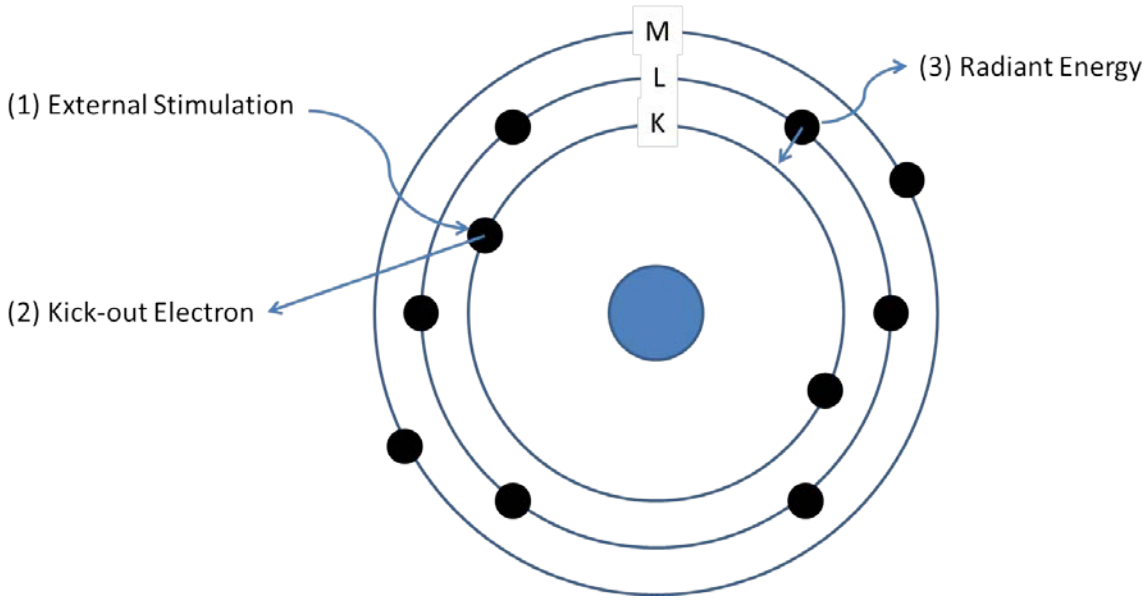

Figure 2-4 – Schematic diagram displaying external stimulation by the electron beam ejecting a core electron, leading to relaxation of an electron from a higher shell causing characteristic radiant X-ray energy from the element under study [82].

2.3.3 Helium Ion Microscopy (HIM)

A helium ion microscope is a form of an ion microscope (as shown in Figure 2-5), which uses a finely focused beam of helium ions. The beam is produced when helium atoms at low temperature are exposed to a metallic (typically tungsten) sharpened needle (whose tip consists of just 3 atoms, a trimer) held at a high positive voltage [84]. The resultant helium ion beam is focused, before being emitted onto the sample surface.

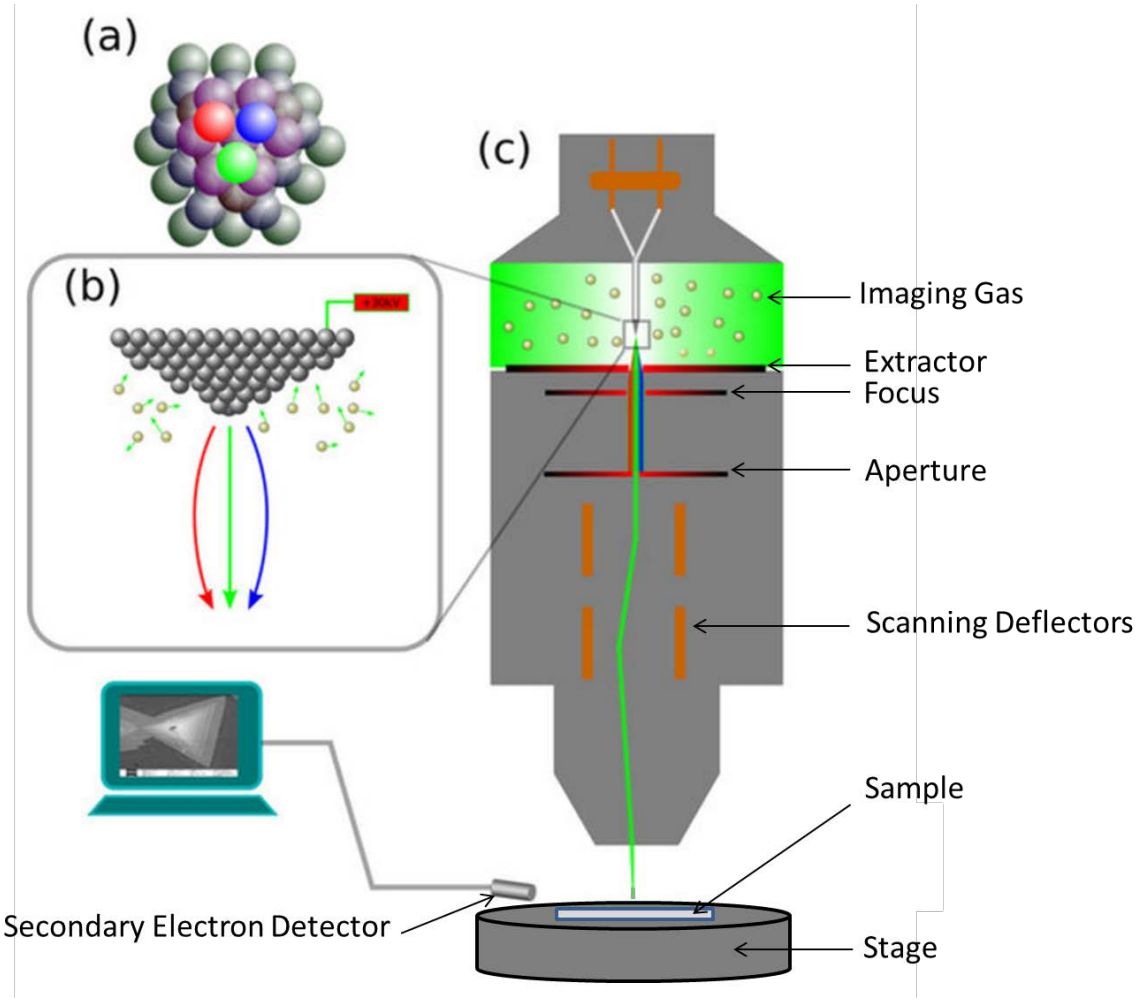

Figure 2-5 – (a) Trimer of helium ion microscope source, (b) source of helium ion microscope, (c) structure of helium ion microscope. Image reproduced and edited from Guo *et al.* [85], who are acknowledged.

An image is formed by the detection of secondary electrons or backscattered ions. In this work images are only created using secondary electrons which are primarily generated via kinetic emission from incoming ions colliding with the sample [86]. Once generated, secondary electrons need to escape the sample in order to be imaged. The escape process can be described as a diffusion process, with the characteristic diffusion length being in the order of a 1 *nm* for nearly all materials [87]. This leads to only the first few nanometres of a sample emitting secondary electrons, which allows a high resolution image of the surface to be formed.

The helium ion beam allows for a higher resolution compared to an electron beam, because the de Broglie wavelength of helium ions is smaller than that of electrons. This allows the helium ions to be focused into a smaller probe size. This provides a much smaller interaction volume at the sample surface compared to electrons [88]. Up to 0.30 *nm* resolution has been reported in the literature [89].

This work uses a Zeiss Orion Helium Ion Microscope for imaging of electrodeposited films which can achieve resolution of 0.5 *nm* [90].

2.3.4 Transmission Electron Microscopy (TEM)

A transmission electron microscope (TEM) (as shown in Figure 2-6) uses a finely focused beam of electrons produced by an electron gun which are transmitted through the sample (~100 *nm* thick). A series of lenses then focus and magnify the transmitted electrons onto either a fluorescent screen which emits photons when irradiated by the electron beam or onto a charge-coupled device camera which is digitising the image for display on a computer.

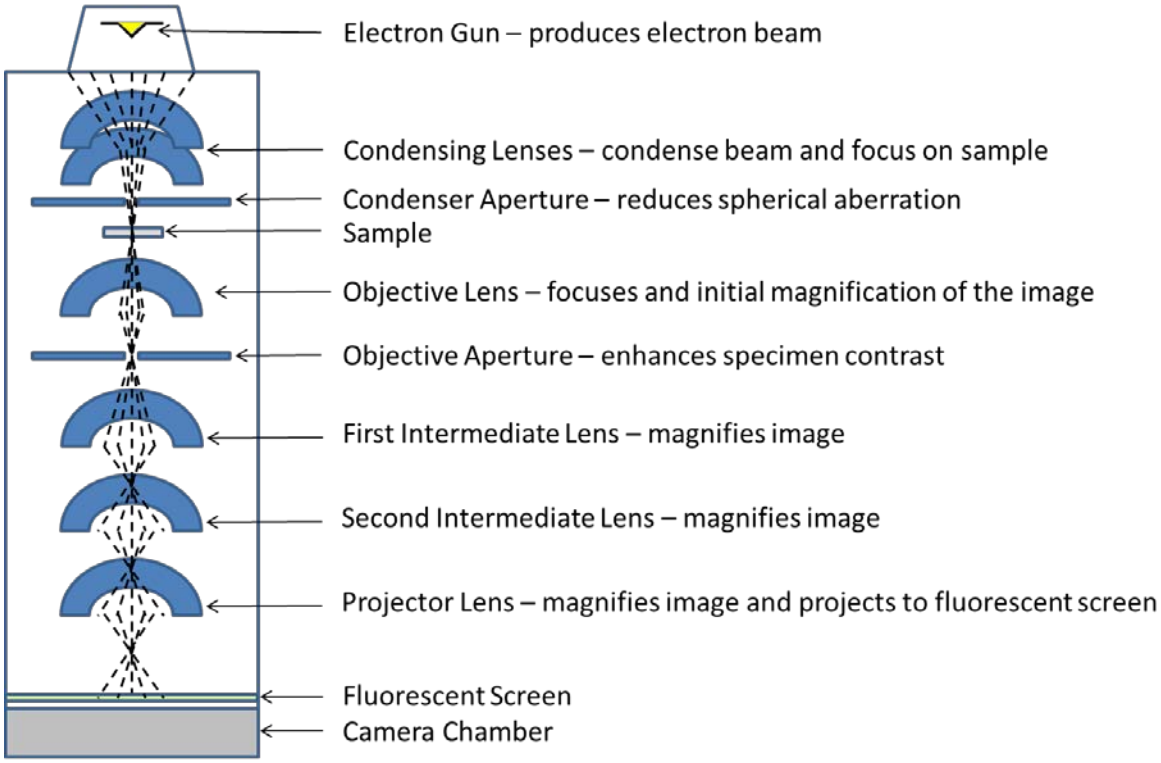

Figure 2-6 - Schematic diagram of a transmission electron microscope (TEM), showing a beam of electrons being finely focussed onto the sample by the condensing lenses, focused and magnified by the objective lens, further magnified by the intermediate lenses and then magnified and projected onto the fluorescent screen by the projector lens. The image is viewed on a fluorescent screen which gives off photons when irradiated by the electron beam, or the screen is raised in order for a digital capture with a computer digitising and archiving a charge-coupled device camera [91].

Samples were prepared for transmission electron microscopy by scraping small sections of nanotemplated films with a scalpel over 400 mesh copper transmission electron microscopy grids (Sigma Aldrich). A FEI Tecnai T12 transmission electron microscopy with an accelerating voltage of

100 *kV* was used to acquire transmission electron microscopy images. A Tecnai T12 can generate a point resolution of up to 0.34 *nm* [92].

2.3.5 X-Ray Diffraction (XRD)

X-Ray Diffraction occurs when constructive interference occurs where atoms are suitably positioned relative to lattice planes meeting the Bragg condition shown in Equation 2.1 [93]. The principle is depicted in Figure 2-7.

$$n\lambda = 2dsin\theta \quad (2.1)$$

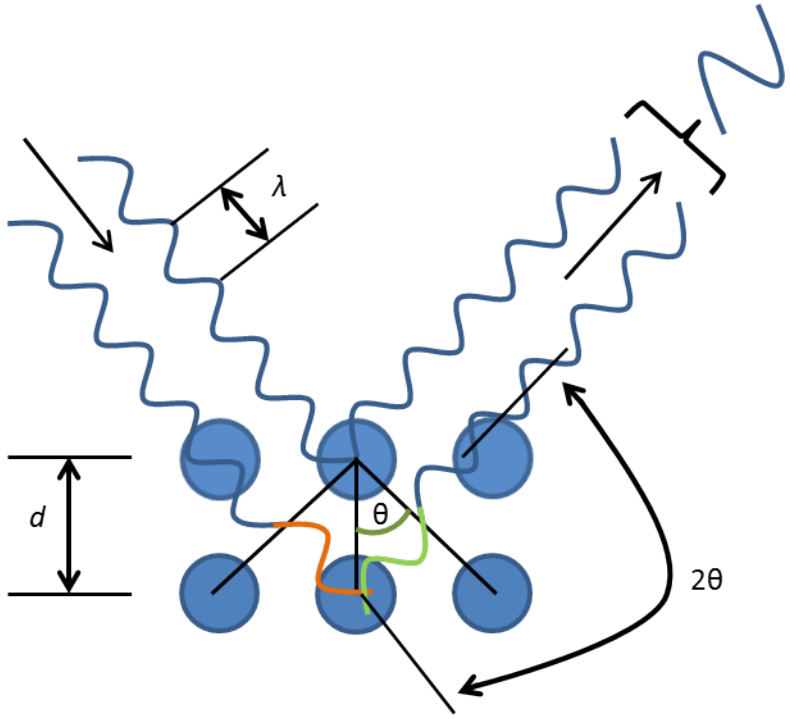

Figure 2-7 - Schematic diagram showing the concepts of Bragg's law. X-rays are scattered by the regular array of atoms and if Bragg's law is obeyed, the waves are added constructively [20].

The resulting x-ray diffraction pattern can be used to identify a compound by comparing it to standard spectrums. This work compares acquired patterns to standard patterns that are available in the diffraction pattern analysis software PDXL (version 2.0, Rigaku). If the detector and source arms are both scanned at an equal angle to the sample, this is called a symmetric scan. In this case, the dominant peak in the spectrum indicates the preferred crystal orientation of the sample. Asymmetric scans are where the source is held at a constant shallow angle to the sample and the detector is scanned through theta values. This technique is typically used for thin films to allow for the production of a greater signal. There is no simple trend for peak intensity and crystal orientation, but the compound can still be identified.

The grain size can also be obtained from a symmetric spectrum. This is achieved by using the Scherrer equation [94], Equation 2.2.

$$D = \frac{0.9\lambda}{\beta cos\theta} \quad (2.2)$$

D is the grain size, λ is the wavelength of the incident x-rays, β is the full half width maximum intensity of the peak (in radians), and θ is the diffraction angle. Here 0.9 is used, as the particles are assumed to be spherical.

Unless otherwise stated this work uses a Rigaku SmartLab x-Ray diffractometer for symmetric and asymmetric diffraction patterns of electrodeposited films. The Rigaku Smartlab uses Cu Kα radiation with a wavelength of 1.5406 *Å*.

2.3.6 Small Angle X-ray Scattering (SAXS)

Small Angle X-Ray Scattering (SAXS) experiments were carried out at the European Synchrotron Radiation Facility on the XMaS beamline and at Diamond Light Source on beamlines i07 and i22.

Results are shown as both 2D diffraction patterns and 1D radial integrations. 1D radial integrations are shown as intensity against both q and 1/d. Unless otherwise stated all SAXS diffraction patterns in this work come from a structure with cubic symmetry, and therefore lattice parameters (a_o) can be calculated from diffraction peaks (d_{hkl}) using Equation 2.3 [95].

$$a_0 = d_{hkl} \times \sqrt{h^2 + k^2 + l^2} \quad (2.3)$$

2.3.6.1 SAXS of Electrolyte with Phytantriol Mixtures

2.3.6.1.1 In Capillary

Boron glass 1.5 *mm* diameter capillaries (Capillary Tube Supplies Ltd), or Quartz 2 *mm* diameter capillaries (Capillary Tube Supplies Ltd) were lined with phytantriol by auto-pipetting a 2:1 w/w phytantriol to ethanol mixture into the capillary. The capillaries had a wall thickness of 0.01 *mm*. After 30 minutes all of the ethanol had evaporated and water was flushed through the capillary to create a homogenous phytantriol layer lining the capillary. The water was left to evaporate for at least an hour before the capillary was filled with the desired electrolyte for study. The capillary was then mounted into a holder and placed in front of the SAXS beam. The capillary was placed in front of the beam over a series of hours, to test the stability of phytantriol with the electrolyte. A schematic diagram of the setup is shown in Figure 2-8.

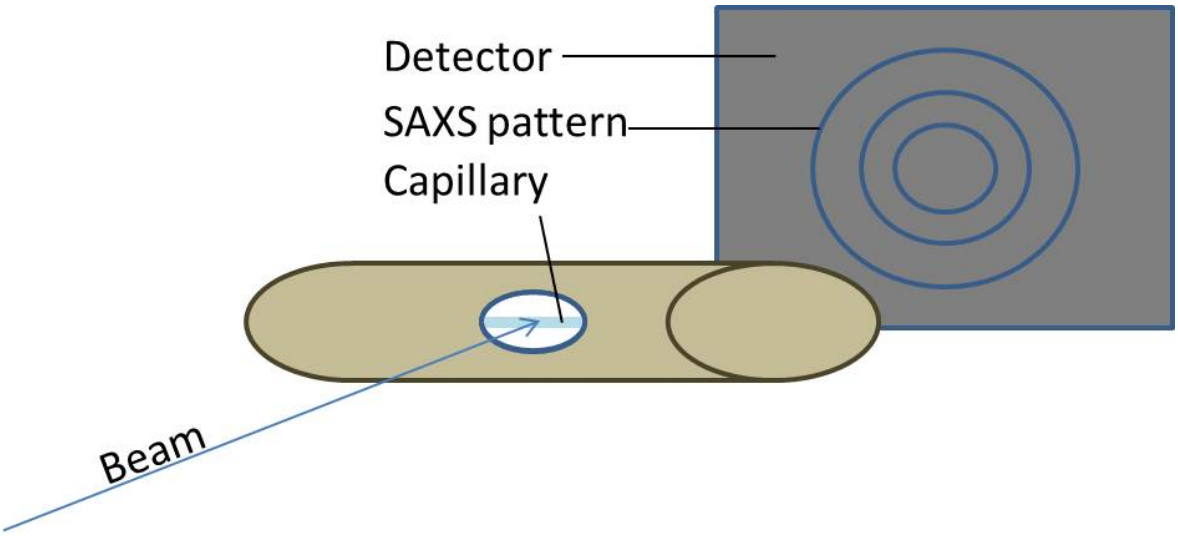

Figure 2-8 - Schematic diagram of the setup used for SAXS stability measurements. The capillary contains the phytantriol electrolyte mixtures which the beam is transmitted through.

2.3.6.1.2 On Au

To investigate the phase of phytantriol on Au when immersed in electrolyte, a bespoke 3D printed cell with polyimide windows was filled with 1 *mL* of electrolyte. To this either a section of Au DVD or a gold foil (5 *mm* × 12.5 *μm* × 0.5 *mm* Au foil (Goodfellow 99.95%)) was added. Prior to placement in the cell Au samples were dipped into a phytantriol mixture (2:1 phytantriol to ethanol by weight) and left for 30 minutes to dry. The beam was aligned onto the Au sample by moving the beam stop, reducing the beam by using a high level of filtersets (this prevented the detector being damaged from direct beam imaging), then scanning the entire setup across the beam. The Au sample was located by looking for the reduction in beam intensity caused by the shadow of the Au sample. The Au sample was centred on the beam, the beam stop moved back into position and the filtersets removed. Figure 2-9 depicts the experimental setup.

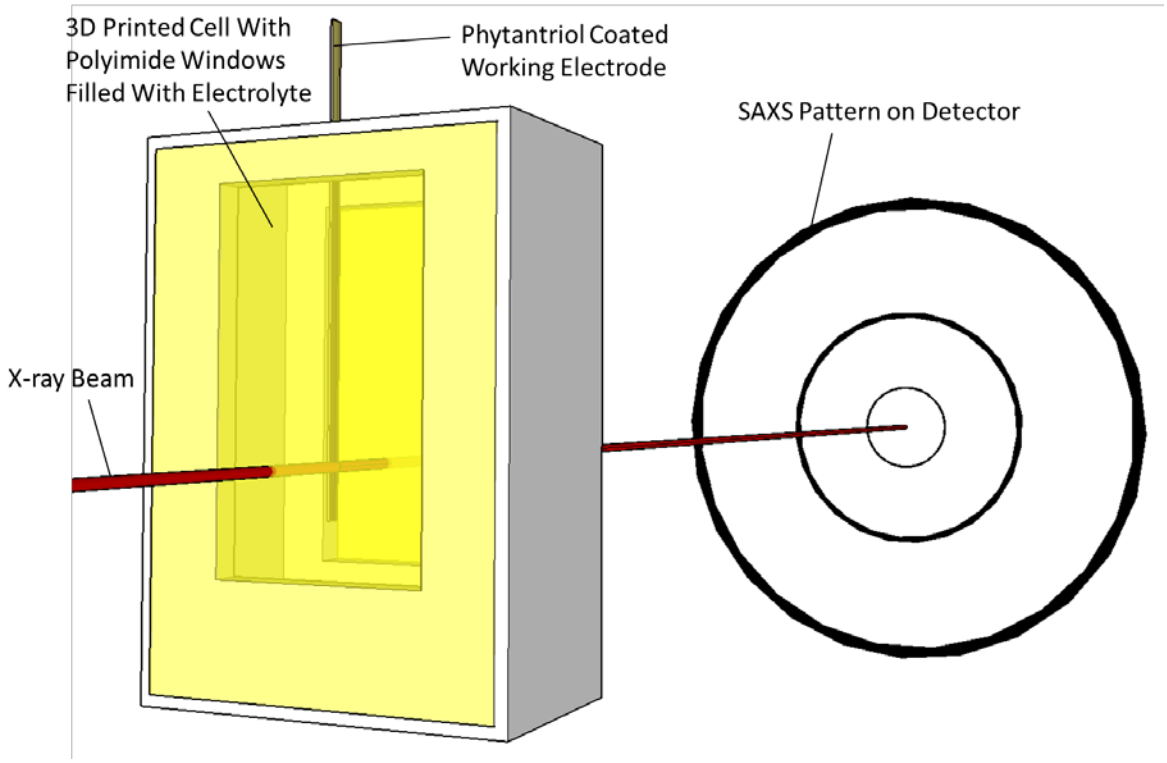

Figure 2-9 - A schematic diagram showing the experimental setup for SAXS on a phytantriol coated working electrode immersed in electrolyte.

2.3.6.2 SAXS of Electrodeposited Samples

Samples were electrodeposited onto Au DVDs (2.1.1.1) for investigation by SAXS. Samples were placed in front of the x-ray beam with the plane of the DVD placed perpendicular to the direction of the x-ray beam. The sample side of the DVD faced the detector. The experimental setup is depicted in Figure 2-10.

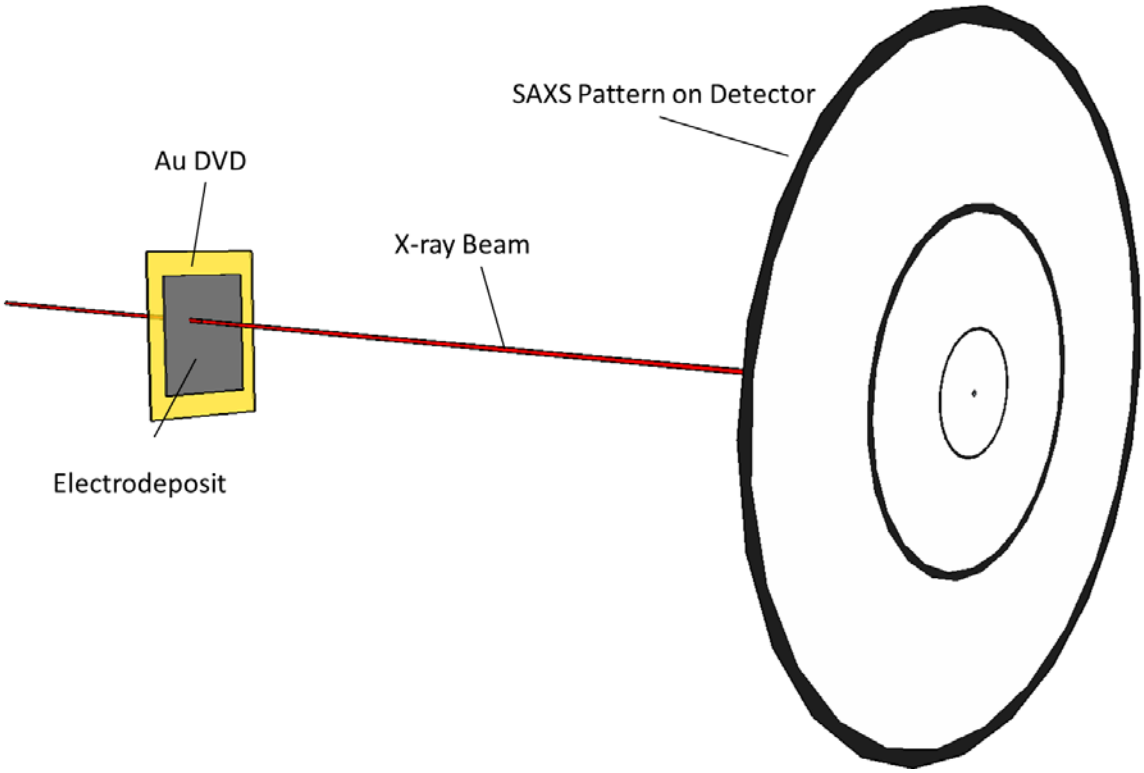

Figure 2-10 – Experimental setup for SAXS of electrodeposited samples.

2.3.7 Seebeck Measurements

The Seebeck voltage (*V*) is defined as the induced thermoelectric voltage created in response to a temperature difference across a material. The Seebeck coefficient *S* ($V\,K^{-1}$) is defined as the induced thermoelectric voltage created per Kelvin in response to a temperature difference across a material. Different materials display different Seebeck coefficients.

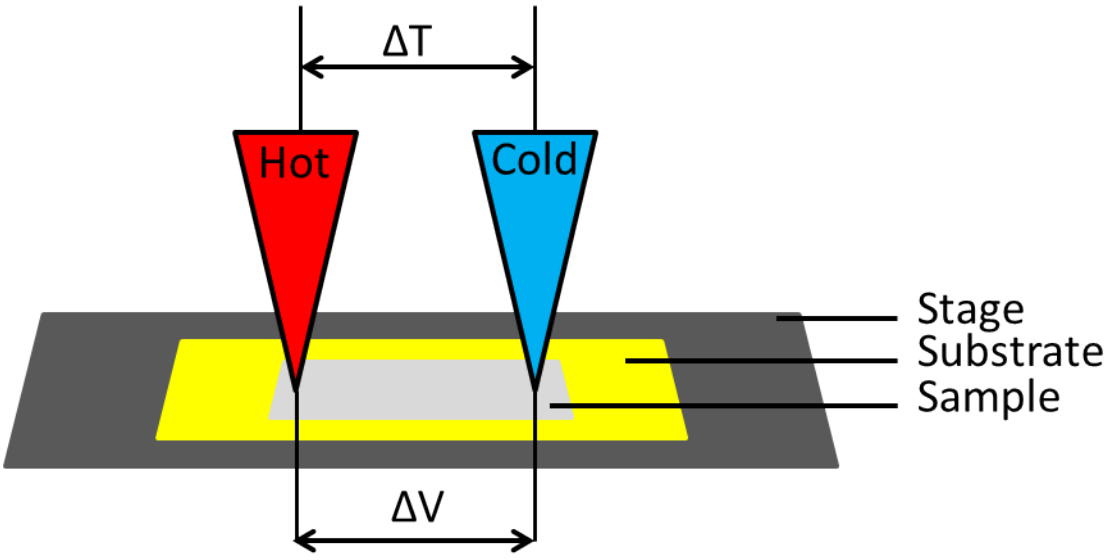

Figure 2-11 – Diagram of a 2 point Seebeck measurement device, which measures the voltage difference between the points of the hot and cold probe touching the sample.

Figure 2-11 shows the setup required to measure the Seebeck coefficient using a 2 point system. In this work Seebeck coefficients of thin film materials were measured using a custom built 2 point Seebeck measurement unit (Figure 2-12) in collaboration with Dr. Elena Koukharenko, a visiting researcher in the School of Electronics and Computer Science at the University of Southampton. The Seebeck measurement unit had been calibrated against a polycrystalline bismuth foil reference standard. The measurement accuracy of the device had been determined to be within 5%, and the system was calibrated using copper-constantan thermocouples and a high precision Keithley DMM 2000/E digital multimeter with 0.1% accuracy [20].

Figure 2-12 – A photograph of the custom built 2 point probe Seebeck measurement unit used in this work. Photograph courtesy of Elena Koukharenko.

In this work Seebeck coefficients were measured with samples on glass or the as deposited gold substrate. Gold was deemed an acceptable substrate due to the negligible contribution to the Seebeck voltage (~0.7 $\mu V K^{-1}$) compared to that of the thin film [96]. Only room temperature Seebeck coefficients were measured, due to the Seebeck measurement equipment not being capable of variable temperature measurements.

2.3.8 Transport Property Measurements

Electrodeposition requires a conductive substrate, but this in turn can short-circuit any voltage along the electrodeposit during electronic measurements. To overcome this prior to transport property measurements, the electrodeposited film needed to be removed from the working electrode substrate. This removed the otherwise dominate electrical conduction given by the Au substrate [97]–[100]. A schematic diagram illustrating how the electrodeposited film was removed from the substrate is shown in Figure 2-13.

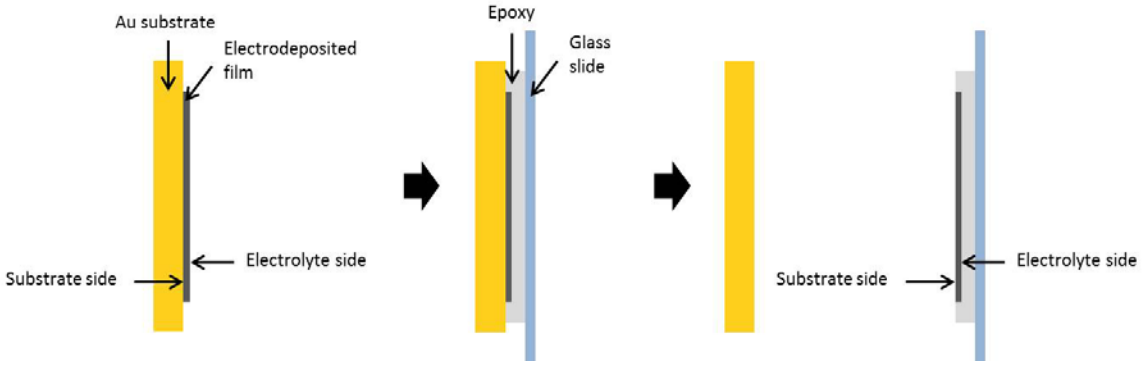

Figure 2-13 - Diagram illustrating the removal of an electrodeposited film from the working electrode substrate using epoxy. The same system is reported in [97]–[100]. The definition of substrate side and electrolyte side is shown, which is used in the results and discussion section to aid explanations.

Epoxy was applied to a glass slide which was then pressed against the electrodeposited film. This was left clamped for 24 *h* to allow the epoxy to fully set. When the epoxy was fully set the glass slide and the Au substrate were pulled apart, leaving the electrodeposited film immersed in epoxy upon a glass slide. The cleavage of the electrodeposit from the substrate can cause defects to the sample, but nonetheless is necessary to prevent conduction through the substrate.

Electrical conductivity, carrier concentration, Hall coefficient and Hall mobility are all measured and calculated using a commercial Hall effect measurement system (Ecopia HMS-3000). A schematic diagram of the system is shown in Figure 2-14.

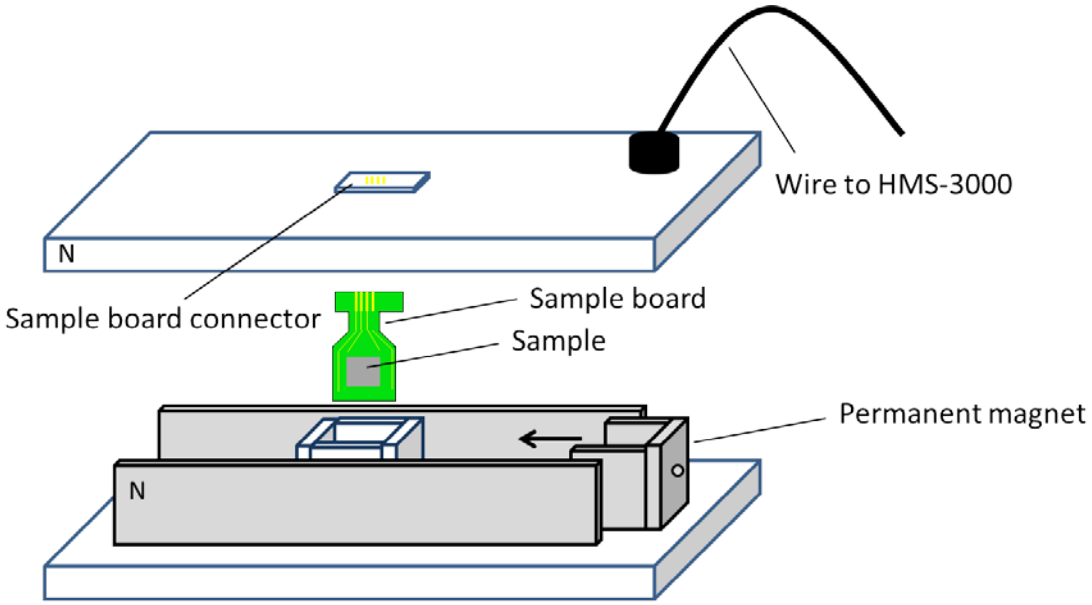

Figure 2-14 – Schematic diagram of the Hall effect measurement system setup [20], [101].

To conduct measurements four ohmic contacts (labelled 1, 2, 3 and 4 in an anticlockwise order) were added at each corner of the electrodeposited film, ensuring that these were as small as possible in size. These were made by attaching copper wire (0.2 *mm* in diameter) with conductive silver epoxy (CircuitWorks CW2400). The other end of the copper wire was soldered (using lead free solder) to the sample board. Four contacts are needed, so that current can be applied between two contacts on the same side and simultaneously the potential can be measured between two contacts on the opposite side.

2.3.8.1 Electrical Resistivity

The electrical resistivity was measured as follows:

- A current I_{21} was applied (positive dc current in amperes injected into contact 2 and taken out of contact 1), whilst the voltage V_{34} was measured
- The polarity of the current was reversed; current I_{12} applied, voltage V_{43} measured
- This was then repeated for the remaining 6 values (V_{41}, V_{14}, V_{12}, V_{21}, V_{23}, V_{32})

Eight values of resistance were yielded from the eight measurements of voltage, all of which must have been positive for the measurement to be valid:

$R_{21,34} = V_{34}/I_{21}$, $R_{12,43} = V_{43}/I_{12}$,

$R_{32,41} = V_{41}/I_{32}$, $R_{23,14} = V_{14}/I_{23}$

$R_{43,12} = V_{12}/I_{43}$, $R_{34,21} = V_{21}/I_{34}$

$R_{14,23} = V_{23}/I_{14}$, $R_{14,32} = V_{32}/I_{41}$

Two characteristic resistances (R_A and R_B) were determined, which allowed the sheet resistance (R_S) to be calculated iteratively using the Van der Pauw equation, Equation 2.4 [102].

$R_A = (R_{21,34} + R_{12,43} + R_{43,12} + R_{34,21}) / 4$

$R_B = (R_{32,41} + R_{23,14} + R_{14,23} + R_{41,32}) / 4$

$$e^{-\pi\frac{R_A}{R_S}} + e^{-\pi\frac{R_B}{R_S}} = 1 \quad (2.4)$$

The thickness (d) of the film was imputed into the software (thickness was calculated using Faraday's law and checked with a profilometer A.2), from which the bulk resistivity (ρ) was calculated from R_s using Equation 2.5 [102].

$$\rho = R_S\, d \quad (2.5)$$

2.3.8.2 Hall Effect

An external magnetic field applied perpendicular to the current flow across the sample will cause a Lorentz force. This will cause electrons to accumulate at the edge of the sample. The Lorentz force on the electrons can be expressed by Equation 2.6.

$$F_L = \frac{IB}{nA} \quad (2.6)$$

The uneven distribution of electrons causes an electric field across the sample, this causes a potential difference across the material which is known as the Hall voltage V_H. The current continues to only flow along the material, this is due to the force on the electrons and the electric field balancing out the Lorentz force. Noting that the force on an electron from an electric field is qE, the strength of the electric field can be shown to be per Equation 2.7:

$$E = \frac{IB}{nAq} \quad (2.7)$$

The Hall voltage is the strength of the electric field multiplied by the width of the sample. The width and area cancelling out leaving just thickness of the sample (d) and hall voltage (V_H), as shown in Equation 2.8. Equation 2.8 has a further simplification, taking into account that sheet density (n_s) is the density of electron by the thickness of the sample.

$$V_H = \frac{IB}{qnd} = \frac{IB}{qn_s} \quad (2.8)$$

Hall mobility (μ) can be determined from Equation 2.9 [102].

$$\mu = \frac{|V_H|}{R_S IB} = \frac{1}{qn_s R_s} \quad (2.9)$$

The procedure for measuring Hall voltage (V_H) was as follows:

- A positive magnetic field *B* was applied
- A current I_{13} was applied to leads 1 and 3 whilst voltage V_{24P} was measured ($_p$ denotes positive magnetic field between current contacts, $_n$ would dictate negative magnetic field between current contacts)
- A current I_{31} was applied which to leads 3 and 1 whilst voltage V_{42P} was measured
- Likewise, V_{13P} and V_{31P} with I_{42} and I_{24} respectively were measured
- The magnetic field was reversed (negative *B*)
- Likewise, V_{24N}, V_{42N}, V_{13N}, and V_{31N} with I_{13}, I_{31}, I_{42}, and I_{24} respectively were measured

This gave eight measurements of Hall voltages V_{24P}, V_{42P}, V_{13P}, V_{31P}, V_{24N}, V_{42N}, V_{13N}, and V_{31N} which revealed the sample type (*n* or *p*) and the sheet carrier density (n_s). If the sum of the P voltages minus the sum of the N voltages was positive, the sample was shown to be p-type, if negative the sample was n-type [103]. In theory each of 4 pairs ($_p$ with $_n$) of Hall voltages measured should have been the same, however non-symmetric contact placement, sample shape, and a temperature differential could have caused slight variations. So an average value is used in a rearrangement of Equation 2.8, to calculate carrier density as shown in Equation 2.10.

$$n_s = \frac{IB}{qV_H} \tag{2.10}$$

The bulk carrier concentration (*n*) was calculated as shown in Equation 2.11.

$$n = \frac{n_s}{d} \tag{2.11}$$

Chapter 3: Cu and Ag Doping of $Bi_2Te_{2.7}Se_{0.3}$

3.1 Introduction

3.1.1 Bismuth Telluride

Bismuth telluride and related materials are chalcogenides, which are currently the most efficient room temperature thermoelectric materials used in commercial devices (e.g. floor heating [10]) [35]. Bismuth telluride crystallises in a rhombohedral system with a space group of R-3m. The structure of bismuth telluride (Bi_2Te_3) consists of fifteen layers stacked along the c axis, which is comprised of three quintet layer stacks of (TeBiTeBiTe) in composition. This structure is shown in Figure 3-1. Each atom in the structure has a distorted octahedron as the coordination polyhedron [104]. Within the (TeBiTeBiTe) quintet, two different Te environments exist, as shown in Figure 3-1. Te1 has six bismuth atoms as nearest neighbours, whilst Te2 has three bismuth atoms as nearest neighbours.

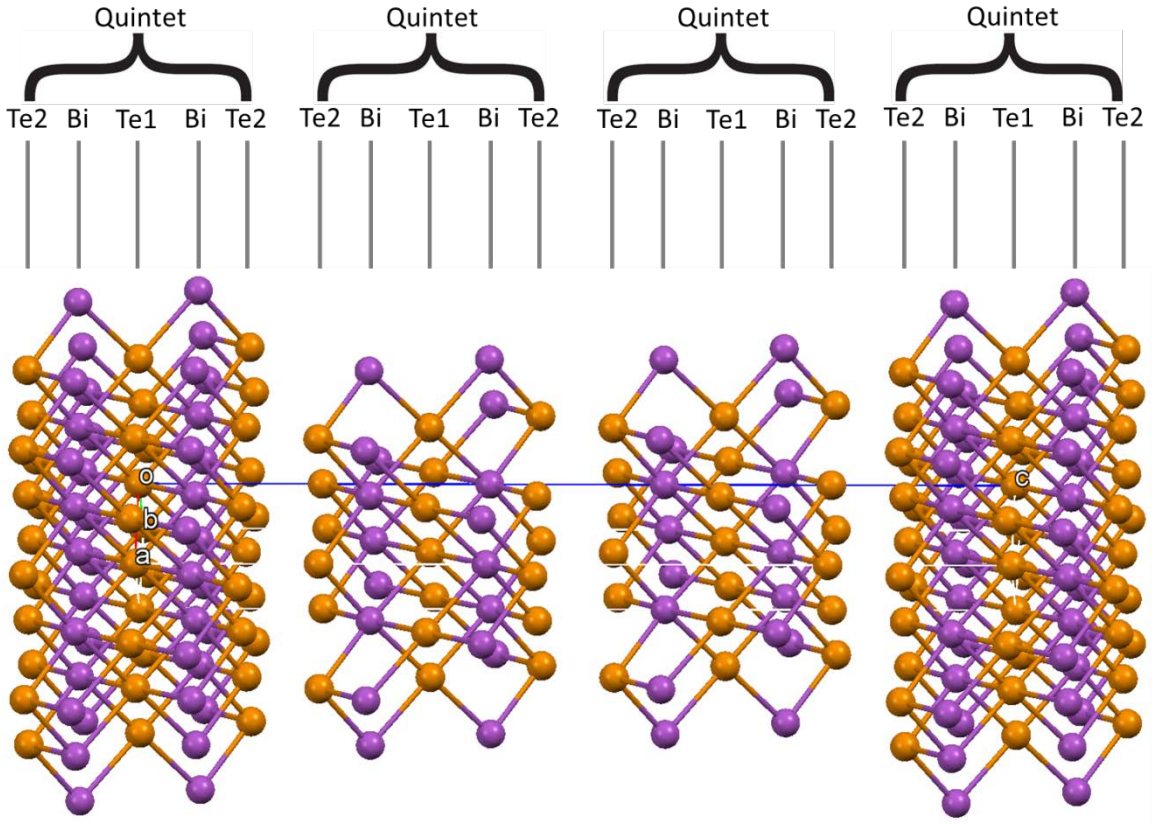

Figure 3-1 – Crystal structure of bismuth telluride, derived by Feutelais *et al.* [104]. The structure consists of 3 stacked quintets along the c axis of (TeBiTeBiTe) in composition. The

space group for the structure is R3m. The crystal structure was plotted on Mercury [105], using ICSD 74348.

Commercial thermoelectric devices typically use bismuth telluride that has been fabricated by chemical vapour deposition (CVD) [106], [107]. This can give Seebeck coefficients of -210 $\mu V\ K^{-1}$ and electrical conductivity of 1000 $S\ cm^{-1}$, at 723 *K* and thermal conductivities in the order of 10.7 $mW\ cm^{-1}\ K^{-1}$ [107]. This yields *ZT* values in excess of 1. CVD does require a vacuum at high temperatures for fabrication, however, making production expensive. The machinery for fabrication is also costly. The same can be said for other fabrication techniques, such as molecular beam epitaxy [108], pulse lase deposition [109], evaporation [110] and sputtering [111]. Electrodeposition offers a fabrication technique that does not require a vacuum, can be performed at room temperature and requires relatively cheaper equipment. From a commercial point of view this is far more favorable, due to the lower cost of production.

3.1.2 Electrodeposition of Bismuth Telluride

Electrodeposition of Bismuth Telluride has been extensively reported in the literature and film deposition is reviewed by Xiao *et al.* [39]. The first reported electrodeposition of Bismuth Telluride was by Takahashi *et al.* [112], [113] on Ti sheets, dissolving Bi_2O and TeO_2 in HNO_3 (pH 0.7 – 1.0). The thin films (up to 1.6 μm) were deposited at -0.25 *V vs. Ag/AgCl* (3.33 *M* KCl) in the diffusion limited region, from electrolytes containing 1.5 *mM* $HTeO_2^+$ and Bi^{3+} varying from 0.15 *mM* to 2.5 *mM*. They were, however, unable to make stoichiometric bismuth telluride (Bi_2Te_3) films and deposits consisted of Te metal and Bi_2Te_3 or BiTe phase. They concluded that the film composition was controlled by the electrolyte concentration and since Bi^{3+} is easily converted to $Bi(OH)_3$ the electrolyte bath was difficult to prepare. An attempt to improve the stability of Bi^{3+} with EDTA was made [114], however, the results showed similar stability of Bi^{3+} as observed without EDTA.

Electrodeposits of bismuth telluride were later improved by controlling the electrolyte concentration and deposition potential/current density by Magri *et al.* [115] and Michel *et al.* [116], [117]. The electrolytes consisted of $Bi(NO_3)_3$ and Te metal dissolved in 1 *M* HNO_3. Electrolytes prepared with a Bi/Te ratio equal to 2:3 with 0.02 *M* $HTeO_2^+$, films deposited between -150 *mV vs SCE* and -195 *mV vs SCE* were slightly Te rich, whilst galvanostatic films prepared between 0.10 $A\ dm^{-2}$ and 1.00 $A\ dm^{-2}$ were also Te rich with higher current densities giving less Te rich films. An electrolyte prepared with a Bi/Te ratio of 1:1, films deposited between -40 *mV vs SCE* and -110 mV vs SCE gave slightly Te rich films, whilst films deposited between -110 *mV vs SCE* and -140 *mV vs SCE* yielded slightly Bi rich films. Bismuth telluride crystal phase films deposited

were preferentially deposited along the (1 1 0) plane, but this preference decreased with increasing Bi content in the films [117].

Martín-González *et al.* [118] conducted work into the electrodeposition of bismuth telluride from nitric acid electrolytes. This lead to the definition of a Pourbaix-type diagram for the electrodeposition of Bi and Te at 25 °*C* and at 1 atmosphere from a solution of 7.5 *mM* Bi and 10 *mM* Te, Figure 3-2. The diagram indicates that bismuth telluride can be formed directly by the reduction of 7.5 *mM* Bi and 10 *mM* Te over the entire pH range (at 25 °*C* and 1 atm). All the potentials quoted are versus the normal hydrogen electrode (NHE).

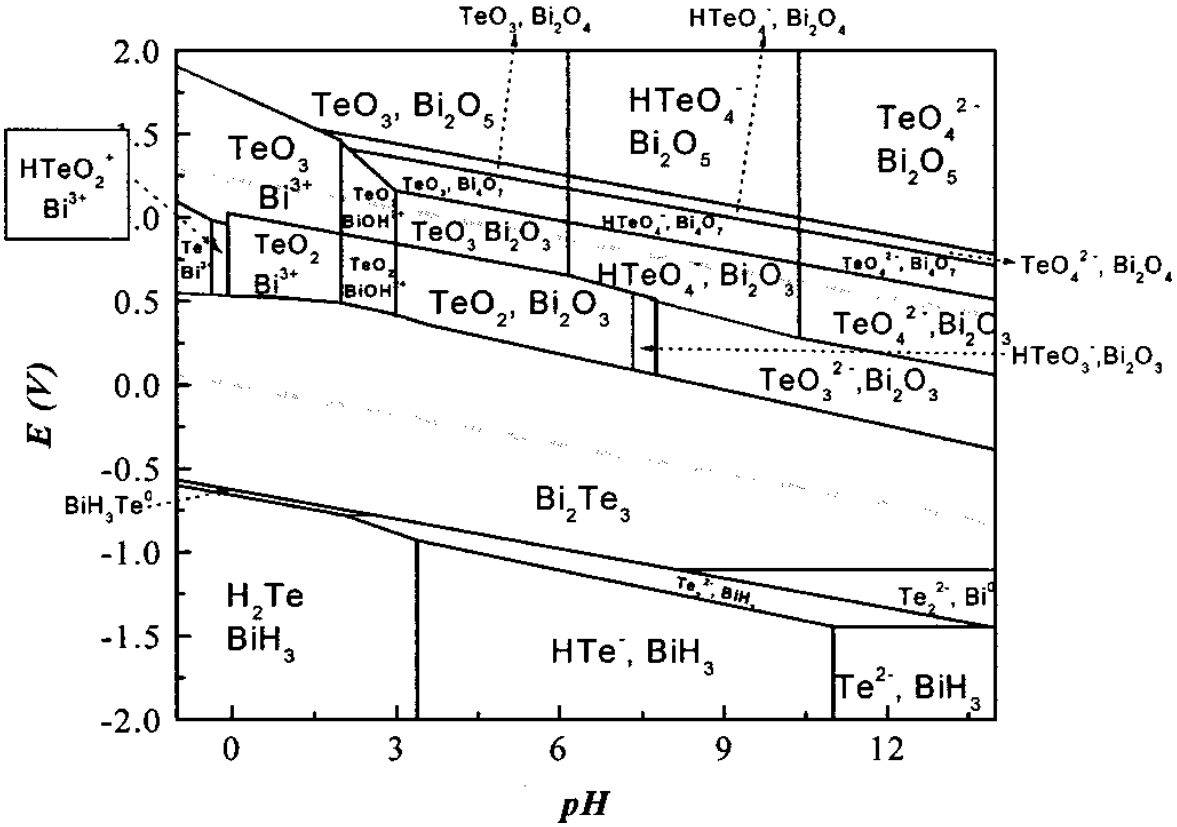

Figure 3-2 - Pourbaix-type diagram for the electrodeposition of Bi and Te (at 25 °*C*, 1 atm, and Bi =7.5 *mM* and Te = 10 *mM*) showing the thermodynamic stability of the dominant species as a function of potential and pH [118]. All potentials are *vs. NHE*. All authors are greatly acknowledged of publication [118] for this diagram. Reproduced by permission of The Electrochemical Society.

They observed that the potential at which reduction occurs when both $HTeO_2^+$ and Bi^{3+} are present in solution (E_{pc} = -62 *mV vs. NHE*; potential at which the peak cathodic current occurs is -62 *mV*) is more positive compared to the reduction of solutions containing only $HTeO_2^+$ (E_{pc} = -240 *mV vs. NHE*) or only Bi^{3+} (E_{pc} = -80 *mV vs. NHE*) for comparable concentrations. This behaviour is due to the formation of a stable compound on the surface of the electrode, which shifts the

potentials. This process is known as underpotential deposition (UPD) of class II as described by Kröger [119].

This type of deposition occurs when the two reversible (Nernst) potentials for the two separate cations are closer than ~250 *mV* and the free energy of formation of the compound provides a sufficient decrease in the anodic terms in the Butler-Volmer equations. Under these conditions net deposition of both elements occurs at comparable rates, at a more positive potential than where either element deposits individually.

Martín-González *et al.* [118] showed that applying potentials more negative than *ca.* -50 *mV vs. NHE*, causes a deposit to form on the working electrode. The identity of the deposit was determined to be bismuth telluride by XRD. They assign this to the reduction of $HTeO2^{+}$ and Bi^{3+} to form bismuth telluride, according to Equation 3.1 and Equation 3.2:

$$3\ HTeO_2^{+} + 12\ e^{-} + 9\ H^{+} \rightarrow 3\ Te_{(s)} + 6\ H_2O \quad (3.1)$$

$$3\ Te + 2\ Bi^{3+} + 6\ e^{-} \rightarrow Bi_2Te_{3\ (s)} \quad (3.2)$$

Equation 3.1 and Equation 3.2 can be written more generally as Equation 3.3.

$$3\ HTeO_2^{+} + 2\ Bi^{3+} + 18\ e^{-} + 9\ H^{+} \rightarrow Bi_2Te_{3\ (s)} + 6\ H_2O \quad (3.3)$$

The direct deposition of bismuth telluride instead of the co-deposition of Bi and Te is consistent with the negative Gibbs free energy of formation for bismuth telluride (-899.088 *KJ mol*$^{-1}$) and with the Pourbaix diagram in Figure 3-2.

From cyclic voltammetry the oxidation of the bismuth telluride electrodeposit is seen to form a peak (E_{pa} = +430 *mV vs. Ag/AgCl*) with a shoulder (E_{pa} = +440 *mV vs. Ag/AgCl*). These are explained by Equation 3.4 and Equation 3.5 respectively.

$$Bi_2Te_3 + 6\ H_2O \rightarrow 3\ HTeO_2^{+} + 2\ Bi + 9\ H^{+} + 12\ e^{-} \quad (3.4)$$

$$Bi \rightarrow Bi^{3+} + 3\ e^{-} \quad (3.5)$$

Although Martín-González *et al.* [118] go into large detail about the electroformation of bismuth telluride, they do not investigate the thermoelectric properties. This is true for most electrodeposition papers concerning thermoelectric materials [120]. The main complication arises due to the nature of electrodeposition requiring a conductive substrate, but this in turn can short-circuit any voltage along the layer during thermoelectric measurements. This can be overcome by embedding electrodeposits in epoxy resin (2.3.8).

In 2010 Boulanger [120] reviewed papers that used epoxy to remove bismuth telluride electrodeposits from the substrate. For non-annealed samples electrical conductivity values were

reported anywhere between 1 $S\ cm^{-1}$ and 2000 $S\ cm^{-1}$ and Seebeck values ranged from -40 $\mu V\ K^{-1}$ to -100 $\mu V\ K^{-1}$. Power factors ranged between 0.07 $mW\ K^{-2}\ m^{-1}$ and 0.74 $mW\ K^{-2}\ m^{-1}$. More recently in 2015 the same group reviewed the thermoelectric properties of electrodeposited bismuth telluride [121]. Although an improvement in Seebeck coefficient to -143 $\mu V\ K^{-1}$ is reported by Cao *et al.* [122], no improvement in electrical conductivity is reported. These values (summarised in Table 3-1) are inferior to other techniques such as co-evaporation which can exhibit Seebeck coefficient values as high as -250 $\mu V\ K^{-1}$ for thin films, with an electrical conductivity of 610 $S\ cm^{-1}$ [123], yielding a power factor of 3.81 $mW\ K^{-2}\ m^{-1}$. It should be noted though, that electrodeposition is a technique far more appealing to industry than co-evaporation, due to cost restraints.

Table 3-1 – Summary of thermoelectric performance values in the literature for electrodeposited bismuth telluride compared against a typical set of values seen for co-evaporated bismuth telluride.

Technique	σ ($S\ cm^{-1}$)	S ($\mu V\ K^{-1}$)	PF ($mW\ K^{-2}\ m^{-1}$)
Electrodeposition [120], [121]	1 to 2000	-40 to -143	0.07 to 0.74
Co-evaporation [123]	610	-250	3.81

3.1.3 Bismuth Tellurium Selenide

The doping of thermoelectric materials with other elements can sometimes be used to optimise thermoelectric properties such as electrical conductivity, Seebeck coefficient and thermal conductivity, or used to switch the material from n- to p-type, or vice versa. The changes are created by altering the crystal structure through adopting elements of a different ionic radius than those of the elements being replaced. The altering of the electrodeposition mechanism by the introduction of a co-depositing element can also affect the microstructural properties, leading to similar variations in thermoelectric properties as those caused by the addition of another element in the crystal structure.

One way to change the thermoelectric performance of bismuth telluride is to dope it with selenium (Se). The crystal structure remains the same as seen for bismuth telluride (Figure 3-1), the general consensus for this is that selenium atoms replace tellurium atom sites in the crystal lattice [124]. The introduction of selenium can cause more severe scattering of phonons, leading to a reduction in lattice thermal conductivity. This is caused by an increased number of crystallite boundaries causing an increased level of disorder in the crystal structure. This increased disorder

can also cause changes in the carrier concentrations and other electronic properties of the material [20].

Reports of bismuth telluride being doped with selenium electrochemically are fairly limited in the literature, but here and in Table 3-2 the few published examples are investigated. Zimmer *et al.* [125] used galvanostatic deposition to deposit $Bi_2(Te_{0.9}Se_{0.1})_3$ and report a Seebeck coefficient of -40 $\mu V\ K^{-1}$ and an electrical conductivity of 169 $S\ cm^{-1}$, giving a power factor of 0.027 $mW\ K^{-2}\ m^{-1}$. Bu *et al.* [126] used potentiostatic deposition to deposit $Bi_2(Te_xSe_{1-x})_3$ and reported a Seebeck coefficient of -62 $\mu V\ K^{-1}$ and an electrical conductivity of 714 $S\ cm^{-1}$ on gold, giving a power factor of 0.274 $mW\ K^{-2}\ m^{-1}$. Schumacher *et al.* [127] report a Seebeck coefficient of -82 $\mu V\ K^{-1}$ and an electrical conductivity of 702 S cm^{-1} for a pulsed voltage deposition technique of $Bi_2(Te_xSe_{1-x})_3$ yielding a power factor of 0.472 $mW\ K^{-2}\ m^{-1}$. Films were annealed in He for 1 *h* then Te for 60 *h* at 250 *°C*. They also report a thermal conductivity of 1.2 $W\ K^{-1}\ m^{-1}$, giving a *ZT* of 0.12. These values are similar to those reported for electrodeposited bismuth telluride, which indicates selenium doping alone cannot produce power factors or *ZT* values akin to those seen for more laborious and expensive techniques.

Table 3-2 – Summary of thermoelectric performance of electrodeposited $Bi_2(Te_xSe_{1-x})_3$ films.

Reference	σ ($S\ cm^{-1}$)	S ($\mu V\ K^{-1}$)	PF ($mW\ K^{-2}\ m^{-1}$)
[125]	169	-40	0.027
[126]	714 (on gold)	-62	0.274
[127]	702 (annealed)	-82	0.472

3.1.4 Cu and Ag Doping of Bismuth Telluride

Doping of bismuth telluride and bismuth tellurium selenide has been conducted in the literature via different fabrication techniques (summarised in Table 3-3), although very little has been conducted by electrodeposition.

Li *et al.* [128] prepared copper doped p-type Bismuth Antimony Telluride ($Cu_xBi_{0.5-x}Sb_{1.5}Te_3$ where x = 0, 0.04, 0.07, 0.1) by mechanical alloying (MA) and subsequent spark plasma sintering (SPS) at a pressure of 50 *MPa* and at temperature up to 673 *K*. They found that copper doping (where x = 0.07 or 0.1) increased the electrical (21000 $S\ m^{-1}$ to 190000 $S\ m^{-1}$ at 337.5 *K*) and thermal conductivities (0.6 $W\ K^{-1}\ m^{-1}$ to 2.7 $W\ K^{-1}\ m^{-1}$ at 298 *K*) whilst simultaneously lowering the Seebeck coefficient (250 $\mu V\ K^{-1}$ to 100 $\mu V\ K^{-1}$ at 337.5 *K*) near room temperature. This lead to an increase

of the power factor (σS^2) from 1.0 $mW\ m^{-1}\ K^{-2}$ to 1.9 $mW\ m^{-1}\ K^{-2}$ at 337.5 *K*, but a drop in *ZT* from 1.0 to 0.4 at the same temperature, due to the increase in thermal conductivity.

Cui *et al.* [129] prepared n-type $(Bi_2Te_3)_{0.9}$-$(Bi_{2-x}Cu_xSe_3)_{0.1}$(x = 0-0.2) by spark plasma sintering (SPS) Bi_2Te_3 and $Bi_{2-x}Cu_xSe_3$ (prepared at 1323 *K* for 10 *h*) at a pressure of 40 *MPa* and a temperature of 633 *K*. They found that copper levels of x = 0.1 caused an increase in Seebeck coefficient (-135 $\mu V\ K^{-1}$ to -150 $\mu V\ K^{-1}$ at 312.5 *K*) and electrical conductivity (75000 $S\ m^{-1}$ to 80000 $S\ m^{-1}$ at 312.5 *K*), but lowered the thermal conductivity (0.95 $W\ K^{-1}\ m^{-1}$ to 0.875 $W\ K^{-1}\ m^{-1}$ at 312.5 *K*). *ZT* was shown to increase from 0.48 to 0.68 at 312.5 *K*. A maximum *ZT* of 0.98 was achieved at 417 *K* when x = 0.1, up from 0.66 in the absence of Cu.

Cui *et al.* [130] also prepared n-type $(Bi_2Te_3)_{0.9}$-$(Bi_{2-x}Ag_xSe_3)_{0.1}$(x = 0-0.4) by spark plasma sintering (SPS) Bi_2Te_3 and $Bi_{2-x}Cu_xSe_3$ (prepared at 1323 K for 10 *h*) at a pressure of 40 *MPa* and a temperature of 633 *K*. They found that silver levels of x = 0.4 caused an increase in Seebeck coefficient (-135 $\mu V\ K^{-1}$ to -165 $\mu V\ K^{-1}$ at 312.5 *K*), but lowered the electrical conductivity (75000 $S\ m^{-1}$ to 52500 $S\ m^{-1}$ at 312.5 *K*) and thermal conductivity (0.95 $W\ K^{-1}\ m^{-1}$ to 0.80 $W\ K^{-1}\ m^{-1}$ at 312.5 *K*). *ZT* was shown to increase from 0.48 to 0.58 at 312.5 *K*. A maximum *ZT* of 0.86 was achieved at 505 *K* when x = 0.4, about 0.2 higher than in the absence of Ag.

Yang *et al.* [131] prepared n-type silver doped $Bi_2(Te_{0.94}Se_{0.06})_3$ by ball milling for 10 *h* then cold and hot pressing under a pressure of 60 *MPa* in Ar atmosphere at 773 *K* for 2 *h*. Measurements were conducted at room temperature and the peak power factor and *ZT* values were achieved of 1.8 $mW\ m^{-1}\ K^{-2}$ and 0.51 respectively with Ag doping levels of 0.20 weight %, increased from 1.3 $mW\ m^{-1}\ K^{-2}$ and 0.39 in the absence of Ag. This was all achieved by an increase in electrical conductivity (40000 $S\ m^{-1}$ to 111111 $S\ m^{-1}$), as the Seebeck coefficient decreased (-178 $\mu V\ K^{-1}$ to -152 $\mu V\ K^{-1}$) and the thermal conductivity increased (0.98 $W\ K^{-1}\ m^{-1}$ to 1.05 $W\ K^{-1}\ m^{-1}$).

Table 3-3 – Summary of peak thermoelectric performance values in Cu and Ag doped bismuth telluride based materials. For measurement temperatures and further information consult text in 3.1.4.

Reference	Material	Fabrication Technique	Σ ($S\ cm^{-1}$)	S ($\mu V\ K^{-1}$)	PF ($mW\ K^{-2}\ m^{-1}$)	K ($W\ m^{-1}\ K^{-1}$)	*ZT*
[128]	$Cu_xBi_{0.5-x}Sb_{1.5}Te_3$	MA + SPS	190000	100	1.9	2.7	0.40
[129]	$(Bi_2Te_3)_{0.9}$-$(Bi_{2-x}Cu_xSe_3)_{0.1}$	SPS	80000	-150	1.8	0.875	0.98
[130]	$(Bi_2Te_3)_{0.9}$-$(Bi_{2-x}Ag_xSe_3)_{0.1}$	SPS	52500	-165	1.4	0.80	0.86
[131]	Ag doped $Bi_2(Te_{0.94}Se_{0.06})_3$	Ball Milling	111111	-152	1.8	1.05	0.51

To date the literature fails to show any doped Bismuth Tellurium Selenide systems created by electrodeposition. This chapter seeks to investigate the effect on thermoelectric properties of doping bismuth tellurium selenide with Cu (extending on work conducted by Naylor [20]) or Ag electrochemically.

3.2 Results and Discussion

3.2.1 Bismuth Telluride

Before any quaternary Bismuth Telluride based systems can be investigated, first Bismuth Telluride itself needs to be investigated to get a fair comparison.

3.2.1.1 Cyclic Voltammetry

Cyclic voltammetry was conducted on a bismuth telluride electrolyte system used by Martín-González *et al.* [118] to check for repeatability on a gold substrate. The same electrolyte system was used by Naylor [20]. The cyclic voltammogram can be seen in Figure 3-3.

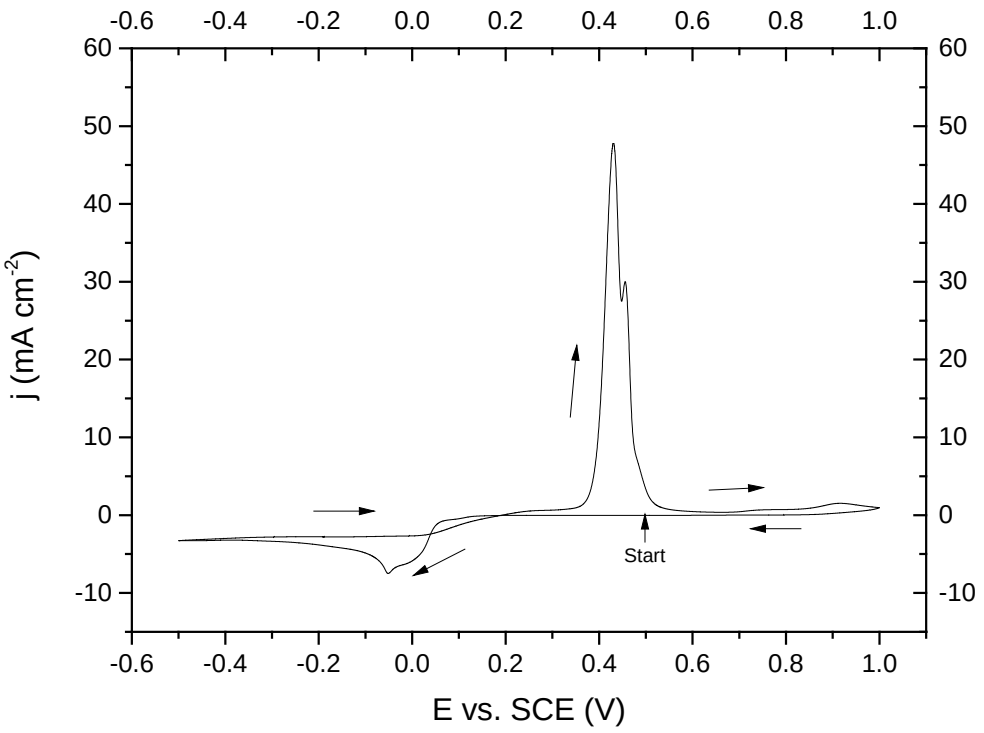

Figure 3-3 - Cyclic voltammogram recorded at 20 *mV* s^{-1} in an electrolyte of 7.5 *mM* Bi and 10.0 *mM* TeO_2 dissolved in 1 *M* HNO_3. The voltammogram started at a potential of +0.50 *V vs. SCE* where no reaction occurs and is scanned between -0.50 *V vs. SCE* and +1.00 *V vs. SCE*. The black arrows indicate the direction of the scan. The working electrode was a 2 *mm* gold disc electrode.

The reduction peak at -50 mV vs. SCE is attributed to be that of a deposit of bismuth telluride, by the reaction shown in Equation 3.3.

$$3\ HTeO_2^+ + 2\ Bi^{3+} + 18\ e^- + 9\ H^+ \rightarrow Bi_2Te_{3\ (s)} + 6\ H_2O \qquad (3.3)$$

The oxidation peak at +430 mV vs. SCE and the shoulder at +460 mV vs. SCE are attributed to Equation 3.4 and Equation 3.5 respectively [118]. The total reaction is the reverse of Equation 3.3.

$$Bi_2Te_3 + 6\ H_2O \rightarrow 3\ HTeO_2^+ + 2\ Bi + 9\ H^+ + 12\ e^- \qquad (3.4)$$

$$Bi \rightarrow Bi^{3+} + 3\ e^- \qquad (3.5)$$

The oxidation process can therefore be described as an oxidation of bismuth telluride to $HTeO_2^+$ (Equation 3.4), followed by an oxidation of Bi to Bi^{3+} (Equation 3.5). The maximum anodic peak is large in comparison to the cathodic peak because the reactant is surface-bound, so there is no mass transport limitation.

The total cathodic charge density was calculated to be 0.201 *C cm*$^{-2}$, assuming 100% faradaic efficiency this equates to a film thickness of 0.116 *μm* (Equation A.1). The total anodic charge density was calculated to be 0.155 *C cm*$^{-2}$, assuming 100% faradaic efficiency this equates to a striping thickness of 0.089 *μm* (Equation A.1). The difference of 0.046 *C cm*$^{-2}$ (estimated to be a thickness of 0.027 *μm*) is likely due to the inability to strip surface-bound species from the electrode on the anodic scan.

The reduction peak of bismuth telluride and oxidation peaks of bismuth telluride (shown in Figure 3-3) are in good agreement with those shown by Martín-González *et al.* [118] and by Naylor [20]. Therefore a deposition potential of +0.00 *V vs. SCE* and a deposition time of 2 *h* was chosen as these yielded the best results by Naylor [20] on a Au DVD substrate. Here a Au on Si substrate was used for the bismuth telluride electrodeposits (2.1.1.1). The current time transient for an electrodeposition can be seen in Figure 3-4.

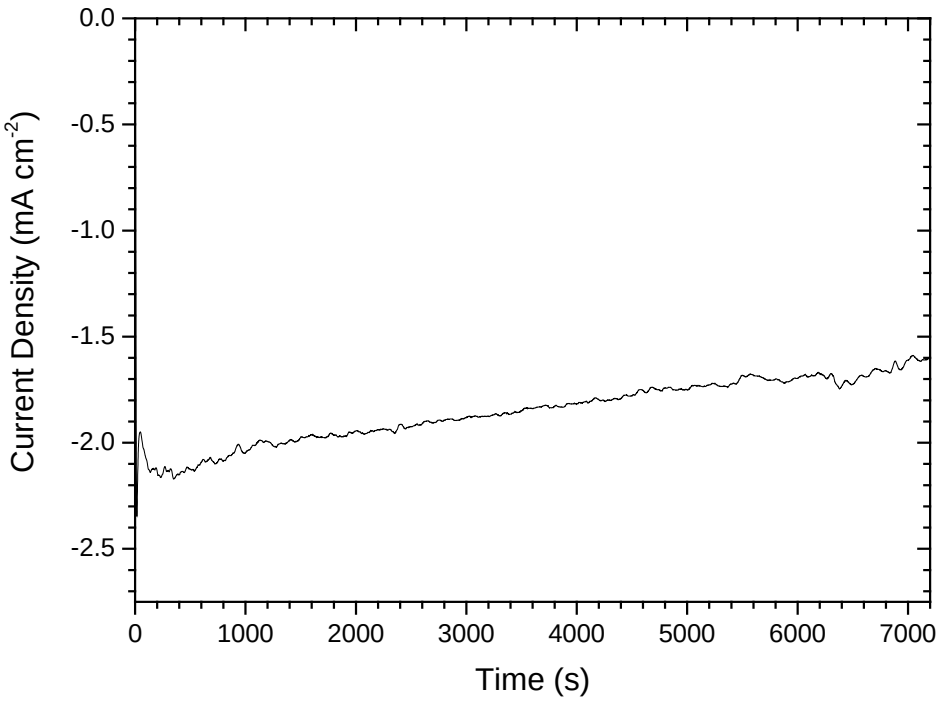

Figure 3-4 – Current time transient of a film electrodeposited from an electrolyte of 7.5 *mM* Bi and 10 *mM* TeO_2 in 1 *M* HNO_3. The deposition potential was +0.00 *V vs. SCE* and deposition time was 2 *h*. The working electrode was a Au on Si substrate with a 10 *mm* × 10 *mm* electrode area. The total deposition charge was -13.33 *C*.

3.2.1.2 Composition

The composition of the electrodeposited films was measured both on the substrate side (thus measuring the section of the film that is first deposited on the working electrode substrate, side exposed after the film had been peeled off the substrate using epoxy resin on a glass slide) and on the electrolyte side (thus measuring the side exposed to the electrolyte at the end of the deposition, side exposed when left as constructed). Figure 2-13 shows a more detailed explanation of electrolyte side and substrate side. This allowed for the composition on both sides of the film to be examined to check for consistency. The average results of 3 films are shown in Table 3-4.

Table 3-4 - Composition determined by EDX of a film electrodeposited from an electrolyte of 7.5 *mM* Bi, 10 *mM* TeO_2 in 1 *M* HNO_3. Deposition potential was +0.00 *V vs. SCE* and deposition time was 2 *h*. The errors represent the 95% confidence limits determined by 3 measurements. For definition of substrate side and electrolyte side see Figure 2-13.

Film side	Bi at. %	Te at. %
Substrate side	39.19 ± 0.40	60.81 ± 0.40
Electrolyte side	36.80 ± 0.41	63.20 ± 0.41

A small difference in stoichiometry is observed between the two sides, which indicates that the film's composition is not entirely consistent throughout. Initially bismuth telluride is deposited with near ideal stoichiometry (2.00:3.00) at a ratio of 1.96:3.04, however, after 2 hours of depositing the stoichiometry has shifted to a ratio of 1.84:3.16. This is in contrast to M. Takahahi *et al.* [97] who found that their electrodeposited films contained an excess of Te near the substrate, which changed to stoichiometric bismuth telluride when the film grew to over half a micron thick. M. Takahahi *et al.* [97] used a Ti substrate (not gold), they also used a Bi-EDTA complex rather than Bi powder. They used 1.00 *mM* TeO_2 (instead of 10.0 *mM*) and 0.86 *mM* Bi-EDTA (not 7.5 *mM* Bi powder). These differences could explain the differences in observed results.

3.2.1.3 XRD

Symmetric scans were used to allow the determination of the preferred plane of crystal orientation. Patterns were produced for both the electrolyte side Figure 3-5a and the substrate side Figure 3-5b (see Figure 2-13 for the definition of electrolyte side and substrate side).

a)

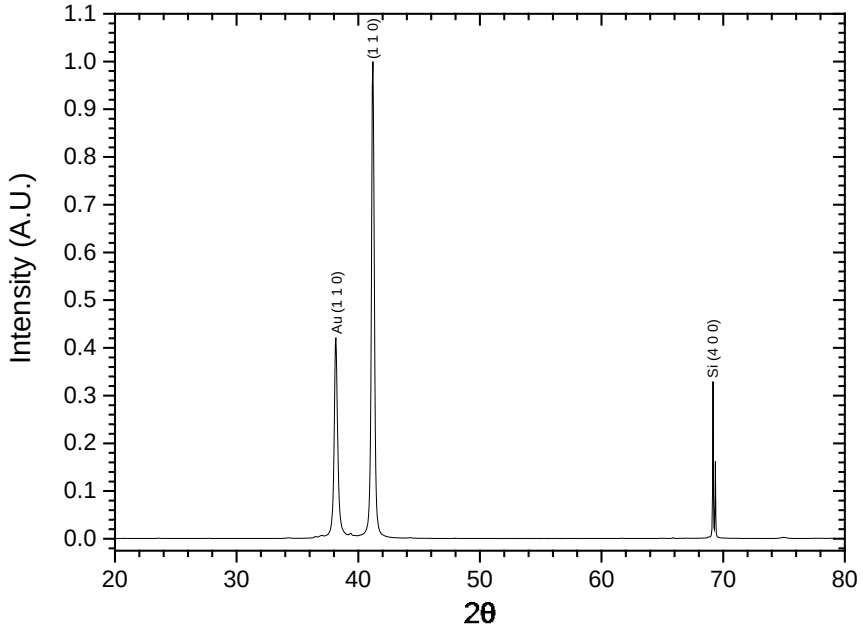

b)

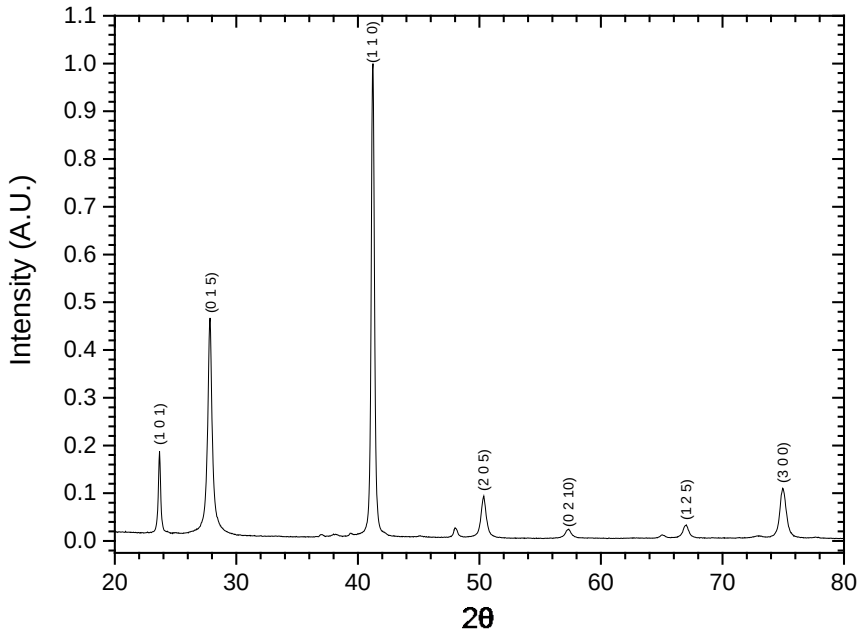

Figure 3-5 - Symmetric XRD scans of a bismuth telluride film electrodeposited from an electrolyte solution containing 7.5 *mM* Bi and 10.0 *mM* TeO_2 in 1 *M* HNO_3: a) electrolyte side, b) substrate side. The deposition conditions were +0.00 *V vs. SCE* for 2 *h*. The Au (1 1 0) peak was fitted from the file "Gold, Au" and the Si (4 0 0) peak was fitted from the file "Silicon, Si", in the PDXL software. All other peaks were fitted from the "Tellurobismuthite" file in the PDXL software No:00-008-0027 (ICDD powder

diffraction file 00-015-0863). The ICDD powder stick pattern can be found in Figure A-1.

Several peaks are shown in Figure 3-5b which index to bismuth telluride when compared to the standard file for Tellurobismuthite (ICDD 00-015-0863), indicating that bismuth telluride has been electrodeposited. The film exhibits a (1 1 0) preferred orientation on the substrate side, which is more pronounced when the film is scanned as deposited on the electrolyte side, as seen in Figure 3-5a. The orientation preference is deduced by comparing intensity of peaks to the stick powder standard in Figure A-1. The (1 1 0) orientation is consistent with results of Martín-González *et al.* [118] for electrodeposited bismuth telluride. This is encouraging as the (1 1 0) orientation has previously been described in the literature as having the most favourable crystallinity for thermoelectric efficiency [51]. This orientation causes layers of bismuth and tellurium to grow perpendicular to the substrate, which offers the best probability of reducing the thermal conductivity in the plane perpendicular to the substrate whilst not diminishing the electrical conductivity.

Using the Scherrer equation (Equation 2.2) on the (1 1 0) peak, the calculated grain size is 36.4 *nm* on the substrate side (using data from the XRD pattern in Figure 3-5b), and the grain size is 42.2 *nm* on the electrolyte side (using data from the XRD pattern in Figure 3-5a). Grain size is important as smaller grains can lead to decreased thermal conductivity due to increased phonon scattering, thus increased figure of merit (*ZT*). However without clean grain boundaries, the defect density at the grain boundaries can be such that smaller grain sizes can degrade the overall thermoelectric performance [132].

$$D = \frac{0.9\lambda}{\beta cos\theta} \tag{2.2}$$

Whilst it is unknown what the optimum grain size for bismuth telluride electrodeposited films is (as there is no study in the literature for this), it should be noted that Takashiri [132] found the larger the grain size (up to 60 nm studied) the higher the *ZT* value for flash-evaporated bismuth telluride films.

Table 3-5 – Comparison of grain size when calculated from different peaks

Peak	Electrolyte Side Grain Size (*nm*)	Substrate Side Grain Size (*nm*)
(1 0 1)	N/A	37.7
(0 1 5)	N/A	24.3

(1 1 0)	42.2	36.4
(2 0 5)	N/A	24.9

From Table 3-5 the grain size can be seen to be larger in the (1 0 1) and (1 1 0) directions, than in the (0 1 5) and (2 0 5) directions. This difference is not substantial and is likely caused by the preferred growth orientations. The larger grain size along different planes is likely to cause anisotropy in thermoelectric performance of the material.

3.2.1.4 SEM

The morphology of the electrodeposited films was examined by scanning electron microscope (SEM) both as deposited, thus seeing the top of the film (electrolyte side); and after the films were peeled off (substrate side), thus seeing the initially deposited layer. The results are shown in Figure 3-6.

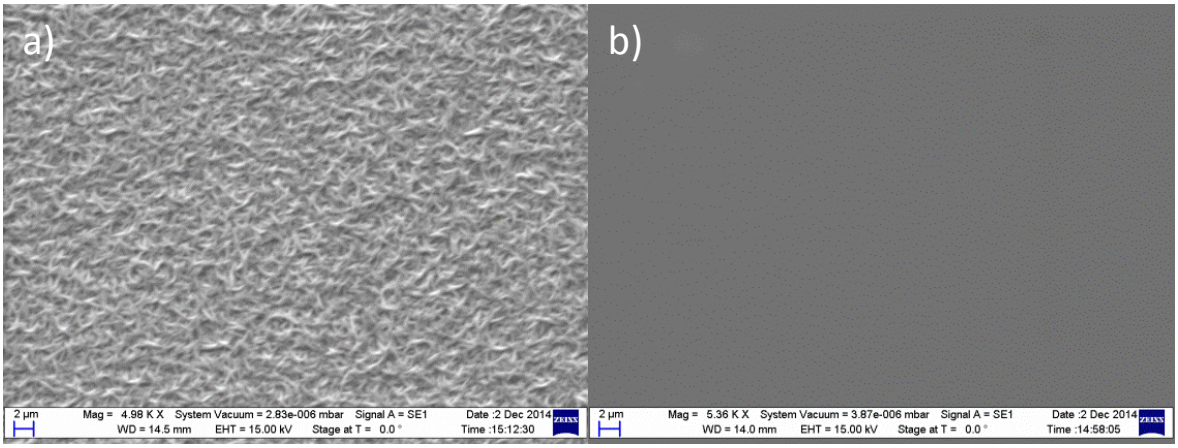

Figure 3-6 - Scanning electron microscopy images of a bismuth telluride film electrodeposited from an electrolyte solution containing 7.5 *mM* Bi and 10.0 *mM* TeO_2 in 1 *M* HNO_3 at 0 *V vs. SCE* for 2 *h*: a) electrolyte side, b) substrate side.

Evident from Figure 3-6 is that the morphology of the deposit forms a needle like texture at the electrolyte side of the film. In contrast when the film is imaged after being peeled of the substrate, thus seeing the substrate side, a flat film with barely any texture is seen. This indicates that the film is compact and uniform on the substrate side, but is textured on the electrolyte side. This accounts for the optical observation of a mirrored surface on the substrate side of the film, compared to a matte appearance on the electrolyte side.

3.2.1.5 Seebeck, Electrical Conductivity/Resistivity, Power Factor and Hall Measurements

The efficiency of a thermoelectric device is related to the figure of merit (*ZT*) shown in Equation 1.5. Two of the three variables are measured in this section, which are the electrical conductivity

(σ, this is the inverse of the electrical resistivity) and the Seebeck coefficient (S). The thermal conductivity has not been measured; there are no facilities in Southampton for this measurement. Thermal conductivity is also extremely difficult to determine accurate values for thin films. The Seebeck coefficient and electrical conductivity will allow for the calculation of the power factor (σS^2, Equation 1.6), which is often viewed as a more important figure when considering viability of practical devices.

The carrier concentration was also measured, as a value in the order of -10^{19} cm^{-3} is thought to be the optimum value to yield the highest power factor for bismuth telluride based materials [133]. An optimum value exists, as high carrier concentrations give high electrical conductivities and low Seebeck coefficients, however low carrier concentrations give low electrical conductivities and high Seebeck coefficients. Hall mobility is another property that is measured, with a higher mobility linked to more freedom for charge transport [4]. These properties were repeated through a period of 12 months, to study the long term thermoelectric performance of the materials.

Table 3-6 – Seebeck, Electrical Conductivity and Hall measurements measured over 12 months on 3 bismuth telluride films electrodeposited from an electrolyte solution containing 7.5 *mM* Bi and 10.0 *mM* TeO_2 in 1 *M* HNO_3. The deposition conditions were 0 *V vs. SCE* for 2 *h*. Errors denote 95% confidence limits calculated by measuring 3 different samples. All measurements were carried out on the same 3 samples, with the exception of the 0 months Seebeck coefficient measurements due to the destructive nature of the measurement. Samples were stored in the dark at room temperature between measurements.

	0 Months	1 Months	7 Months	12 Months
Seebeck Coefficient ($\mu V\ K^{-1}$)	-43.8 (±0.5)	N/A	N/A	-46.9 (±1.3)
Electrical Conductivity (S cm^{-1})	820 (±72)	809 (±93)	800 (±39)	797 (±103)
Bulk Carrier Concentration (cm^{-3})	-3.42×10^{20} ($\pm 0.50 \times 10^{20}$)	-2.96×10^{20} ($\pm 1.07 \times 10^{20}$)	-3.77×10^{20} ($\pm 5.05 \times 10^{20}$)	-1.76×10^{20} ($\pm 1.11 \times 10^{20}$)
Hall Mobility ($cm^2\ V^{-1}\ s^{-1}$)	16.7 (±8.3)	33.6 (±61.5)	71.2 (±19.6)	48.0 (±14.1)
Power factor (mW m^{-1} K^{-2})	0.158 (±0.008)	N/A	N/A	0.175 (±0.017)

The initial electrical conductivity value of 820 (±72) $S\ cm^{-1}$ is in line with the 952 $S\ cm^{-1}$ reported by Fleurial *et al.* [134], for which similar deposition conditions were used. Boulanger [120] reviews

electrical conductivity values for electrodeposited bismuth telluride which values vary from 1 *S* cm^{-1} – 2000 *S* cm^{-1}. This means that these samples exhibit a typical value of electrical conductivity.

The initial Seebeck coefficient values are also in line with the ones reported for non-annealed electrodeposited bismuth telluride samples by Boulanger [120], which range from -40 $\mu V K^{-1}$ to -100 $\mu V K^{-1}$. The Seebeck coefficient is seen to slightly increase over time, whilst the electrical conductivity is seen to slightly diminish. Although the change is seen to be within error, examination of each of the samples separately shows this trend to be consistent throughout all the individual samples. This would be observable in Table 3-6 however one sample exhibits a slightly lower electrical conductivity with higher Seebeck coefficient than the other 2 samples, which increases the observed error. The resultant power factor (σS^2) is seen to have a marginal increase. The changes observed however are small, which would have little effect on the efficiency of a device containing these samples.

Within error bulk carrier concentration is shown to remain constant. The value is in the order of -10^{20} cm^{-3}, which is only a factor of 10 higher than the optimum value to yield the highest power factor for bismuth telluride based materials [133]. Strangely Hall mobility is seen to increase over time, despite electrical conductivity decreasing. Normally an increase in mobility would be seen as a positive (as typically that would lead to an increase in electrical conductivity), here the higher mobility could indicate an increased thermal conductivity (κ) due to an increase in the carrier contribution to thermal conductivity (κ_e).

3.2.2 Bismuth Tellurium Selenide

3.2.2.1 Cyclic Voltammetry

A bismuth, tellurium and selenium electrolyte system (8 *mM* Bi, 9 *mM* TeO_2 and 1 *mM* SeO_2 in 1 *M* HNO_3) was used by Qiu *et al.* [124] to produce bismuth tellurium selenide thin films (stainless steel substrates, 1800 *s* deposition time, with deposition potentials between -150 to 25 *mV vs. SCE*). Here the same system is used here to check for repeatability. The cyclic voltammogram can be seen in Figure 3-7.

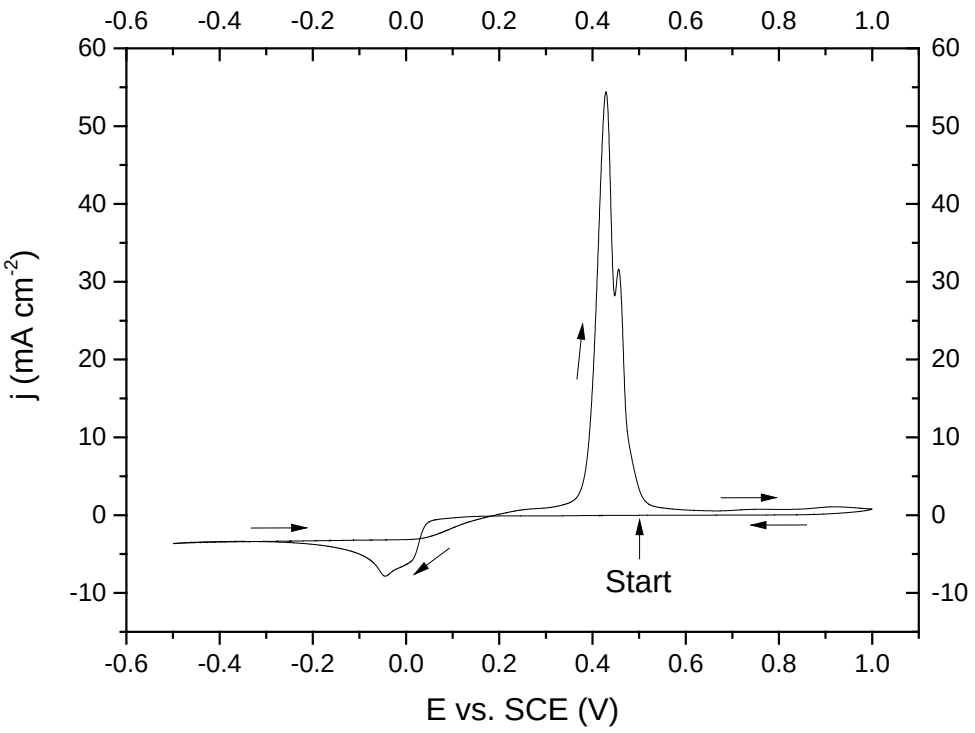

Figure 3-7 - Cyclic voltammogram recorded at 20 *mV s*$^{-1}$ in an electrolyte of 8.0 *mM* Bi, 9.0 *mM* TeO_2, and 1.0 *mM* SeO_2 dissolved in 1 *M* HNO_3. The voltammogram started at a potential of +0.50 *V vs. SCE* where no reaction occurs and is scanned between -0.50 *V vs. SCE* and +1.00 *V vs. SCE*. The black arrows indicate the direction of the scan. The working electrode was a 2 *mm* gold disc electrode. Reduction charge equals 0.155 *C cm*$^{-2}$, oxidation charge equals 0.15 *C cm*$^{-2}$.

The reduction peak at -50 *mV vs. SCE* is attributed to be that of a deposit of $Bi_2Te_{3-x}Se_x$, by the reaction shown in Equation 3.6 [124].

$$(3 - x)HTeO_2^+ + (x)H_2SeO_3 + 2Bi^{3+} + 18e^- + (9 + x)H^+ \rightarrow Bi_2Te_{3-x}Se_x\,(s) + (6 + x)H_2O \quad (3.6)$$

The oxidation peak at +430 *mV vs. SCE* and the shoulder at +460 *mV vs. SCE* are attributed to Equation 3.7 and Equation 3.8 respectively [124]. The total reaction is the reverse of Equation 3.6.

$$Bi_2Te_{3-x}Se_x + (6 - x)H_2O \rightarrow (3 - x)HTeO_2^+ + (x)H_2SeO_3 + 2Bi + (9 + x)H^+ + 12e^- \quad (3.7)$$

$$Bi \rightarrow Bi^{3+} + 3\,e^- \quad (3.8)$$

The oxidation process can therefore be described as an oxidation of $Bi_2Te_{3-x}Se_x$ to $(3 - x)HTeO_2^+$ to $(x)H_2SeO_3$ (Equation 3.7), followed by an oxidation of Bi to Bi^{3+} (Equation 3.8) [124]. The maximum anodic peak is large in comparison to the cathodic peak because the reactant is surface-bound, so there is no mass transport limitation.

The total cathodic charge density was calculated to be 0.200 *C cm*$^{-2}$, assuming 100% faradaic efficiency this equates to a film thickness of 0.115 *μm* (Equation A.1). The total anodic charge density was calculated to be 0.155 *C cm*$^{-2}$, assuming 100% faradaic efficiency this equates to a striping thickness of 0.089 *μm* (Equation A.1). The difference of 0.045 *C cm*$^{-2}$ (estimated to be a thickness of 0.026 *μm*) is likely due to the inability to strip surface-bound species from the electrode on the anodic scan.

The reduction peak of $Bi_2Te_{3-x}Se_x$ and oxidation peaks of $Bi_2Te_{3-x}Se_x$ (shown in Figure 3-7) are in good agreement with those shown by Qiu *et al.* [124] and by Naylor [20]. Therefore a deposition potential of +0.05 *V vs. SCE* and a deposition time of 2 *h* was chosen as these yielded the best results by Naylor [20] on a Au DVD substrate. Here a Au on Si substrate was used for the $Bi_2Te_{3-x}Se_x$ electrodeposits (2.1.1.1). The current time transient for an electrodeposition can be seen in Figure 3-8.

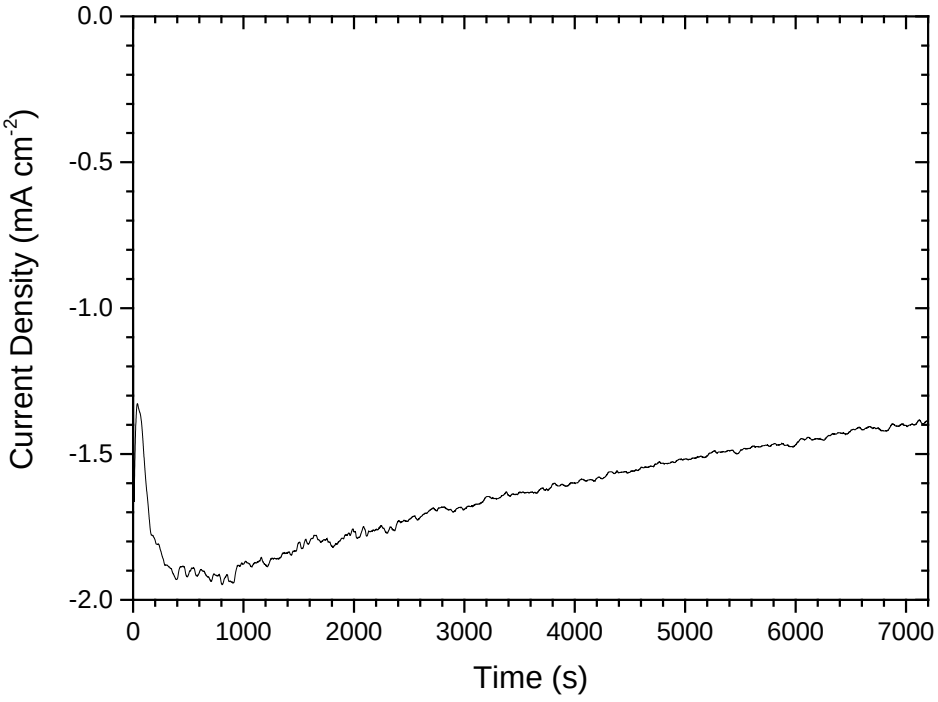

Figure 3-8 - Current time transient of a film electrodeposited from an electrolyte of 8.0 *mM* Bi, 9.0 *mM* TeO_2 and 1.0 *mM* SeO_2 in 1 *M* HNO_3. The deposition potential was +0.05 *V vs. SCE* and deposition time was 2 *h*. The working electrode was a Au on Si substrate with a 10 *mm* × 10 *mm* electrode area. The total deposition charge was -11.77 *C*.

3.2.2.2 Composition

The composition of the electrodeposited film was measured on both the substrate side and the electrolyte side (see Figure 2-13 for a more detailed explanation). This allowed for the composition on both sides of the film to be examined to check for consistency. The results are shown in Table 3-7.

Table 3-7 - Composition determined by EDX of a film electrodeposited from an electrolyte of 8.0 *mM* Bi, 9.0 *mM* TeO_2 and 1.0 *mM* SeO_2 in 1 *M* HNO_3. Deposition potential was +0.05 *V vs. SCE* and deposition time was 2 *h*. The errors represent the 95% confidence limits determined by 3 measurements. For definition of substrate side and electrolyte side see Figure 2-13.

Film side	Bi at. %	Te at. %	Se at. %
Substrate side	37.57 (±0.40)	54.81 (±0.35)	7.61 (±0.11)
Electrolyte side	38.21 (±0.62)	55.66 (±0.70)	7.13 (±0.16)

There was seen to be negligible difference in stoichiometry between the two sides, which indicates that the film's composition was consistent on either side of the film. The average bismuth, tellurium, selenium ratio deposited was 1.89:2.76:0.37, which is near the believed ideal stoichiometry (2.00:2.70:0.30) for bismuth tellurium selenide [124].

3.2.2.3 XRD

Symmetric scans were used to allow the determination of the preferred plane of crystal orientation. Patterns were produced for both the electrolyte side Figure 3-9a and the substrate side Figure 3-9b (see Figure 2-13 for the definition of electrolyte side and substrate side).

a)

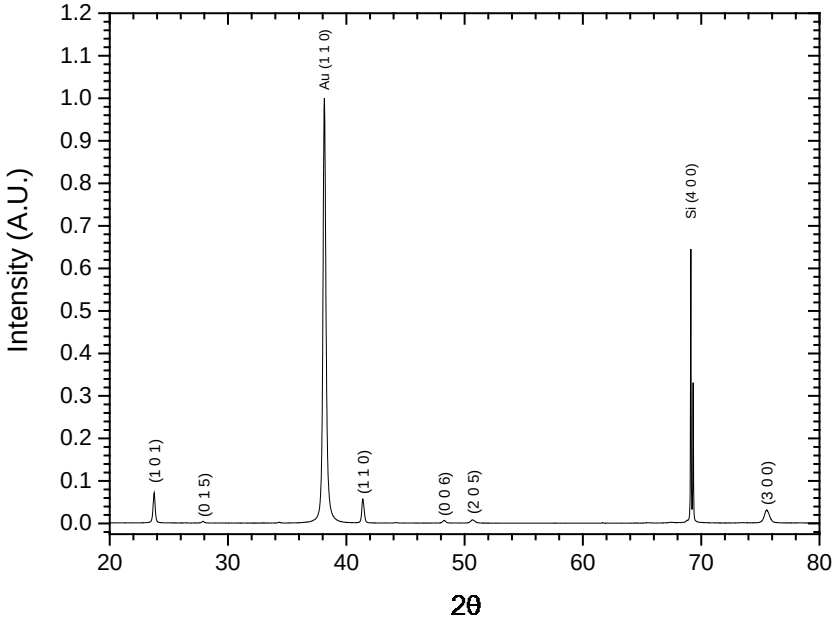

b)

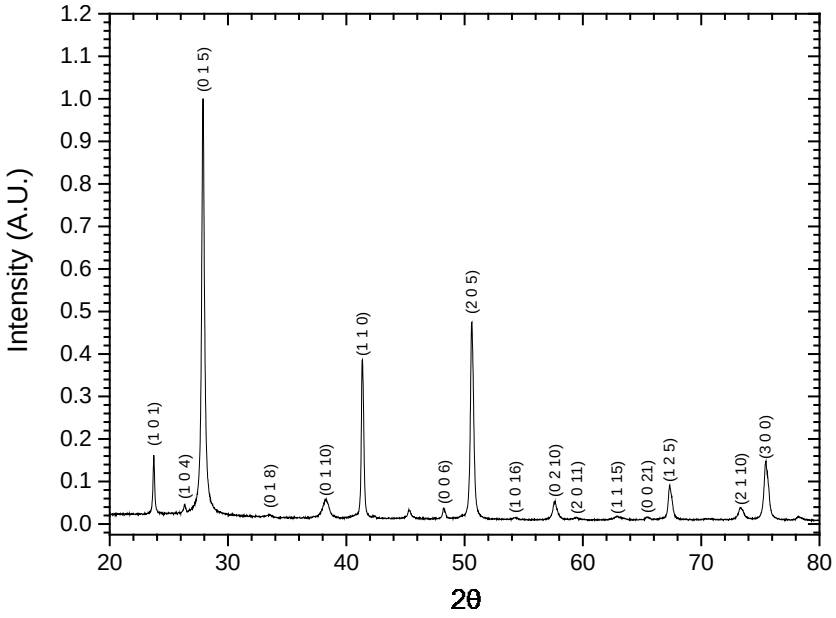

Figure 3-9 - Symmetric XRD scans of a bismuth tellurium selenide film electrodeposited from an electrolyte solution containing 8.0 *mM* Bi, 9.0 *mM* TeO_2 and 1.0 *mM* SeO_2 in 1 *M* HNO_3: a) electrolyte side, b) substrate side. The deposition conditions were +0.05 *V vs. SCE* for 2 *h*. The Au (1 1 0) peak was fitted from the file "Gold, Au" and the Si (4 0 0) peak was fitted from the file "Silicon, Si", in the PDXL software. All other peaks up to 70° were fitted from the "Bismuth Tellurium Selenide" file in the PDXL software No:00-051-0643 (COD file 1511976). The COD powder stick pattern can be found in Figure A-2. Peaks after 70° were fitted from the "Tellurobismuthite" file in the PDXL

software No:00-008-0027 (ICDD powder diffraction file 00-015-0863). The ICDD powder stick pattern can be found in Figure A-1.

Several peaks are shown in Figure 3-9b which index to bismuth tellurium selenide when compared to the standard file for Bismuth Tellurium Selenide (COD 1511976), indicating that Bismuth Tellurium Selenide has been electrodeposited. The film exhibits a (2 0 5) preferred orientation on the substrate side, whilst the film exhibits a (1 0 1) preferred orientation on the electrolyte side, as seen in Figure 3-9a. Orientation preference deduced by comparing intensity of peaks to the stick powder standard in Figure A-2.

Using the Scherrer equation (Equation 2.2) on the (1 0 1) peak, the calculated grain size is 18.3 *nm* on the substrate side (using data from the XRD pattern in Figure 3-9b), and the grain size is 43.3 *nm* on the electrolyte side (using data from the XRD pattern in Figure 3-9a). Grain size is important as smaller grains can lead to decreased thermal conductivity due to increased phonon scattering, thus increased figure of merit (*ZT*). However without clean grain boundaries, the defect density at the grain boundaries can be such that smaller grain sizes can degrade the overall thermoelectric performance [132]. These results indicate that the grain size is initially smaller compared to bismuth telluride (3.2.1.3), however becomes larger as the film grows and the grain size becomes on par with bismuth telluride. This observation could easily be caused by the higher deposition potential, which could have allowed more time for grains to initially grow.

$$D = \frac{0.9\lambda}{\beta cos\theta} \tag{2.2}$$

Table 3-8 - Comparison of grain size when calculated from different peaks.

Peak	Electrolyte Side Grain Size (*nm*)	Substrate Side Grain Size (*nm*)
(1 0 1)	43.3	18.3
(0 1 5)	31.0	18.7
(1 1 0)	46.0	24.9
(2 0 5)	29.1	19.0

From Table 3-8 the grain size can be seen to be larger in the (1 1 0) and (1 0 1) directions on the electrolyte side most likely due to preferred growth in those directions, whilst on the substrate side the (1 1 0) direction has the largest grain size. In other directions the grain sizes are very similar. This larger grain size along different planes is likely to cause anisotropy in thermoelectric performance of the material.

3.2.2.4 SEM

The morphology of the electrodeposited films was examined by scanning electron microscope (SEM) both as deposited, thus seeing the top of the film (electrolyte side); and after the films were peeled off (substrate side), thus seeing the initially deposited layer. The results are shown in Figure 3-10.

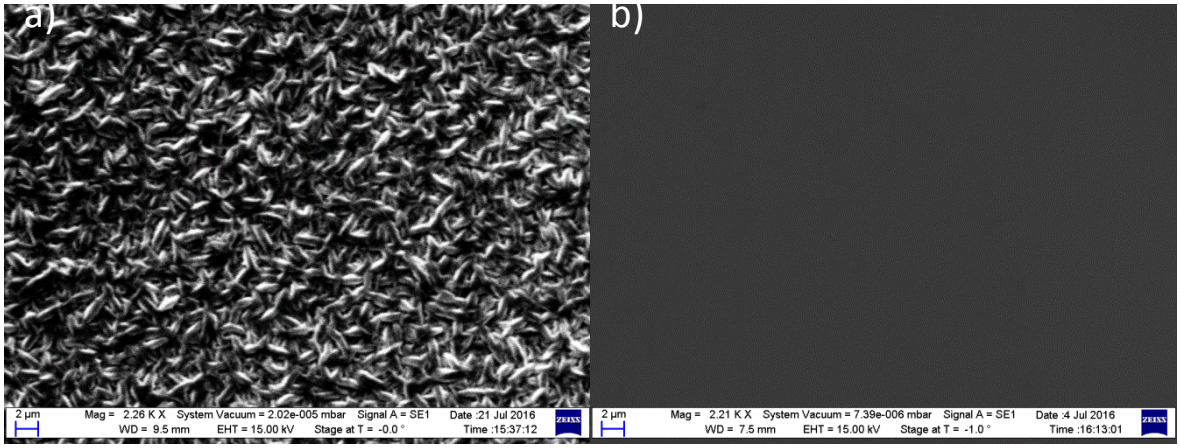

Figure 3-10 - Scanning electron microscopy images of a bismuth telluride film electrodeposited from an electrolyte solution containing 8.0 *mM* Bi, 9.0 *mM* TeO_2 and 1.0 *mM* SeO_2 in 1 *M* HNO_3 at +0.05 *V vs. SCE* for 2 *h*: a) electrolyte side, b) substrate side.

As was seen for bismuth telluride (Figure 3-6), the substrate side is compact, reflecting the uniformity of the Au on Si substrate. The electrolyte side shows compact growths with average grain sizes in the region of 2 *µm*, as reported by Naylor [20]. The substrate side shows no visible cracks, indicating the films have not sustained substantial deformations during separation from the deposition substrate. The lack of deformations allows for reliable electrical measurements to be conducted on the film.

3.2.2.5 Seebeck, Electrical Conductivity/Resistivity, Power Factor and Hall Measurements

Seebeck, electrical and Hall effect properties were measured over the course of a year to test for stability and to allow for comparison to literature values.

Table 3-9 - Seebeck, Electrical Conductivity and Hall measurements measured over 12 months on bismuth tellurium selenide films electrodeposited from an electrolyte solution containing 8.0 *mM* Bi, 9.0 *mM* TeO_2 and 1.0 *mM* SeO_2 in 1 *M* HNO_3. The deposition conditions were +0.05 *V vs. SCE* for 2 *h*. Errors denote 95% confidence limits calculated by measuring 3 different samples. All measurements were carried out on the same 3 samples, with the exception of the 0 months Seebeck coefficient measurements due to the destructive nature of the measurement. Samples were stored in the dark at room temperature between measurements.

	0 Months	1 Months	7 Months	12 Months
Seebeck Coefficient ($\mu V\ K^{-1}$)	-54.7 (±0.4)	N/A	N/A	-56.5 (±1.4)
Electrical Conductivity (S cm^{-1})	580 (±101)	562 (±91)	550 (±90)	547 (±90)
Bulk Carrier Concentration (cm^{-3})	-3.75×10^{20} ($\pm 6.10 \times 10^{20}$)	-2.02×10^{20} ($\pm 1.16 \times 10^{20}$)	-3.84×10^{20} ($\pm 4.37 \times 10^{20}$)	-9.79×10^{19} ($\pm 1.01 \times 10^{20}$)
Hall Mobility ($cm^2\ V^{-1}\ s^{-1}$)	21.2 (±5.7)	31.2 (±18.1)	49.2 (±66.2)	50.2 (±60.2)
Power factor (mW $m^{-1}\ K^{-2}$)	0.173 (±0.023)	N/A	N/A	0.175 (±0.037)

The initial electrical conductivity value of 580 (±101) *S* cm^{-1} is in line with the 714 *S* cm^{-1} reported by Bu *et al.* [126], for which similar deposition conditions were used. Boulanger [120] reviews electrical conductivity values for electrodeposited thermoelectric materials, $Bi_2(Te_xSe_{1-x})_3$ values vary from 169 *S* cm^{-1} – 1250 *S* cm^{-1}. This means that these samples have a typical value of electrical conductivity.

The initial Seebeck coefficient values within the range reported for electrodeposited $Bi_2(Te_xSe_{1-x})_3$ samples by Boulanger [120], which span from -40 $\mu V\ K^{-1}$ to -150 $\mu V\ K^{-1}$. The Seebeck coefficient was seen to increase with time whilst the electrical conductivity decreased over time, as was observed for bismuth telluride samples measured in Table 3-6. Although electrical conductivity as shown in Table 3-9 is not seen to change outside of error, studying each of the 3 samples individually shows that each sample exhibited a slowly reducing electrical conductivity over time. The overall effect on power factor over time resulted in no observable change. These results

indicate that the efficiency of a device made using legs of electrodeposited bismuth tellurium selenide made in this manner would not substantially change over the course of a year.

Within error bulk carrier concentration is shown to remain constant. The value is in the order of -10^{20} cm^{-3}, which is only a factor of 10 higher than the optimum value to yield the highest power factor for bismuth telluride based materials [133]. Mobility is seen to remain constant within error.

3.2.3 Copper Doped Bismuth Tellurium Selenide

Following on from work conducted by Naylor [20], where copper doping of the electrolyte was conducted up to 0.75 *mM* $Cu(NO_3)_2$, this section expands doping levels up to 2.00 *mM* $Cu(NO_3)_2$ to investigate the effects of higher doping levels on crystallinity, morphology and thermoelectric performance. Here unlike Naylor [20], electrodeposited films were removed from the conducting substrate to perform thermoelectric characterisations on non-conductive epoxy upon glass, this removed any measurement contributions from the substrate to electrical measurements [97]–[100].

3.2.3.1 Cyclic Voltammetry

The same bismuth, tellurium and selenium electrolyte as used by Qiu *et al.* [124] to produce bismuth tellurium selenide thin films was used here, however to the electrolyte various levels of $Cu(NO_3)_2$ was added up to levels of 2.00 *mM*. Cyclic voltammogram of each copper doping level can be seen in Figure 3-11.

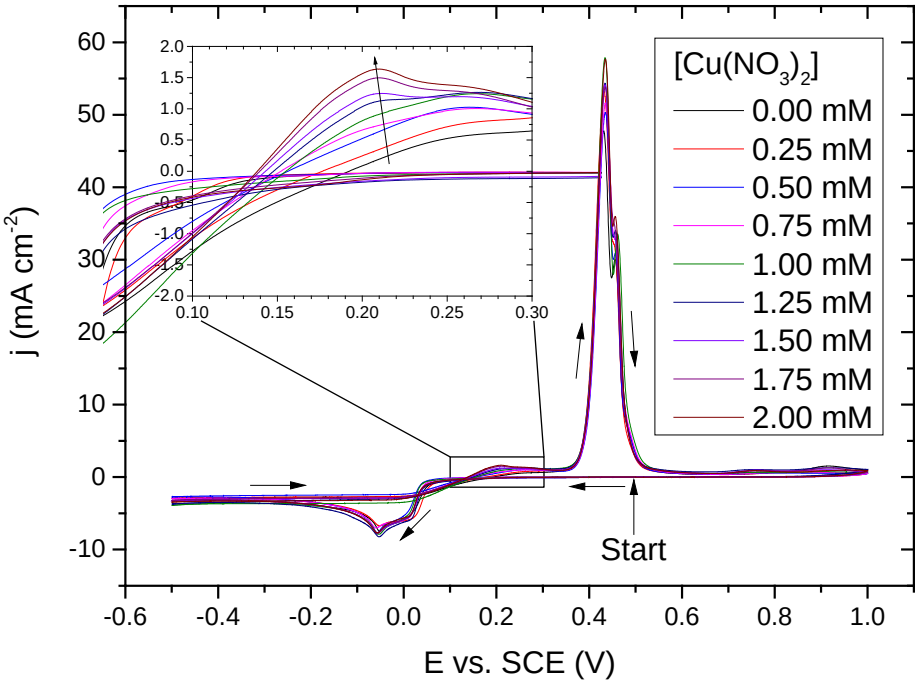

Figure 3-11 - Cyclic voltammograms recorded at 20 *mV* s^{-1} in an electrolyte of 8.00 *mM* Bi, 9.00 *mM* TeO_2, 1.00 *mM* SeO_2 and between 0.00 *mM* and 2.00 *mM* $Cu(NO_3)_2$, dissolved in 1 *M* HNO_3. The voltammogram started at a potential of +0.50 *V vs. SCE* where no reaction occurs and is scanned between -0.50 *V vs. SCE* and +1.00 *V vs. SCE*. The black arrows indicate the direction of the scan. The working electrode was a 2 *mm* gold disc electrode.

Whilst doping appears to have no significant effect on the reduction peak at -50 *mV vs. SCE* (attributed to be that of a deposit of $Bi_2Te_{3-x}Se_x$, by the reaction shown in Equation 3.6 [124]), or the oxidation peaks at +430 *mV vs. SCE* and the shoulder at +460 *mV vs. SCE* (attributed to Equation 3.7 and Equation 3.8 respectively), there is an increasing oxidation peak seen at +20 *mV vs. SCE*. This trend can be seen more clearly in the inlay in Figure 3-11. The peak also becomes more negative as the peak increases, as is predicted by the Nernst equation. This peak is in line with the oxidation of Cu^{2+} from an electrolyte of 1.00 *mM* $Cu(NO_3)_2$ in 1 *M* HNO_3 (Figure C-1) and therefore can be attributed to the oxidation of Cu^{2+} from bismuth tellurium selenide.

3.2.3.2 Composition

Copper doped bismuth tellurium selenide thin films (~6 *μm*, see Table A-12) were deposited at a potential of +0.05 *V vs. SCE* for 2 hours. Films were deposited from electrolytes with up to 2.00

mM $Cu(NO_3)_2$ present. A current time transient for a film deposited with 2.00 *mM* $Cu(NO_3)_2$ present in the electrolyte is shown in Figure 3-12.

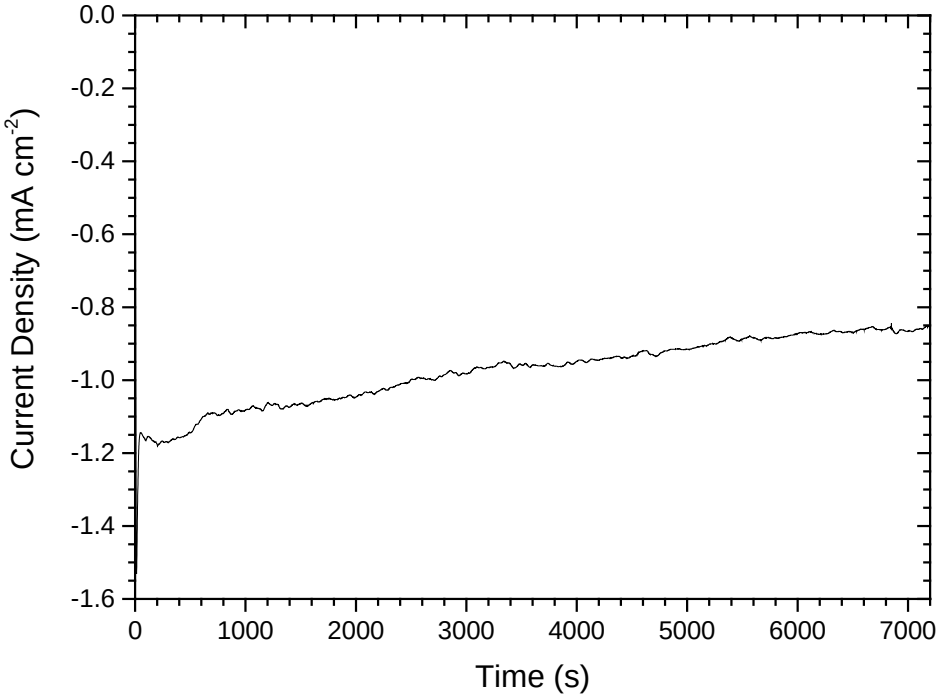

Figure 3-12 - Current time transient of a film electrodeposited from an electrolyte of 8.0 *mM* Bi, 9.0 *mM* TeO_2, 1.0 *mM* SeO_2 and 2.00 *mM* $Cu(NO_3)_2$ in 1 *M* HNO_3. The deposition potential was +0.05 *V vs. SCE* and deposition time was 2 *h*. The working electrode was a Au on Si substrate with a 10 *mm* × 10 *mm* electrode area. The total deposition charge was -7.02 *C*.

The electrodeposited films were set in epoxy on glass and peeled off of the deposition substrate prior to EDX analysis (see Figure 2-13). The resulting EDX analysis can be seen in Figure 3-13.

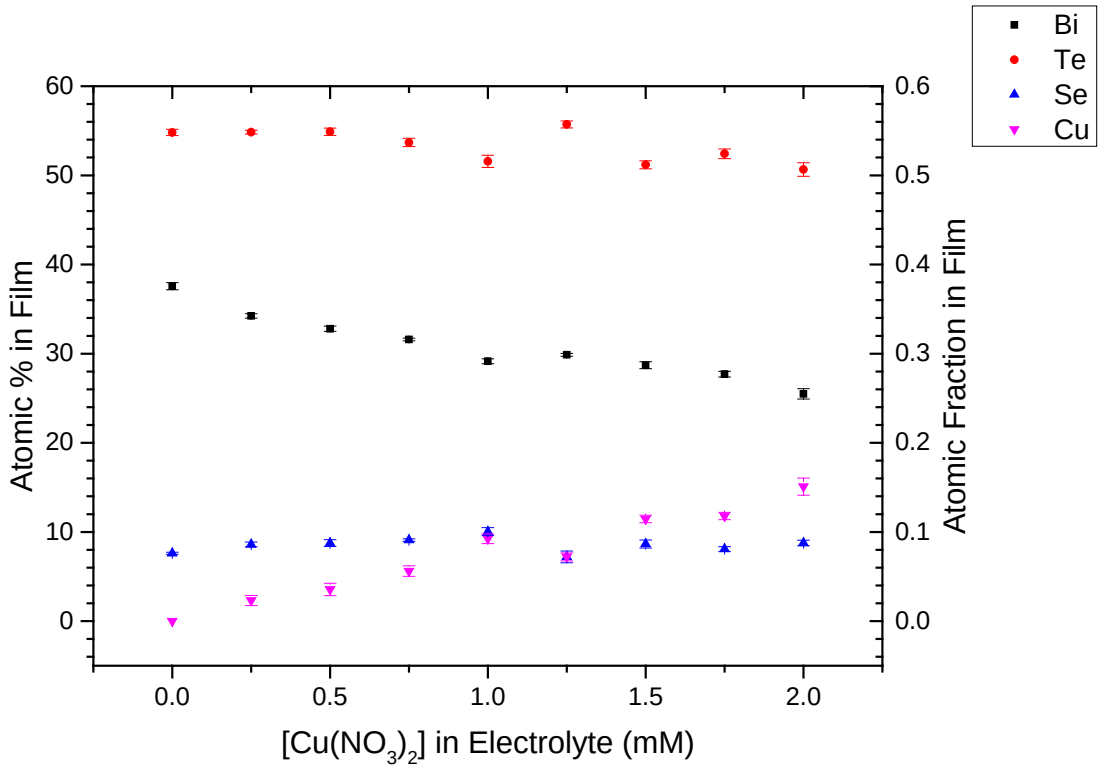

Figure 3-13 – EDX analysis of elemental composition of films electrodeposited from an electrolyte of 8.00 *mM* Bi, 9.00 *mM* TeO_2, 1.00 *mM* SeO_2 and between 0.00 and 2.00 *mM* $Cu(NO_3)_2$, dissolved in 1 *M* HNO_3. The films were deposited potentiostatically at +0.05 *V vs. SCE* for 2 *h*. The deposition substrate was Au on Si. The films were removed onto epoxy on glass before EDX analysis was performed, to remove the possibility of Au on the spectrum. The errors represent the 95% confidence limits determined by 3 measurements.

The level of Cu incorporation in the electrodeposited films increases with increasing Cu levels in the electrolyte. Cu incorporation appears to be linear, with a 15% incorporation of Cu when 2.00 *mM* of $Cu(NO_3)_2$ is present in the electrolyte. Interestingly however, the levels of Bi, Te and Se do not appear to lower equally. Levels of Se appear to remain roughly constant throughout, whilst the level of Te is lowered by around 3% at maximum Cu doping levels. Bi levels seem to linearly decrease with increasing $Cu(NO_3)_2$ concentration, decreasing by 13% when maximum Cu concentration is present in the electrolyte.

The observations seen in Figure 3-13 appear to suggest that Cu is not only being deposited, but is being incorporated into the crystal structure by replacing Bi. To help corroborate this hypothesis, XRD was conducted.

3.2.3.3 XRD

To help understand the nature of Cu incorporation in the electrodeposited films, XRD was conducted to investigate the effect of Cu doping on the crystal structure of bismuth tellurium selenide. The results can be seen in Figure 3-14.

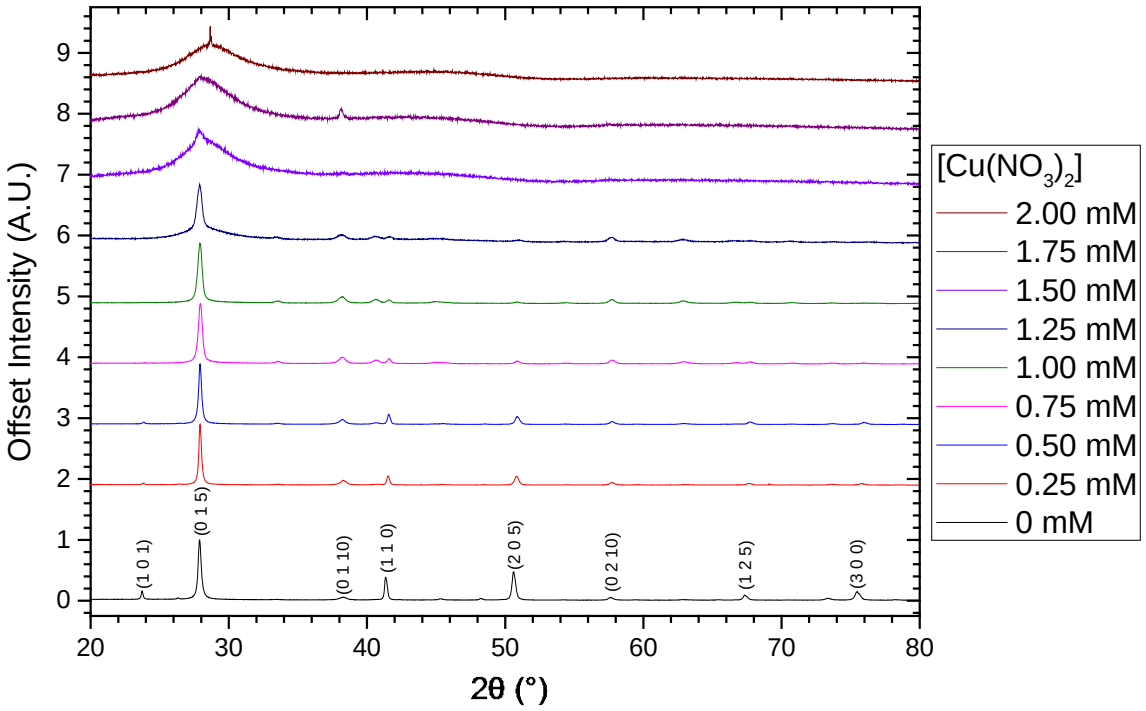

Figure 3-14 - Symmetric XRD scans of films electrodeposited from an electrolyte of 8.00 *mM* Bi, 9.00 *mM* TeO_2, 1.00 *mM* SeO_2 and between 0.00 and 2.00 *mM* $Cu(NO_3)_2$, dissolved in 1 *M* HNO_3. The films were deposited potentiostatically at +0.05 *V vs. SCE* for 2 *h*. The deposition substrate was Au on Si. The films were removed onto epoxy on glass before XRD analysis was performed, to remove Au from the spectrum. All peaks up to 70° were fitted from the "Bismuth Tellurium Selenide" file in the PDXL software, No: 00-051-0643. The COD powder stick pattern can be found in Figure A-2. Peaks after 70° were fitted from the "Tellurobismuthite" file in the PDXL software No:00-008-0027 (ICDD powder diffraction file 00-015-0863). The ICDD powder stick pattern can be found in Figure A-1.

A (2 0 5) preferred orientation is seen with no Cu doping, then all films maintain a (0 1 5) orientation through all doping levels and can be seen to be identified as having the R-3m space group of bismuth telluride and bismuth tellurium selenide. The COD stick powder pattern for "Bismuth Tellurium Selenide" can be found in Figure A-2. Crystallite size is seen to vary with

increasing Cu doping levels, as seen in Table 3-10 which uses the (0 1 5) peak to calculate grain size. The initially the addition of Cu into the electrolyte is seen to increase the grain size, however further addition of Cu is seen to continually decrease the grain size. This can be seen in Figure 3-14 by the broadening of peaks. By the time 2.00 *mM* of $Cu(NO_3)_2$ is reached, the grain size calculated from the (0 1 5) peak is seen to be as small as 2.03 *nm*.

These XRD patterns would seem to suggest, that whilst Cu incorporation into the films is not changing the crystal structure, the incorporation is having an effect on the grain size. The expected outcome in reduction of grain size would be a reduction in conductivity, with the possibility of an increase in the Seebeck coefficient.

Table 3-10 – Comparison of grain size with increasing levels of $Cu(NO_3)_2$ in the electrolyte using the (0 1 5) peak in Figure 3-14.

$[Cu(NO_3)_2]$ (*mM*)	(0 1 5) Grain Size (*nm*)
0.00	18.7
0.25	41.2
0.50	36.6
0.75	25.3
1.00	23.3
1.25	16.2
1.50	2.88
1.75	2.29
2.00	2.03

3.2.3.4 SEM

To investigate the effect on morphology the incorporation of Cu has on bismuth tellurium selenide electrodeposited films, a series of samples were prepared for SEM analysis. The films were deposited and not removed from the deposition substrate (Au on Si). The results can be seen in Table 3-11.

Table 3-11 - Scanning electron microscopy images of copper doped bismuth tellurium selenide films electrodeposited from an electrolyte solution containing 8.00 *mM* Bi, 9.00 *mM* TeO_2, 1.00 *mM* SeO_2 and between 0.00 and 2.00 *mM* $Cu(NO_3)_2$, dissolved in 1 *M* HNO_3. The films were deposited potentiostatically at +0.05 *V vs. SCE* for 2 *h*. Images are of the electrolyte side.

0.25 *mM* $Cu(NO_3)_2$	0.50 *mM* $Cu(NO_3)_2$
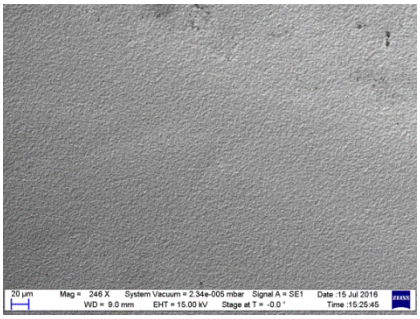	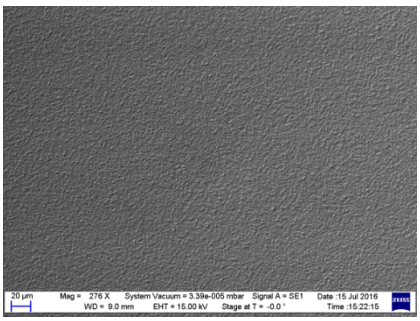
0.75 *mM* $Cu(NO_3)_2$	1.00 *mM* $Cu(NO_3)_2$
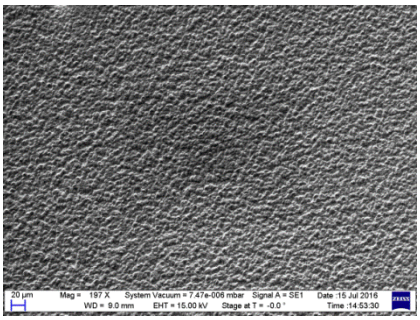	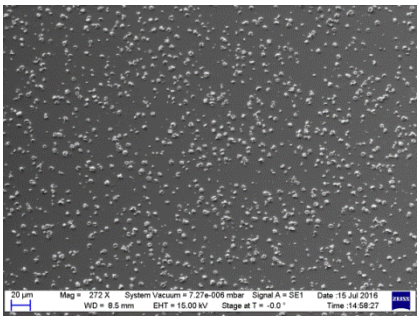
1.25 *mM* $Cu(NO_3)_2$	1.50 *mM* $Cu(NO_3)_2$
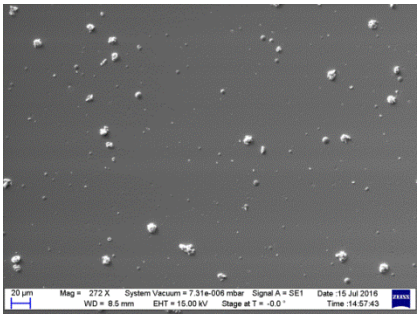	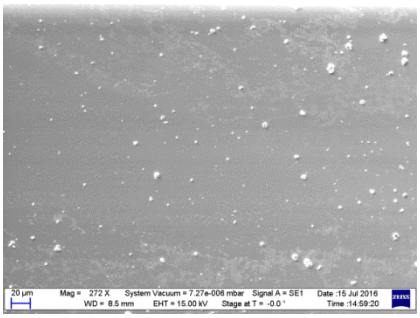
1.75 *mM* $Cu(NO_3)_2$	2.00 *mM* $Cu(NO_3)_2$
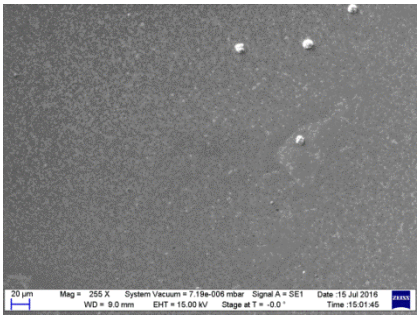	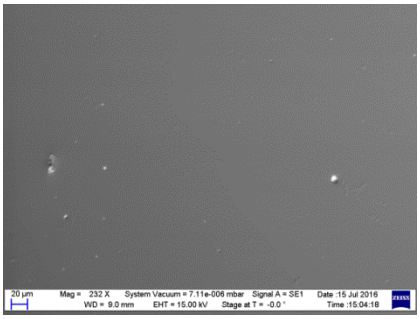

The distinct observation with increasing Cu doping in the morphology is that the level of islands of growth continuously diminishes. This is most likely caused by the increased lack of crystallinity caused by increasing Cu doping levels, as is shown by XRD in Figure 3-14.

3.2.3.5 Seebeck, Electrical Conductivity/Resistivity, Power Factor and Hall Measurements

Whilst the levels of Cu doping and effects on crystallinity have been established, the effect on thermoelectric performance has not yet been investigated. Here the effects on electrical conductivity, Seebeck coefficient and the resulting power factors are investigated to see if there is a level of Cu doping that can improve thermoelectric performance. These experiments were conducted using electrolytes with up to 0.75 *mM* $Cu(NO_3)_2$ by Naylor [20], although the films were not removed from the conducting deposition substrate (Au on Si). Here films are studied with up to 2.00 *mM* $Cu(NO_3)_2$ doping in the electrolyte, and the films are removed from the conducting substrate (Au on Si) to a nonconductive substrate (epoxy on glass) to insure that the substrate does not have any effect of thermoelectric characterisation.

The errors bars seen in Figure 3-15, Figure 3-16 and Figure 3-17 are limited solely to repeat measurements of the same sample, and therefore carry little significance compared to variation seen between samples prepared in the same way that are shown in these figures.

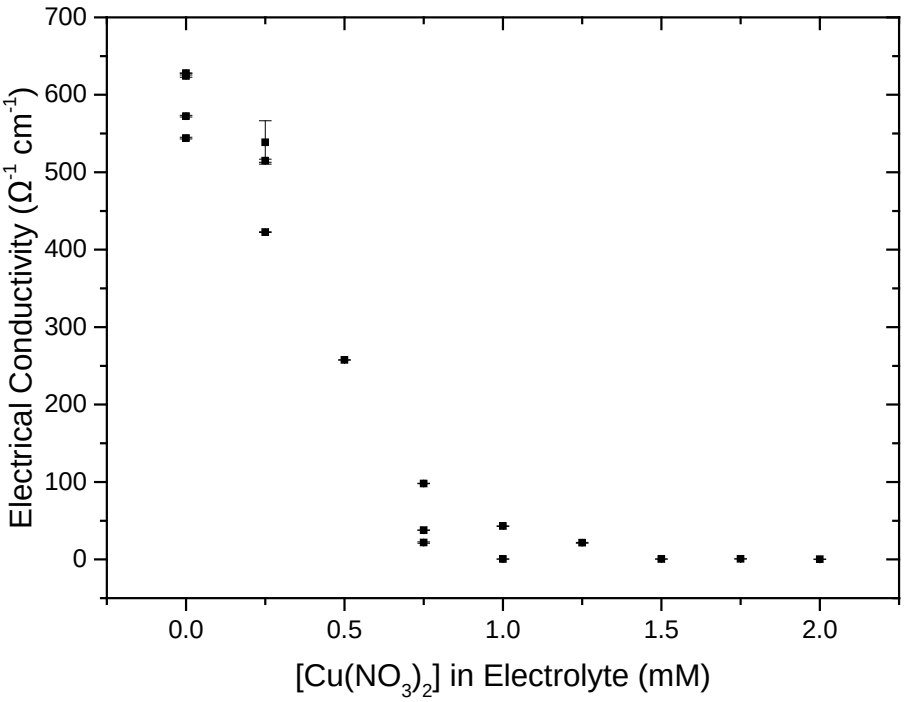

Figure 3-15 – Electrical conductivity of films electrodeposited from an electrolyte of 8 *mM* Bi, 9 *mM* TeO_2, 1 *mM* SeO_2 and between 0.00 and 2.00 *mM* Cu, dissolved in 1 *M* HNO_3.

The films were deposited potentiostatically at +0.05 *V vs. SCE* for 2 *h*. The deposition substrate was Au on Si. The films were removed onto epoxy on glass before conductivity measurements were taken, to remove conductance through Au being measured. The errors represent the 95% confidence limits determined by repeat measurements.

Electrical conductivity, as seen in Figure 3-15, is seen to exponentially decay with increasing $Cu(NO_3)_2$ concentration in the electrolyte. Therefore Cu doping (as $[Cu(NO_3)_2]$ in the electrolyte $\propto$ Cu doping, Figure 3-13) of bismuth telluride selenide via electrodeposition would appear to have a detrimental effect on this aspect for thermoelectric applications. This observation can be rationalised when considering the smaller crystallites in the microstructure generated by the Cu incorporation (Figure 3-14) [132].

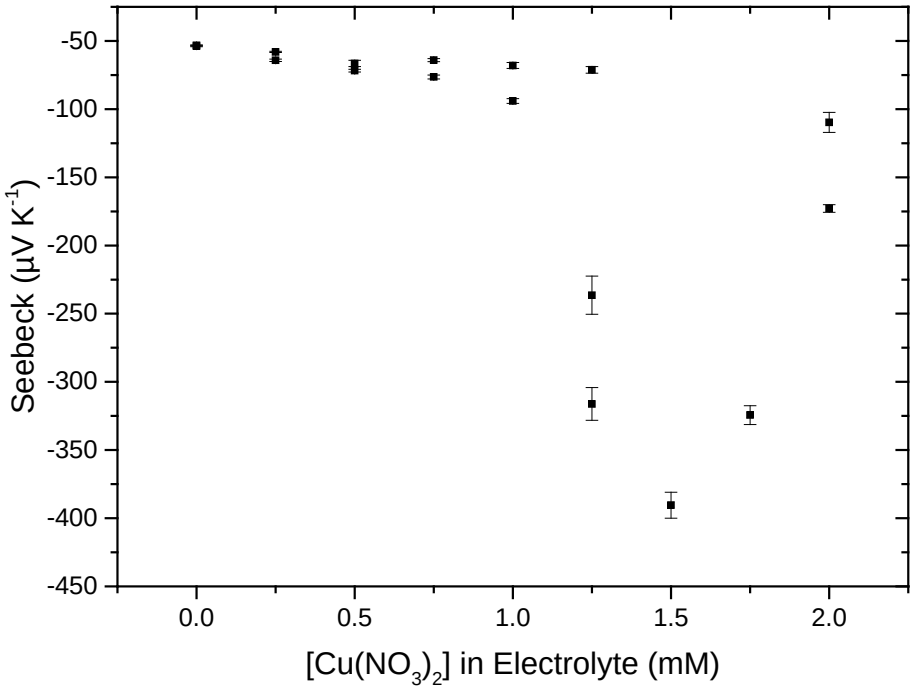

Figure 3-16 – Seebeck coefficient of films electrodeposited from an electrolyte of 8 *mM* Bi, 9 *mM* TeO_2, 1 *mM* SeO_2 and between 0.00 and 2.00 *mM* Cu, dissolved in 1 *M* HNO_3. The films were deposited potentiostatically at +0.05 *V vs. SCE* for 2 *h*. The deposition substrate was Au on Si. The films were removed onto epoxy on glass before Seebeck measurements were taken. The errors represent the 95% confidence limits determined by repeat measurements.

The Seebeck coefficient, as shown in Figure 3-16, tends to become more negative as the levels of Cu are increased. A value as high as -390 $\mu V K^{-1}$ was obtained when 1.50 *mM* $Cu(NO_3)_2$ was

present in the electrolyte. To the best of knowledge, this is the highest Seebeck value ever recorded for an electrodeposited bismuth telluride based material. The Seebeck coefficient should not be looked at in isolation however, and should be considered along with other thermoelectric performance indicators.

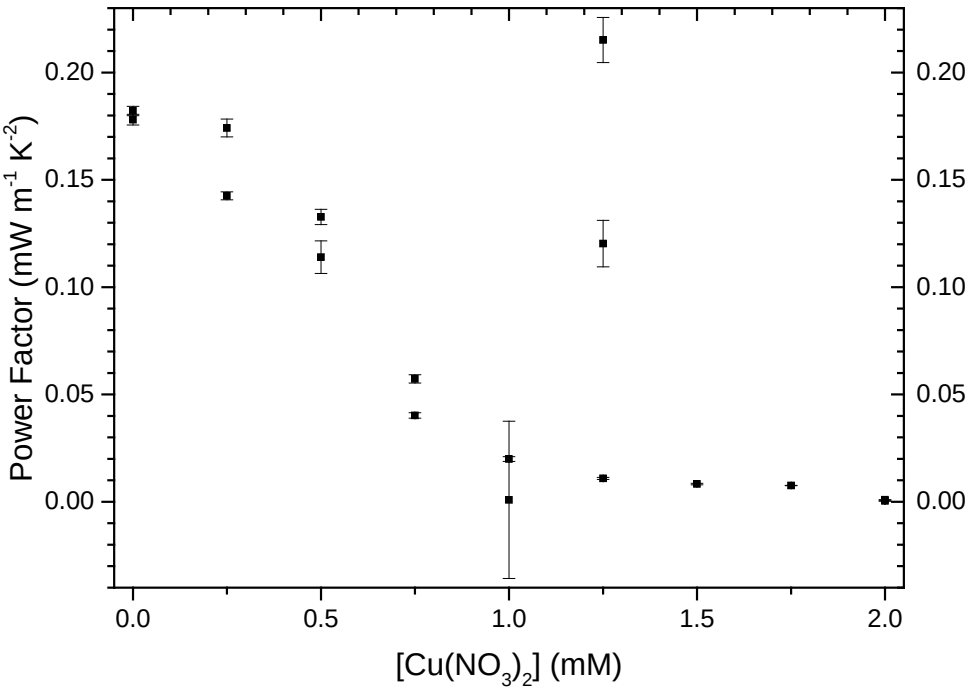

Figure 3-17 – Power factor of films electrodeposited from an electrolyte of 8 *mM* Bi, 9 *mM* TeO_2, 1 *mM* SeO_2 and between 0.00 and 2.00 *mM* Cu, dissolved in 1 *M* HNO_3. The films were deposited potentiostatically at +0.05 *V vs. SCE* for 2 *h*. The deposition substrate was Au on Si. The films were removed onto epoxy on glass before Seebeck measurements were taken. The errors represent the 95% confidence limits determined by repeat measurements.

Whilst the ability of Cu doping to improve the Seebeck coefficient has led to an improved power factor for one of the 1.25 mM $Cu(NO_3)_2$ samples (from 0.18 *mW m^1 K^{-1}* to 0.22 *mW m^1 K^{-1}*), this increase is only marginal and not reproducible. The overall trend in power factor, shown in Figure 3-17, is a decrease with increasing Cu doping levels. All that can be concluded from this data is that there is no reproducible increase in power factor.

3.2.4 Silver Doped Bismuth Tellurium Selenide

3.2.4.1 Cyclic Voltammetry

The effect of the addition of $Ag(NO_3)$ to the electrolyte was studied via cyclic voltammetry. The resulting voltammograms are depicted in Figure 3-18. A saturated mercury-mercury sulphate electrode was used instead of a saturated calomel electrode as to prevent the formation and precipitation of AgCl. The reference was found to have potential of -0.444 *vs SCE*, so the potential limits in the cyclic voltammetry were adjusted accordingly to produce the same limits as used in previous voltammograms.

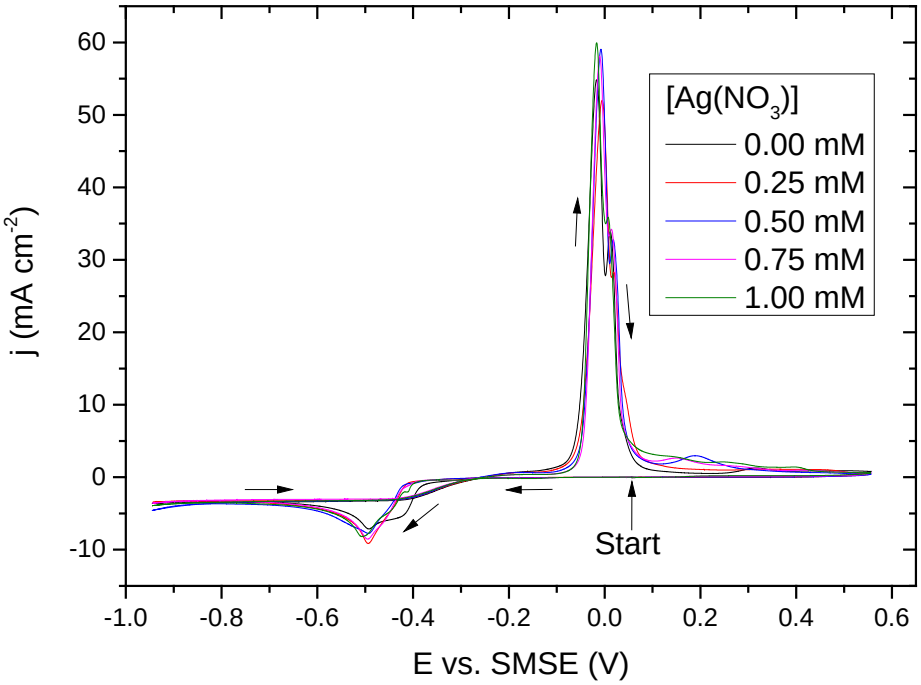

Figure 3-18 - Cyclic voltammograms recorded at 20 *mV* s^{-1} in an electrolyte of 8.00 *mM* Bi, 9.00 *mM* TeO_2, 1.00 *mM* SeO_2 and between 0.00 *mM* and 1.00 *mM* $Ag(NO_3)$, dissolved in 1 *M* HNO_3. The voltammogram started at a potential of +0.056 *V vs. SMSE* where no reaction occurs and is scanned between -0.944 *V vs. SMSE* and +0.556 *V vs. SMSE*. The black arrows indicate the direction of the scan.

From Figure 3-18 it can be observed that the addition of 0.25 *mM* $Ag(NO_3)$ shifts the initial deposition potential of bismuth tellurium selenide cathodically by 40 *mV*. This shift is not increased by the addition of more $Ag(NO_3)$, up to 1.00 *mM* as studied here. Despite the initial shift in deposition potential, the peak deposition potential does not shift and stays at -494 *mV vs. SMSE*. This indicates that whilst initially nucleation is made more unfavourable by the presence of

Ag, there are no other electrochemical effects. There is no distinct separate oxidation peak for Ag, as was seen for Cu in Figure 3-11, therefore it is assumed that Ag is stripped at the same time as the rest of the electrodeposit.

The reduction peak at -494 *mV vs. SMSE* can be attributed to be that of a deposit of $Bi_2Te_{3-x}Se_x$, by the reaction shown in Equation 3.6 [124]. The oxidation peaks at -14 *mV vs. SMSE* and the shoulder at +16 *mV vs. SMSE* can be attributed to Equation 3.7 and Equation 3.8 respectively. Ag doping deposition is believed to reduced and oxidised within those peaks. To test if Ag is actually being deposited EDX analysis was conducted.

3.2.4.2 Composition

Silver doped bismuth tellurium selenide thin films (~9 μm, see Table A-13) were initially deposited at a potential of -0.394 *V vs. SMSE* for 2 hours. This allowed for a deposition potential that is equivocal to +0.05 *V vs. SCE* used for Cu doped films. Despite several attempts, the film would not peel off from the substrate and as a result was damaged. To resolve this issue the deposition potential was shifted to -0.444 *V vs. SMSE* and the deposition time remained the same at 2 hours. Films were deposited from electrolytes with up to 1.00 *mM* $Ag(NO_3)$ present. A current time transient for a film deposited with 1.00 *mM* $Ag(NO_3)$ present in the electrolyte is shown in Figure 3-19.

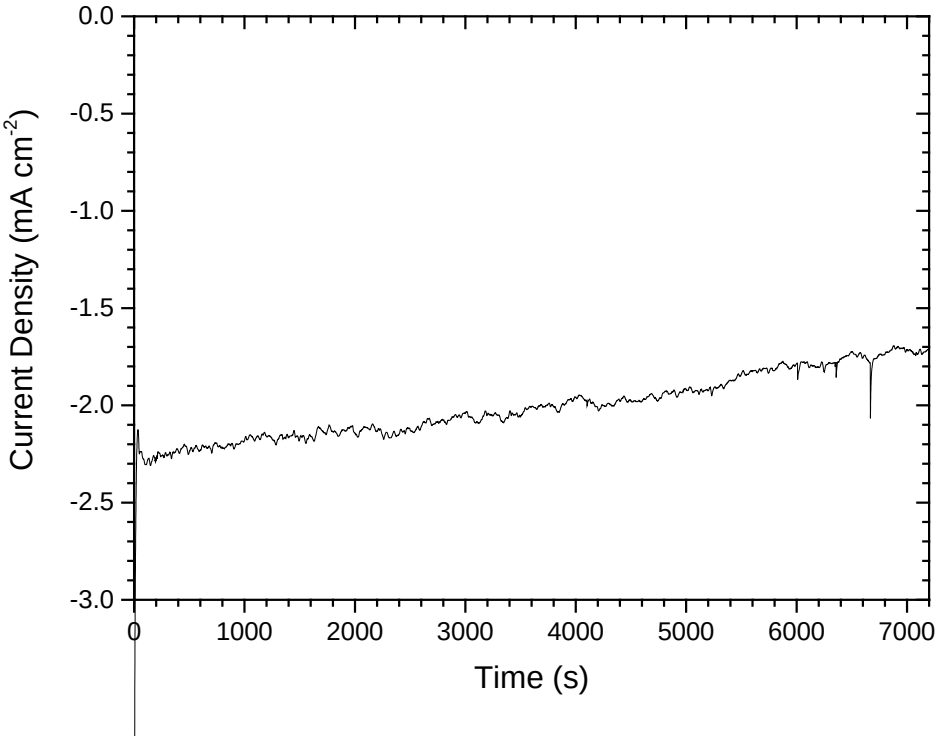

Figure 3-19 - Current time transient of a film electrodeposited from an electrolyte of 8.0 *mM* Bi, 9.0 *mM* TeO_2, 1.0 *mM* SeO_2 and 1.00 *mM* $Ag(NO_3)$ in 1 *M* HNO_3. The deposition potential was -0.444 *V vs. SMSE* and deposition time was 2 *h*. The working electrode was a Au on Si substrate with a 10 *mm* × 10 *mm* electrode area. The total deposition charge was -14.48 *C*.

The electrodeposited films were set in epoxy on glass and peeled off the substrate prior to EDX analysis (see Figure 2-13). The resulting EDX analysis can be seen in Figure 3-20.

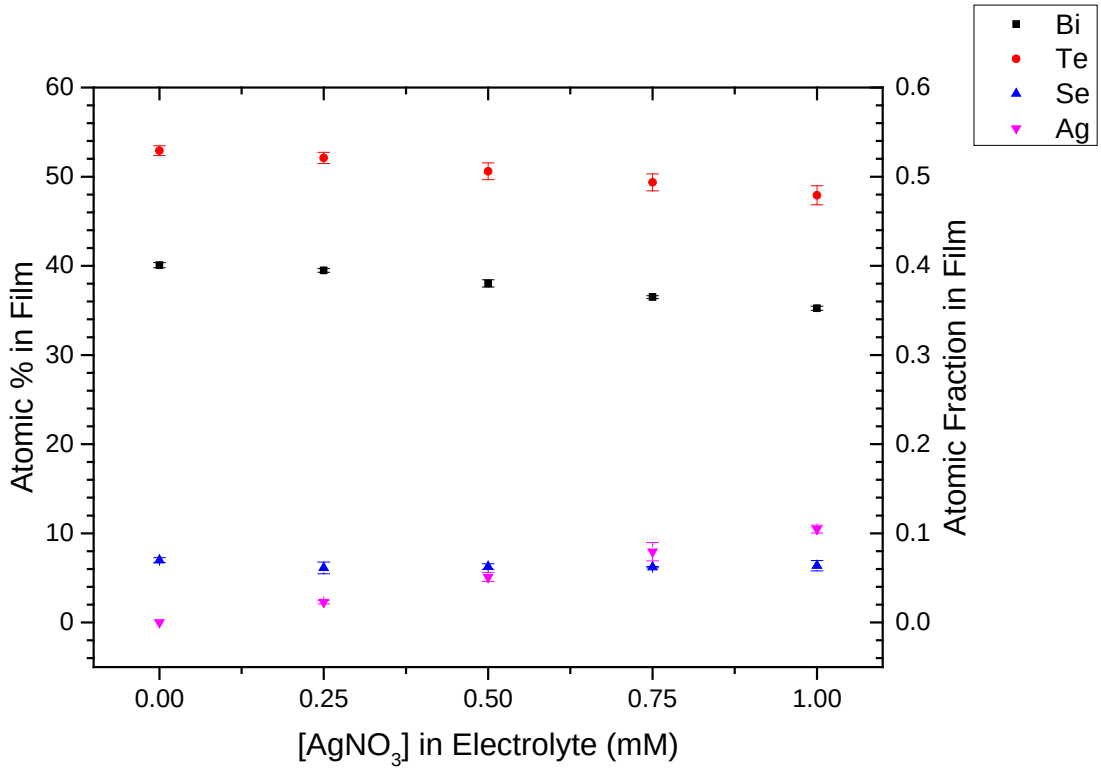

Figure 3-20 - EDX analysis of elemental composition of films electrodeposited from an electrolyte of 8.00 *mM* Bi, 9.00 *mM* TeO_2, 1.00 *mM* SeO_2 and between 0.00 and 1.00 *mM* $Ag(NO_3)$, dissolved in 1 *M* HNO_3. The films were deposited potentiostatically at -0.444 *V vs. SMSE* for 2 *h*. The deposition substrate was Au on Si. The films were removed onto epoxy on glass before EDX analysis was performed, to remove the possibility of Au on the spectrum. The errors represent the 95% confidence limits determined by 3 measurements.

The level of Ag incorporation in the electrodeposited films increases with increasing Ag levels in the electrolyte. The trend appears to be linear, with a 11% incorporation of Ag when 1.00 *mM* of $Ag(NO_3)$ is present in the electrolyte. Interestingly in contrast to Cu doping (see Figure 3-13), the levels of Bi, Te and Se all appear to lower equally relative to their original levels.

The observations seen in Figure 3-20 appear to suggest that Ag is being deposited, but not replacing any atom in the crystal structure. To help corroborate this hypothesis, XRD was conducted.

3.2.4.3 XRD

To help understand the nature of Ag incorporation in the electrodeposited films, XRD was conducted to investigate the effect of Ag doping on the crystal structure of bismuth tellurium selenide. The results can be seen in Figure 3-21.

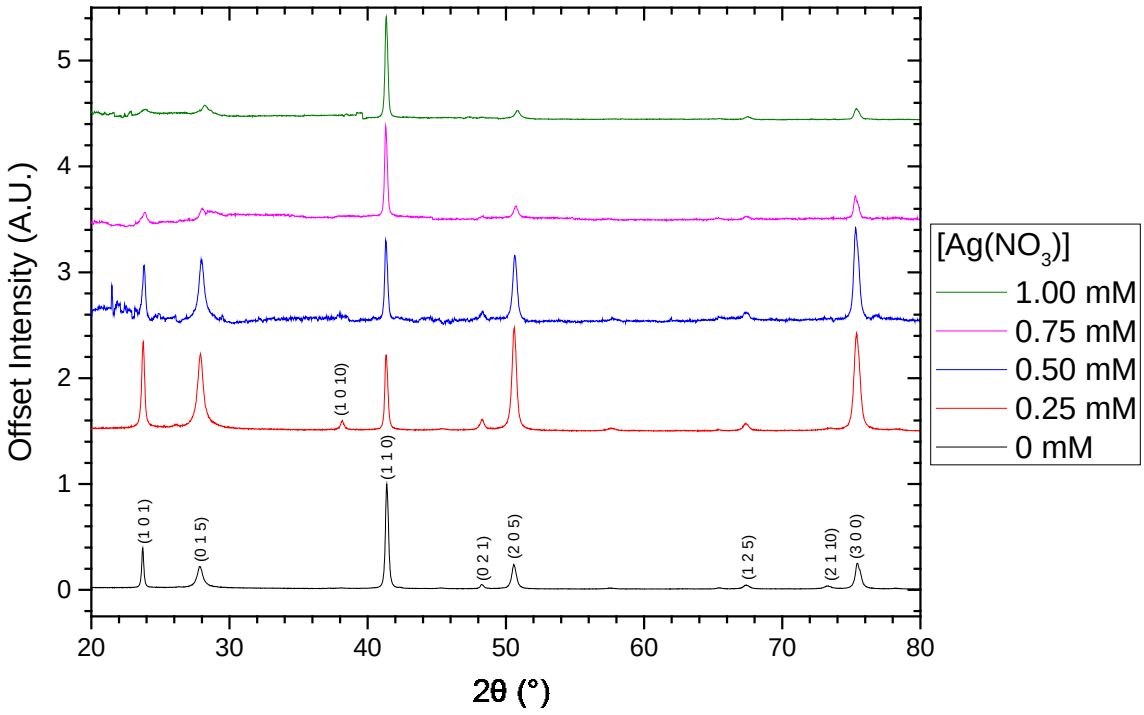

Figure 3-21 - Symmetric XRD scans of films electrodeposited from an electrolyte of 8.00 *mM* Bi, 9.00 *mM* TeO_2, 1.00 *mM* SeO_2 and between 0.00 and 1.00 *mM* $Ag(NO_3)$, dissolved in 1 *M* HNO_3. The films were deposited potentiostatically at -0.444 *V vs. SMSE* for 2 *h*. The deposition substrate was Au on Si. The films were removed onto epoxy on glass before XRD analysis was performed, to remove Au from the spectrum. All peaks up to 70° were fitted from the "Bismuth Tellurium Selenide" file in the PDXL software, No: 00-051-0643. The COD powder stick pattern can be found in Figure A-2. Peaks after 70° were fitted from the "Tellurobismuthite" file in the PDXL software No:00-008-0027 (ICDD powder diffraction file 00-015-0863). The ICDD powder stick pattern can be found in Figure A-1.

All the films maintain a (1 1 0) orientation through all doping levels, with the exception of 0.25 *mM* $Ag(NO_3)$ and 0.50 *mM* $Ag(NO_3)$ which exhibit no dominate orientation. The structure can be identified as having the R-3m structure of bismuth telluride and bismuth tellurium selenide, as the peaks align with their diffraction standards (Tellurobismuthite ICDD file 00-015-0863, and Bismuth Tellurium Selenide COD file 1511976). The degree of order, however, is seen to decrease through increased Ag doping levels. This is evident from the increased noise to signal ratio seen in the patterns in Figure 3-21 as Ag levels increase. At no point can a set of separate silver peaks be identified, which leads to the conclusion that either silver is depositing separately with no crystal structure, or is being incorporated into the R3m structure of bismuth tellurium selenide.

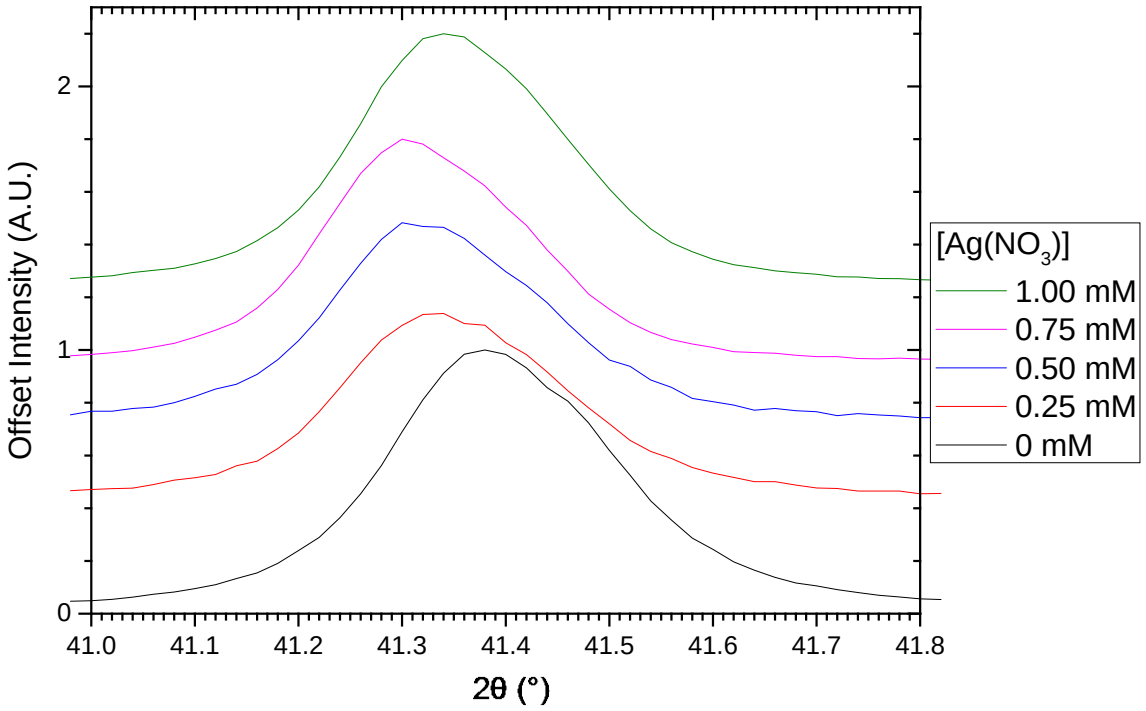

Figure 3-22 – Enlargement of the (1 1 0) peak seen in Figure 3-21.

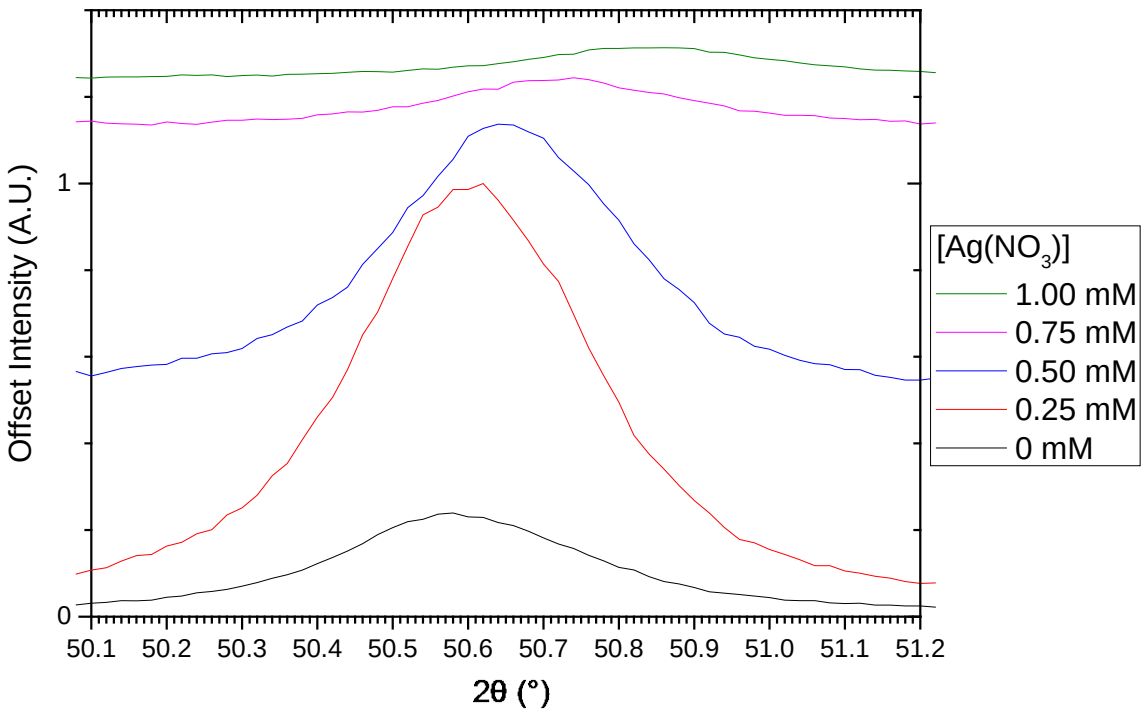

Figure 3-23 - Enlargement of the (2 0 5) peak seen in Figure 3-21.

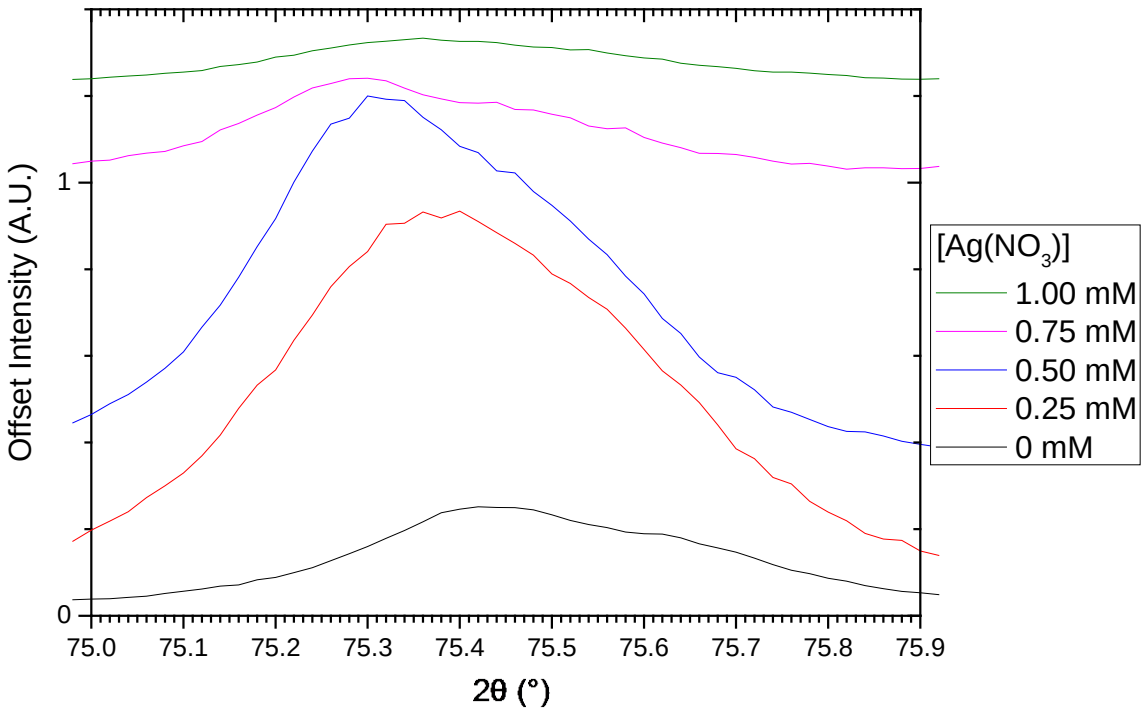

Figure 3-24 - Enlargement of the (3 0 0) peak seen in Figure 3-21.

A close inspection of the (1 1 0), (2 0 5) and (3 0 0) peaks, as shown in Figure 3-22, Figure 3-23 and Figure 3-24 respectively reveals that for the (1 1 0) and (2 0 5) peaks a shift in the peak to smaller 2θ angles with increasing $Ag(NO_3)$ levels up to 0.75 *mM* is seen. At a $Ag(NO_3)$ concentration of 1.00 *mM* the peak is shown to shift to smaller 2θ relative to 0.75 *mM* $Ag(NO_3)$, but this is still smaller than in the absence of $Ag(NO)_3$. For the (3 0 0) peak however the peaks are shown to shift to increasing 2θ values with increasing $Ag(NO_3)$ concentration. This observation seems to suggest that Ag has caused asymmetric distortion in the unit cell, which would appear to indicate that silver is being incorporated into the crystal structure.

These XRD patterns would seem to suggest, that whilst Ag is not changing the crystal structure, there is a destabilising effect. When this is coupled with the EDX data in Figure 3-13 , it would appear that Ag is being incorporation in the structure, reducing levels of bismuth tellurium selenide thus reducing the signal to noise ratio.

3.2.4.4 SEM

To investigate the effect on morphology the incorporation of Ag has on bismuth tellurium selenide electrodeposited films, a series of samples were prepared for SEM analysis. All films were deposited and not removed from the deposition substrate (Au on Si), with the exception of one undoped sample. The results can be seen in Table 3-12.

Table 3-12 - Scanning electron microscopy images of silver doped bismuth tellurium selenide films electrodeposited from an electrolyte solution containing 8.00 *mM* Bi, 9.00 *mM* TeO_2, 1.00 *mM* SeO_2 and between 0.00 and 1.00 *mM* $Ag(NO_3)$, dissolved in 1 *M* HNO_3. The films were deposited potentiostatically at -0.444 *V vs. SMSE* for 2 *h*.

0.00 *mM* $Ag(NO_3)$, electrolyte side	0.00 *mM* $Ag(NO_3)$, substrate side
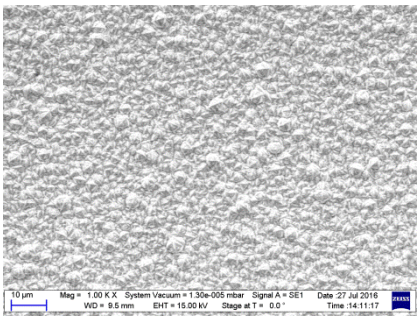	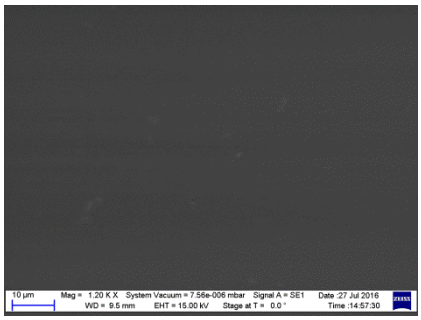
0.25 *mM* $Ag(NO_3)$, electrolyte side	0.50 *mM* $Ag(NO_3)$, electrolyte side
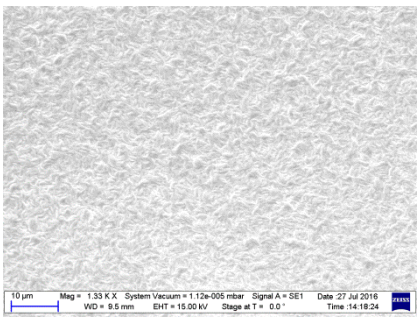	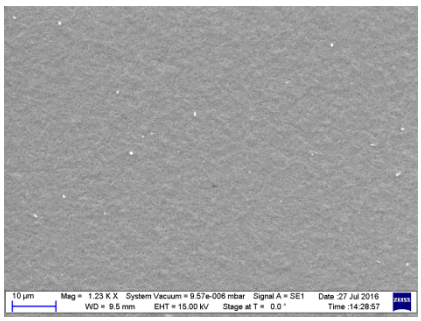
0.75 *mM* $Ag(NO_3)$, electrolyte side	1.00 *mM* $Ag(NO_3)$, electrolyte side
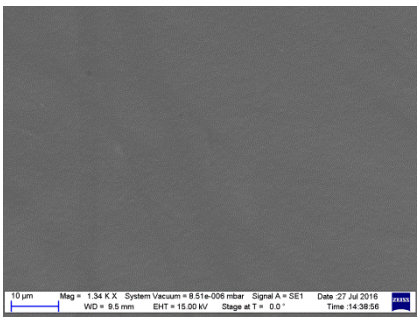	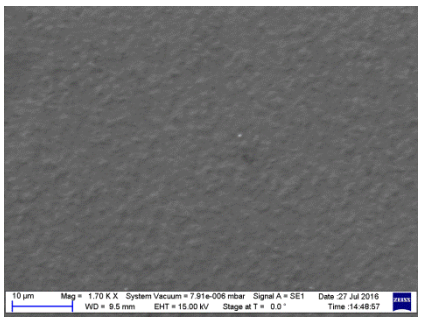

There appears to be no distinct change in the morphology with increasing Ag doping. This leads to the conclusion that Ag is not being incorporated into the structure, rather it is being separately deposited.

3.2.4.5 Seebeck, Electrical Conductivity/Resistivity and Hall Measurements

Whilst the levels of Ag doping and effects on crystallinity have been established, the effect on thermoelectric performance has not yet been investigated. Here the effects on electrical conductivity, Seebeck coefficient and the resulting power factors are investigated to see if there is

a level of Ag doping that can improve thermoelectric performance. Here films are studied with up to a concentration of 1.00 *mM* $Ag(NO_3)$ in the electrolyte, and the films are removed from the conducting substrate (Au on Si) to a non-conductive substrate (epoxy on glass) to ensure that the substrate does not have any effect on thermoelectric characterisation.

The errors bars seen in Figure 3-25, Figure 3-26 and Figure 3-27 are limited solely to repeat measurements of the same sample, and therefore likely carry little significance compared to variation that may be seen between samples prepared in the same way.

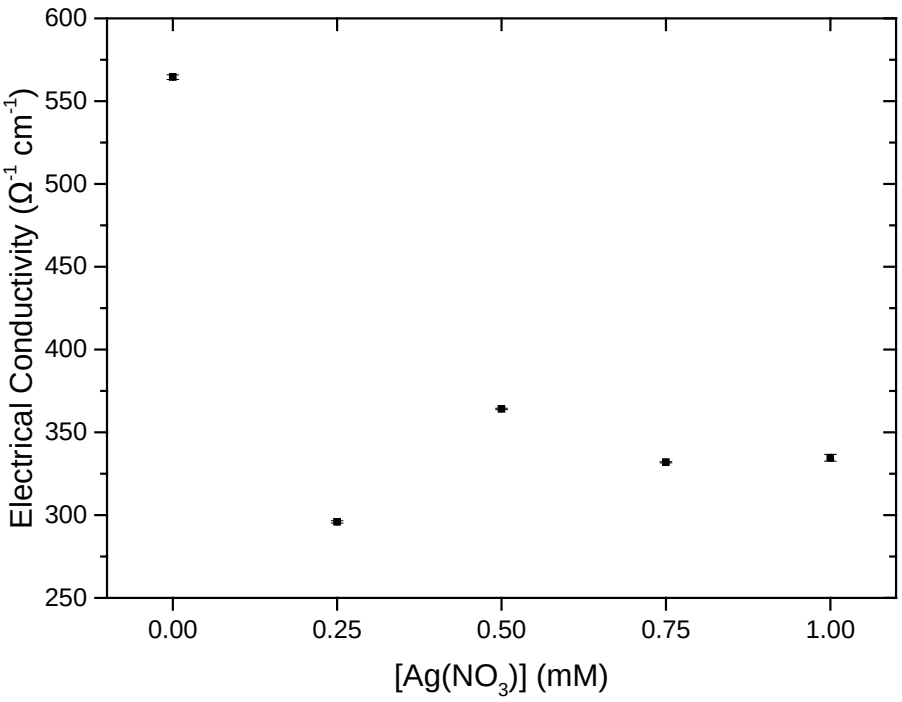

Figure 3-25 - Electrical conductivity of films electrodeposited from an electrolyte of 8 *mM* Bi, 9 *mM* TeO_2, 1 *mM* SeO_2 and between 0.00 and 1.00 *mM* $Ag(NO_3)$, dissolved in 1 *M* HNO_3. The films were deposited potentiostatically at -0.444 *V vs. SMSE* for 2 *h*. The deposition substrate was Au on Si. The films were removed onto epoxy on glass before conductivity measurements were taken, to remove conductance through Au being measured. The errors represent the 95% confidence limits determined by repeat measurements.

Electrical conductivity, as seen in Figure 3-25, is seen to initially decay with the addition of $Ag(NO_3)$ into the electrolyte, however there is no exponential decay in electrical conductivity as was seen with Cu doping. Electrical conductivity is seen to remain at a similar level throughout

with further increase in Ag doping levels. Whilst Ag doping of bismuth telluride selenide via electrodeposition would appear to have a detrimental effect on this aspect for thermoelectric applications, the extent is nowhere near as severe as was seen for Cu. The power factor could well still be increased, provided that the Seebeck coefficient is improved.

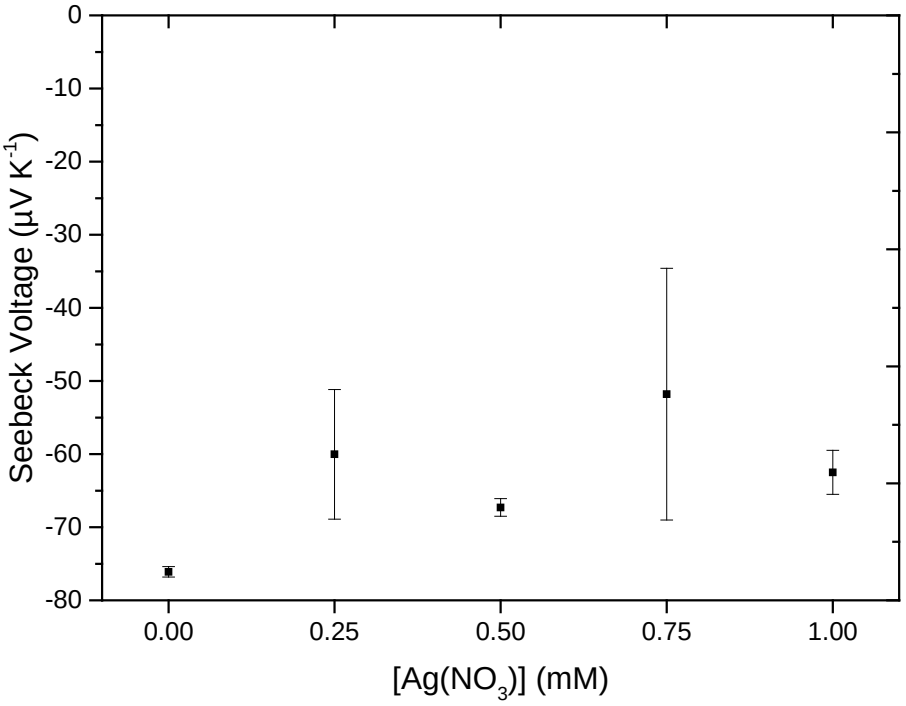

Figure 3-26 - Seebeck coefficient of films electrodeposited from an electrolyte of 8 *mM* Bi, 9 *mM* TeO_2, 1 *mM* SeO_2 and between 0.00 and 1.00 *mM* $Ag(NO_3)$, dissolved in 1 *M* HNO_3. The films were deposited potentiostatically at -0.444 *V vs. SMSE* for 2 *h*. The deposition substrate was Au on Si. The films were removed onto epoxy on glass before Seebeck measurements were taken. The errors represent the 95% confidence limits determined by repeat measurements.

The Seebeck coefficient, as shown in Figure 3-26, initially becomes less negative with the addition of Ag. The further addition of silver is shown to have no more effect within error. This leads to the conclusion that the addition of silver is detrimental to the thermoelectric performance of electrodeposited bismuth tellurium selenide thin (~9 μm, see Table A-13) films. Interestingly the Seebeck coefficient for the undoped film was -76.1 (±0.7) $\mu V\ K^{-1}$, which is higher than was seen previously for undoped bismuth tellurium selenide (-54.7 (±0.4) $\mu V\ K^{-1}$) in this work. There were two possible causes for this, either the change in deposition potential or the change in reference

electrode. A film was made using an SCE with a deposition potential of +0.00 *V*. This gave the same potential as the rest of the work on Ag doping, as the difference between the SCEs and SMSE references was -0.444 *V*. The Seebeck coefficient for this film was measured to be -42.5 (±0.8) $\mu V\ K^{-1}$. Therefore the difference in Seebeck coefficient can be attributed to the reference electrode. Most likely the presence of Cl in the electrolyte from the SCE reference electrode has a detrimental effect on the electrodeposition of bismuth tellurium selenide films.

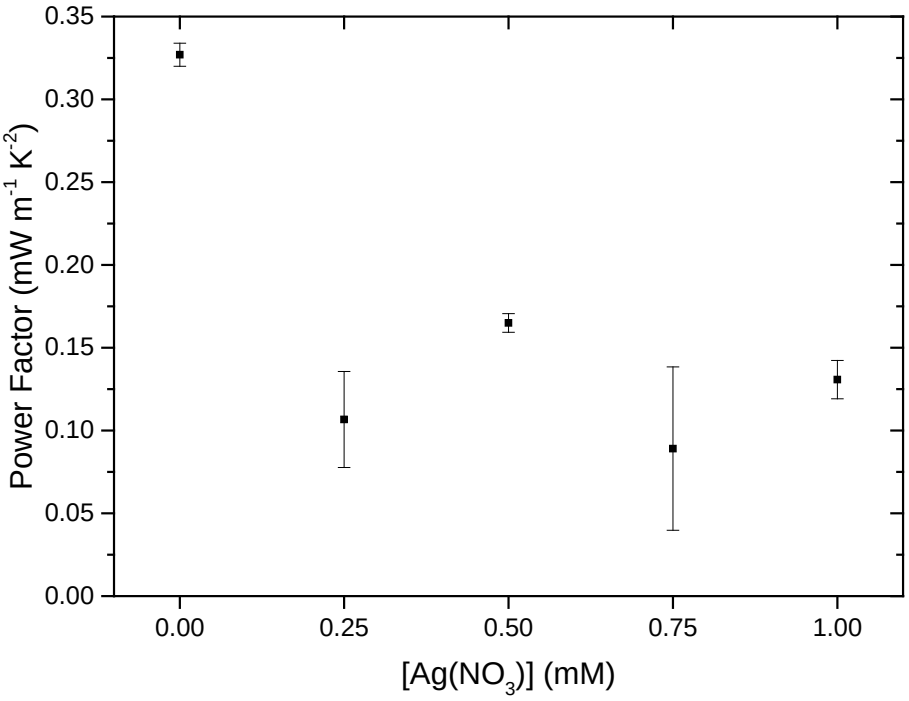

Figure 3-27 – Power factor of films electrodeposited from an electrolyte of 8 *mM* Bi, 9 *mM* TeO_2, 1 *mM* SeO_2 and between 0.00 and 1.00 *mM* $Ag(NO_3)$, dissolved in 1 *M* HNO_3. The films were deposited potentiostatically at -0.444 *V vs. SMSE* for 2 *h*. The deposition substrate was Au on Si. The films were removed onto epoxy on glass before Seebeck measurements were taken. The errors represent the 95% confidence limits determined by repeat measurements.

As expected from the electrical conductivity and Seebeck coefficient data, the power factor for silver doped films is diminished when compared to undoped bismuth tellurium selenide. It is clear that silver doping of electrodeposited bismuth tellurium selenide is detrimental to thermoelectric performance.

3.2.5 Effect of Reference Electrode

Of note is that the best power factor observed in this chapter is that of 0.00 *mM* $Ag(NO_3)$, which shows a power factor of 0.33 $mW\ m^1\ K^{-1}$, which is significantly larger when compared to 0.00 *mM* $Cu(NO_3)_2$ which had a power factor of 0.18 $mW\ m^1\ K^{-1}$. The 0.00 *mM* $Cu(NO_3)_2$ film was produced using a voltage 50 *mV* higher. A film produced at the same voltage as the Ag doped films with a SCE reference electrode, had a Seebeck coefficient of -42.5 (±0.8) $\mu V\ K^{-1}$ (compared to -76.1 (±0.8) $\mu V\ K^{-1}$ using SMSE), an electrical conductivity of 714 (± 2) $S\ cm^{-1}$ (compared to 564 (± 2) $S\ cm^{-1}$, yielding a power factor of 0.13 $mW\ m^1\ K^{-1}$. Therefore use of a SMSE reference electrode instead of a SCE reference electrode produced a film with higher thermoelectric performance.

The source of the difference in thermoelectric performance is believed to be caused by Cl^- entering the electrolyte from the SCE reference electrode, which in turn affects the electrodeposition process. Another potential cause could be down to low levels of K incorporation into films produced with a SMSE reference electrode, this is less likely however as K was not detected in the films by EDX. To examine these hypotheses further experiments not conducted in this work would need to be carried out. The use of a third type of reference electrode not containing Cl^- of K^+ (e.g. Mercury / Mercury Oxide), would help further understand the underlying cause of the increase in thermoelectric performance.

3.3 Conclusions

Bismuth telluride thin films (~8 μm, see Table A-11) were successfully electrodeposited from an electrolyte of 8 *mM* Bi and 10 *mM* TeO_2 dissolved in 1 *M* HNO_3. The films were deposited potentiostatically at 0.00 *V vs. SCE* for 2 *h*. The deposition substrate was Au on Si. EDX showed a slight Te excess, which increased as the film grew. XRD confirmed that the films were bismuth telluride and showed a preferential crystal orientation of (1 1 0). To remove any influence of the Au conducting substrate on the electrical measurements, films were removed onto epoxy on glass before thermoelectric measurements were conducted. A Seebeck coefficient of -43.8 (±0.5) $\mu V\ K^{-1}$, an electrical conductivity of 820 (±72) S cm^{-1} and a power factor of 0.158 (±0.008) $mW\ m^{-1}\ K^{-2}$ were measured. These values are in line with electrodeposited bismuth telluride films reviewed by Boulanger [120]. The thermoelectric measurements were performed throughout the course of 12 months. The Seebeck coefficient was seen to slightly increase to -46.9 (±1.3) $\mu V\ K^{-1}$, whilst the electrical conductivity slightly decreased to 797 (±103) S cm^{-1}, which lead to a slightly increased power factor of 0.175 (±0.017) $mW\ m^{-1}\ K^{-2}$. These results show that electrodeposited bismuth telluride is stable for thermoelectric applications, and could make durable thermoelectric generators that would not diminish in power over time.

Bismuth tellurium selenide thin films (~7 *μm*, see Table A-11) were successfully electrodeposited from an electrolyte of 8 *mM* Bi, 9 *mM* TeO_2 and 1 *mM* SeO_2 dissolved in 1 *M* HNO_3. The films were deposited potentiostatically at +0.05 *V vs. SCE* for 2 *h*. The deposition substrate was Au on Si. EDX showed a slight Te and Se excess from the ideal stoichiometry. XRD confirmed that the films were bismuth tellurium selenide with no strong preferential crystal orientation. To remove any influence of the Au conducting substrate, films were removed onto epoxy on glass before thermoelectric measurements were conducted. A Seebeck coefficient of -54.7 (±0.4) $\mu V K^{-1}$, an electrical conductivity of 580 (±101) S cm^{-1} and a power factor of 0.173 (±0.023) $mW m^{-1} K^{-2}$ were measured. These values are in line with electrodeposited bismuth telluride films reviewed by Boulanger [120]. The thermoelectric measurements were performed throughout the course of 12 months. The Seebeck coefficient was seen to slightly increase to -56.5 (±1.4) $\mu V K^{-1}$, whilst the electrical conductivity slightly decreased to 547 (±90) S cm^{-1}, which lead to a slightly increased power factor of 0.175 (±0.037) $mW m^{-1} K^{-2}$. These results show that electrodeposited bismuth tellurium selenide is stable for thermoelectric applications, and could make durable thermoelectric generators that would not diminish in power over time. Their power factor shows very similar levels of performance compared to bismuth telluride, however with a lower electrical conductivity. This would lead to a conclusion of a probable lower thermal conductivity and thus higher *ZT* figure of merit compared to bismuth telluride electrodeposited films.

Cu doped bismuth tellurium selenide thin films (~6 *μm*, see Table A-12) were electrodeposited from an electrolyte of 8.00 *mM* Bi, 9.00 *mM* TeO_2, 1.00 *mM* SeO_2 and between 0.00 and 2.00 *mM* $Cu(NO_3)_2$, dissolved in 1 *M* HNO_3. Cu doping in electrodeposited films was seen to increase linearly with Cu concentration in the electrolyte, with 2.00 *mM* $Cu(NO_3)_2$ yielding films with a 15% Cu composition. Cu was seen to predominantly replace Bi in the films. All Cu doped films maintain a (0 1 5) orientation through all doping levels and remained the R-3m space group of bismuth tellurium selenide. The grain size was seen to initially increase with the addition of Cu into the electrodeposited films, however further addition of Cu continually reduced the grain size. Electrical conductivity was seen to exponentially decay with increasing Cu incorporation, whilst the Seebeck coefficient was seen to increase by nearly an order of magnitude when films were made with 1.50 *mM* $Cu(NO_3)_2$ present in the electrolyte. A power factor was recorded of 0.22 $mW m^{1} K^{-1}$ for a sample prepared with 1.25 *mM* $Cu(NO_3)_2$ in the electrolyte (increased from 0.18 $mW m^{1} K^{-1}$ shown without Cu), this increase is however was only marginal and not reproducible.

Ag doped bismuth tellurium selenide thin films (~9 *μm*, see Table A-13) were electrodeposited from an electrolyte of 8.00 *mM* Bi, 9.00 *mM* TeO_2, 1.00 *mM* SeO_2 and between 0.00 and 1.00 *mM* $Ag(NO_3)$, dissolved in 1 *M* HNO_3. Ag doping in electrodeposited films was seen to increase linearly with Ag concentration in the electrolyte, with 1.00 *mM* $Ag(NO_3)$ yielding films with a 11% Ag

composition. A (1 1 0) orientation is largely kept through Ag doping, and the crystal structure remained R3m. A shift in the (1 1 0), (2 0 5) and (3 0 0) peaks analysed indicated that the incorporation of Ag was causing an asymmetric change in the unit cell. Electrical conductivity was seen to initially decrease with Ag incorporation, although did not deteriorate further upon more Ag doping. The Seebeck coefficient was seen to similarly initially decrease with Ag incorporation, although did not deteriorate further upon more Ag doping. The same result was seen for power factors.

Chapter 4: Bismuth Telluride Nanostructuring

4.1 Introduction

Since 1993 when Dresselhaus *et al.* first postulated that reduced dimensionality in quantum wires (1D) [38] and quantum wells (2D) [37] offer a strategy for increasing *ZT* relative to bulk values, there has been a drive to fabricate nanostructured thermoelectric materials. Nanowires have been a key feature of that, with a *ZT* value of 14 theorised for nanowires with 0.5 *nm* diameters [38]. So far, however, no study has achieved close to these values. Many different techniques have been used to fabricate bismuth telluride nanowires and nanomaterials, such as vapour liquid solid [135], solvothermal [136], solution phase synthesis [137]–[139] and electrodeposition [140]–[144].

4.1.1 Non-Templated Bismuth Telluride Nanomaterials and Related Materials

Bismuth telluride nanomaterials and related materials have been synthesised in the absence of templates, both directly or with the aid of a base structure.

Bismuth telluride nanomaterials have been synthesised directly using different techniques that include solvothermal [136], vapour liquid solid [135] and microwave assisted wet chemical synthesis [145]. Deng *et al.* [136] synthesised a nanocomposite of bismuth telluride and Te, by using Te rods (100-400 *nm* diameter) synthesised by a solvothermal process as a parent template to growth bismuth telluride onto using a second solvothermal step. This yielded sheet-rod hybrids with diameters between 300-500 *nm*. No thermoelectric characterisation was performed. An earlier paper shows that solvothermal synthesis can be used to make bismuth telluride rods, nanosheets what they define as “rags” too [146]. Hamdou *et al.* [135] used vapour liquid solid synthesis to grow bismuth telluride nanowires on gold nanoparticles. Diameters of the nanowires ranged between 30 *nm* and 150 *nm* and a Seebeck coefficient of 140 $\mu V\ K^{-1}$ was exhibited at 300 *K*. Fan *et al.* [145] used a microwave assisted wet chemical method to synthesise hexagonal plate-like crystals, that possessed a length of 0.5-2.0 *μm* and a thickness of less than 100 *nm*. A homogenous blend of alloyed bismuth telluride powders and the hexagonal plate like crystals gave a *ZT* value of 0.39 when the blend contained 15% by weight of the hexagonal nano-plates. Purkayastha *et al.* [147] used the biomolecular surfactant, L-glutathionic acid (LGTA) to direct the synthesis of branched bismuth telluride/sufide core/shell nanords. The widths of the nanorods were between 35-290 *nm*, no thermoelectric characterisation was conducted.

Bismuth telluride nanomaterials have been formed using a base structure in the following papers. Yu *et al.* [137] synthesised bismuth telluride nanowires by first producing Te nanowires in a solution based synthesis, in a second step these were converted to bismuth telluride nanowires. This technique used temperatures of 200 *°C* for several hours to synthesise the nanowires. Nanowires with diameters down to 67.8 *nm* were produced. No thermoelectric characterisation was conducted. Zhang *et al.* [138] used to same technique, however, nanowire diameters as low as 8 *nm* were achieved which exhibited a peak *ZT* value of 0.96 at 380 *K* when turned into composites using spark plasma sintering. Zhang *et al.* [139] also used the same technique generating Te-Bi_2Te_3 "barbells" with diameters in excess of 35 *nm*, with a figure of merit (*ZT*) of 0.24 measured at 400 *K*. Xiao *et al.* [148] synthesised bismuth telluride nanotubes by exploiting galvanic displacement of Ni nanowires. The tube thickness was approximately 20 *nm* with the tube diameter being about 140 *nm*. No thermoelectric characterisation was performed.

Although these template free methods have managed to fabricate high quantities of bismuth telluride nanomaterials, they have failed to integrate the produced nanomaterials into devices, or achieve dimensions low enough (0.5 *nm* diameter for nanowires) to exploit the full increased *ZT* values that are theorised by Dresselhaus [37], [38].

4.1.2 Templated Bismuth Telluride and Related Nanowires

Template controlled synthesis is a popular technique used to fabricate bismuth telluride nanowires. There are two types of porous membranes that have typically been used: either porous anodic alumina [49], [149]–[161], and ion track-etched membranes [50], [51], [162]–[167].

4.1.2.1 Porous Anodic Alumina

Porous anodic alumina membranes can be prepared by a 2 step process. First aluminium membranes are anodized in oxalic acid, which yields self-organised templates with porosities of 10% [140]–[144]. To allow for mechanical stability for further processing steps, membranes are typically between 60 and 80 *µm* thick. Following treatment with oxalic acid, pores with diameters of approximately 40 *nm* are produced. These however fail to transverse through the whole membrane, which is essential to allow the production of a working electrode. The channels are fully opened by wet chemical etching in 5 wt% phosphoric acid solution at 45 *°C*. This process results in pore widening to diameters between 50 and 80 *nm*.

The working electrode is then created by sputtering a gold seed layer, followed by electrodeposition of a larger gold layer from a commercial electroplating solution. This allows for a homogenous layer of gold to be deposited that closes the pores at one end [144].

These templates have been reported widely in the literature to produce bismuth telluride nanowires [49], [149]–[160], there will undoubtedly be several other papers. To the best of my knowledge, the smallest reported nanowires produced using porous anodic alumina templates was by Martìn *et al.* [160] at 15 *nm*. There is however a limitation with porous anodic alumina templates, in that as the pores get smaller electrolytes are less likely to fill the pores as they are too viscous [168]. This leads to a limit in wire diameter using alumina templates with conventional electrolytes.

Alumina templates being incorporated into thermoelectric devices would prove counterproductive, as the thermal conductivity of alumina is 1.9 $W\,m^{-1}\,K^{-1}$ at 300 *K* [169] which would outweigh any reduction in thermal conductivity of bismuth telluride gained through nanostructuring. Therefore there is a need to remove the template. To achieve the removal of the template requires aggressive chemicals such as NaOH or a mixture of H_3PO_4 and H_2CrO_4 for several days at 45 °C [144]. This is unappealing industrially on safety grounds and on production time.

4.1.2.2 Polymer Membranes

To avoid the high thermal conductivity of alumina templates, several groups have used polymer membranes to deposit thermoelectric material nanowires, due to their lower thermal conductivities (e.g. 0.21 $W\,m^{-1}\,K^{-1}$ at 300 *K* for polycarbonate [170]). Two different polymers have been reported in the literature, polyimide [50], [51] and polycarbonate [162]–[167].

The preparation of polymer membranes is a two-step process [144]. The first involves irradiation by fast heavy-ions, which can be at a large accelerator such as GANIL (Caen, France). It should be noted that membranes can be bought, which have already been irradiated by heavy ions [171]. The second involves chemical etching, using the required etching solution [172]. The etching conditions (temperature, concentration and composition of etchant) can determine the geometry of the channels. Channels ranging from ~10 to ~300 *nm* can be created using this technique [144].

As was the case for porous anodic alumina membranes a gold layer is sputtered onto one side of the membrane to allow for a working electrode to be formed. This can either be entirely sputtered, or a gold seed layer sputtered followed by electrodeposition of a larger gold layer.

Picht *et al.* [164] report bismuth telluride nanowire diameters down to 15 *nm* by electrodeposition into polycarbonate membranes, whilst Koukharenko *et al.* [51] achieved bismuth telluride nanowires down to 80 nm by electrodeposition into polyimide membranes.

Whilst not essential for use in devices (as thermal conductivities of polymer membranes are low), it is possible to remove polymer membranes. This is required for more detailed sample characterisation. Polycarbonate membranes can be removed with solvents such as dichloromethane or dimethylformanide [144], which whilst less chemically aggressive than the strong acids or bases used to remove alumina membranes, still pose their own hazard.

If the aspect ratio for freestanding nanowires is greater than 10, the nanowires will collapse onto the substrate [144]. Whilst it is possible in theory to overfill channels in templates and allow an electrodeposition layer to grow on top of the template which links the nanowires together allowing for a freestanding nanowire array, this has only been shown in practice using Pt [173].

Recently Wagner *et al.* [174] created an interconnected nanowire network of Sb by electrodepositing into a polycarbonate membrane. Firstly they created an interconnected channel network in a polycarbonate membrane by irradiating the polymer membrane 4 times, each time rotating the foil by 90° around the foil normal. This was followed by a pulsed potential electrodeposition technique. The smallest nanowire diameter they achieved using this technique was 100 *nm*, but they did successfully create a freestanding network.

4.1.3 Lyotropic liquid Crystal Templates

Whilst both alumina and polymeric templates have proven to be successful in the fabrication of bismuth telluride nanowires, they have their flaws. Alumina has a high thermal conductivity (1.9 W mK^{-1} at 300 *K* [169]) and requires harsh acidic or alkaline conductions to be removed, then isolated nanowires collapse unless they have an aspect ratio less than 10. Polymeric templates seem more promising, in that they have low thermal conductivities (0.21 W mK^{-1} at 300 *K* for polycarbonate [170]), template removal is easier as it can be achieved using solvents such as dichloromethane or dimethylformanide [144] and freestanding interconnected networks can even be achieved (as was shown with Sb [174]). Polymeric membranes still require a lengthy fabrication however, and require unpleasant solvents such as dichloromethane or dimethylformanide if removal of template is desired post deposition.

Lyotropic liquid crystal templates, however, can be formed simply by the addition of a suitable amphiphile into a suitable solvent (typically water). Template removal can be achieved using simple solvents, such as water or ethanol and different structures can be created as different liquid crystal mesophases can be created (see 1.5 for more information).

4.1.3.1 Type I Liquid Crystal Templating

In 1992 liquid crystal templating was first reported in the literature [175], [176], where they used calcination of silicates inside what they believed to be micellar aggregates of hexadecyltrimethylammonium or the hexagonal phase. Attard *et al.* in 1995 [177] used high concentrations of the surfactants $C_{12}EO_8$ and $C_{16}EO_8$ to template silica mesostructures from ordered liquid crystalline mesophases. They did not observe regular mesostructures in materials prepared with low concentrations of surfactant, leading to the conclusion that it was the liquid crystalline phase that was directing the templating and not micellar aggregates as previously debated.

Attard in 1997 [178] went on to fabricate hexagonally structured mesoporous platinum by chemical reduction of hexachloroplatinic acid (HCPA) and ammonium tetrachloroplatinate (ATCP) in the hexagonal phase of $C_{16}EO_8$ with larger than 3 *mm* pieces of less noble metals (Fe, Zn, Mg) producing powders. Coherent platinum films were later produced by electrochemical reduction of HCPA onto gold electrodes [56].

Electrodeposition inside the hexagonal phase of $C_{16}EO_8$ lead to a series of templated structures, which are summarised by Bartlett [54]. The review shows that the method can be applied to a wide range of nanostructured materials which can be electrodeposited from aqueous solutions including metals (Pt, Sn, Co and Pd) [56], [58]–[60], [179], metal oxides (ZnO and Cu_2O) [61], semimetals (Se) [62], polymers (poly-(1,2-diaminobenzene)) [64], and bimetallic layered structures (Pd with Rh) [65]. The method has been applied to semiconductors too (CdTe) [55].

4.1.3.2 Type II Liquid Crystal Templating

Phytantriol (3,7,11,15-tetramethyl-1,2,3-hexadecanetriol) as shown in Figure 4-1 is a non-ionic lipid surfactant, which can exhibit the lamellar, type 2 hexagonal (H_{II}) and type 2 bicontinuous cubic liquid crystal phases. The phase diagram for phytantriol/water system was deduced by Barauskas and Landh [180] and is shown in Figure 4-2.

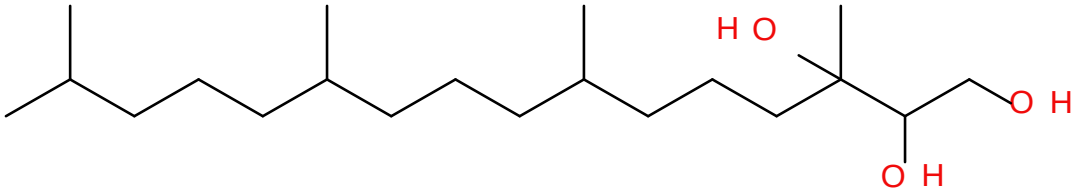

Figure 4-1 – Chemical structure of phytantriol (3,7,11,15-tetramethyl-1,2,3-hexadecanetriol).

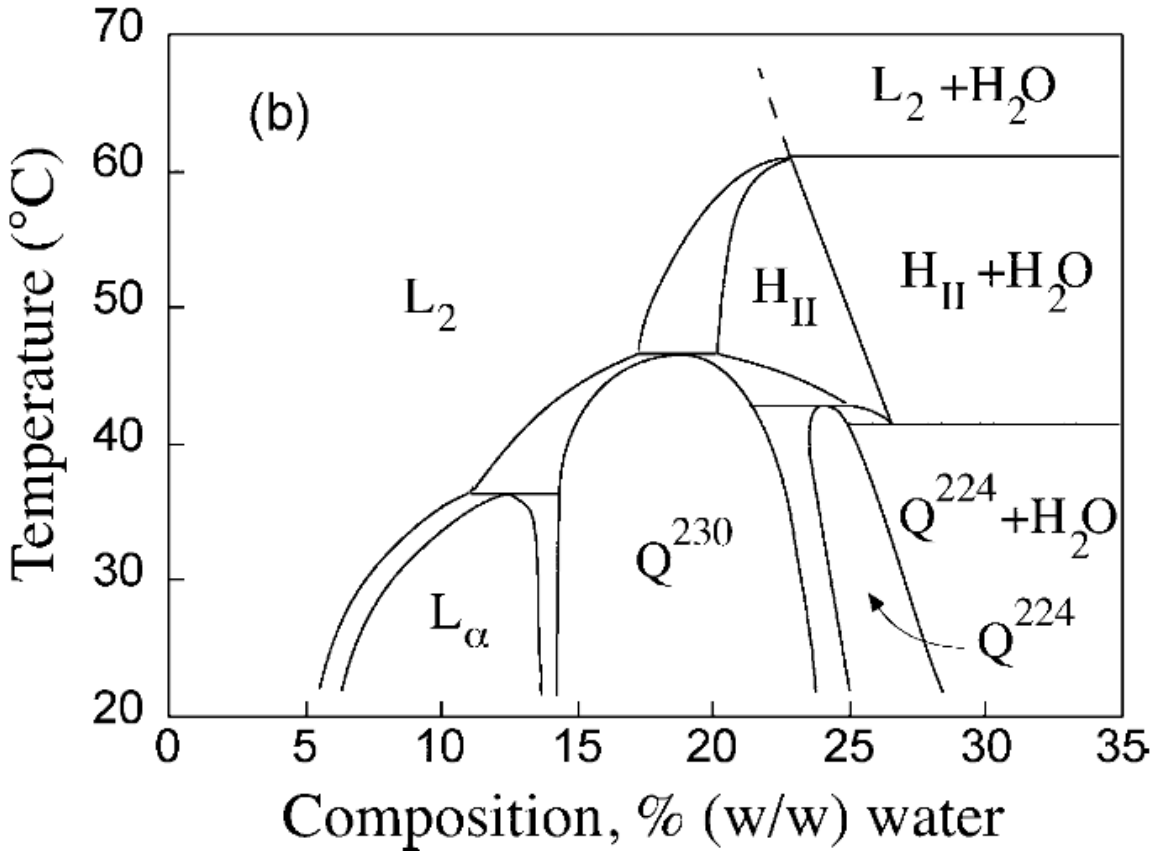

Figure 4-2 - Phase diagram of the phytantriol/water system over the temperature range 20-70 °C (L_2, type 2 micellar; L_α, lamellar; Q^{230}, type 2 cubic of crystallographic space group Ia3d; Q^{224}, type 2 cubic of space group Pn3m; H_{II}, type 2 hexagonal). Reprinted with permission from [180]. Copyright 2003 American Chemical Society. Nomenclature of the various phases, according to the system used by Luzzati *et al.* [181].

In 2013 Akbar *et al.* [57] successfully electrodeposited platinum 3D nanowire network films of Q_{227} "single diamond" symmetry through the Q_{224} "double diamond" phase of phytantriol (3,7,11,15-tetramethyl-1,2,3-hexadecanetriol), see Figure 4-3. This was done by dip coating a gold working electrode in a mixture of phytantriol and ethanol (w/w ratio of 1:2), and allowing the ethanol to evaporate for not less than two hours. This left a thin film of phytantriol covering the working electrode. When this was immersed into the electrolyte of aqueous HCPA, the phytantriol layer spontaneously assembled into an inverse bicontinuous phase (Q_{224}). One of the two water channels of the Q_{224} phase is believed to be blocked to the outside aqueous region to preserve the bilayer topology [57], [182], [183], causing deposition to occur down only one water channel, producing the Q_{227} symmetry of the films.

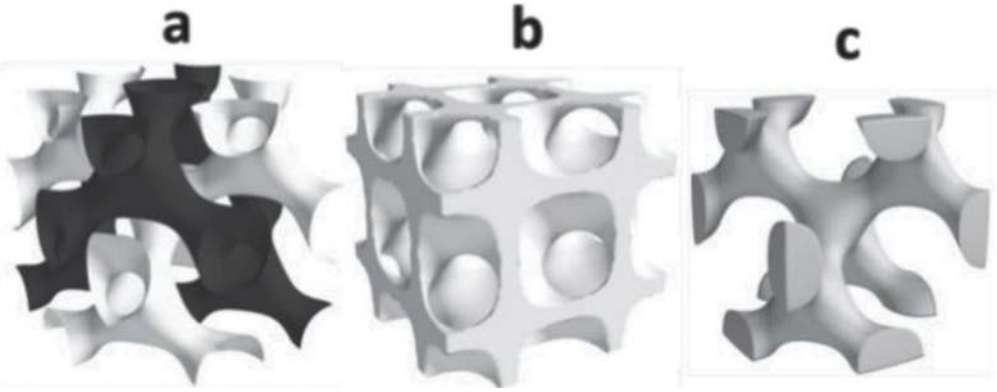

Figure 4-3 - Diagram used by Akbar *et al.* [57] to show the structures of phytantriol: a) the two water channels networks of the Q_{224} (double diamond) phase, b) the corresponding lipid bilayer of the Q_{224} (double diamond) phase, c) the reported Q_{227} (single diamond) structure of platinum produced by electrodepositing through phytantriol in the Q_{224} phase. Reprinted with permission from [57]. Copyright 2012 Wiley.

In 2016 Richardson *et al.* [95] followed Akbar's [57] procedure to produce "single diamond" Pt. This was the first work published which showed a Small Angle X-Ray Scattering (SAXS) pattern of the electrodeposit before the phytantriol template had been removed. This pattern showed both peaks for "double diamond" and "single diamond" symmetries in one diffraction pattern, indicating that the "single diamond" symmetry was present inside the "double diamond" symmetry of the template. This explains the electrodeposition down 1 of the 2 water channels of the "double diamond" phase.

In the same work Richardson *et al.* [95] studied Pt electrodeposits with thicknesses from 1.9 μm – 3.3 μm by SAXS. This revealed that initially the electrodeposits are (1 1 1) orientated with the plane parallel to the substrate, however, when the thickness surpasses 1.9 μm the films show (1 1 0) orientation along with (1 1 1) orientation. As the thickness of the electrodeposit further increases any orientation parallel to the substrate is lost. This reveals that there is orientation of the electrodeposit close to the substrate and by inference there is orientation of the phytantriol template close to the substrate.

This chapter will detail the use of phytantriol as a template for the electrodeposition of a freestanding bismuth telluride nanostructure, with the aim of improving the thermoelectric efficiency (1.3.1). The template removal for this nanostructure will involve the use of the mild solvents ethanol and water. The resulting nanostructure will then be characterised for composition, crystallinity, morphology and the nature of the nanostructure via SAXS and helium ion microscopy.

4.2 Results and Discussion

4.2.1 Cyclic Voltammetry (CV)

To examine the effect a phytantriol template has on the electrochemistry of Bi and TeO_2 in 1 *M* HNO_3, CVs were conducted covering both the deposition and stripping regions of bismuth telluride. Figure 4-4 depicts CVs that were conducted on a phytantriol coated gold disc electrode. Different electrolytes were used with various concentrations of Bi, although they all contained 10 *mM* TeO_2 and 1 *M* HNO_3. A comparative CV done in the absence of phytantriol can be seen in Figure 3-3.

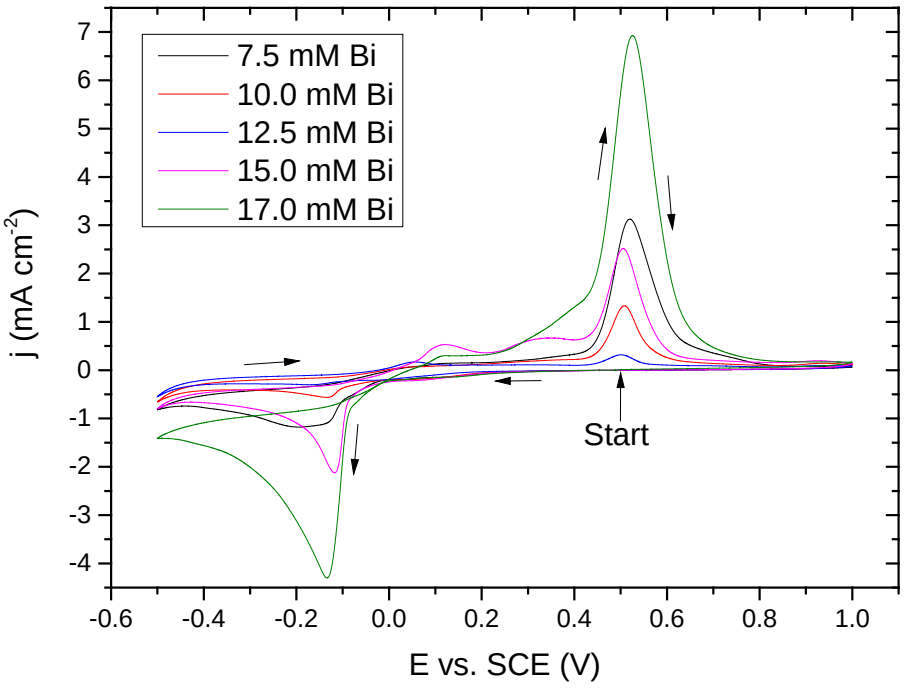

Figure 4-4 - Cyclic voltammogram recorded at 20 $mV\ s^{-1}$ in an electrolyte of 10.0 *mM* TeO_2 and between 7.5 *mM* and 17.0 *mM* Bi dissolved in 1 *M* HNO_3 with a phytantriol coated working electrode. The voltammogram started at a potential of +0.50 *V vs. SCE* where no reaction occurs and is scanned between -0.50 *V vs. SCE* and +1.00 *V vs. SCE*. The black arrows indicate the direction of the scan.

The reduction peaks seen at ~-130 *mV vs. SCE* can be attributed to be that of deposition of bismuth telluride, by the reaction shown in Equation 3.3.

$$3\ HTeO_2^+ + 2\ Bi^{3+} + 18\ e^- + 9\ H^+ \rightarrow Bi_2Te_{3\ (s)} + 6\ H_2O \qquad (3.3)$$

The oxidation peaks at ~+520 *mV vs. SCE* can be attributed to Equation 3.4 and Equation 3.5. The total reaction is the reverse of Equation 3.3.

$$Bi_2Te_3 + 6\ H_2O \rightarrow 3\ HTeO_2^+ + 2\ Bi + 9\ H^+ + 12\ e^- \quad (3.4)$$

$$Bi \rightarrow Bi^{3+} + 3\ e^- \quad (3.5)$$

The oxidation process can therefore be described as an oxidation of bismuth telluride to $HTeO_2^+$ (Equation 3.4), followed by an oxidation of Bi to Bi^{3+} (Equation 3.5) [118].

The reduction peaks and oxidation of bismuth telluride peaks (shown in Figure 4-4) are moved cathodically and anodically respectively, when compared to a CV in the absence of a phytantriol template (Figure 3-3). This observation in reduction peak is unexpected as it indicates that the electrodeposition is energetically less favourable in the presence of the phytantriol template. An explanation for this could be due to the increased edges caused by the template, forming less energetically favourable deposition sites. The anodic move in the oxidation peak could be explained by slower diffusion of Bi^{3+} and $HTeO_2^+$ away from the working electrode due to the presence of the template, making further oxidation less favourable than was seen in the absence of a template.

4.2.2 Composition

4.2.2.1 Composition Potential Dependency

Initially 7.5 *mM* Bi and 10 *mM* TeO_2 in 1 *M* HNO_3 was used to try and electrodeposit films of bismuth telluride through a phytantriol template. This electrolyte was successfully used to electrodeposit stoichiometric bismuth telluride films in the absence of a template (3.2.1.2), therefore if the template had no effect on the deposition this electrolyte concentration should produce a film of stoichiometric bismuth telluride. Films were deposited from an electrolyte of 7.5 *mM* Bi and 10 *mM* TeO_2 in 1 *M* HNO_3 at potentials between -0.375 *V* and -0.05 *V vs. SCE* and for a deposition time of 2 *h*. The resulting films were studied for analysed by EDX to assess

composition. These results can be seen in Figure 4-5.

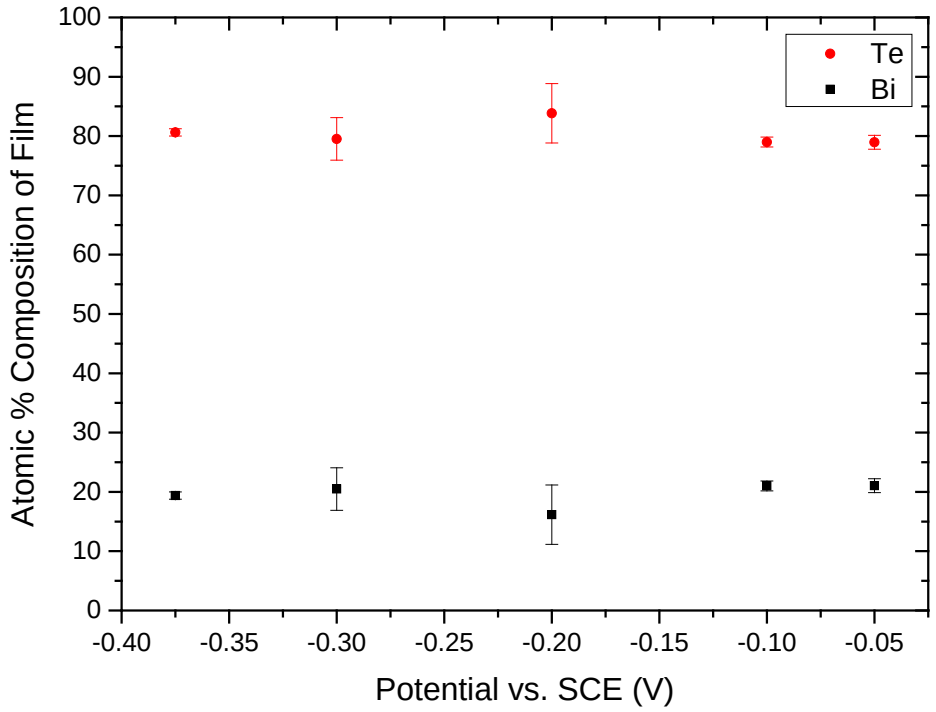

Figure 4-5 - EDX of electrodeposited thin films of Bismuth Telluride deposited from an electrolyte composed of 7.5 *mM* Bi, 10 *mM* TeO_2 and 1 *M* HNO_3, at potentials of -0.375, -0.30, -0.20, -0.10 and -0.05 *V vs SCE*. Deposition was through phytantriol for a time of 2 *h*. Error bars donate the 95% confidence limits.

The composition of films using 7.5 *mM* Bi and 10 *mM* TeO2 in 1 *M* HNO_3 deposited through phytantriol, are shown not to be stoichiometric by EDX, as shown in Figure 4-5. The composition was measured to have a Bi:Te ratio of 1:4 (ideal being 2:3), which proved to be independent of potential. This lack of a potential composition trend is consistent with literature reports [97], [114]. The cause of deviation from ideal stoichiometry is believed to be due to an uneven change in the diffusion coefficients of Bi^{3+} and $HTeO_2^+$ through phytantriol (Bi^{3+} slowed more than $HTeO_2^+$), compared to diffusion of these ions in the absence of phytantriol. This would lead to a relative increase of $HTeO_2^+$ compared to Bi^{3+} reaching the working electrode than was seen in the absence of a template, thus causing an increased Te content relative to Bi in the electrodeposited bismuth telluride films.

4.2.2.2 Composition Electrolyte Dependency

The composition of the electrolyte was altered in an effort to make a stoichiometric film. This has previously shown to be successful for non-templated electrodeposition of bismuth telluride [48], [114].

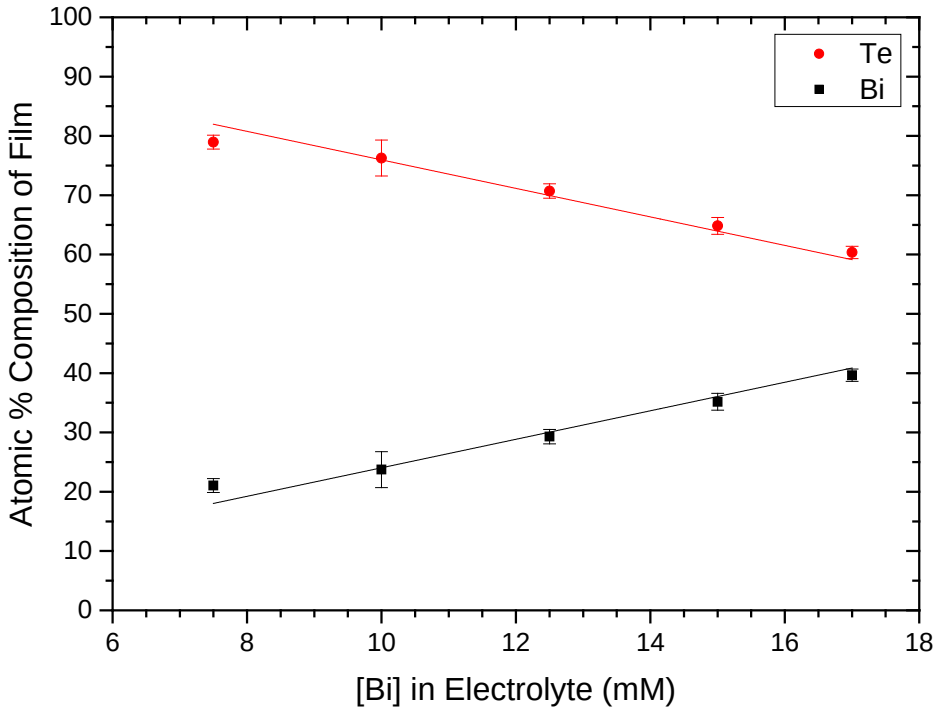

Figure 4-6 - EDX of electrodeposited thin films of Bismuth Telluride deposited from an electrolyte of 10 *mM* TeO_2, and 7.5, 10.0, 12.5, 15.0 or 17.0 *mM* Bi dissolved in 1 *M* HNO_3 at a potential of -0.05 *V vs SCE*. Deposition was through phytantriol for a time of 2 *h*. The linear fits are fixed to intercept at 0% and 100% for Bi and Te respectively. Error bars donate the 95% confidence limits.

EDX shows that an increase in the concentration of Bi relative to TeO_2 in the electrolyte causes an increase in the Bi percentage composition in the electrodeposited film compared to the Te percentage composition. A stoichiometric film was produced by using 17 *mM* Bi and 10 *mM* TeO_2, as seen in Figure 4-6. The trend appears linear with an intercept through 0% Bi in the film when no Bi is present in the electrolyte. An EDX trace for a film produced by using 17 *mM* Bi and 10 *mM* TeO_2 is seen in Figure 4-7.

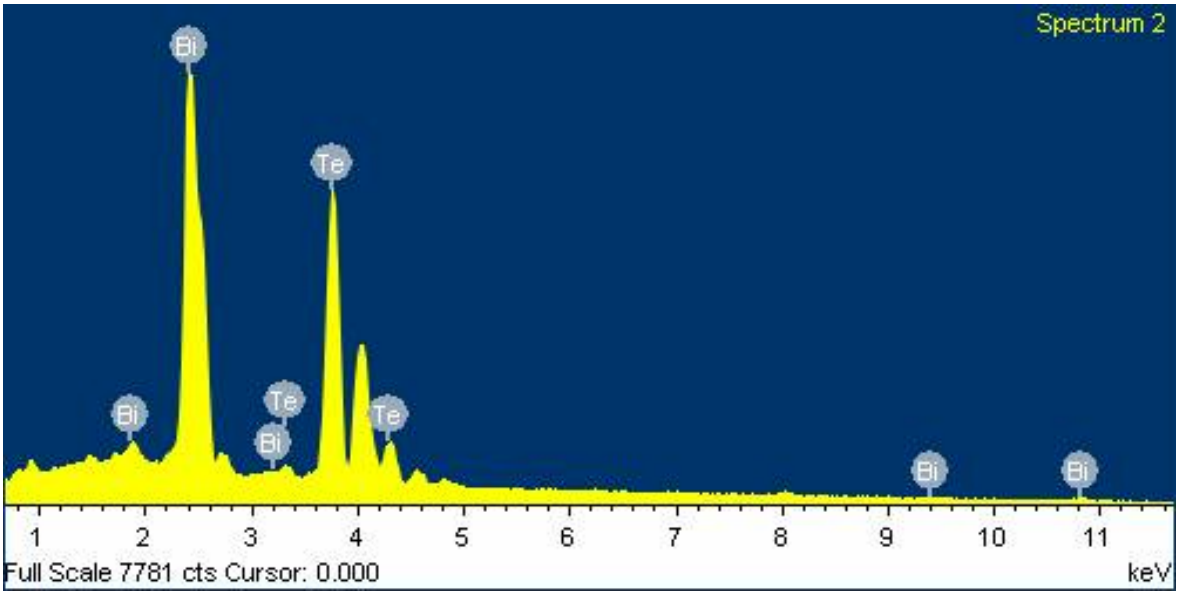

Figure 4-7 – EDX trace of a film electrodeposited through a phytantriol template from an electrolyte solution containing 17 *mM* Bi and 10 *mM* TeO_2 in 1 *M* HNO_3. The deposition conditions were -0.05 *V vs. SCE* for 2 *h*. The working electrode was a Au on Si substrate with a 10 *mm* × 10 *mm* electrode area. The total deposition charge was -4.43 *C*.

Whilst a stoichiometric composition was observed when using an electrolyte of 17 *mM* Bi and 10 *mM* TeO_2 in 1 *M* HNO_3, this observation (and all those seen in Figure 4-6) is for the average stoichiometry of the film. A consequence of this is that there could be variation in composition at different thicknesses in the film, with initial deposition layers being Bi rich and the top of the film being Te rich. The variation of stoichiometry through the film could result from different rates of diffusion for Bi^{3+} and $HTeO_2^+$. Whilst this is not examined here, films of different thicknesses could be made to examine variation of stoichiometry through the film. If variation in stoichiometry was observed to be an issue, a pulsed deposition method could be tested which would give time for diffusion layers to dissipate during deposition.

A current time transient for a film deposited form an electrolyte of 17 *mM* Bi and 10 *mM* TeO_2 is shown in Figure 4-8.

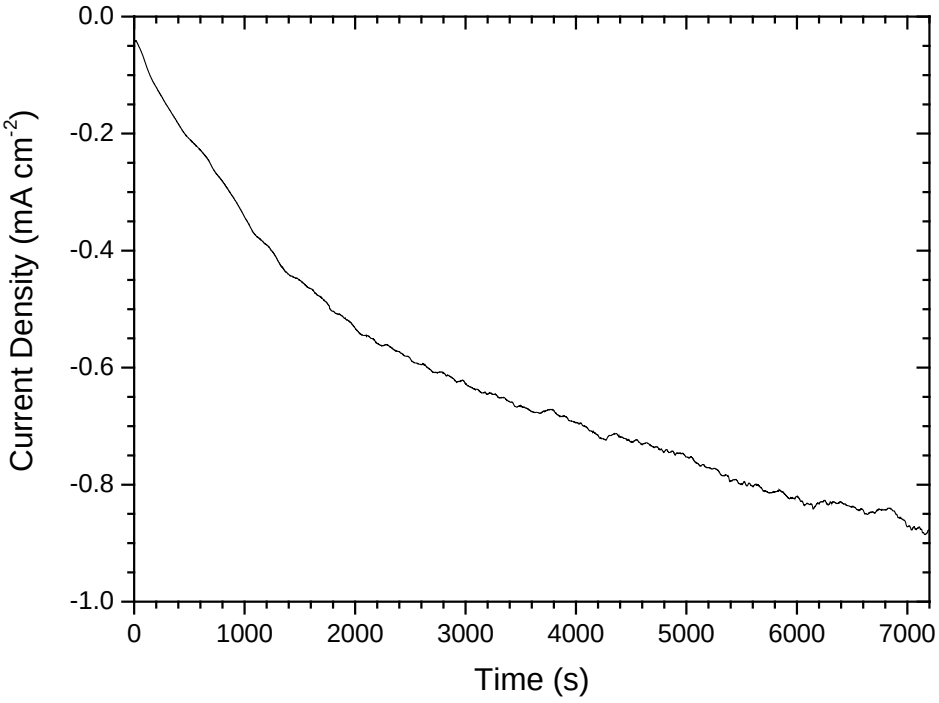

Figure 4-8 - Current time transient of a film electrodeposited through a phytantriol template from an electrolyte solution containing 17 *mM* Bi and 10 *mM* TeO_2 in 1 *M* HNO_3. The deposition conditions were -0.05 *V vs. SCE* for 2 *h*. The working electrode was a Au on Si substrate with a 10 *mm* × 10 *mm* electrode area. The total deposition charge was -4.43 *C*.

4.2.3 XRD

Asymmetric x-ray diffraction was used to confirm the electrodeposited films (seen to have bismuth telluride stoichiometry by EDX), were bismuth telluride instead of deposits of Bi and Te. An asymmetric scan can be seen in Figure 4-9. Symmetric scans were used to determine the preferred plane of crystal orientation and grain size. A symmetric scan can be seen in Figure 4-10.

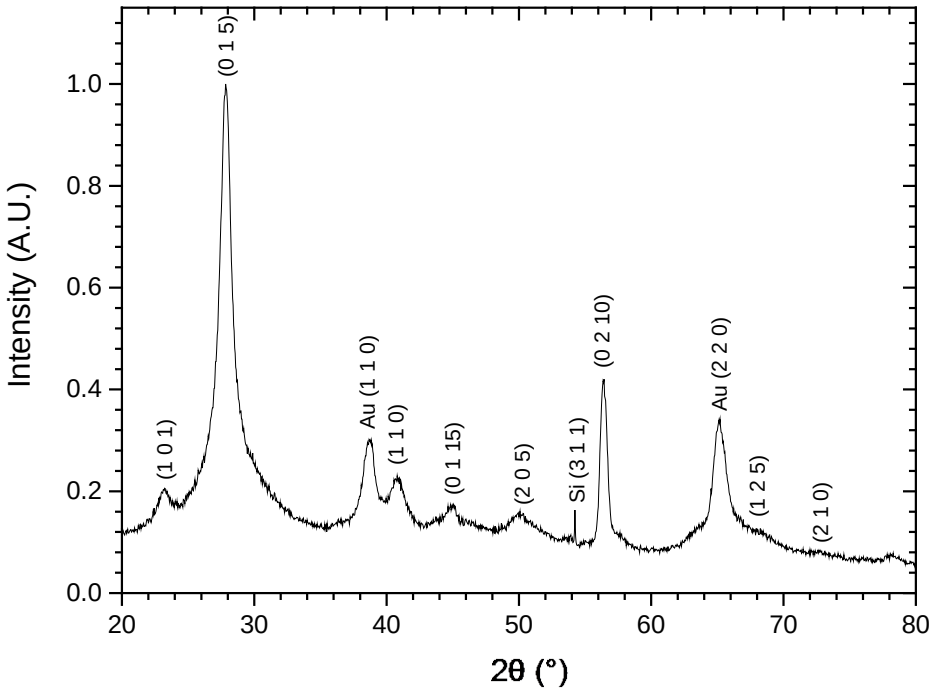

Figure 4-9 - Asymmetric XRD scan of a bismuth telluride film electrodeposited through a phytantriol template from an electrolyte solution containing 17 *mM* Bi and 10 *mM* TeO_2 in 1 *M* HNO_3. The deposition conditions were -0.05 *V vs. SCE* for 2 *h*. The substrate was Au on Si. Peaks are fitted from the "Tellurobismuthite" file in PDXL No:00-008-0027 (ICDD powder diffraction file 00-015-0863), unless stated Au where they are fitted from the "Gold, Au" file in PDXL and the Si (3 1 1) peak was fitted from the file "Silicon, Si", in the PDXL software.

The peaks seen in Figure 4-9 can be, unless otherwise labelled, attributed to bismuth telluride. This is evidence that the deposit is bismuth telluride. A symmetric scan, see Figure 4-10, was conducted to deduce the preferred plane of crystal orientation and grain size.

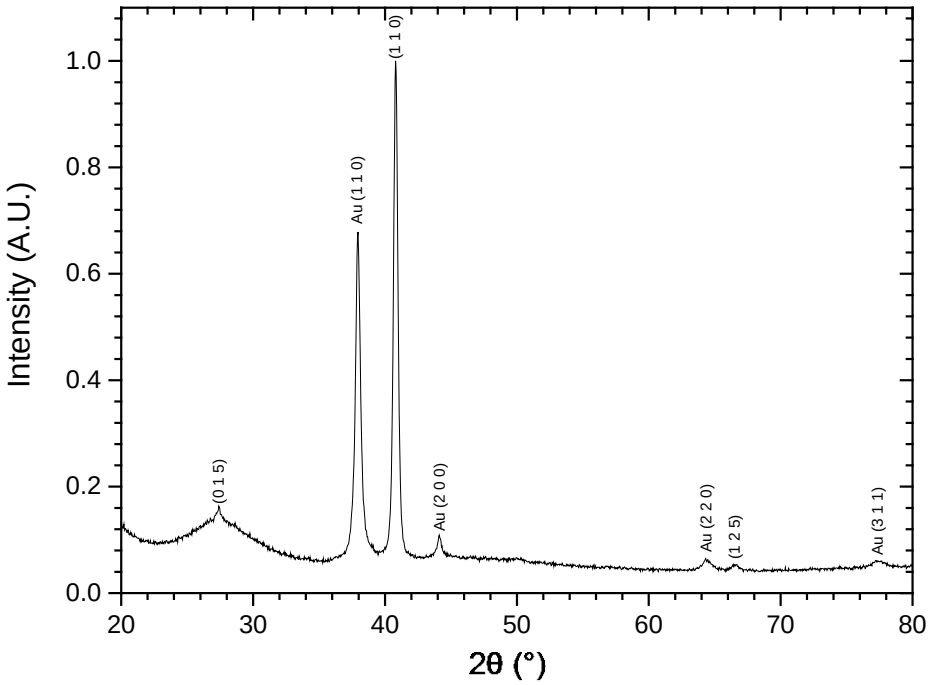

Figure 4-10 - Symmetric XRD scan of a bismuth telluride film electrodeposited through a phytantriol template from an electrolyte solution containing 17 *mM* Bi and 10 *mM* TeO_2 in 1 *M* HNO_3. The deposition conditions were -0.05 *V vs. SCE* for 2 *h*. The substrate was a section of a Au DVD. Peaks are fitted from the "Tellurobismuthite" file in PDXL, unless stated Au where they are fitted from the "Gold, Au" file in PDXL.

The symmetric scan shown in Figure 4-10 shows the (0 1 5) and (1 1 0) peaks for bismuth telluride, with the (1 1 0) peak being far more intense. This indicates that the preferred crystal orientation is (1 1 0) which is consistent with the XRD results in the absence of a template. The orientation preference is deduced by comparing intensity of peaks to the stick powder standard in Figure A-1.

Using the Scherrer equation (Equation 2.2) on the (1 1 0) peak, the calculated grain size is 26.2 *nm* on the electrolyte side (using data from the XRD pattern in Figure 4-10), where as in the absence of a template the grain size was shown to be 42.2 *nm* on the electrolyte side (using data from the XRD pattern in Figure 3-5). This indicates that phytantriol is reducing the grain size of the bismuth telluride electrodeposit. This could potentially lead to a lowering of thermal conductivity, if there is not a large defect density at the grain boundaries [132].

Table 4-1 - Comparison of grain size between non-templated and phytantriol templated electrodeposited bismuth telluride. Grain sizes are also compared for different peaks when available.

Peak	No Template Substrate Side Grain Size (*nm*)	No Template Electrolyte Side Grain Size (*nm)*	Phytantriol Electrolyte Side Grain Size (*nm*)
(0 1 5)	24.3	N/A	1.62
(1 1 0)	36.4	42.2	26.2

From Table 4-1 the grain size can be seen to be much larger in the (1 1 0) direction, compared to the (0 1 5) direction for phytantriol templated bismuth telluride on the electrolyte side. For non-templated bismuth telluride only the (1 1 0) peak was seen on the electrolyte side, so no direct comparison can be made. On the substrate side for non-templated bismuth telluride however, the grain size was seen to not vary by more than a factor of 2 (see Table 3-5 for more detail). This anisotropy is likely caused by the preferred growth direction of the film being (1 1 0) and potentially exacerbated by the template. The larger grain size along the (1 1 0) plane compared to the (0 1 5) plane is likely to cause anisotropy in the thermoelectric performance of the material.

4.2.4 SAXS

Hydrated phytantriol is known to cause Bragg scattering at low angles [180], therefore SAXS was used to examine the phase phytantriol forms when immersed in the electrolyte (thus the template structure) and to examine if any nanostructure was present on the films electrodeposited through the template.

4.2.4.1 Phytantriol and Electrolyte SAXS

To see what liquid crystal phase is formed when a phytantriol coated surface is immersed into the bismuth telluride electrolyte, a phytantriol lined borosilicate capillary (2.3.6.1) was filled with the bismuth telluride electrolyte of 17 *mM* Bi and 10 *mM* TeO_2 in 1 *M* HNO_3. This was left to equilibrate for 150 minutes, before being placed in front of the SAXS beam. The resultant 2D and 1D integrated radial SAXS pattern can be seen in Figure 4-11.

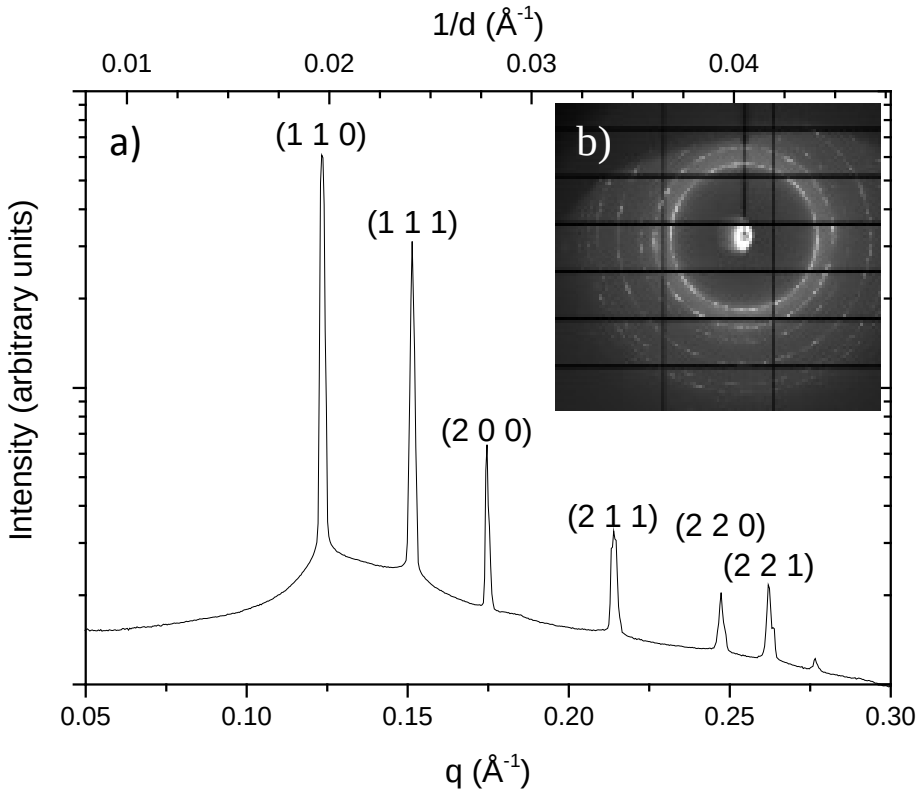

Figure 4-11 – a) 1D integrated SAXS pattern of a phytantriol lined 1.5 *mm* borosilicate glass capillary filled with 17.0 *mM* Bi, 10.0 *mM* TeO_2 in 1 *M* HNO_3. b) The corresponding 2D pattern.

Phytantriol is seen to form the Q_{224} "double diamond" structure (seen in Figure 4-2 and Figure 4-3) showing the first 6 peaks when mixed with excess bismuth telluride precursor electrolyte, as shown in Figure 4-11. The lattice parameter can be calculated to be 71.9 (± 0.7) *Å* (B.1). This result shows that phytantriol forms a Q_{224} "double diamond" phase, that has previously been utilised as a template to electrodeposit nanostructured Pt [141].

To test that the same liquid crystal phase would form on gold, a gold DVD was dip coated into phytantriol, then immersed into a cell of the bismuth telluride precursor electrolyte and placed in front of the SAXS beam. The resultant 1D pattern can be seen in Figure 4-12.

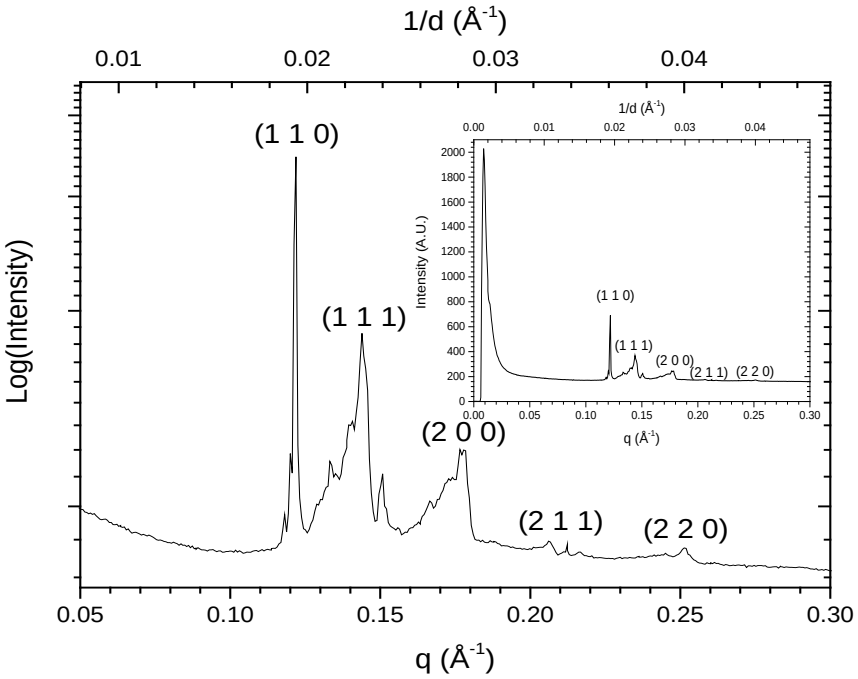

Figure 4-12 - 1D integrated SAXS pattern of a phytantriol coated gold DVD immersed in 17.0 *mM* Bi, 10.0 *mM* TeO_2 in 1 *M* HNO_3. The foil was dip coated in a solution of phytantriol and ethanol 1:2 by weight. The foil was allowed to dry for 30 minutes prior to being immersed in the electrolyte and the Au DVD was allowed to hydrate for 30 minutes prior to the SAXS pattern being taken. The electrolyte was inside a Kapton windowed vessel with a path length of 7 *mm*. The inset in the upper right corner allows for a direct comparison with Figure 4-13, by showing q values to 0 $Å^{-1}$ and with linear intensity being shown.

The setup for SAXS of phytantriol in solution was far from ideal, which resulted in the very noisy SAXS pattern that can be seen in Figure 4-12. That being said, five peaks can still be observed. These five peaks can be assigned as (1 1 0), (1 1 1), (2 0 0), (2 1 1) and (2 2 0). From the line spacing ratio of these peaks the phase is determined as the double diamond phase (Q_{224}), the lattice parameter of which is 72.4 (± 0.7) *Å*. The same phase was seen by Akbar *et al.* [57] for phytantriol immersed in aqueous hexachloroplatinic acid (HCPA).

4.2.4.2 Film SAXS

Bismuth telluride films electrodeposited at -0.05 *V vs. SCE* for 7200 *s* through the Q_{224} "double diamond" phase of phytantriol were placed in the SAXS beam to investigate what nanostructure, if any, had been formed. A resulting integrated diffraction pattern can be seen in Figure 4-13.

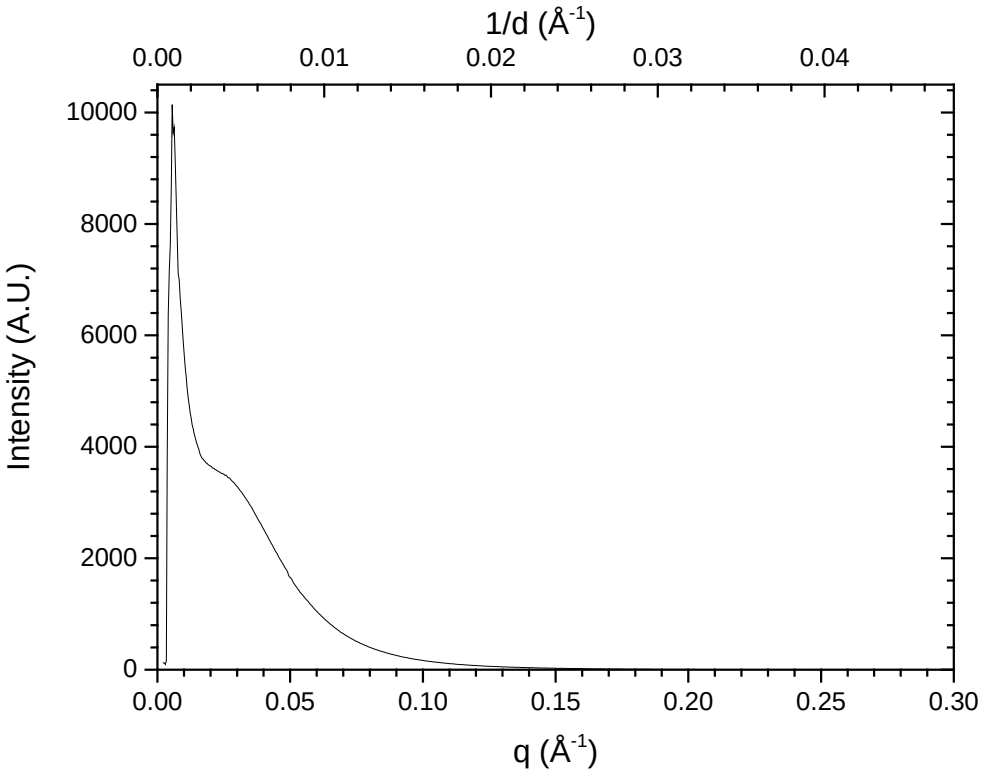

Figure 4-13 - 1D integrated SAXS pattern of a bismuth telluride thin film electrodeposited on a phytantriol coated Au DVD. The electrolyte was 17 *mM* Bi and 10 *mM* TeO_2 in 1 *M* HNO_3 and the deposition conditions were 7200 *s* at -0.05 *V vs SCE*.

Figure 4-13 shows a broad peak with an approximate peak at a q value of 0.028 $Å^{-1}$ (1/d value of 0.0045 $Å^{-1}$). The peak is not observed for a phytantriol coated DVD in the electrolyte as shown in Figure 4-12 (please note the max intensity in Figure 4-12 is much lower than in Figure 4-13, this is due to the x-rays travelling through 7 *mm* of electrolyte which reduced the intensity of x-rays hitting the detector). Whilst the symmetry cannot be assessed by SAXS without a second peak, if the structure was cubic (making the peak (1 1 0)) it would give a lattice parameter of approximately 320 *Å*. Another possible symmetry of the structure is hexagonal, this is due to phytantriol being able to form the hexagonal mesophase in water [180]. If the electrodeposited film possesses a hexagonal symmetry that would give a lattice parameter of approximately 224 *Å*. Either symmetry gives a unique result. The only previous templating through phytantriol was first conducted by Akbar *et al.* [57] who saw the formation of a single diamond (Q_{227}) structure upon the electrodeposition of Pt through the double diamond (Q_{224}) phase of phytantriol. This was demonstrated by SAXS peaks for the electrodeposited film with q values half that of the template, due to halving of the symmetry. For electrodeposited bismuth telluride films however, this was not observed as the first peak occurs at a q value lower than half the q value of the template. In order to determine what nanostructure has been formed, further studies were conducted.

4.2.4.3 9-Cistricosene SAXS

The branched alkene 9-cistricosene has been previously used to change the phase of phytantriol in excess water from double diamond (Q_{224}) to hexagonal [184] upon a doping level of 4.7% 9-cistricosene (95.3% phytantriol : 4.7% 9-cistricosene, w:w). To help understand the observations seen in Figure 4-13, here 9-cistricosene is used to access the stability of the double diamond (Q_{224}) phase in the bismuth telluride precursor electrolyte.

Firstly control capillaries were lined with varying levels of 9-cistricosene doped phytantriol. To these capillaries water was added. After 1 hour had passed (to allow the phytantriol mixtures to hydrate) the capillaries were placed in front of a SAXS beam. The results are depicted in Figure 4-14.

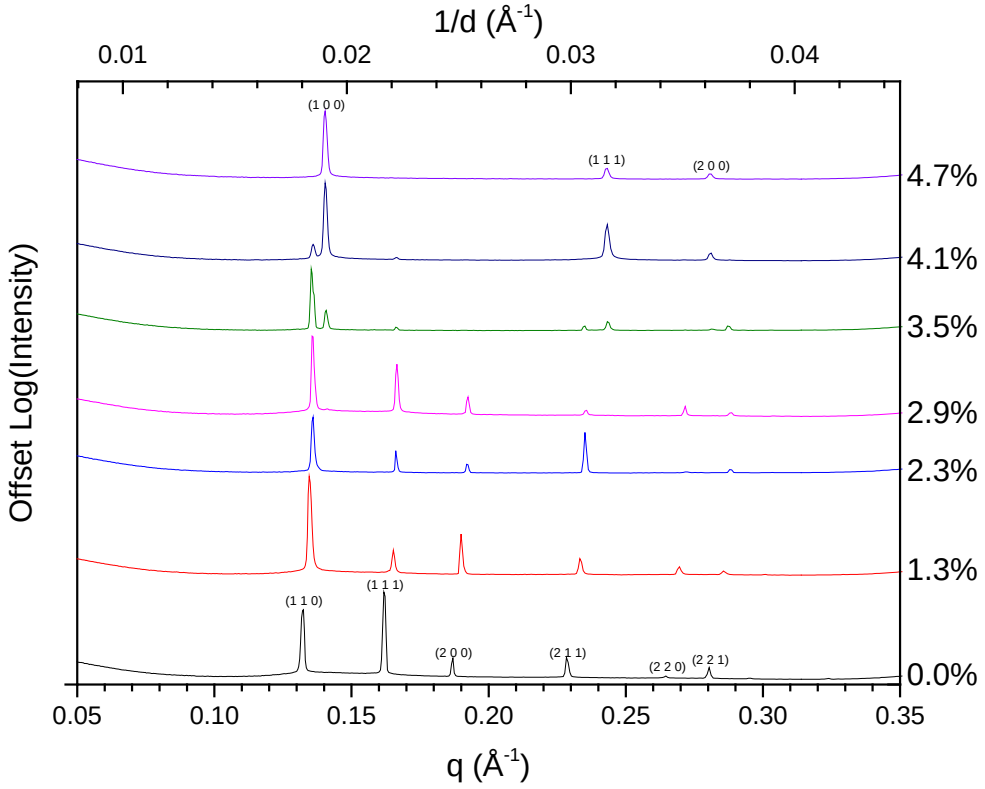

Figure 4-14 - 1D integrated SAXS patterns of 1.5 *mm* borosilicate glass capillaries lined with a phytantriol and 9-cistricosene mixture, with the weight percentage of 9-cistricosene presented. The solution was diluted 1:2 with ethanol before being added to the capillary. The capillaries were filled with deionised water and the mixtures were left for 1 hour hydrating before being placed in the SAXS beam.

The results seen in Figure 4-14 are consistent with the control results seen by Akbar [184], in that a hexagonal phase is solely formed when a doping level of 4.7% (by weight) of 9-cistricosene is used. Akbar [184] also went on to show that the same 4.7% doping level was required to form the

hexagonal phase when using the Pt precursor electrolyte. In Figure 4-15 the experiment is repeated, however, the bismuth telluride precursor electrolyte is studied instead.

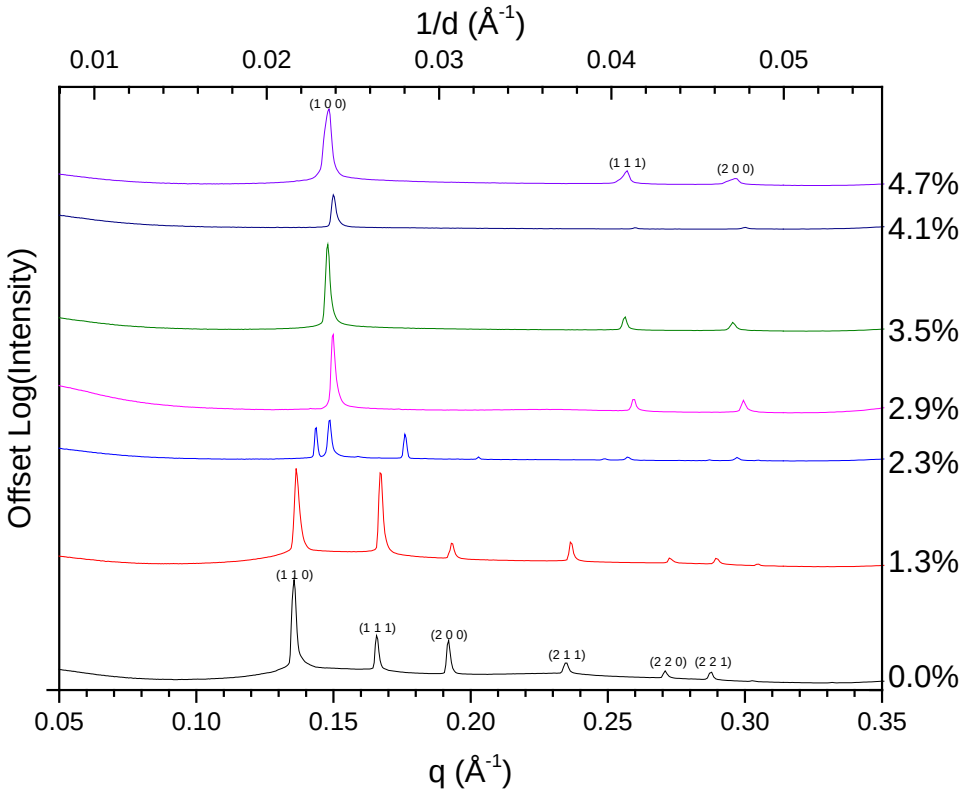

Figure 4-15 - 1D integrated SAXS patterns of 1.5 *mm* borosilicate glass capillaries lined with a phytantriol and 9-cistricosene mixture, with the weight percentage of 9-cistricosene presented. The solution was diluted 1:2 with ethanol before being added to the capillary. The capillaries were filled with 17.0 *mM* Bi, 10.0 *mM* TeO_2 in 1 *M* HNO_3. After the capillaries were filled they were left for one hour before SAXS patterns were taken.

From Figure 4-15 it can be seen that the hexagonal phase is solely formed upon 2.9% doping of 9-cistricosene. This is sustainably lower than the 4.7% required for water (Figure 4-14 and [184]) or Pt precursor electrolyte [184]. This observation shows that the stability of the double diamond (Q_{224}) phase is lower in the bismuth telluride precursor electrolyte, than it is in either water or a Pt precursor electrolyte. This could help explain why a single diamond nanostructure was not observed for bismuth telluride as it was for Pt [57].

4.2.5 Electron and Ion Beam Microscopy

Whilst SAXS has shown that a nanostructured bismuth telluride electrodeposit is being formed (Figure 4-13), the exact structure of the deposit is unknown due to only a single peak being

present in the diffraction pattern. To help further understand the structure of the electrodeposit, microscopy was conducted to try and visualise the structure in real space.

4.2.5.1 Scanning Electron Microscopy (SEM)

Scanning electron microscopy (SEM) was used to assess the morphology of films deposited at different potentials and from different [Bi] electrolytes. No signs of nanostructure are expected to be seen, as the resolution of SEM is not high enough to observe the lattice parameters determined by SAXS.

Table 4-2 - Scanning electron microscopy images of thin films electrodeposited through phytantriol from an electrolyte solution containing 7.5 *mM* Bi and 10.0 *mM* TeO_2 dissolved in 1 *M* HNO_3. The films were deposited potentiostatically for 2 *h* at between -0.05 *V vs. SCE* and -0.375 *V vs. SCE*. Images are of the electrolyte side.

-0.05 *V vs. SCE*

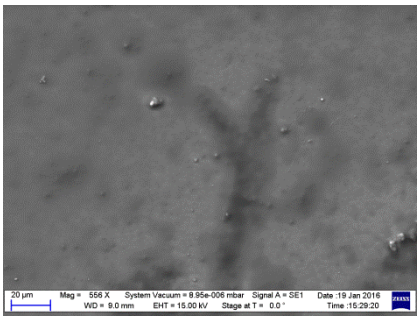

-0.10 *V vs. SCE*

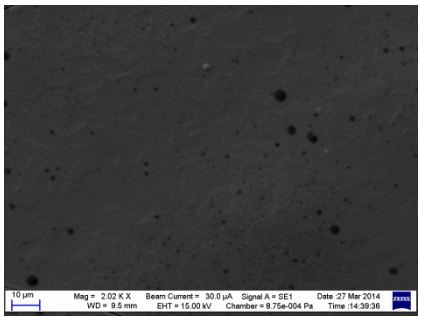

-0.20 *V vs. SCE*

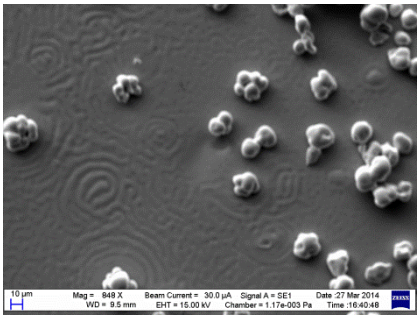

-0.30 *V vs. SCE*

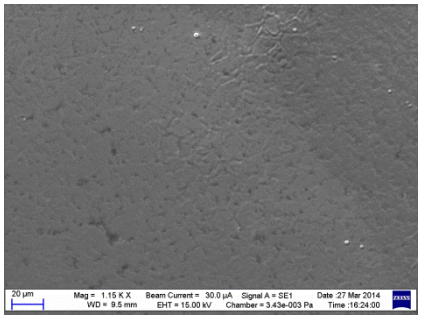

-0.375 *V vs. SCE*

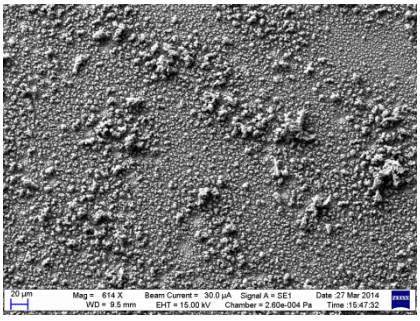

Table 4-3 - Scanning electron microscopy images of thin films electrodeposited through phytantriol from an electrolyte solution containing 10.0 *mM* TeO_2 and between 7.5 *mM* and 17.0 *mM* Bi, dissolved in 1 *M* HNO_3. The films were deposited potentiostatically at -0.05 *V vs. SCE* for 2 *h*. Images are of the electrolyte side.

7.5 *mM* Bi	10.0 *mM* Bi
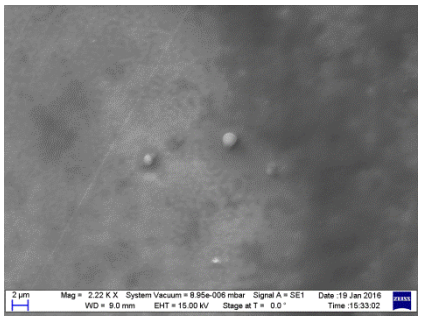	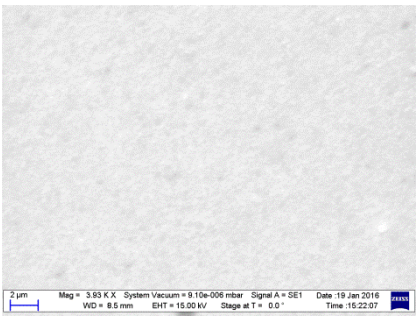
12.5 *mM* Bi	**15.0 *mM* Bi**
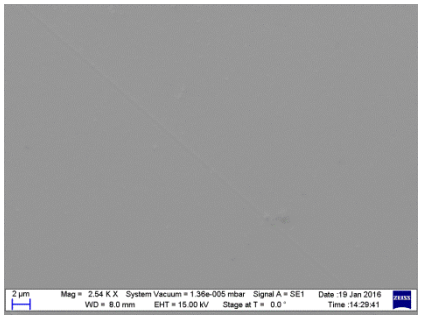	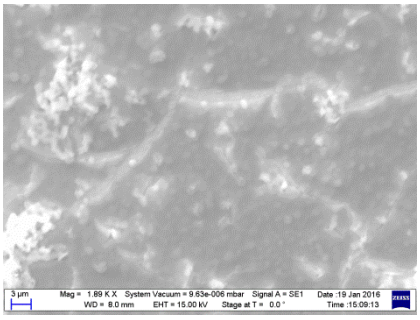
17.0 *mM* Bi	
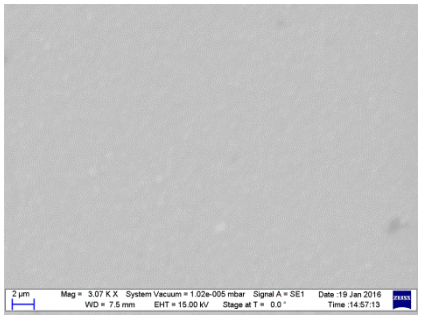	

From Table 4-3 it can be noted that there is no signs of observable nanostructure from any of the films. The SAXS pattern in Figure 4-13 shows that the nanostructure is most likely to have a lattice parameter in the range of 300 *Å*, therefore it is not surprising that the SEM images did not observe any nanostructure as the resolution of SEM is not high enough to observe features on that length scale.

4.2.5.2 Helium Ion Microscopy (HIM)

The resolution of HIM (0.30 *nm*) is high enough to visualise the intended nanostructure of films electrodeposited through phytantriol. Therefore if a nanostructure has been formed it should be observable with a Helium Ion Microscope. HIM images are shown in Figure 4-16.

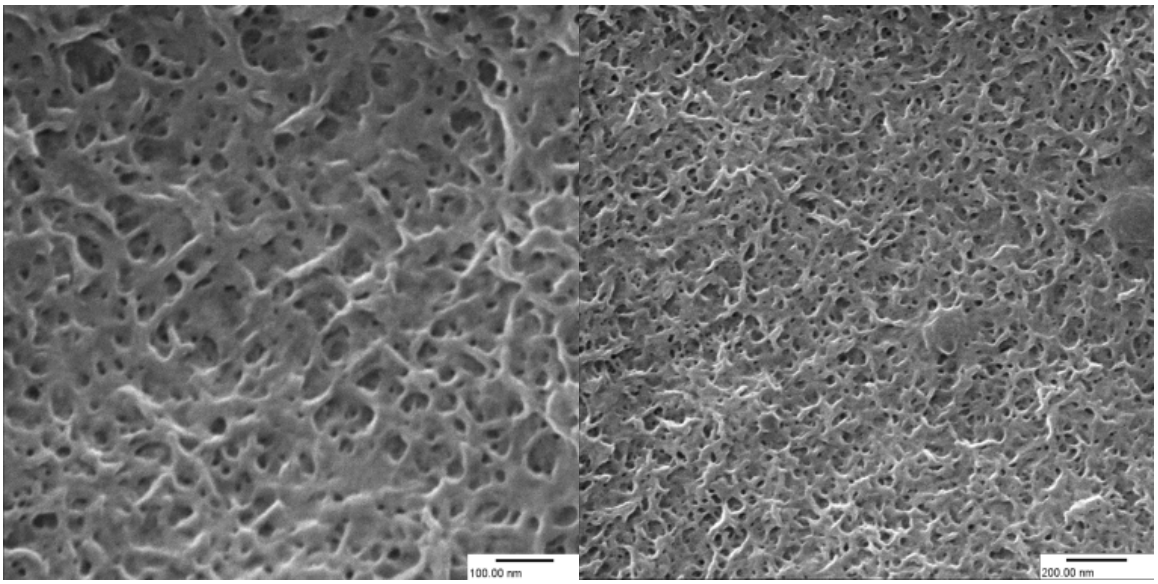

Figure 4-16 - HIM of electrodeposited film of stoichiometric bismuth telluride from an electrolyte of 17 *mM* Bi and 10 *mM* TeO_2 in 1 *M* HNO_3, deposited through a phytantriol template. The deposition potential was -0.05 *V vs. SCE* and deposition time 7200 *s*.

Evident from Figure 4-16 is that the bismuth telluride electrodeposits do display a disordered nanostructure, which appears to be somewhat cubic in appearance. From the SAXS pattern shown in Figure 4-13 the lattice parameter of a cubic nanostructure would be 320 *Å*. This is plausible from sections of these images. It should be remembered that the SAXS pattern displayed a broad peak, which indicates a range of lattice parameters. This is in line with the high level of disorder seen in these images.

Although a single diamond nanostructure was not deposited as was expected from phytantriol [57], this is not necessarily of consequence for thermoelectric applications as this nanostructure will still cause an increase in phonon scattering. The nanostructure is still a freestanding interconnected network of nanowires. Diameters of the nanowires are as low as 6 *nm*, which is lower than any other literature reports of electrodeposited bismuth telluride nanowires. The smallest reported in the literature is 15 *nm* [160]. Here the diameter range does vary and diameters of up to at least 15 *nm* are observed. Nevertheless this nanostructure is promising, and it is theorized that nanowires with diameters of less than 10 *nm* may lead to an increase in

Seebeck coefficient due to the quantum confinement effect on the electron density of states [185].

It is of noteworthiness that helium ion is an ion beam technology that can be used for ion beam lithography [186], as a consequence HIM can be unintentionally damaging to samples that are being imaged.

Figure 4-17 shows the extent of beam damage that can be caused between images taken in the same space immediately after each other. Therefore it is logical to conclude that there will be a degree of beam damage present in the initial images. All efforts were made to not expose a section of sample to the beam, until that section was being imaged. This would minimise the degree of beam damaged caused. Nevertheless a small level of beam damage is probably still seen in the images in Figure 4-16, however, as all efforts were taken to minimise this effect the levels of damage should not be of significance.

Fourier transform analysis was tried on images seen in Figure 4-16 and Figure 4-17, however no features were observed in the Fourier transform.

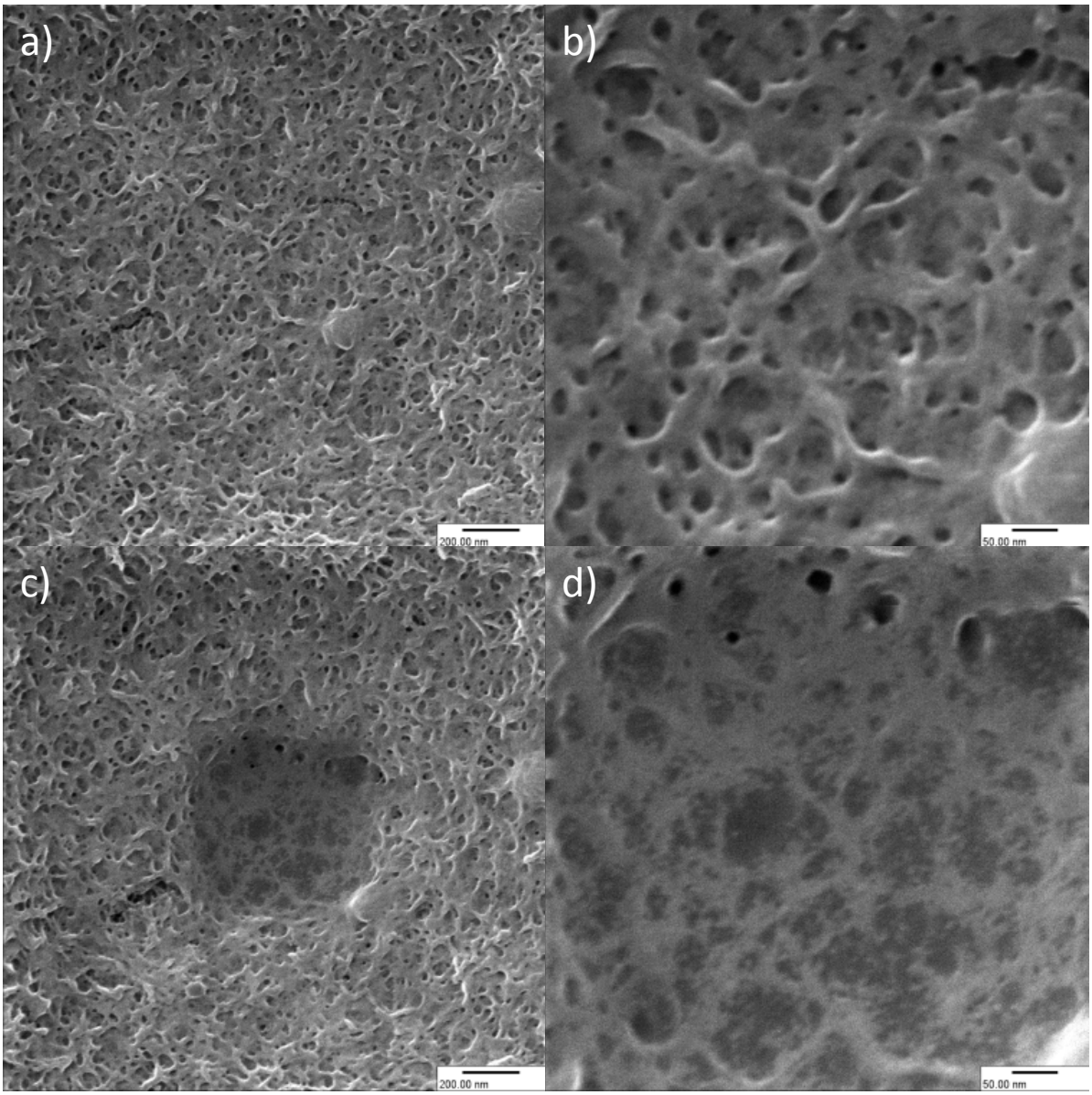

Figure 4-17 - HIM detailing beam damage. The same film as shown in Figure 4-16 is used. a) The initial image taken. b) The middle of a zoomed in. d) Image taken at the same location as b, immediately after image b was taken. c) Is taken after d, which is at the same magnification and the same place as a.

4.2.6 Seebeck

In order to determine if the nanostructuring has increased the thermoelectric performance, the Seebeck coefficient of the electrodeposited nanostructures were measured. The results are depicted in Figure 4-18.

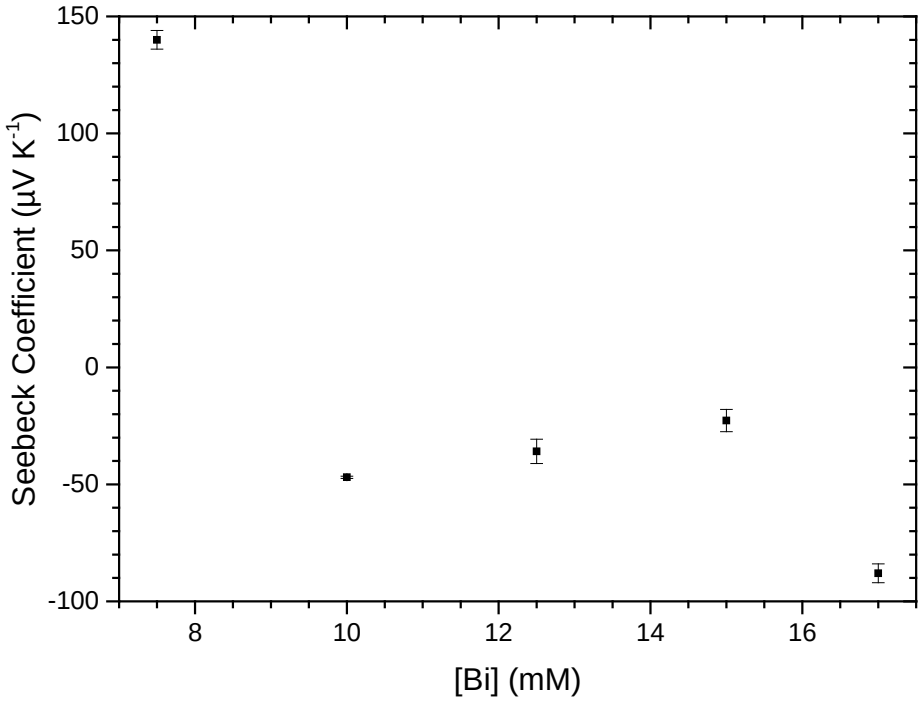

Figure 4-18 - Seebeck coefficient of films electrodeposited through phytantriol from an electrolyte of 10 *mM* TeO_2, and 7.5, 10.0, 12.5, 15.0 or 17.0 *mM* Bi dissolved in 1 *M* HNO_3. The films were deposited potentiostatically at -0.05 *V vs. SCE* for 2 *h*. The deposition substrate was Au on Si. The errors represent the 95% confidence limits determined by repeat measurements.

The Seebeck coefficient, as shown in Figure 4-18, is seen to fluctuate with the concentration of Bi in the electrolyte. A positive Seebeck coefficient (thus p-type) is seen for 7.5 *mM* Bi, which relates to a film with a low Bi percentage in the film. Typically Te rich films are n-type [187], therefore this is an unusual result. Due to the very low levels of Bi (<20%), however, the p-type behaviour can be explained if this sample is viewed as Bi doped Te ([188]) rather than Te rich bismuth telluride. Whilst this is a large Seebeck coefficient compared to bismuth telluride, the electrical conductivity of Te is low and is expected to be for this Bi doped Te. Therefore this Seebeck coefficient is not of noteworthiness. Te rich bismuth telluride films (10 *mM* Bi – 15 *mM* Bi) were all seen to be n-type as expected.

Stoichiometric bismuth telluride deposited from an electrolyte of 17 *mM* Bi and 10 *mM* TeO_2 in 1 *M* HNO_3 is seen to have a Seebeck coefficient of -88 (±4) $\mu V\ K^{-1}$. This is approximately a doubling in Seebeck coefficient from -43.8 (±0.5) $\mu V\ K^{-1}$ seen for non-templated electrodeposited bismuth telluride (Table 3-6). This is an indication that the nanostructuring using phytantriol, producing an

interconnected nanowire network has improved the thermoelectric performance of the material. This is in line with theoretical work [38], [185].

Whilst the measured Seebeck coefficients in Figure 4-18 allude to the ability to increase the Seebeck coefficient of electrodeposited bismuth telluride by depositing through a phytantriol template, this observation is limited in significance because these are measurements on single samples. The error bars donate the variance in the Seebeck coefficient of one sample, but not the variance that might be observed between samples made in the same way. To strengthen the significance of the measured Seebeck coefficients, these measurements should be repeated on different samples.

Attempts were made to measure the electrical conductivity of the interconnected nanowires, however, due to the requirement to remove the electrodeposit from the substrate and attach conductive silver epoxy (CircuitWorks CW2400) contacts a high degree of oxidation had occurred (~60 atomic % oxygen observed by EDX). This lead to an electrical conductivity value of 19.48 (± 0.14) $S\ cm^{-1}$ being measured. Oxidation of bismuth telluride nanowires is well documented in the literature and is a challenge for transport measurement [189].

4.3 Conclusions

Phytantriol was used as a template by coating the working electrode with phytantriol and then immersing the electrode into the electrolyte. The composition of the electrodeposited films was shown to be altered by the presence of phytantriol (compared to films produced using the same electrolyte in the absence of any template), to a Bi:Te ratio of 1:4, which was independent of potential. Increasing the Bismuth concentration in the electrolyte (whilst keeping the TeO_2 concentration at 10 *mM*), was shown to increase the Bi composition in the electrodeposited films linearly. An electrolyte concentration of 17 *mM* Bi, produced a stoichiometric bismuth telluride film. XRD confirmed the deposited compound to be bismuth telluride, with a crystal orientation of (1 1 0), the same as was exhibited in the absence of a template.

SAXS studies showed that the phytantriol covering the electrode formed a double diamond phase (Q_{224}) when immersed in the electrolyte, the lattice parameter being 72.4 (± 0.7) *Å*. SAXS studies on the electrodeposited films did not show the anticipated single diamond (Q_{227}) structure [57], however, a broad peak with a q value of 0.028 $Å^{-1}$ (1/d value of 0.0045 $Å^{-1}$) was observed. HIM images showed that the SAXS was indicating a disordered cubic nanostructure, with a lattice parameter of approximately 320 *Å*.

A Seebeck value of -88 (±4) $\mu V K^{-1}$ was measured for stoichiometric nanostructured bismuth telluride, which is double the value recorded for electrodeposited non-templated bismuth telluride films.

Chapter 5: Bismuth Sulphide Nanostructuring

5.1 Introduction

Despite bismuth telluride based materials exhibiting the best room temperature thermoelectric properties for commercial applications [10] and consequently dominating the market [190], there is a need to move away from Te based materials due to the rarity and toxicity of Te. Te's abundance in the Earth's crust is comparable to that of Pt (~1 $\mu g\ kg^{-1}$), making Te one of the rarest stable elements [191]. Comparatively the rarest lanthanides have abundances of 500 $\mu g\ kg^{-1}$ in the Earth's crust [192]. Te is also considered very hazardous if ingested, and the National Institute for Occupational Safety and Health consider air concentrations of 25 $mg\ m^{-3}$ immediately dangerous to life and health [193].

Sulphur like tellurium is a group 16 (chalcogen), but unlike tellurium sulphur is abundant making 0.042% (by weight) of the Earth's crust [194]. Sulphur is also considered non-toxic. Bismuth sulphide (Bi_2S_3), therefore, could seem a logical alternative to bismuth telluride and has recently attracted interest for thermoelectric applications [195]–[198].

Bismuth sulphide however is a wide-gap semiconductor with a band gap energy of 1.3 *eV* [199], compared to a narrow band gap of 0.15 *eV* in bismuth telluride [25]. Wide band gap semiconductors are not used for low temperature thermoelectric applications as the ideal band gap for a given temperature is theorised to be $10k_bT$ (where k_B is the Boltzmann constant and T is the operating temperature of the device in Kelvin) [200]. High doping densities, however, cause band gaps to shrink. This is because the wavefunctions of the electrons bound to the impurity atoms start to overlap as the density of the impurities increase. The overlap forces energies to form an energy band rather than a discreet level. The amount that the impurity band reduces the energy band of the host material is shown in Equation 5.1 [201]. Therefore in theory doping could allow bismuth sulphide to function as thermoelectric material for room temperature applications.

$$\Delta E_g(N) = -\frac{3q^2}{16\pi\varepsilon_s}\sqrt{\frac{q^2N}{\varepsilon_s k_B T}} \tag{5.1}$$

where E_g is the band gap, N is the doping density, q is the electronic charge, ε_s is the dielectric constant of the semiconductor, k_B is the Boltzmann constant and T is the temperature in Kelvin.

The crystal structure of bismuth sulphide was derived by Caracas *et al.* [202] and is depicted in Figure 5-1. The structure consists of ribbons of $[Bi_4S_6]_n$ that are parallel to the b-axis. The space group for the structure is Pnma. There are 2 different Bi atom environments, both of which have

seven coordinating Bi atoms. There are four Bi atoms in a near planar rectangle and three more distant, producing an irregular 7-coordination group [203].

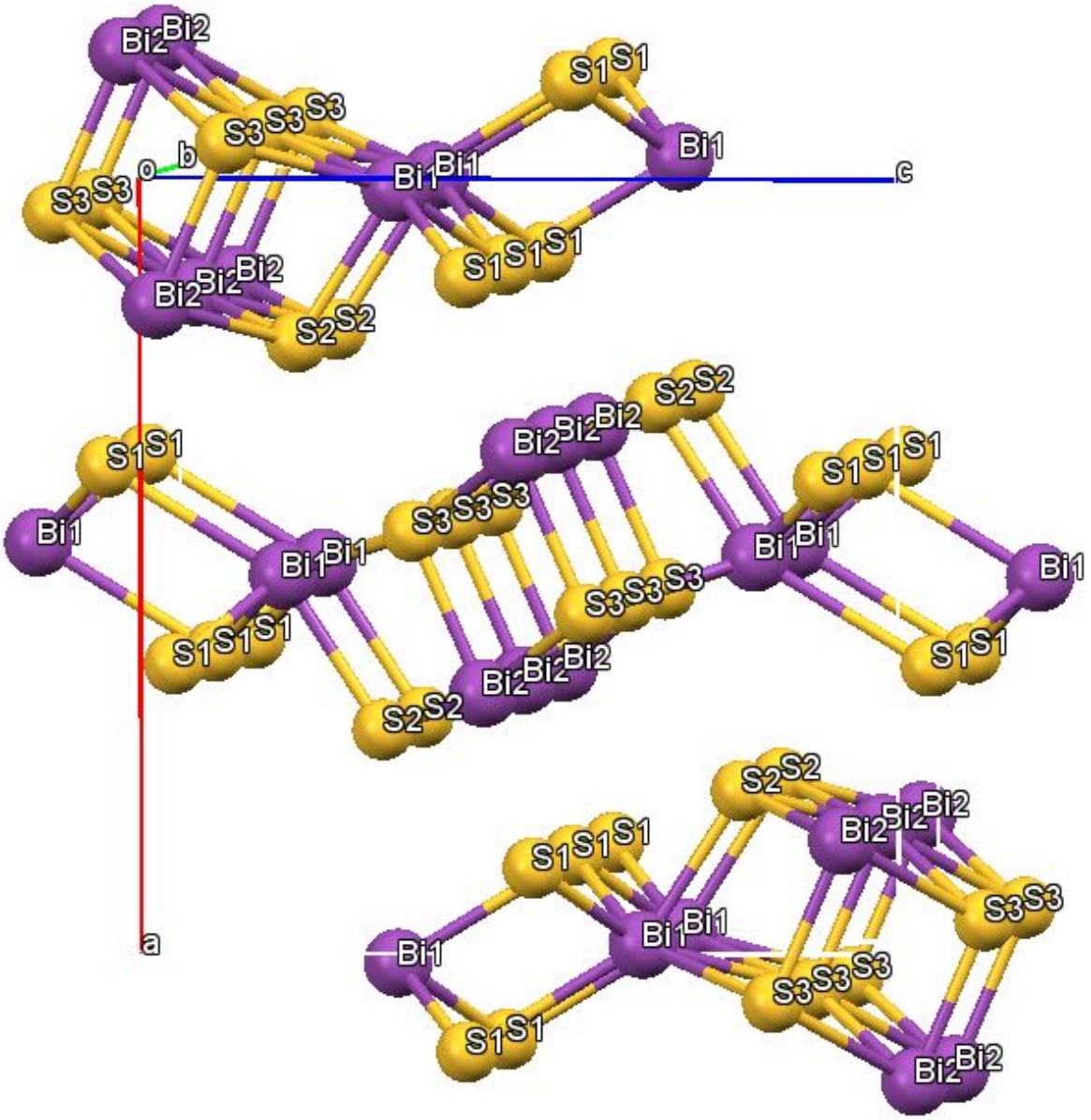

Figure 5-1 - Crystal structure of bismuth sulphide (Bi_2S_3), derived by Caracas *et al.* [202]. The structure consists of ribbons of $[Bi_4S_6]_n$ that are parallel to the b-axis. The space group for the structure is Pnma. The crystal structure was plotted on Mercury [105], using Crystallography Open Database (COD) 9007375.

Chen *et al.* [199] first reported the thermoelectric properties of bismuth sulphide below room temperature. They report that bismuth sulphide compounds can have comparable or even lower thermal conductivities (1.25 $W\ m^{-1}\ K^{-1}$ at 300 *K* for $KBi_{6.33}S_{10}$) than that of bismuth telluride (1.65 $W\ m^{-1}\ K^{-1}$ at 300 *K* for bismuth telluride). They state that intrinsic bismuth sulphide has a room temperature electrical conductivity of $10^{-4}\ S\ cm^{-1}$, yet show a sulphur deficient bismuth sulphide sample to have a room temperature electrical conductivity of 20 $S\ cm^{-1}$. They attribute this 5-6

orders of magnitude increase in electrical conductivity down to sulphur vacancies acting as a source of electrons. They point out that Mizoguchi *et al.* [204] annealed bismuth sulphide in a sulphur rich atmosphere, which lead to a dramatic reduction in electrical conductivity as sulphur vacancies were being filled. Chen *et al.* [199] report a room temperature Seebeck coefficient of -325 $\mu V\ K^{-1}$ for their sulphur deficient bismuth sulphide and a room temperature thermal conductivity of 1.2 $W\ m^{-1}\ K^{-1}$, leading to a *ZT* value of 0.05 at room temperature.

Ge *et al.* [205] synthesised polycrystalline bismuth sulphide using a mixture of ball-milling and spark plasma sintering. Polycrystalline n-type bismuth sulphide was synthesised with >95% density. They conclude that an appropriate amount of sulphur vacancies increase the carrier concentration and thus electrical conductivity, however excessive sulphur vacancies lowered the carrier mobility and thus electrical conductivity. The best electrical conductivity value measured was around 8 $S\ cm^{-1}$, with the best Seebeck coefficient being -450 $\mu V\ K^{-1}$ at 323 *K* (-390 $\mu V\ K^{-1}$ at 573 *K*). The best power factor was 233 $\mu W\ m^{-1}\ K^{-2}$ at 573 *K*, which they report as the highest to date for non-textured bismuth sulphide. The thermal conductivity of this sample was 0.7 $W\ m^{-1}\ K^{-1}$ at 573 *K*, yielding a *ZT* figure of merit of 0.19. These values are summarised in Table 5-1. The *ZT* value of 0.19 was a 72% increase on the 0.11 *ZT* figure of merit they had previously reported using the same techniques [206], which was the best *ZT* value reported for bismuth sulphide when published.

Table 5-1 – Highest thermoelectric properties measured by Ge *et al.* [205] for bismuth sulphide synthesised using a mixture of ball-milling and spark plasma sintering. All measurement are conducted at 573 *K* unless otherwise stated.

σ ($S\ cm^{-1}$)	S ($\mu V\ K^{-1}$)	PF ($\mu W\ m^{-1}\ K^{-2}$)	κ ($W\ m^{-1}\ K^{-1}$)	*ZT*
8	-390 (-450 at 323 *K*)	233	0.7	0.19

To the best of knowledge the *ZT* value of 0.19 reported by Ge *et al.* [205] is the current highest value for bulk bismuth sulphide. This is far lower, however, than *ZT* values seen for bismuth telluride and related materials. Two strategies to try and increase the figure of merit (*ZT*) are to dope with other elements and to nanostructure.

5.1.1 Doping of Bismuth Sulphide

ZT values of up to 0.6 can be achieved when doping bismuth sulphide with other elements (i.e. not Bi or S) like Cl [195], [207], [208]. Due to the complexities of electrodepositing nanostructured bismuth sulphide, however, doping with other elements is not perused in this research and therefore doping with other elements is not discussed any further here.

5.1.2 Nanostructured Bismuth Sulphide

Another technique that should yield increased thermoelectric performance of bismuth sulphide is nanostructuring [37], [38] (1.3.1).

Yu *et al.* [209] synthesised bismuth sulphide nanowires with a diameter of around 60 nm by a one-step hydrothermal synthesis by reacting $Bi(NO_3)_3 \cdot 5H_2O$ and $Na_2S \cdot 9H_2O$ in tetramethylammonium hydroxide. The nanowire lengths ranged between tens of microns to a few millimetres and were produced with some freestanding nanowires and bundles of nanowires. The electrical conductivity of a single nanowire was shown to be 0.83 S cm^{-1}, no other thermoelectric measurements were conducted.

Sigman *et al.* [210] produced bismuth sulphide nanorods and nanowires, synthesised by solventless thermolysis of bismuth alkylthiolate precursors. The nanowires had an average diameter of 26.0 *nm*. Crossed nanowire networks were achieved by using higher reaction temperatures (240 *°C* instead of 225 *°C*). The nanowire networks formed an interlocking square lattice of interwoven nanowires, which exhibited a high degree of order. There was a very low yield of nanowire networks though, <1% of the total nanocrystal mass. No thermoelectric characterisation was conducted.

Liufu *et al.* [211] initially synthesised bismuth sulphide films onto p-type silicon substrates from acidic baths of 10 *mL* 0.1 *M* $Bi(NO_3)_3$ and 60 *mL* 0.1 *M* thiourea by controlling precursor solution conditions, although no thermoelectric characterisation was performed. Later Liufu *et al.* [212] used the same technique to synthesise one-dimensional nanorods into bismuth sulphide films with enhanced thermoelectric transport properties. They observed an electrical conductivity of 50 S cm^{-1} and a Seebeck coefficient of -755 $\mu V K^{-1}$ at 300 *K*, and an electrical conductivity of 22 $S\ cm^{-1}$ and a Seebeck coefficient of -1351 $\mu V K^{-1}$ at 450 *K*, which yield a slightly higher power factor of $39.7 \times 10^{-4}\ W\ m^{-1}\ K^{-2}$ compared to $28.5 \times 10^{-4}\ W\ m^{-1}\ K^{-2}$ at 300 *K*.

5.1.3 Electrodeposition of Bismuth Sulphide

Electrodeposition is a technique that has been reported very little in the literature for the synthesis of bismuth sulphide. A few papers do exist on the subject however, these are discussed here and summarised in Table 5-2.

Lokhande and Bhosale [213] report the electrodeposition of bismuth sulphide from an electrolyte of 100 *mM* $Bi(NO_3)_3$ and 100 *mM* $Na_2S_2O_3$ at a pH value between 2 and 3 in double distilled water. The deposition potentials were between -70 *mV* and -100 *mV vs. SCE*. The corresponding current densities were between 0.5 and 2 $mA\ cm^{-2}$. Both stainless steel (SS) and fluorine doped tin oxide

(FTO) coated glass substrates were used. Adherent films on the order of 3-4 microns are reported. The films were investigated for photoelectrochemical properties, so no thermoelectric characterisation was performed.

Yesugade *et al.*[214] report the electrodeposition of bismuth sulphide from an electrolyte of 100 *mM* $Bi(NO_3)_3$ and 100 *mM* $Na_2S_2O_3$ and up to 200 *mM* ethylenediaminetetraacetic acid (EDTA). Deposition potentials were estimated to be between -0.20 and -0.27 *V vs. SCE* on substrates of brass, copper, stainless steel and titanium and around -0.90 *V vs. SCE* on FTO. Films were deposited on stainless steel galvonstatically at 2 $mA\ cm^{-2}$ for 1800 *s*, giving thicknesses of around 0.6 μm. No thermoelectric properties were investigated.

Georges *et al.* [215] report the electrodeposition of bismuth sulphide from an electrolyte of 0.055 *M* $BiCl_3$, 0.050 *M* S and 0.3 *M* $LiClO_4$ in dimethysulfoxide (DMSO). The electrolyte is reported to have been produced by mixing at 80 *°C* for 1 hour. FTO covered glass was used as the substrate for all electrochemical experiments and deposition temperatures ranged from 80-150 *°C*. The films were deposited galvanostatically with good adherence being reported for current densities between 0.75 and 3.5 $mA\ cm^{-2}$. No thermoelectric characterisation was conducted.

Peng *et al.* [216] potentiostatically electrodeposited bismuth sulphide at 80-120 *°C* into anodic alumina membranes (AAM). The electrolyte consisted of 0.055 *M* $BiCl_3$ and 0.19 *M* elemental S dissolved in DMSO, deposition was conducted at 393 ± 0.5 *K*, with a potential of -0.1 *V vs. Ag/AgCl* and a deposition time of 7200 *s*. Following deposition the films were washed in DMSO at 353 *K* for 1200 *s*, rinsed in water then annealed in argon atmosphere at 623 *K* for 3 *h* to improve crystallinity. The nanowire arrays were quite uniform with diameters around 40 *nm* and lengths around 5 μm. They had an absorption band gap of 1.56 *eV*, but no thermoelectric characterisation was conducted.

There has not been an attempt in the literature to fabricate nanostructured bismuth sulphide by using lyotropic liquid crystals. This chapter will detail the fabrication and characterisation of bismuth sulphide, firstly deposited in the absence of and then in the presence of a phytantriol template.

Table 5-2 – Summary of the electrodeposition of bismuth sulphide reported in the literature.

Reference	[213]	[214]	[215]	[216]
Electrolyte	100 *mM* $Bi(NO_3)_3$, 100 *mM* $Na_2S_2O_3$, in double distilled water	100 *mM* $Bi(NO_3)_3$, 100 *mM* $Na_2S_2O_3$, up to 200 *mM* EDTA in double distilled water	0.055 *M* $BiCl_3$, 0.050 *M* S, 0.3 *M* $LiClO_4$ in DMSO	0.055 *M* $BiCl_3$, 0.19 *M* S in DMSO
Deposition method	Potentiostatic	Galvanostatic	Galvanostatic	Potentiostatic
Deposition potential / current density	-70 *mV* to -100 *mV vs. SCE*	2 *mA* cm^{-2}	0.75 and 3.5 *mA* cm^{-2}	-0.1 *V vs. Ag/AgCl*
Deposition Temperature	Room Temperature	Room Temperature	80-150 *℃*	120 *℃*
Deposition time	N/A	1800 *s*	N/A	7200 *s*
Substrate	SS and FTO	SS	FTO	Au
Sample thickness	3-4 *μm*	0.6 *μm*	N/A	5 *μm*
Template	None	None	None	AAM

5.2 Results and Discussion

5.2.1 Non-templated Deposition of Bismuth Sulphide

Before phytantriol was used as a template, bismuth sulphide was first electrodeposited in the absence of phytantriol. This allowed for testing of the electrolyte system and to act as a comparison to films electrodeposited through phytantriol. This section details those results.

5.2.1.1 Cyclic Voltammetry

An electrolyte consisting of 100 *mM* $Bi(NO_3)$, 100 *mM* $Na_2S_2O_3$ and 200 *mM* EDTA in Milli-Q deionised water was made. This aqueous electrolyte (which will allow phytantriol to form a known phase) was detailed by Yesugase *et al.* [214]. Upon the addition of water a brown precipitate was observed, which turned black after 24 hours. This was left to settle for 2 days and

the electrolyte was only taken from the clear layer above the precipitate. A CV conducted using this electrolyte is shown in Figure 5-2.

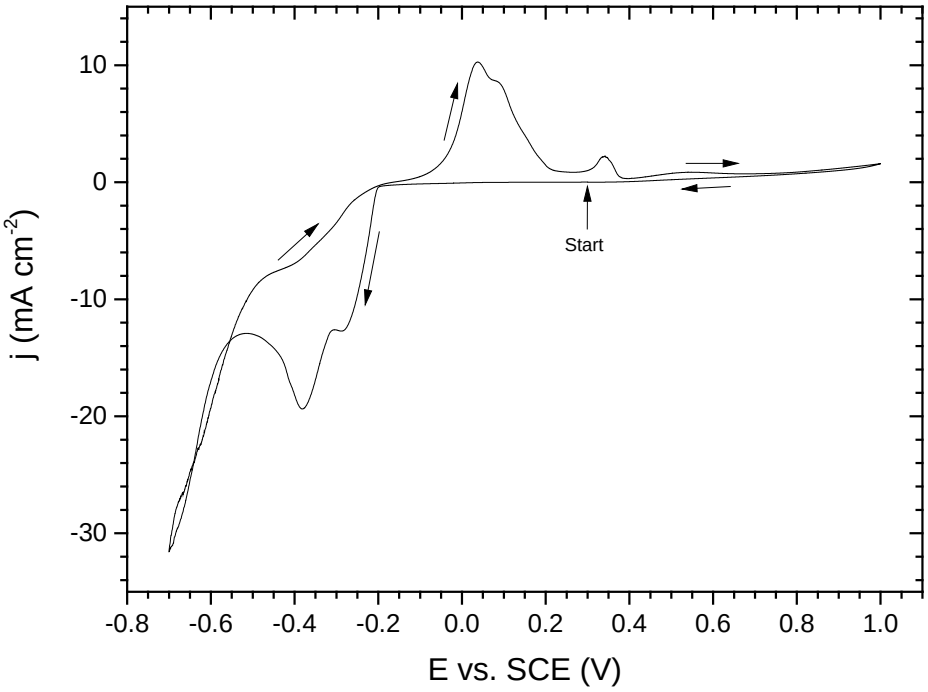

Figure 5-2 - Cyclic voltammogram recorded at 20 *mV* s^{-1} in an electrolyte made by adding 100 *mM* $Bi(NO_3)$, 100 *mM* $Na_2S_2O_3$ and 200 *mM* EDTA to deionised water. The black precipitate was left untouched. The working electrode was a 2 *mm* gold disc electrode. The voltammogram started at a potential of +0.30 *V vs. SCE* where no reaction occurs and is scanned between -0.70 *V vs. SCE* and +1.00 *V vs. SCE*. The black arrows indicate the direction of the scan.

On the cathodic sweep in Figure 5-2 a deposition region is seen from -0.20 *V* to -0.52 *V vs. SCE*, after which the onset of hydrogen evolution begins. On the anodic sweep stripping is seen to occur between -0.20 *V* to +0.39 *V vs. SCE*, with oxygen evolution beginning at +0.85 *V vs. SCE*. To investigate if the deposition peak was that of bismuth sulphide or another species, films were deposited at -0.40 *V vs. SCE* for 4 hours. The current time transient for an electrodeposition can be seen in Figure 5-3.

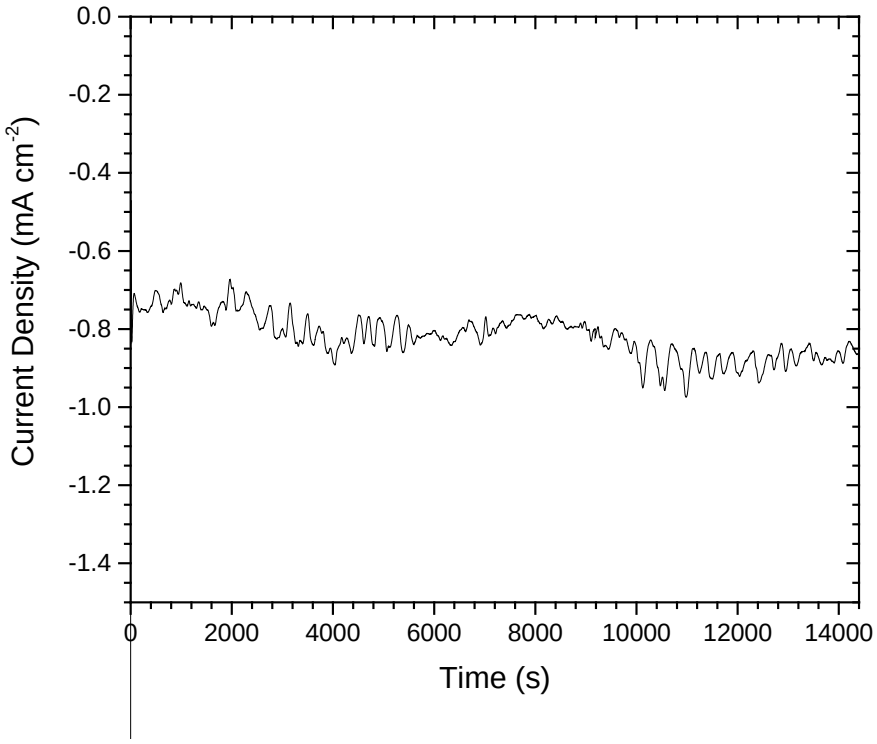

Figure 5-3 - Current time transient of a film electrodeposited from an electrolyte made by adding 100 *mM* $Bi(NO_3)$, 100 *mM* $Na_2S_2O_3$ and 200 *mM* EDTA to deionised water. The deposition potential was -0.40 *V vs. SCE* and deposition time was 4 *h*. The working electrode was a Au on Si substrate with a 10 *mm* × 10 *mm* electrode area. The total deposition charge was -11.77 *C*.

5.2.1.2 SEM and EDX

The deposits initially appeared as black and powdery thin films. To investigate the deposits deposited at -0.40 V vs. SCE SEM and EDX was conducted. SEM results can be seen in Figure 5-4.

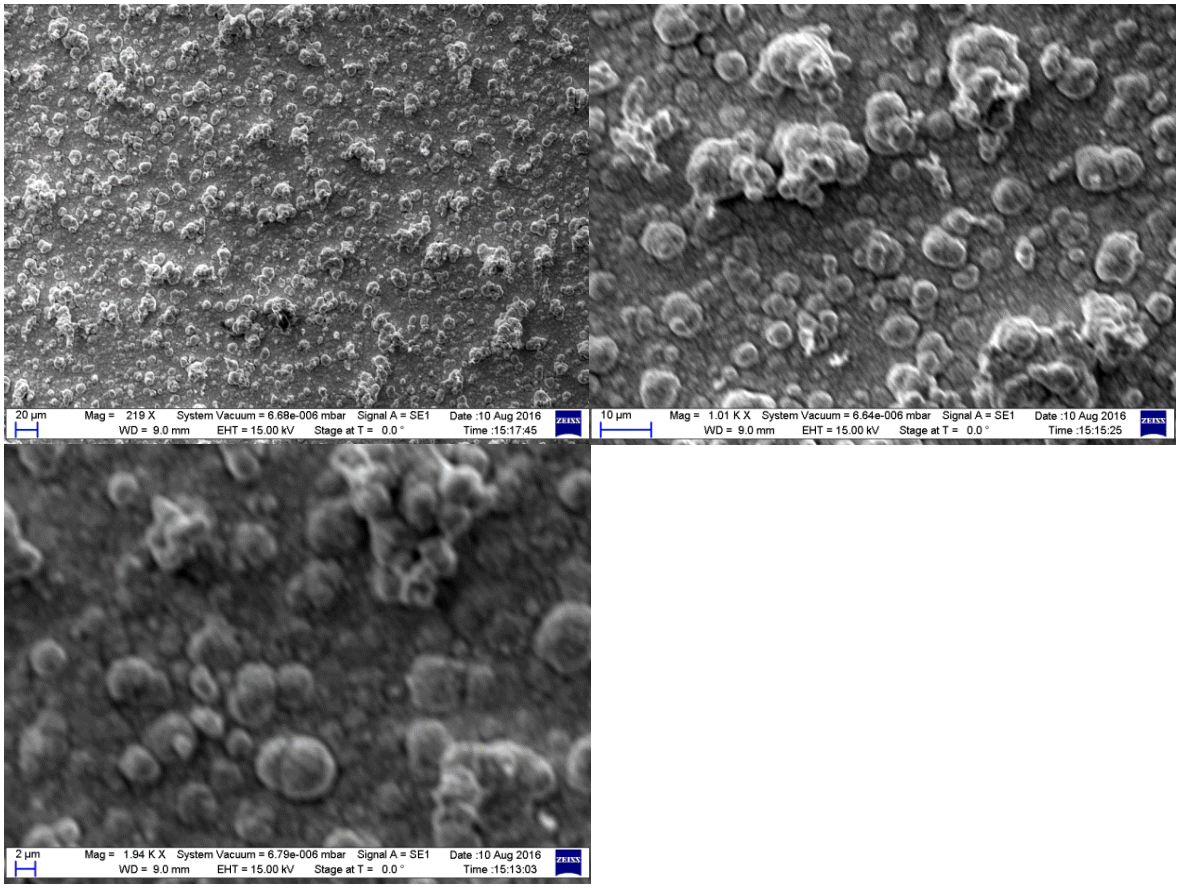

Figure 5-4 – Scanning electron microscopy images of a bismuth sulphide film electrodeposited from an electrolyte solution containing 100 *mM* $Bi(NO_3)_3$, 100 *mM* $Na_2S_2O_3$ and 200 *mM* EDTA in deionised water. The film was deposited potentiostatically at a potential of -0.4 *V vs. SMSE* for 4 *h*.

From Figure 5-4 the morphology of the deposit can be seen to be very uneven. The whole surface of the electrode is covered, although the thickness is very variable. This accounts for the optical observation of a powdery thin film. EDX of the film showed the composition to be 37.5 (± 0.3)% Bi and 62.5 (± 0.3)% S, giving a composition of $Bi_{1.88}S_{3.12}$ which is slightly S rich from the ideal stoichiometry of bismuth sulphide (Bi_2S_3), however within EDX instrumental error (~3% [217]) this is stoichiometric.

5.2.1.3 XRD

To confirm whether the deposits were indeed bismuth sulphide, XRD diffraction of the electrodeposited films was conducted to compare the diffraction peaks to a bismuth sulphide standard. The results of this XRD can be seen in Figure 5-5.

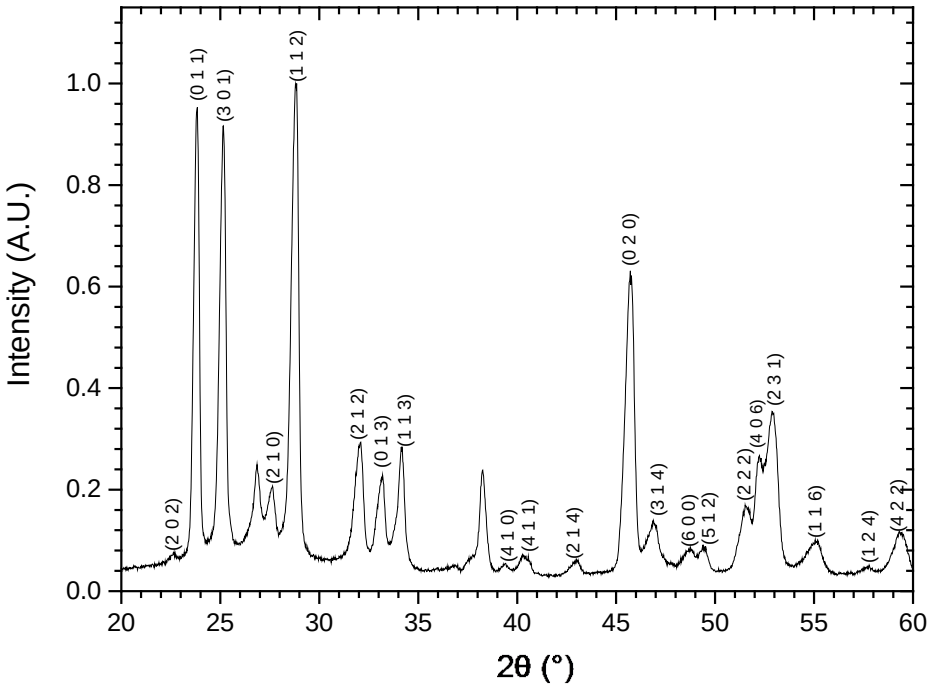

Figure 5-5 - GI XRD scan of a film electrodeposited from an electrolyte of 100 *mM* $Bi(NO_3)_3$, 100 *mM* $Na_2S_2O_3$ and 200 *mM* EDTA dissolved in Milli-Q purified deionised water. The film was deposited potentiostatically at -0.40 *V vs. SCE* for 4 *h*. The deposition substrate was Au on Si. All peaks were fitted from the "Bismuthinite" file in the PDXL software, No: 9007375, CSD: data_9007375(COD).

The diffraction pattern seen in Figure 5-5 is in good agreement with that of the crystallographic open database (COD) file 9007375 "Bismuthinite", which is the mineral name for bismuth sulphide. The stick pattern for the COD file can be found in Figure A-3.

The XRD coupled with the EDX data confirms that the electrodeposited films are indeed bismuth sulphide.

5.2.1.4 Seebeck

Due to the uneven nature of the electrodeposited films, no Hall or electrical conductivity measurements could be conducted, as these require uniform films which were not produced. Seebeck measurements could be conducted however, as they do not require such uniform electrodeposits. A Seebeck value of -29.8 (± 10.3) $\mu V\,K^{-1}$ was recorded for these electrodeposits. The large error is down to the variability in the film thickness due to the uneven morphology of the electrodeposits. This value is very low compared to values reported in the literature for

bismuth sulphide prepared by other techniques (such as ball milling -450 $\mu V K^{-1}$ at 323 *K*). The value cannot be compared to an electrodeposition value as none are reported in the literature.

The peak Seebeck coefficient is likely to be higher than the -29.8 (± 10.3) $\mu V K^{-1}$ value recorded. This is because the Seebeck coefficient is temperature dependant. Larger temperatures allow for a greater diffusion of carriers causing a larger Seebeck value, however, a high enough temperature will allow electrons to cross the band gap causing there to be both n-type carriers in the conduction band and p-type carriers in the valence band causing the resultant Seebeck value to be reduced [4]. Therefore the Seebeck coefficient changes with temperature and there is an optimum temperature for a peak Seebeck coefficient. Due to the large band gap of bismuth sulphide the peak Seebeck coefficient is likely to be at a higher temperature than room temperature, therefore, higher temperature Seebeck coefficients should be measured to observe the peak Seebeck coefficient. Elevated temperature Seebeck coefficients have not been measured however, due to the Seebeck measurement equipment only allowing room temperature measurements (2.3.7).

5.2.2 Nanostructuring Bismuth Sulphide

In this section phytantriol was used as a template in an attempt to fabricate nanostructured bismuth sulphide via electrodeposition. Electrodes were dip coated in a mixture of phytantriol and ethanol 1:2 by weight, and left to dry for a minimum of 30 minutes before use. They were also left in the electrolyte for 1 hour to form the Q_{224} "double diamond" mesophase, before electrochemical experiments were conducted. All electrochemical parameters were kept constant when compared to electrochemistry in the absence of phytantriol. This section details those results.

5.2.2.1 Cyclic Voltammetry

An electrolyte consisting of 100 *mM* $Bi(NO_3)$, 100 *mM* $Na_2S_2O_3$ and 200 *mM* EDTA in Milli-Q deionised water was made as detailed in 5.2.1.1, this is the electrolyte detailed by Yesugase *et al.* [214]. A CV conducted using this electrolyte on a 2 *mm* gold disc electrode with a phytantriol coating is shown in Figure 5-6.

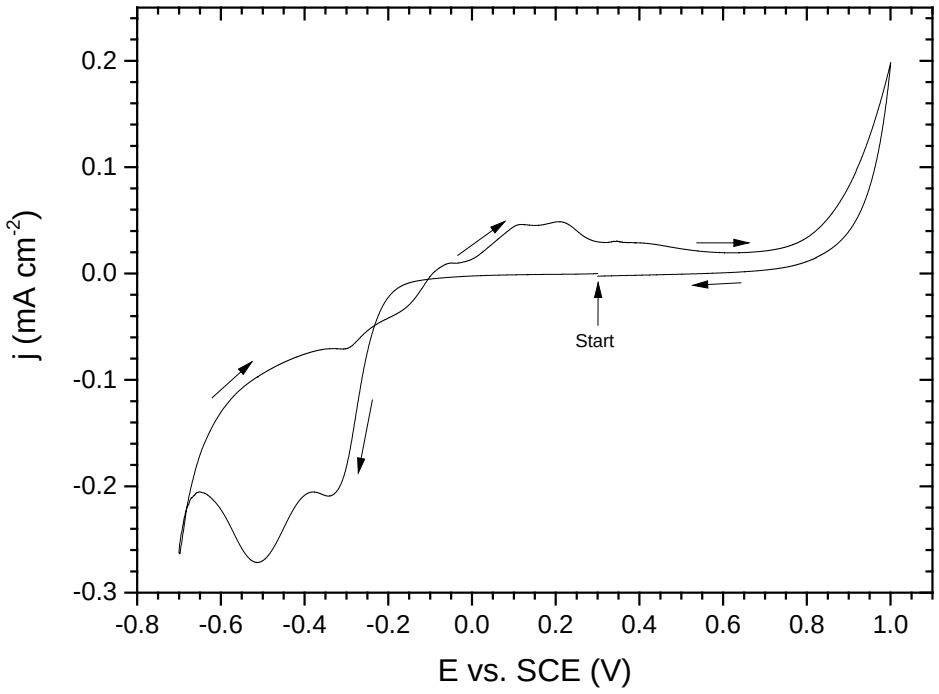

Figure 5-6 - Cyclic voltammogram recorded at 20 *mV* s^{-1} in an electrolyte made by adding 100 *mM* $Bi(NO_3)_3$, 100 *mM* $Na_2S_2O_3$ and 200 *mM* EDTA to deionised water. The black precipitate was left untouched. The working electrode was coated in phytantriol. The voltammogram started at a potential of +0.50 *V vs. SCE* where no reaction occurs and is scanned between -0.50 *V vs. SCE* and +1.00 *V vs. SCE*. The black arrows indicate the direction of the scan.

On the cathodic sweep in Figure 5-6 a deposition region is seen from -0.16 *V* to -0.65 *V vs. SCE*, after which the onset of hydrogen evolution begins. On the anodic sweep stripping is seen to occur between -0.10 *V* to +0.55 *V vs. SCE*, with oxygen evolution beginning at +0.75 *V vs. SCE*. The potentials have shifted slightly, but on the whole are the same as those recorded in the absence of phytantriol. A big change in the CV, when compared to Figure 5-6, is that the current densities have decreased by around a factor of 100 (e.g. peak deposition potential decreased from -19.36 *mA* cm^{-2} to -0.27 *mA* cm^{-2}). The template is covering the working electrode, causing sections of the electrode to not be in contact with the aqueous electrolyte and also causing slower diffusion, thus explaining the lower current densities. The same deposition conditions (-0.40 *V vs. SCE* for 4 hours) were applied as those used for non-templated bismuth sulphide films, as potentials on the CV were not significantly different to those seen in the absence of phytantriol. The current time transient for an electrodeposition can be seen in Figure 5-7.

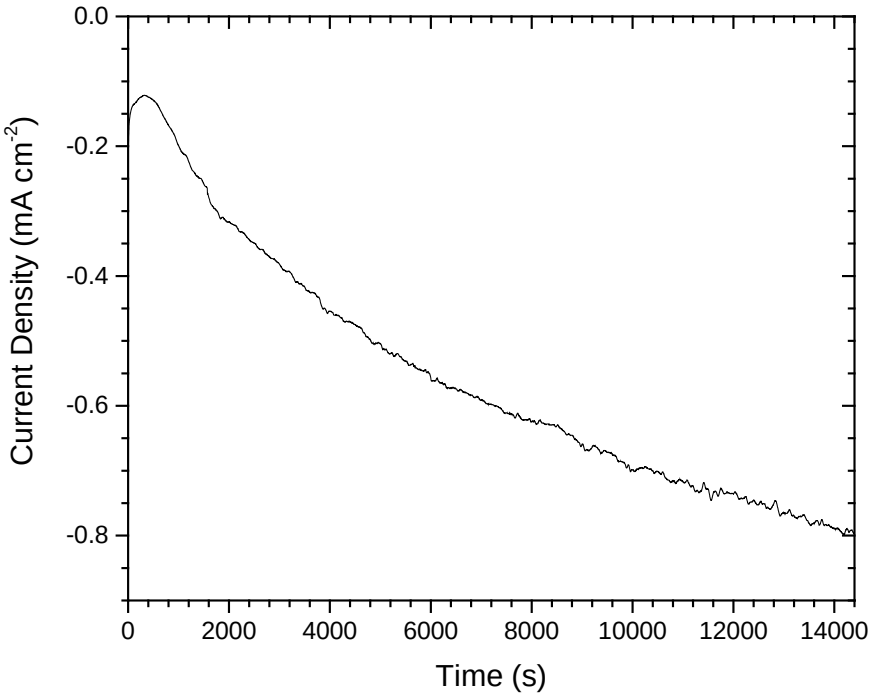

Figure 5-7 - Current time transient of a film electrodeposited through a phytantriol template from an electrolyte made by adding 100 *mM* $Bi(NO_3)$, 100 *mM* $Na_2S_2O_3$ and 200 *mM* EDTA to deionised water. The deposition potential was -0.40 *V vs. SCE* and deposition time was 4 *h*. The working electrode was a Au on Si substrate with a 10 *mm* × 10 *mm* electrode area. The total deposition charge was -7.96 *C*.

Interestingly, the level of current density observed in Figure 5-7 is very similar to the level of current density that was observed for the electrodeposition of bismuth telluride through phytantriol seen in Figure 4-8. The current density in Figure 5-7 is slightly lower, but with -7.96 *C* passed over 4 *h* compared to -4.43 *C* passed over 2 *h*, the levels are very similar.

5.2.2.2 SEM and EDX

As was the case with non-templated bismuth sulphide electrodeposits, the electrodeposits deposited through phytantriol had an optical appearance of a black and powdery thin film. To investigate the micro-structure, the films were investigated by SEM and EDX. SEM results can be seen in Figure 5-8.

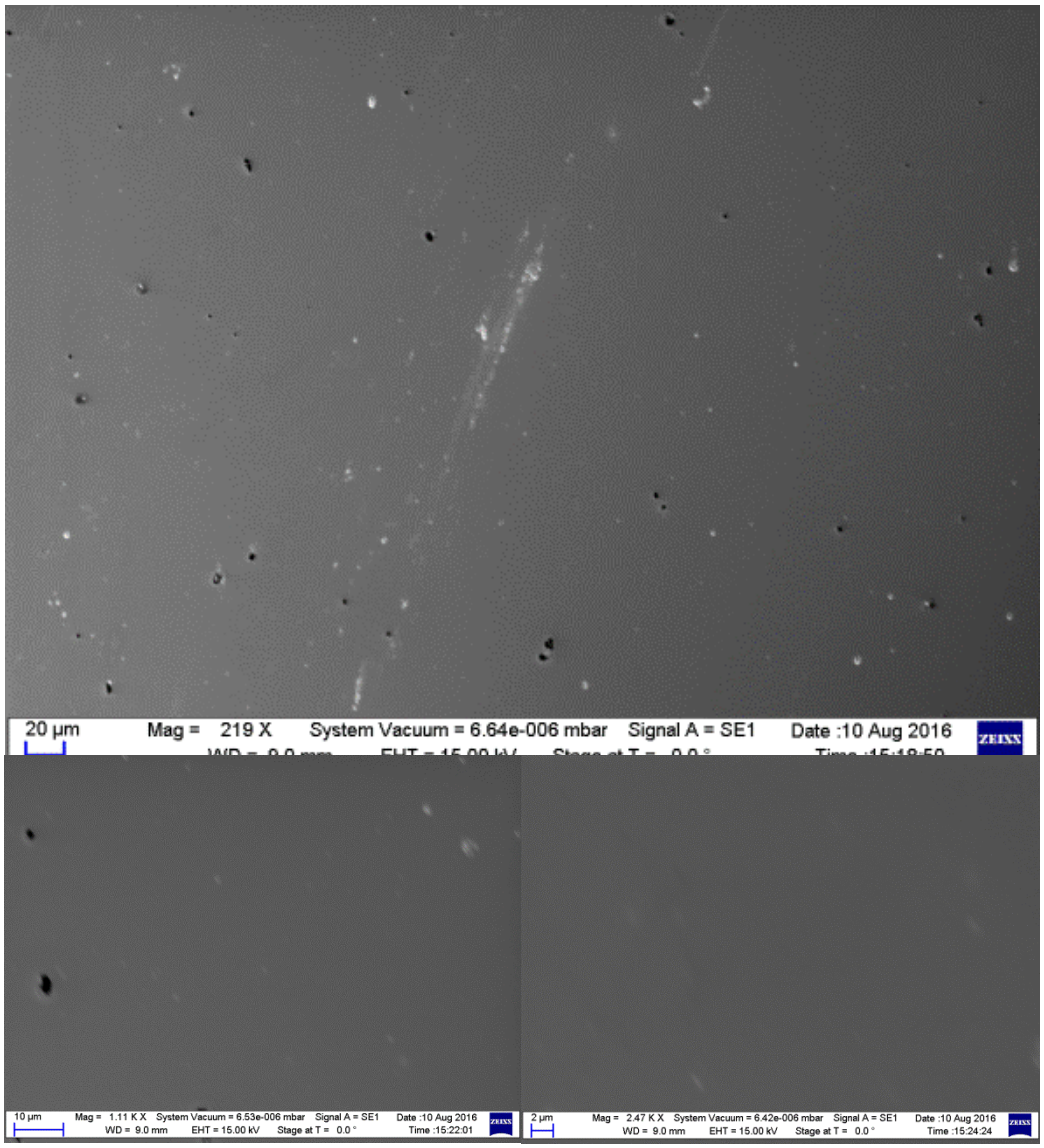

Figure 5-8 - Scanning electron microscopy images at different magnifications of a bismuth sulphide film electrodeposited through a phytantriol template from an electrolyte solution containing 100 *mM* $Bi(NO_3)_3$, 100 *mM* $Na_2S_2O_3$ and 200 *mM* EDTA in deionised water. The film was deposited potentiostatically at a potential of -0.4 *V vs. SCE* for 4 *h*.

From Figure 5-8 the morphology of the deposit can be seen to be smooth to the magnifications achievable by the instrument, however there is a series of approximately 2 *µm* diameter holes across the film. The smooth texture is an indication of a nanostructured material, as a smooth homogeneous texture has been seen in SEM images previously for nanostructured electrodeposited films [55]. The 2 *µm* holes appear to have opened up post deposition, as there are raised edges around them, indicating the film has lifted off of the substrate in that section. This is most likely damage caused from washing off the phytantriol template. EDX of various locations on the film showed the composition to be 40.1 (± 5.5)% Bi and 59.9 (± 5.5)% S, giving a

composition of $Bi_{2.00}S_{3.00}$ which on average is the ideal stoichiometry of bismuth sulphide although there is a variation across films and within films on the composition.

5.2.2.3 XRD

To confirm the deposit is that of bismuth sulphide, XRD diffraction of an electrodeposited film was conducted. The results of this XRD can be seen in Figure 5-9.

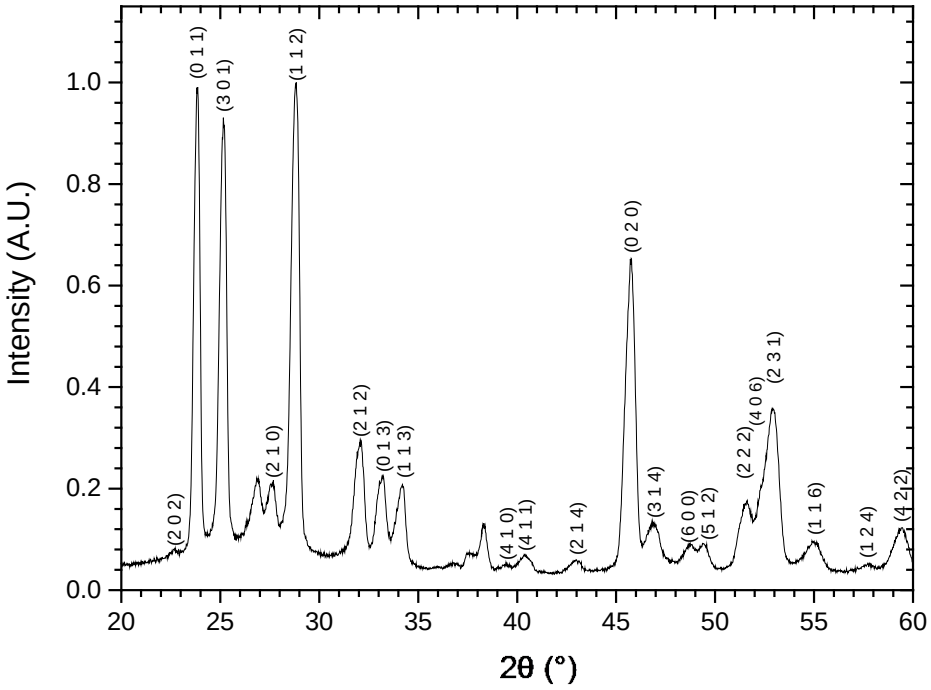

Figure 5-9 - GI XRD scan of a film electrodeposited through a phytantriol template from an electrolyte of 100 *mM* $Bi(NO_3)_3$, 100 *mM* $Na_2S_2O_3$ and 200 *mM* EDTA dissolved in Milli-Q purified deionised water. The film was deposited potentiostatically at -0.40 *V vs. SCE* for 4 *h*. The deposition substrate was Au DVD. All peaks were fitted from the "Bismuthinite" file in the PDXL software, No: 9007375, CSD: data_9007375(COD).

The diffraction pattern seen in Figure 5-9 is in good alignment with that of the crystallographic open database (COD) file 9007375 "Bismuthinite", which is the mineral name for bismuth sulphide. The stick pattern for the COD file can be found in Figure A-3. The same observation was seen for non-templated electrodeposited bismuth sulphide Figure 5-5. The XRD coupled with the EDX data, leaves no doubt that the electrodeposited film is indeed that of bismuth sulphide, as seen in the absence of phytantriol in this work and by Yesugade *et al.* [214].

5.2.2.4 Small Angle X-Ray Scattering (SAXS)

Whilst the film electrodeposited through phytantriol has been established as bismuth sulphide, there has been no characterisation to see if a nanostructure has been formed. Small angle x-ray scattering (SAXS) was conducted to investigate what phase phytantriol forms in the presence of the bismuth sulphide electrolyte, and if any nanostructure is present in the resulting films electrodeposited using the bismuth sulphide electrolyte through phytantriol.

5.2.2.4.1 Phytantriol and Electrolyte SAXS

To see what liquid crystal phase is formed when a phytantriol coated surface is immersed into the bismuth sulphide electrolyte, a phytantriol lined Quartz capillary (2.3.6.1) was filled with the bismuth sulphide electrolyte of 100 *mM* $Bi(NO_3)_3$, 100 *mM* $Na_2S_2O_3$ and 200 *mM* EDTA dissolved in Milli-Q purified deionised water. This was left to equilibrate for 150 minutes, before being placed in front of the SAXS beam. The resultant 2D and 1D radial integrated SAXS patterns can be seen in Figure 5-10. The capillary was then reimaged approximately every 20 minutes until the electrolyte had been present in the capillary for 8 hours. The 1D pattern of these runs can also be seen in Figure 5-10.

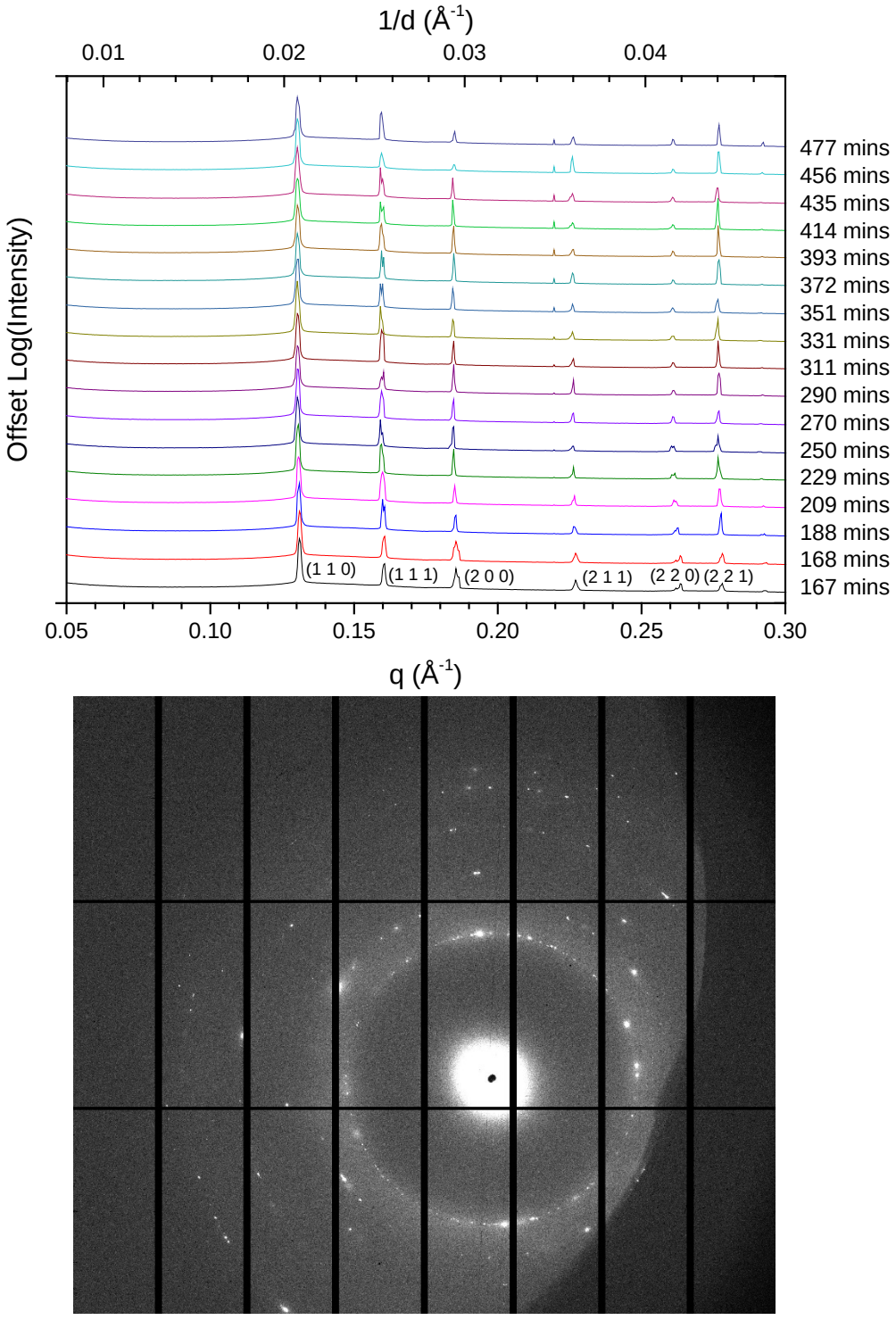

Figure 5-10 - 1D integrated SAXS pattern of a phytantriol lined capillary filled with 100 *mM* $Bi(NO_3)_3$, 100 *mM* $Na_2S_2O_3$ and 200 *mM* EDTA in deionised water. The capillary was observed over 5 and a half hours. The times denote time passed since the electrolyte was added to the capillary. The corresponding 2D pattern for 167 minutes is included below.

Phytantriol when mixed with excess bismuth sulphide precursor electrolyte is seen show six peaks, (1 1 0), (1 1 1), (2 0 0), (2 1 1), (2 2 0) and (2 2 1). From the line spacing ratio of these peaks the phase can be determined to be Q_{224} "double diamond" [180]. The phase is seen to be stable for 8 hours, as shown in Figure 5-10. The lattice parameter was calculated using Equation 2.3 to be 68.1 (± 0.2) *Å* (B.2). An extra peak with a q value of 0.22 occurs after 290 minutes. This could be a sign of beam damage or degradation due to the electrolyte. The phase looks intact otherwise. This result shows that phytantriol forms a phase that can be electrodeposited in to form a nanostructure [57] and that it is stable enough over the periods of time that would be used in any experiments to form nanostructured electrodeposits.

To test that the same liquid crystal phase would form on gold, a gold foil was dip coated into phytantriol, then immersed into a cell of the bismuth sulphide precursor electrolyte and placed in front of the SAXS beam. The resultant 1D and 2D patterns can be seen in Figure 5-11.

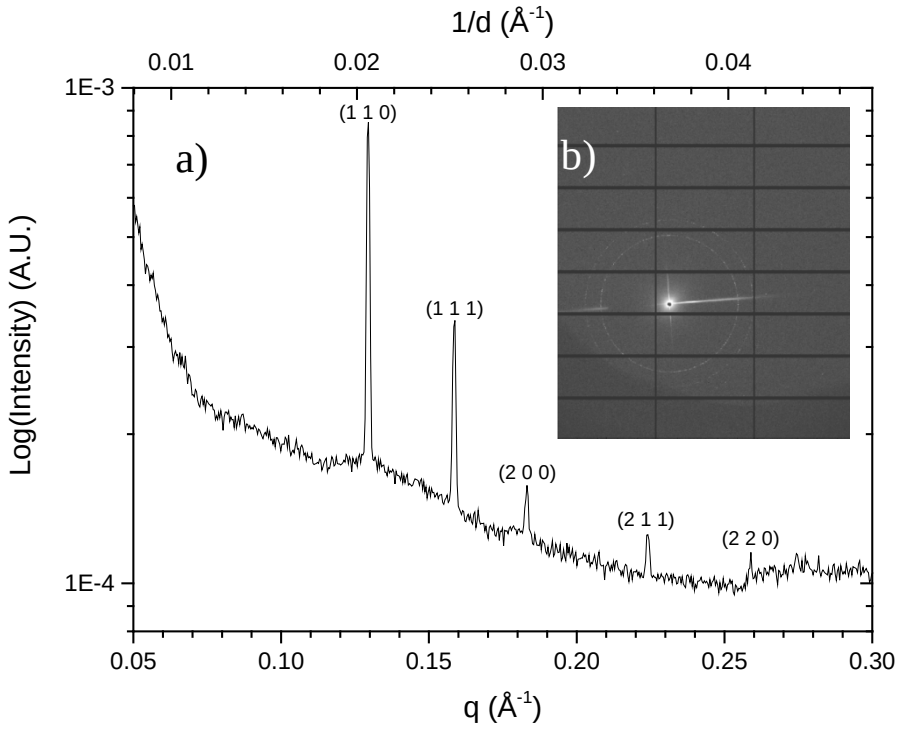

Figure 5-11 – a) 1D integrated SAXS pattern of a phytantriol coated gold foil immersed in 100 *mM* $Bi(NO_3)_3$, 100 *mM* $Na_2S_2O_3$ and 200 *mM* EDTA in deionised water. The foil was dip coated in a solution of phytantriol and ethanol 1:2 by weight. The foil was allowed to dry for 30 minutes prior to being immersed in the electrolyte and the foil was allowed to hydrate for 30 minutes prior to the SAXS pattern being taken. b) The corresponding 2D pattern.

Phytantriol is seen to produce five peaks on gold foil: (1 1 0), (1 1 1), (2 0 0), (2 1 1) and (2 2 0) as shown in Figure 5-11, which index to the Q_{224} "double diamond" phase. The lattice parameter was

calculated using Equation 2.3 to be 68.9 (± 0.9) *Å* (B.2). This shows that phytantriol can form the Q_{224} phase on gold in the presence of bismuth sulphide electrolyte thus permitting deposition of bismuth sulphide through it.

5.2.2.4.2 SAXS of Bismuth Sulphide Films Electrodeposited Through Phytantriol

Bismuth sulphide films electrodeposited through the Q_{224} "double diamond" phase of phytantriol were placed in the SAXS beam to investigate what nanostructure had formed. A resulting diffraction pattern and the 1D integration can be seen in Figure 5-12.

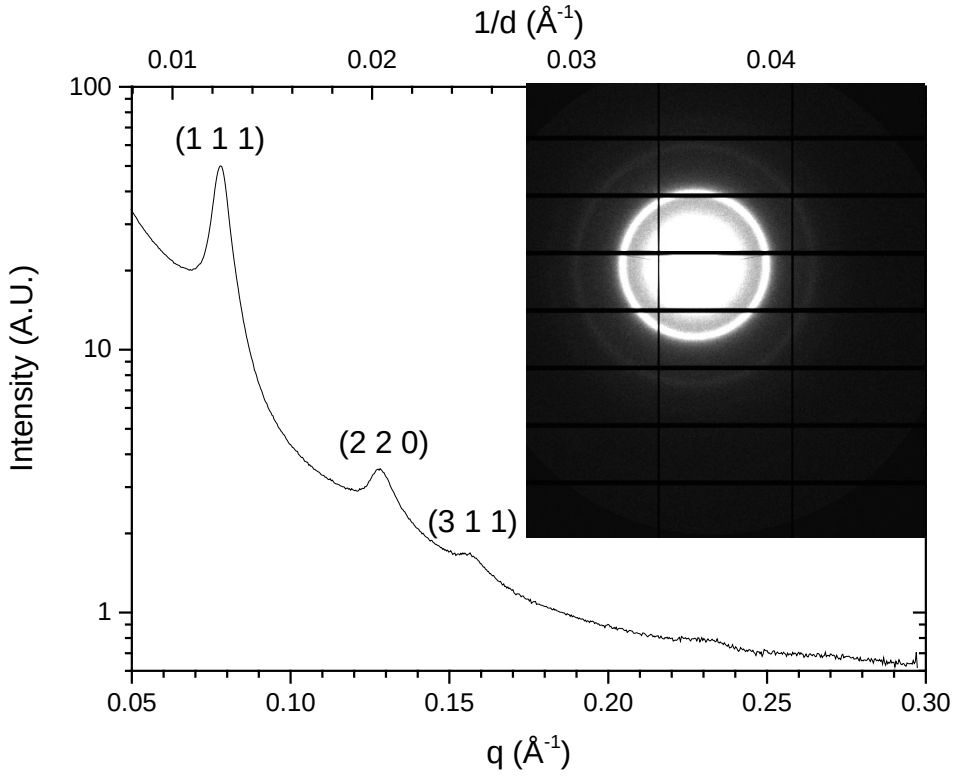

Figure 5-12 - 1D integrated SAXS pattern of a bismuth sulphide thin film electrodeposited on a phytantriol coated Au DVD. The electrolyte was 100 *mM* $Bi(NO_3)_3$, 100 *mM* $Na_2S_2O_3$ and 200 *mM* EDTA in deionised water and the deposition conditions were 14400 *s* at -0.4 *V vs SCE*. The corresponding 2D pattern is included in the upper right segment.

The electrodeposited bismuth sulphide films can be seen to give three clear diffraction peaks: (1 1 1), (2 2 0) and (3 1 1) in Figure 5-12. These peaks assign to the Q_{227} "single diamond" geometry with a lattice parameter of 139.6 (± 3.2) *Å*. This is within error, double the lattice parameter of phytantriol on gold in the electrolyte (68.9 (± 0.9) *Å*). This is consistent with electrodeposition occurring in one water channel of the double diamond structure, resulting in a single diamond nanostructure with a doubled lattice parameter due to a reduction in symmetry. These results are

in line with those seen for Pt [57], which does not include the 3rd peak. A follow up paper does however [95].

5.2.2.5 TEM

To further corroborate the SAXS results seen for electrodeposited bismuth sulphide through phytantriol, transmission electron microscopy was conducted to visualise the nanostructure. A selection of resulting images can be seen in Figure 5-13.

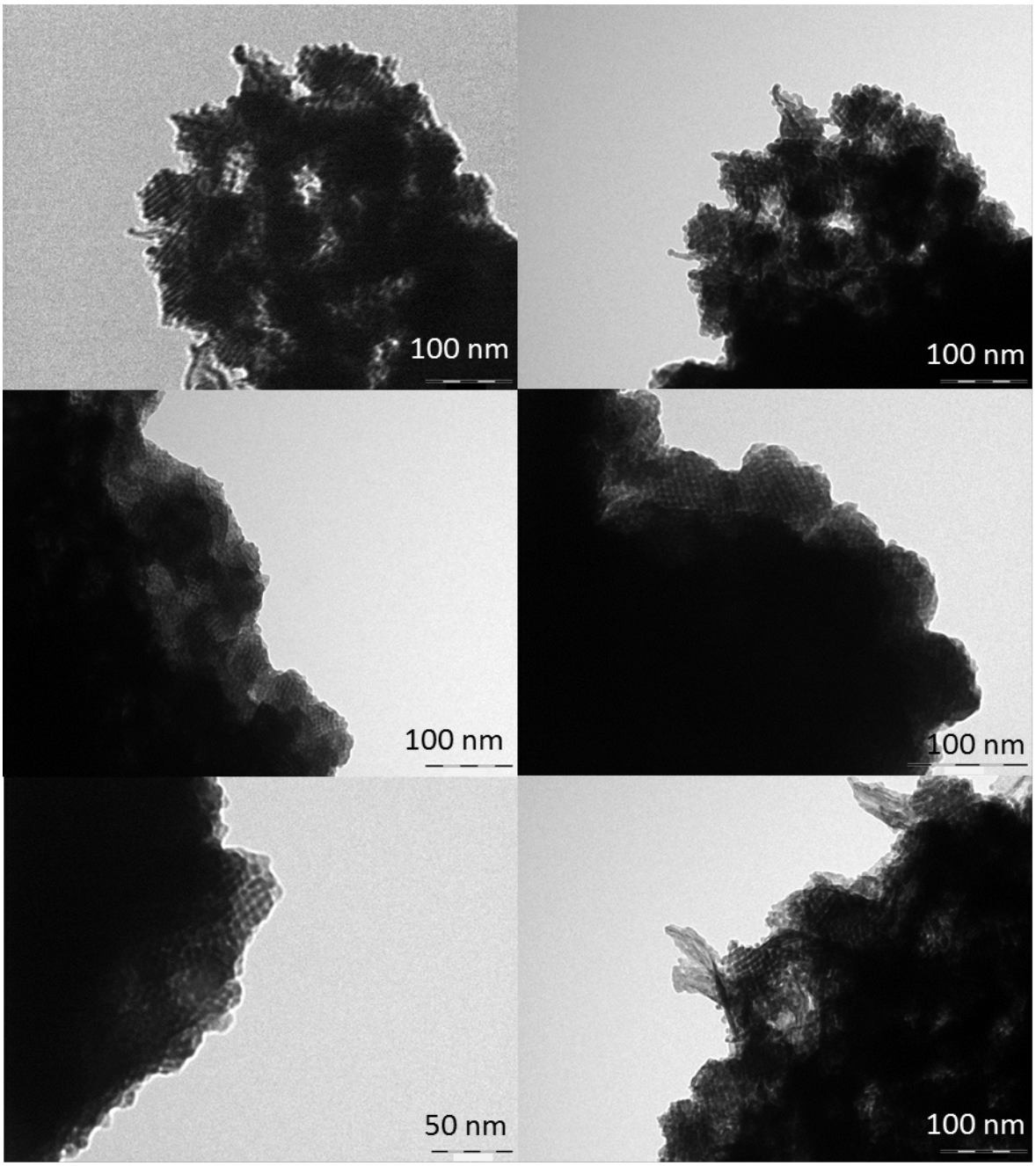

Figure 5-13 – TEM images of a bismuth sulphide thin film electrodeposited on a phytantriol coated Au DVD. The electrolyte was 100 *mM* $Bi(NO_3)_3$, 100 *mM* $Na_2S_2O_3$ and 200 *mM* EDTA in deionised water and the deposition conditions were 14400 *s* at -0.4 *V vs SCE*. The film was then scrapped off above a TEM grid.

The images in Figure 5-13 depict a nanostructure that is consistent with a single diamond phase. A MatLab projection of the single diamond structure (courtesy of Dr Adam Squires a collaborative lecturer from the University of Reading) is placed in sections of the images in Figure 5-14.

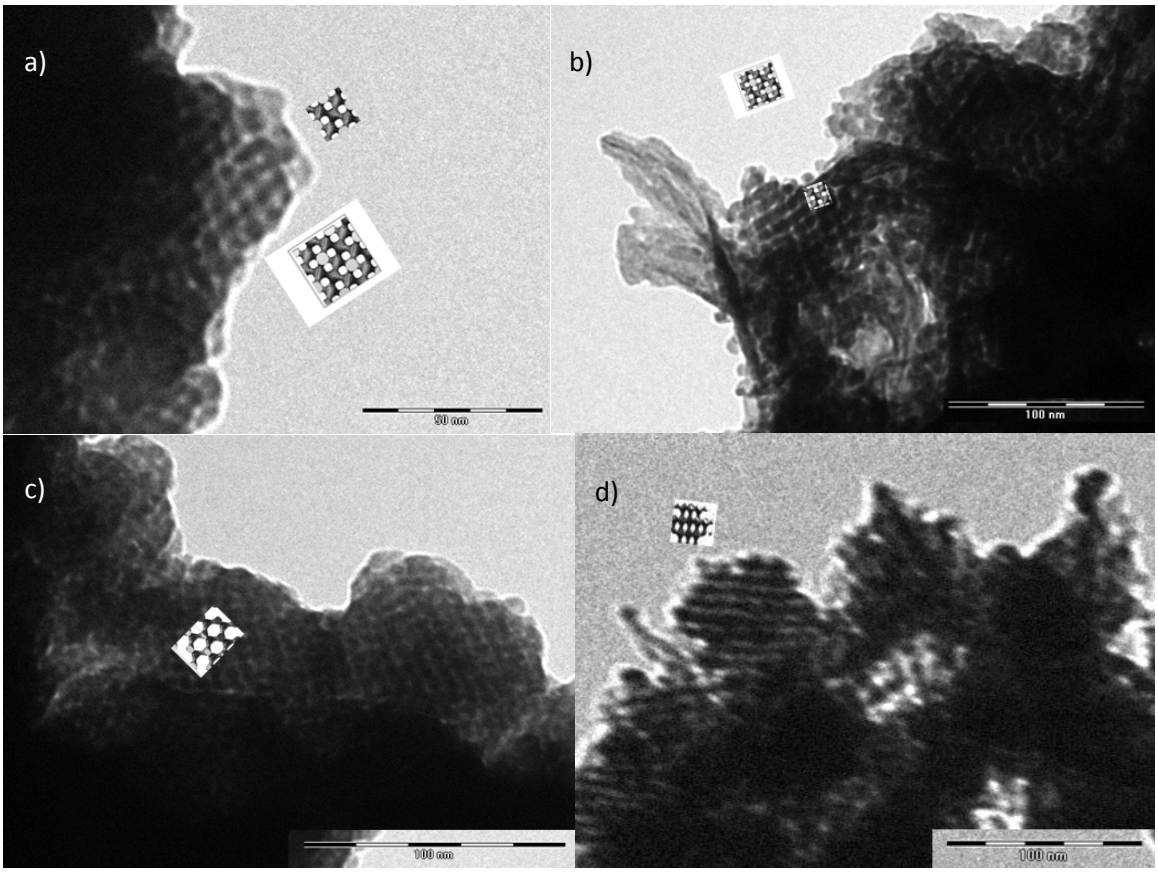

Figure 5-14 – Matlab single diamond (Q_{227}) projections (courtesy of Dr Adam Squires) overlaid onto TEM images of single diamond bismuth sulphide. The projection planes are as follows, a) 100, b) 100, c) 110 and d) 211.

The projections are in line with the structures seen in the TEM images. From the projections, estimations of the lattice parameter were calculated. These were found to be a) 115 *Å* b) 125 *Å*, c) 109 *Å* and d) 124 *Å*. Whilst these are all smaller than the 139.6 (± 3.2) *Å* lattice parameter determined by SAXS, the degree of error here is large (the 95% confidence range from these projection calculations is 106-130 *Å*, based solely on variation) as the projections have to be manually aligned with the TEM images. Therefore it can be concluded these are within error in agreement with SAXS observations.

5.2.2.6 Seebeck

Due to inability to cleanly separate the electrodeposited films form the conducting substrate, no Hall or electrical conductivity measurements could be conducted, as the separated films were uneven in thickness. Seebeck measurements could be conducted however, as they do not require

the electrodeposits to be removed from the substrate. A Seebeck value of -12.3 (±1.8) $\mu V K^{-1}$ was recorded for these electrodeposits. This value is very low compared to values reported in the literature for bismuth sulphide prepared by other techniques (such as ball milling -450 $\mu V K^{-1}$ at 323 *K*) and lower than that seen for non-templated bismuth sulphide electrodeposited here (-29.8 (±10.3) $\mu V K^{-1}$). Whilst the Seebeck coefficient of -12.3 (±1.8) $\mu V K^{-1}$ at room temperature for templated bismuth sulphide is smaller than -29.8 (±10.3) $\mu V K^{-1}$ at room temperature for non-templated bismuth sulphide, the peak Seebeck coefficient could be higher for templated bismuth sulphide. This is because the Seebeck coefficient is temperature dependant. The Seebeck coefficients have not been measured over variable temperatures however, due to the Seebeck measurement equipment only allowing room temperature measurements (2.3.7).

5.3 Conclusions

Bismuth sulphide was successfully electrodeposited from an electrolyte of 100 *mM* $Bi(NO_3)$, 100 *mM* $Na_2S_2O_3$ and 200 *mM* EDTA in Milli-Q deionised water onto a Au substrate. The deposition potential was -0.4 *V vs SCE* and the deposition time was 4 *h*. This was confirmed to be bismuth sulphide by EDX and XRD.

Following successful electrodeposition of bismuth sulphide, nanostructured bismuth sulphide was formed by using phytantriol as a template. This was achieved by applying a phytantriol coating on Au DVD working electrodes and allowing the layer to hydrate in the bismuth sulphide precursor electrolyte to the Q_{224} "double diamond" phase, as confirmed by SAXS. The lattice parameter of the template was deduced to be 68.9 (± 0.9) *Å* by SAXS. Bismuth sulphide films were electrodeposited through the template, producing Q_{227} "single diamond" bismuth sulphide, as shown by SAXS and TEM. The Q_{227} structure had a lattice parameter of 139.6 (± 3.2) *Å*, as determined by SAXS. These results are consistent with those seen for Pt [57], where this observation is rationalised by one of the two water channels of the Q_{224} phase being blocked to the outside aqueous region to preserve the bilayer topology [57], [182], [183], causing deposition to occur down only one water channel, producing Q_{227} symmetry of the films. This chapter however, details the first formation of a single diamond nanostructured semiconductor using a phytantriol template.

Whilst initial Seebeck coefficient measurements were low for both non-templated bismuth sulphide (-29.8 (±10.3) $\mu V K^{-1}$) and single diamond bismuth sulphide (-12.3 (±1.8) $\mu V K^{-1}$), bismuth sulphide is a large band gap semiconductor so in theory should exhibit greatly enhanced Seebeck coefficients at elevated temperatures.

Chapter 6: Pd Nanostructuring

6.1 Introduction

Nanostructured palladium has potential applications in gas sensors [66], [70], [71], electrochemical biosensors [67] and supercapacitors [68], [69]. However, the largest area of interest is fuel cells. The ever increasing global anthropogenic energy requirements, coupled with the looming prospect of climate change have stimulated research into sustainable alternatives to fossil fuels such as wind, solar, tidal, geothermal and fuel cells. Fuel cells are seen as a key new green technology with applications in transport and portable power generation. Currently fuel cells are electrocatalysed by platinum based materials, but the cost and limited supply of Pt makes this option far from ideal. Comparatively Pd has a three times higher abundance in the Earth's crust compared to Pt, 0.015 ppm by weight and 0.005 ppm by weight respectively [72]. This results in the price of Pt being $1056 per ounce, whilst Pd is $696 per ounce (Kitco Gold Index, Sep 23, 2016). The price of Pd is still higher than is acceptable for commercial applications, but with the use of nanomaterials the levels of Pd required can be lowered making the use of Pd more appealing. This is because by introducing a nanostructure the surface area to volume ratio can be increased which can increase the catalytic activity, along with the potential for more efficient facets of palladium being accessible which can also increase catalytic activity.

6.1.1 Fuel Cells

A fuel cell is a device that converts chemical energy into electrical energy through the chemical reaction of an oxidising agent with a fuel. Examples of these fuels are hydrogen, methanol, ethanol and glycerol to mention a few. An alkaline methanol fuel cell is depicted in Figure 6-1. Fuel cells differ from batteries in that they require a continuous source of fuel. They can however, continually produce electricity. A key component of a fuel cell is the catalytic layers.

In this work alkaline fuel cells are considered due to Pd being inactive for the electrooxidation of methanol [72], ethanol and glycerol [79] in acidic conditions. Anion exchange membranes required for alkaline polymer exchange membrane fuel cells are being researched, but are still in development for commercial applications [218] so this work focuses on liquid fuel cells. Whilst the hydrogen polymer exchange membrane fuel cell has higher power densities than that of liquid fuel cells, an advantage of liquid fuel cells is that the liquid fuels are easier to transport and store compared to hydrogen for hydrogen fuelled polymer exchange membrane fuel cells [72].

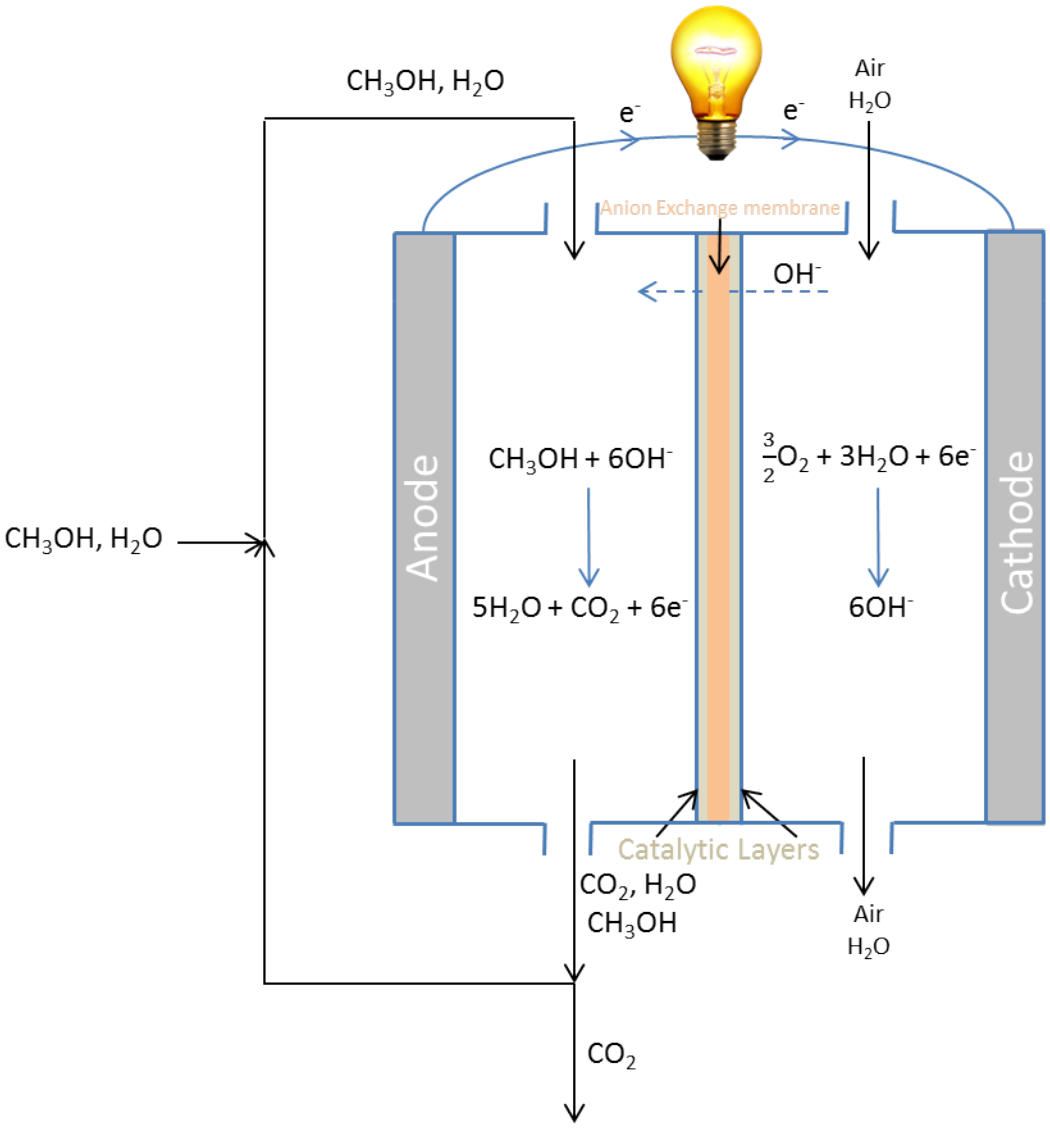

Figure 6-1 – A schematic diagram illustrating the setup and function of an alkaline methanol fuel cell.

Direct alcohol fuel cells (DAFCs) have gained much interest recently due to their potential applications as portable power sources for electric cars and electrical devices. Methanol, ethanol, and glycerol are all examples of appealing options for DAFCs due to their high energy density, and ease of storage and transportation compared to hydrogen for hydrogen fuelled polymer electrolyte membrane fuel cells.

6.1.1.1 Methanol Fuel Cells

The most common type of DAFCs are direct methanol fuel cells (DMFCs). DMFCs are advantageous in that they have high energy conversion efficiencies, system simplicity, low pollution and environmental compatibility [72]. Pt-based catalysts are widely used for DMFCS, however, they suffer from poor anode kinetics, methanol crossover and CO adsorbate poisoning.

This means there is a real interest in developing catalytic materials based on other metals such as Pd to improve the kinetics and to limit the effects of CO catalyst poisoning [72].

Whilst it is recognised that Pd is totally inactive towards the electrooxidation of methanol in acidic conditions [73], [219], methanol can be completely oxidised by Pd in alkaline media. Equation 6.1 and Equation 6.2 outline the proposed mechanism for the electrooxidation of methanol:

$$Pd + CH_3OH \leftrightarrow Pd\text{-}CH_3OH_{ads} \quad (6.1)$$

$$Pd\text{-}CH_3OH_{ads} + nOH^{-} \rightarrow Pd\text{-intermediates} + nH_2O + ne^{-} \quad (6.2)$$

The methanol oxidation intermediates are organic species such as $–CH_3O_{ads}$, $-CH_2O_{ads}$, $-CO_{ads}$, -COOH, etc. The Pd surface sites can be dissociated from these intermediates by OH^- species, with the ideal end products being H_2O and CO_2 [72].

6.1.1.2 Ethanol Fuel Cells

Methanol fuel cells have limited commercial applications due to the toxicity of methanol and the crossover of methanol from the anode to the cathode reducing cell performance [73]–[75]. This has led to substantial attention for alternative fuel cells, one example being ethanol fuel cells. Ethanol has a reduced toxicity and a higher theoretical energy density (8.1 $kW\ h\ kg^{-1}$ for ethanol and 6.1 $kW\ h\ kg^{-1}$ for methanol [72]) compared to methanol. The production of ethanol is also less dependent on fossil fuels [77], [220].

Pd in alkaline conditions could potentially be used as a catalyst to replace Pt in ethanol fuel cells. The ethanol oxidation reaction is a complex reaction in alkaline media with many pathways, ensuing 2, 4 or 12 electron transfers [72]. The generic reactions for ethanol electrooxidation on Pd can be summarised by Equation 6.3 and Equation 6.4.

$$Pd + CH_3CH_2OH \leftrightarrow Pd\text{-}CH_3\ CH_2OH_{ads} \quad (6.3)$$

$$Pd\text{-}CH_3\ CH_2OH_{ads} + nOH^{-} \rightarrow Pd\text{-intermediates} + nH_2O + ne^{-} \quad (6.4)$$

6.1.1.3 Glycerol Fuel Cells

Whilst ethanol has the highest energy density (8.1 $kW\ h\ kg^{-1}$ [72]) of fuel cell fuels, C-C bond breaking at room temperature is difficult to realise leading to the reaction's main products being acetaldehyde and acetate [78], [221]. This in turn leads to a low faradic efficiency of 17-33% of the theoretical energy available [79]. Polyol fuel cells are an alternative to methanol or ethanol fuels. Polyols such as glycerol are less toxic than methanol [79] and display similar theoretical energy densities (5.0 $kW\ h\ kg^{-1}$ for glycerol compared to 8.1 $kW\ h\ kg^{-1}$ for ethanol and

6.1 *kW h kg*$^{-1}$ for methanol [72], [79]) compared to methanol and ethanol. Each carbon in glycerol carries an alcohol group, which means the partial oxidation of glycerol to mesoxalate (Equation 6.5-6.10) can yield 71.5% of the theoretical energy available without breaking a C-C bond.

Pd in alkaline conditions could potentially be used as a catalyst to replace Pt in glycerol fuel cells. The glycerol oxidation reaction is a complex reaction in alkaline media with the entire pathway unknown. The reactions for glycerol electrooxidation on Pd without breaking C-C are summarised by Equation 6.5-6.10 [79], with Equation 6.5-6.7 confirmed by Simões e*t al.* [79] on Pd nano-crystals and Equation 6.8-6.10 postulated by Simões e*t al.* [79]. The C-C bond breaking is summarised by Equation 6.11.

$$Pd + CH_2OHCHOHCH_2OH \leftrightarrow Pd\text{-}\ CH_2OHCHOHCH_2OH_{ads} \quad (6.5)$$

$$Pd\text{-}\ CH_2OHCHOHCH_2OH_{ads} + 2OH^{-} \rightarrow Pd\text{-}\ CH_2OHCHOHCHO_{ads} + 2H_2O + 2e^{-} \quad (6.6)$$

$$Pd\text{-}\ CH_2OHCHOHCHO_{ads} + 3OH^{-} \rightarrow Pd\text{-}\ CH_2OHCHOHCO_2^{-}{}_{ads} + 2H_2O + 2e^{-} \quad (6.7)$$

$$Pd\text{-}\ CH_2OHCHOHCO_2^{-}{}_{ads} + 2OH^{-} \rightarrow Pd\text{-}\ CHOCHOHCO_2^{-}{}_{ads} + 2H_2O + 2e^{-} \quad (6.8)$$

$$Pd\text{-}\ CHOCHOHCO_2^{-}{}_{ads} + 3OH^{-} \rightarrow Pd\text{-}\ CO_2^{-}CHOHCO_2^{-}{}_{ads} + 2H_2O + 2e^{-} \quad (6.9)$$

$$Pd\text{-}\ CO_2^{-}CHOHCO_2^{-}{}_{ads} + 2OH^{-} \rightarrow Pd\text{-}\ CO_2^{-}COCO_2^{-}{}_{ads} + 2H_2O + 2e^{-} \quad (6.10)$$

$$Pd\text{-}\ CO_2^{-}COCO_2^{-}{}_{ads} + Pd + 8OH^{-} \rightarrow 2(Pd\text{-}\ CO_3^{2-}{}_{ads}) + 4H_2O + 4e^{-} \quad (6.11)$$

6.1.2 Current Pd Nanomaterials

Palladium based nanomaterials can be used in the catalytic layers for DAFCs and palladium based nanomaterials have been created using many techniques. Physical techniques used include sputtering [222]–[225], ion or electron beam deposition [226], [227] and laser ablation [228], [229]. Hydrothermal techniques [230]–[232] and chemical reactions [233]–[237] have also been used. These techniques for palladium nanomaterial formation are summarised by Chen *et al.* [72].

This work uses electrochemical deposition to form a Pd nanomaterial. Electrochemical deposition of palladium based nanomaterials has been conducted without templates with techniques as simple as cyclic voltammetry [238]–[242], although this produces nanostructures with thicknesses of up to around 150 *nm* [238]. The technique often relies on another element such as Pt [239] and the depositions form non-periodic nanostructures [242]. Template free synthesis of Pd nanomaterials has been achieved by square wave voltammetry [243], [244], chronoamperometry [245]–[249], chronopotentiometry [250], [251], chronocoulometry [252] and by pulse deposition [253] (both chronoamperometry and chronopotentiometry). The produced Pd nanomaterials are

largely based off increased roughness, partial coverage of the substrate electrode (which sustainably limits the levels of Pd that can be created on a set area) or addiction of ionic liquids to the electrolyte.

Template-assisted growth of periodic Pd nanomaterials has been achieved with electrodeposition. The most common template used is anodised aluminium oxide (AAO) [254]–[257]. Wang *et al.* [254] successfully electrodeposited Pd in AAO producing a nanowire array with an average diameter of 80 *nm*. These nanowires were shown to have a 3 fold increase in the electrooxidation of ethanol by cyclic voltammetry studies compared to a non-templated Pd film. Porous anodic alumina (PAA) has also successfully been used to fabricate nanostructured Pd. Bai *et al.* [258] electrodeposited Pd into CdS modified PAA to produce Pd nanotubes with an average diameter of 200 *nm*. The tubes were used as part of a non-enzymatic glucose sensor, so the effectiveness for a fuel cell was not tested.

Bartlett *et al.* [60] used Type 1 hexagonal lyotropic liquid crystal phase of non-ionic surfactants $C_{16}EO_8$ and Brij® 56 as a template to fabricate $H_{1\text{-}e}$ nanostructured Pd films by electrodeposition. The pore diameters and wall thicknesses were about 3 *nm* each, whilst the pore centre to pore centre distance was measured to be 5.8 *nm*. No fuel cell related electrooxidation experiments were conducted.

In this work the Type 2 bicontinuous cubic lyotropic liquid crystal phases of phytantriol will be used in an attempt to fabricate an ordered Pd nanomaterial. The nanomaterial will be studied via SAXS and TEM for the presence of a nanostructure. The nanomaterial will then be tested against a non-templated Pd electrodeposited film and Pd black for the effectiveness of the catalysation of methanol, ethanol and glycerol in alkaline conditions.

6.2 Results and Discussion

The only prior electrodeposition of Pd through a lyotropic liquid crystal phase was conducted by Bartlett *et al.* [60], who electrodeposited Pd through $C_{16}EO_8$ to prepare nanostructured Pd using an electrolyte of 50 *mM* $(NH_4)_2PdCl_4$, 1 *M* NH_4Cl and 1 *M* HCl.

6.2.1 Non-templated Pd

Initially palladium studies were conducted in the absence of a template, this allowed for the electrolyte to be tested and non-templated films to be produced for comparison in catalytic studies.

6.2.1.1 Cyclic Voltammetry to Determine Deposition Potential

Firstly an electrolyte of 50 *mM* $(NH_4)_2PdCl_4$ and 1 *M* NH_4Cl dissolved in 1 *M* HCl, as used by Bartlett *et al.* [60], was purged with argon for 20 minutes to remove any dissolved oxygen prior to use. A cyclic voltammogram (CV) was recorded at a 2 *mm* gold disc electrode which is presented in Figure 6-2.

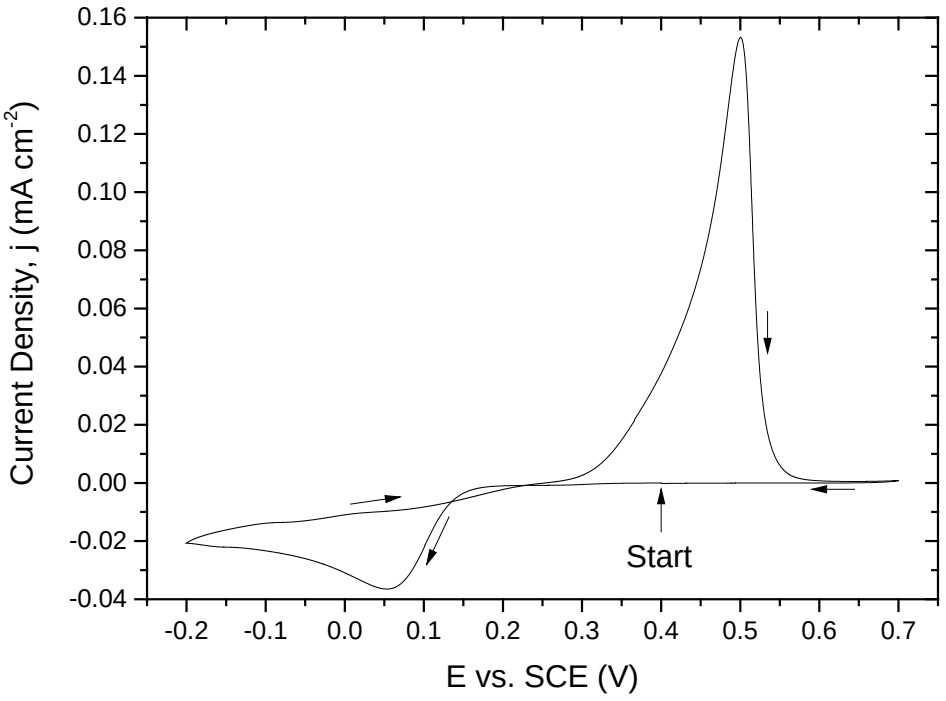

Figure 6-2 - Cyclic voltammogram recorded at 50 $mV\ s^{-1}$ in 50 *mM* $(NH_4)_2PdCl_4$ and 1 *M* NH_4Cl dissolved in 1 *M* HCl. The voltammogram started at a potential of +0.40 *V vs. SCE* where no reaction occurs and is scanned between -0.20 *V vs. SCE* and +0.70 *V vs. SCE*. The black arrows indicate the direction of the scan.

The peak at +0.06 *V vs. SCE* is attributed to the reduction of Pd^{2+} to Pd, with the peak at +0.50 *V vs. SCE* corresponding to the oxidation of Pd to Pd^{2+} as per Equation 6.12 and Equation 6.13 respectively. It was therefore decided to perform electrodeposition at +0.1 *V vs. SCE*. This potential was picked as it lay in the electron kinetic limited region of the deposition curve and therefore is more likely to avoid dendritic and non-adherent films than depositing in the diffusion limited region. The deposition substrate was Au on Si.

$$Pd^{2+} + 2\ e^- \rightarrow Pd\ (s) \qquad (6.12)$$

$$Pd\ (s) \rightarrow Pd^{2+} + 2\ e^- \qquad (6.13)$$

The current time transient for an electrodeposition can be seen in Figure 6-3.

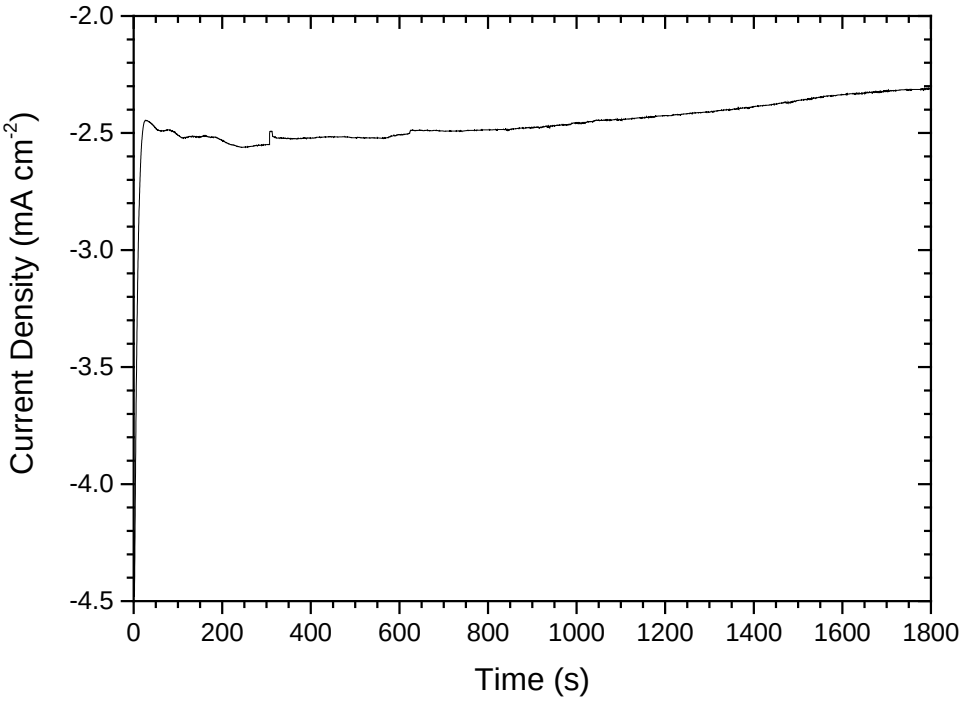

Figure 6-3 - Current time transient of a film electrodeposited from an electrolyte of 50 *mM* $(NH_4)_2PdCl_4$, 1 *M* NH_4Cl and 1 *M* HCl. The deposition potential was +0.1 *V vs. SCE* and the deposition time was 1800 s. The substrate was Au on Si with an area of 10 *mm* × 10 *mm*. The deposition charge was -4.43 *C*.

6.2.1.2 X-Ray Diffraction (XRD)

XRD was conducted on electrodeposited Pd films, the resulting pattern can be seen in Figure 6-4 with peaks assigned using the crystallography open database (COD) information card 1011110. The XRD pattern shown in Figure 6-4 shows 2 peaks that indicate the film is palladium with a (1 1 1) orientation, when compared to the COD stick powder pattern shown in Figure A-4.

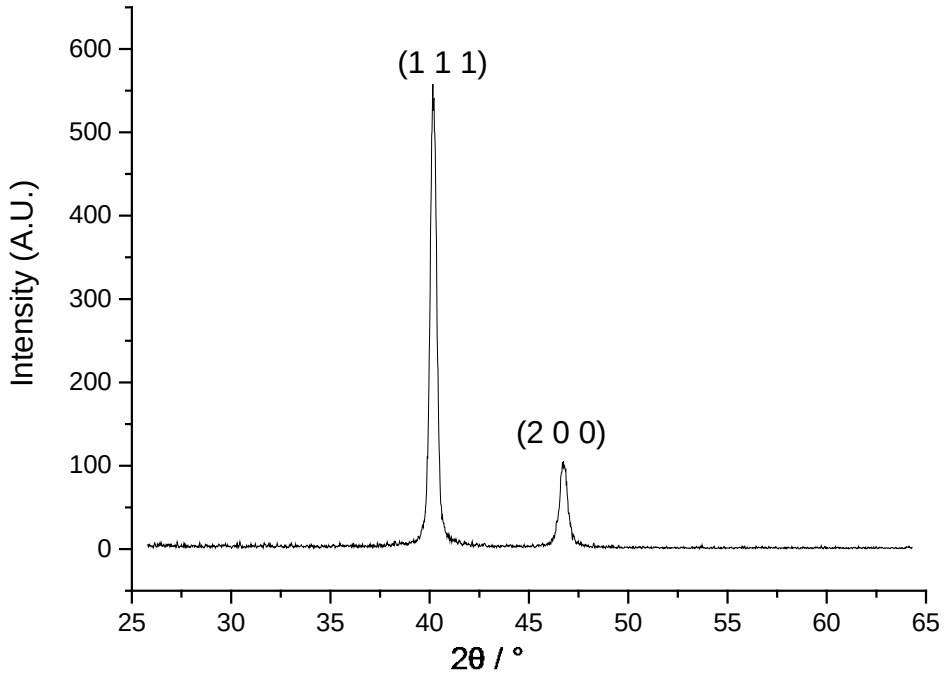

Figure 6-4 – Symmetric scan XRD pattern of a thin film deposited from a solution contained 50 *mM* $(NH_4)_2PdCl_4$, 1 *M* NH_4Cl and 1 *M* HCl. The deposition potential was 0.1 *V vs. SCE* and the deposition time was 1800 *s*. The deposition substrate was Au on Si. All peaks were fitted from the "Palladium" file in the PDXL software, No: 1011110, CSD: data_1011110(COD). The stick pattern for which can be found in Figure A-4. Here a Bruker C2 diffractometer was used with Cu Kα radiation.

6.2.1.3 Scanning Electron Microscopy (SEM) and Energy-Dispersive X-Ray Spectroscopy (EDX)

In order to confirm the deposit is purely Pd, SEM with EDX was conducted. A sample of SEM images of a non-templated film can be seen in Figure 6-5.

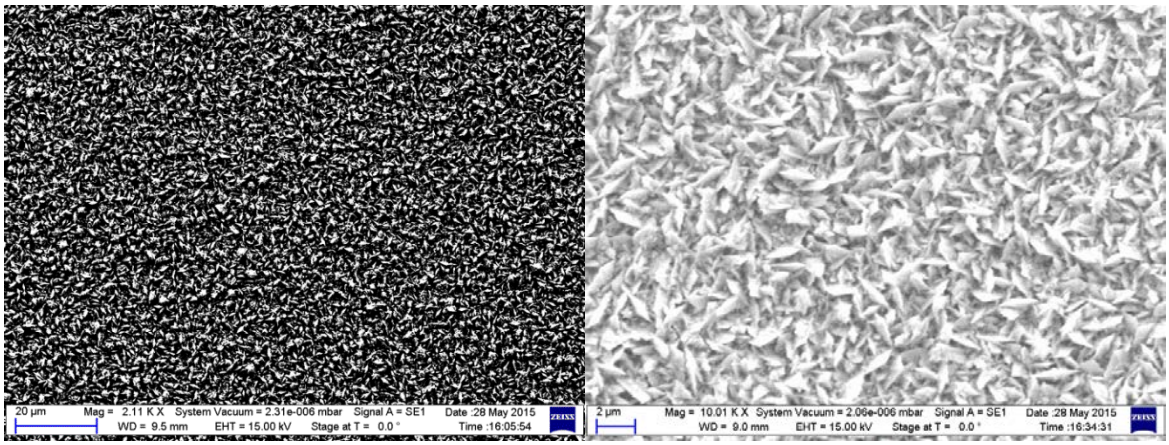

Figure 6-5 - SEM of a thin film deposited from a solution contained 50 *mM* $(NH_4)_2PdCl_4$, 1 *M* NH_4Cl and 1 *M* HCl. The deposition potential was 0.1 *V vs. SCE* and the deposition time was 1800 s. The substrate was Au on Si with an area of 10 *mm* × 10 *mm*. The deposition charge was -4.43 *C*.

The deposition charge of the sample shown in Figure 6-5 was -4.43 *C*. Using equation A.1 the thickness was estimated to be 2.032 *µm*, with the number of electrons in the reaction being 2, the molar mass of Pd being 106.42 $g\ mol^{-1}$ and the density of Pd being 12.023 $g\ cm^{-3}$. When the thickness of the film was measured using a profilometer, the thickness was determined to be 1.96 *µm*. This is in close agreement with the estimation of thickness based on charge assuming 100% faradic efficiency.

As is evident from Figure 6-5 the surface of the Pd film is rough which is typical for electrodeposition Pd. EDX confirmed that the deposited film composed of 100 atomic weight percent Pd. It was therefore decided that this electrolyte may also be suitable for making templated nanostructured Pd. Films made in the absence of a template can be used as a non-templated Pd standard to compare against any nanomaterial generated.

6.2.2 Nanostructured Pd

6.2.2.1 Cyclic Voltammetry to Determine Deposition Potential

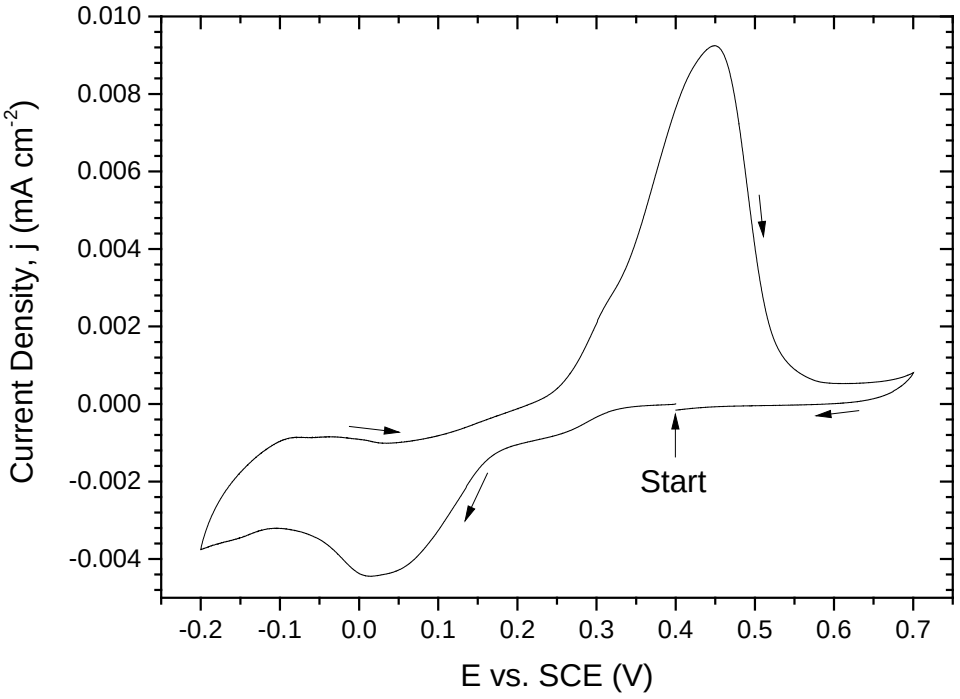

Figure 6-6 - Cyclic voltammogram recorded at 50 *mV* s^{-1} in 50 *mM* $(NH_4)_2PdCl_4$ and 1 *M* NH_4Cl dissolved in 1 *M* HCl with a phytantriol coated working electrode. The voltammogram started at a potential of +0.40 *V vs. SCE* where no reaction occurs and is scanned between -0.20 *V vs. SCE* and +0.70 *V vs. SCE*. The black arrows indicate the direction of the scan.

The CV in Figure 6-6 shows a reduction peak on the cathodic scan at +0.02 *V vs. SCE* and an oxidation peak on the anodic scan at +0.45 *V vs. SCE*. These peaks can be attributed to Equation 6.12 and Equation 6.13 respectively. These attributions were investigated by electrodepositing films and analysing them by XRD and EDX.

The peak positions in Figure 6-6 are similar to those seen for non-templated (+0.06 *V vs. SCE* and +0.50 *V vs. SCE*), however, the peak intensities have diminished by around a factor of 10 (e.g. templated reduction peak -0.004 *mA* cm^{-2}, non-templated reduction peak -0.037 *mA* cm^{-2}). This observation can be rationalised when considering the template is covering the working electrode, causing sections of the electrode to not be in contact with the aqueous electrolyte and also causing slower diffusion. The current time transient for an electrodeposition can be seen in Figure 6-7.

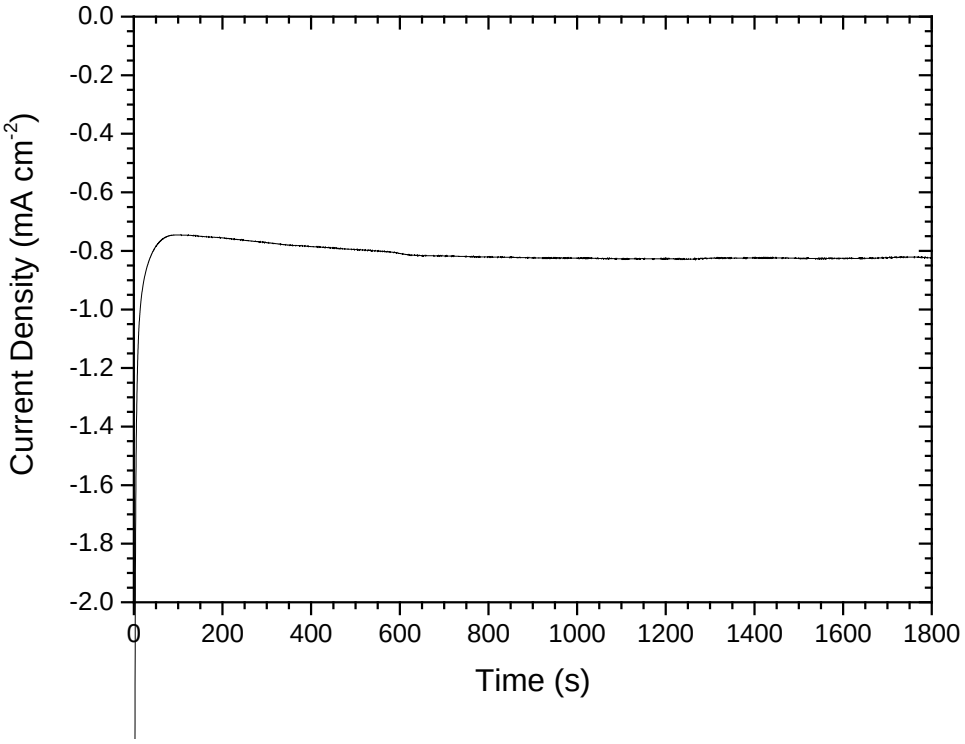

Figure 6-7 - Current time transient of a film electrodeposited through a phytantriol template from an electrolyte of 50 *mM* $(NH_4)_2PdCl_4$, 1 *M* NH_4Cl and 1 *M* HCl. The deposition potential was +0.1 *V vs. SCE* and the deposition time was 1800 s. The substrate was Au on Si with an area of 10 *mm* × 10 *mm*. The deposition charge was -1.47 *C*.

6.2.2.2 X-Ray Diffraction (XRD)

To confirm whether the deposit corresponds to Pd, XRD of an electrodeposited film was conducted. The results of this XRD can be seen in Figure 6-8.

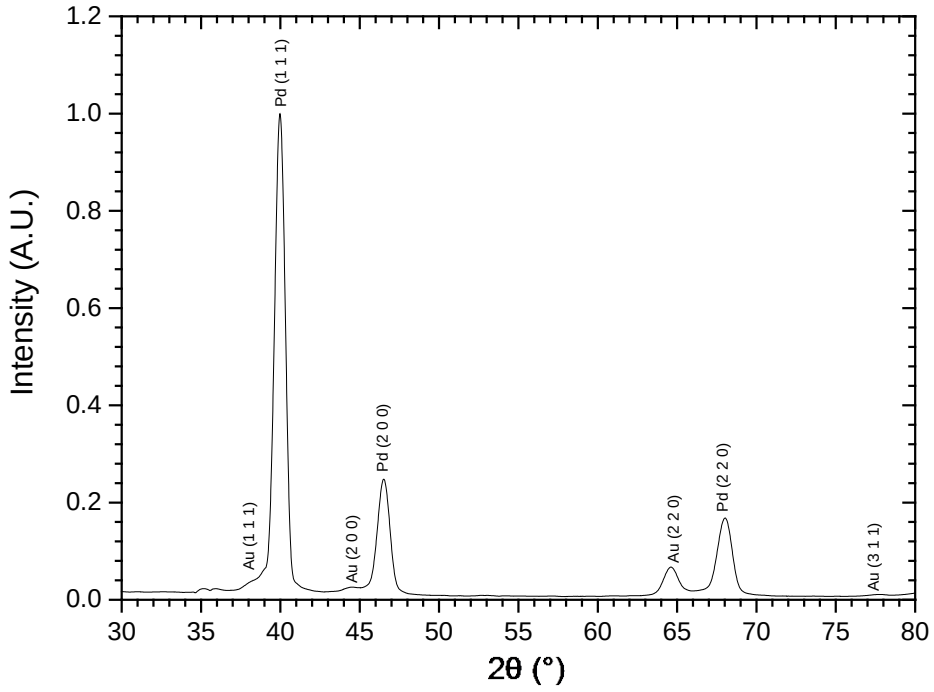

Figure 6-8 – GI XRD pattern of a thin film of Pd deposited from a solution contained 50 *mM* $(NH_4)_2PdCl_4$, 1 *M* NH_4Cl and 1 *M* HCl through a phytantriol template. The deposition potential was +0.1 *V vs. SCE* and the deposition time was 1800 *s*. The substrate was Au on Si. Pd peaks were fitted from the "Palladium" file in the PDXL software, No: 1011110, CSD: data_1011110(COD). The stick pattern for which can be found in Figure A-4. Au peaks where they are fitted from the "Gold" file in PDXL software, No: 9013039, CSD: data_9013039(COD).

The diffraction pattern seen in Figure 6-8 is in good alignment with that of the crystallographic open database (COD) file 1011110 "Palladium" (the stick pattern for which can be found in Figure A-4), the gold peaks are observed due to the deposition substrate.

6.2.2.3 Scanning Electron Microscopy (SEM) and Energy-Dispersive X-Ray Spectroscopy (EDX)

As was the case with non-templated Pd electrodeposits, the electrodeposits deposited through phytantriol had an optical appearance of a silver thin film that was well adherent. To investigate the micro-structure, the films were investigated by SEM and EDX was conducted to analyse the composition. SEM results can be seen in Figure 6-9.

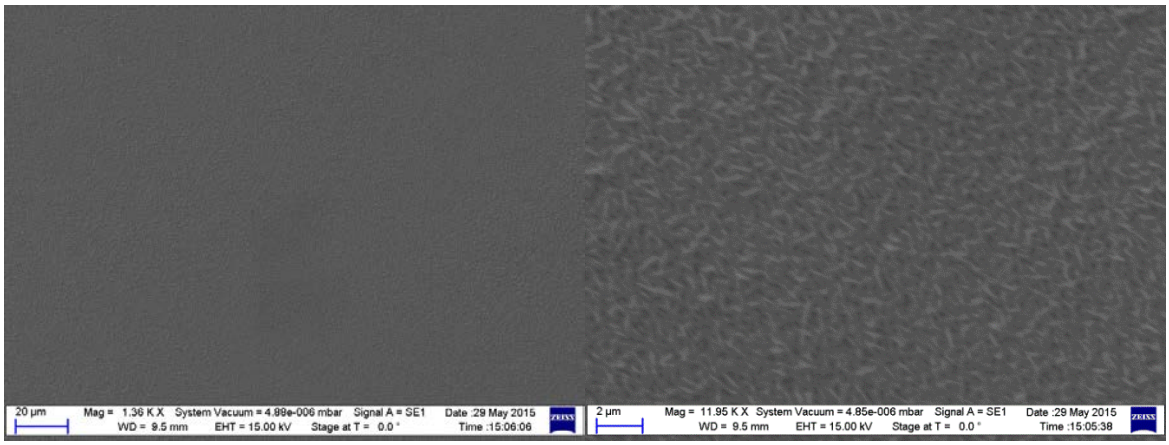

Figure 6-9 - SEM of a thin film deposited from a solution contained 50 *mM* $(NH_4)_2PdCl_4$, 1 *M* NH_4Cl and 1 *M* HCl, through a phytantriol template. The deposition was potential was +0.1 *V vs. SCE* and the deposition time was 1800 *s*. The substrate was Au on Si.

From Figure 6-9 the morphology of the deposit can be seen to be rough on the micro scale, as was seen for non-templated Pd (Figure 6-5). The films fully cover the underlying substrate without any defects or holes. EDX of the film showed the composition to be 100% Pd. Hence the EDX data coupled with XRD data confirms that the electrodeposit is that of pure palladium.

6.2.2.4 Small Angle X-Ray Scattering (SAXS)

6.2.2.4.1 Phytantriol and Electrolyte SAXS Phase Study

To see what liquid crystal phase is formed when a phytantriol coated surface is immersed into the Pd electrolyte, a phytantriol lined 2.0 *mm* Quartz diameter capillary (2.3.6.1) was filled with the Pd electrolyte of 50 *mM* $(NH_4)_2PdCl_4$, 1 *M* NH_4Cl and 1 *M* HCl in Milli-Q deionised water. This was left to equilibrate for 30 minutes, before being placed in front of the SAXS beam. The resultant 2D and 1D radial integrated profiles can be seen in Figure 6-10.

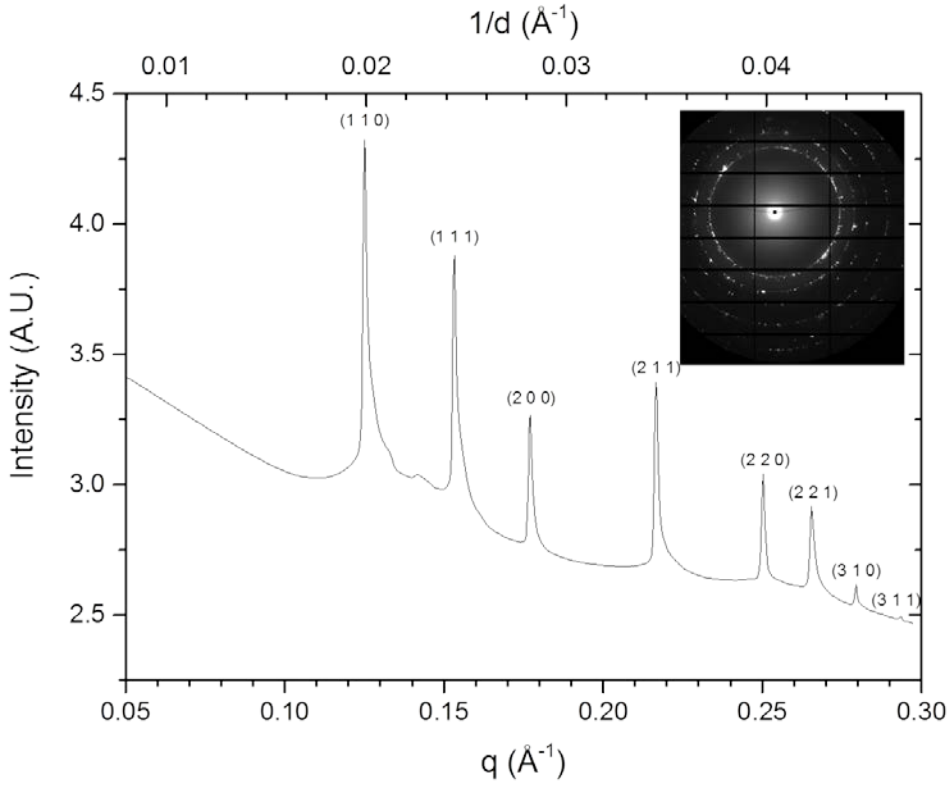

Figure 6-10 - 1D integrated SAXS pattern of a phytantriol lined capillary filled with 50 *mM* $(NH_4)_2PdCl_4$ and 1 *M* HN_4Cl in 1 *M* HCl. The corresponding 2D pattern is included in the upper right segment.

From the line spacing ratio of the 8 peaks seen in Figure 6-10, the phase can be indexed as double diamond [180]. The lattice parameter can be calculated to be 71.0 (± 0.5) *Å* (B.3). This is consistent with observations that have been seen for Pt [57], bismuth telluride (4.2.4.1) and bismuth sulphide (5.2.2.4.1).

6.2.2.4.2 Phase of Electrodeposited Film SAXS Study

Pd films electrodeposited through the Q_{224} "double diamond" phase of phytantriol were placed in the SAXS beam to investigate what nanostructure had formed. A resulting 2D diffraction pattern and the 1D integration can be seen in Figure 5-12.

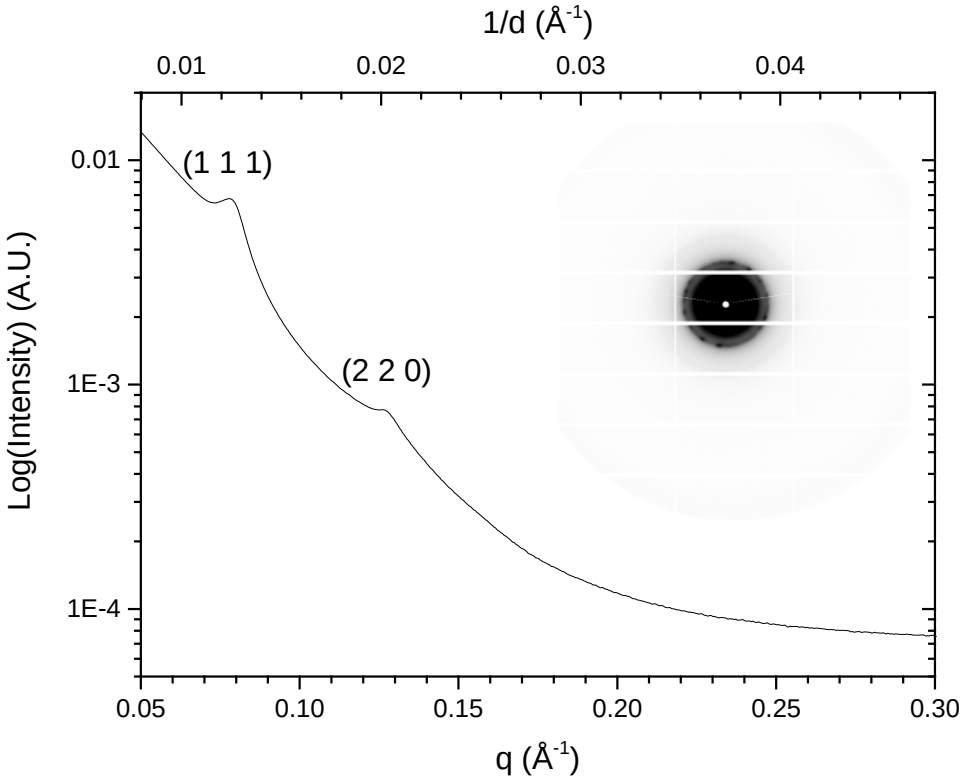

Figure 6-11 - 1D integrated SAXS pattern of a Pd thin film electrodeposited on a phytantriol coated Au DVD. The electrolyte was 50 *mM* $(NH_4)_2PdCl_4$ and 1 *M* HN_4Cl in 1 *M* HCl and the deposition conditions were 1800 *s* at +0.1 *V vs SCE*. The corresponding 2D pattern is included in the upper right segment.

The first two peaks of the single diamond geometry can be observed in Figure 6-11, which give a lattice parameter of 140.0 (± 4.6) *Å* (B.3). This is within error double the lattice parameter of phytantriol in the electrolyte (71.0 (± 0.5) *Å*). This is consistent with electrodeposition occurring in only one of two possible water channels of the double diamond structure, resulting in a single diamond nanostructure with a doubled lattice parameter due to a reduction in symmetry. These results are in line with those seen for Pt [57] and bismuth sulphide (5.2.2.4.2).

6.2.2.5 Transmission Electron Microscopy (TEM)

To further confirm the SAXS results seen for electrodeposited Pd through phytantriol, transmission electron microscopy (TEM) was conducted to try and image the nanostructure. A selection of resulting images can be seen in Figure 6-12.

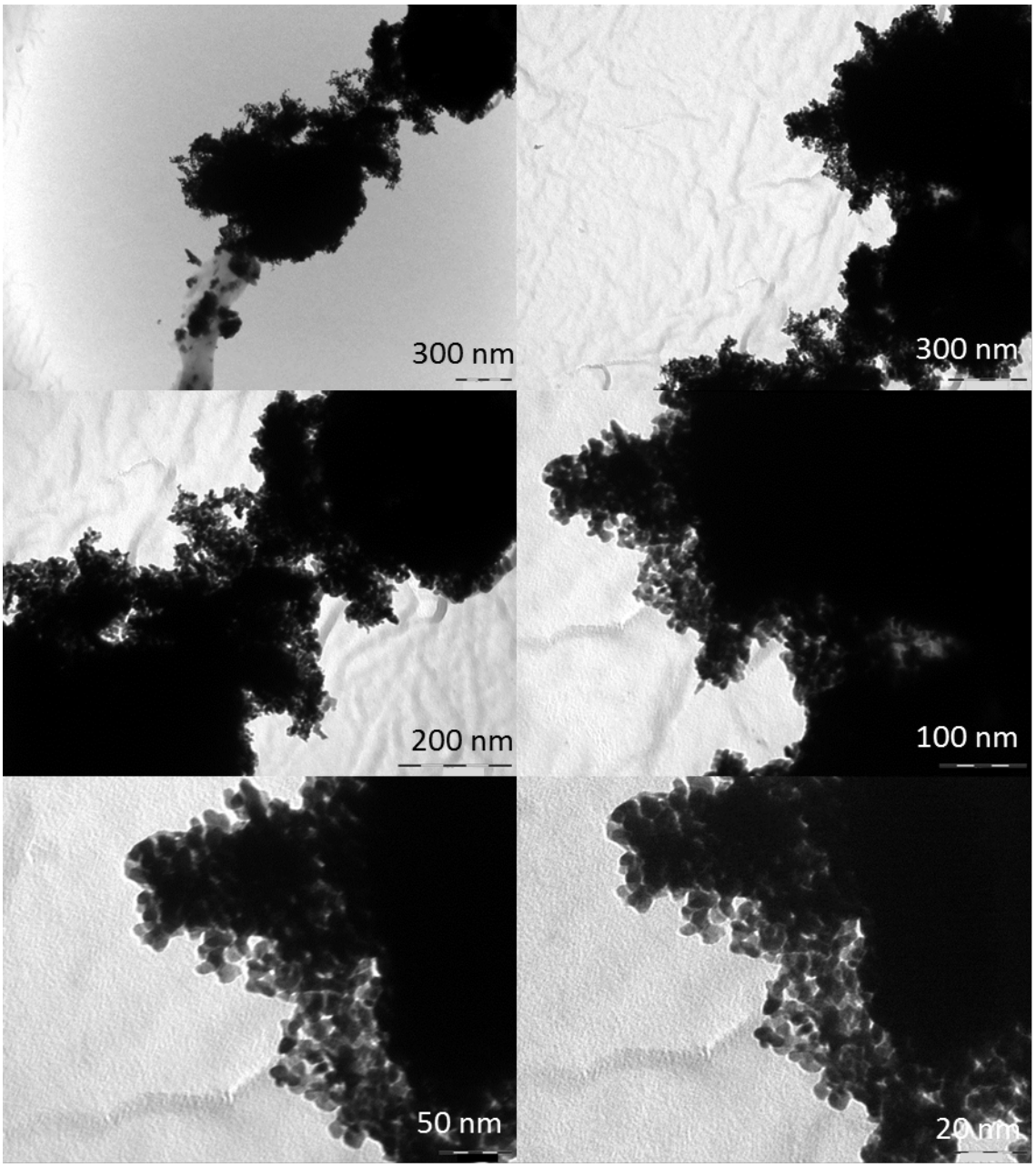

Figure 6-12 – TEM images of sections of a thin film deposited from a solution containing 50 *mM* $(NH_4)_2PdCl_4$, 1 *M* NH_4Cl and 1 *M* HCl, through a phytantriol template. The deposition was potential was 0.1 *V vs. SCE* and the deposition time was 1800 s. The substrate was a 2 *mm* diameter Au disc electrode.

Whilst a nanostructure can be seen in Figure 6-12, there is no clear sign of an ordered structure as was seen for bismuth sulphide in Figure 5-13. Nonetheless there is a clear nanostructure. The structure shown in Figure 6-12 is still branched, which is consistent with a Q_{227} "single diamond" structure. The length scales are also in line with that seen in Figure 5-13, which is also consistent with a Q_{227} "single diamond" nanostructure with a lattice parameter of 71.0 (± 0.5) *Å* which was shown by SAXS (6.2.2.4.2). The process of TEM sample preparation is quite intrusive, which may well have caused damage to the samples. The SAXS peaks are also less well defined for Pd

(Figure 6-11), than was observed for bismuth sulphide (Figure 5-12). These are the likely explanations for why no clear repeating pattern can be observed.

6.2.3 Cyclic Voltammetry to Determine Surface Area

A further way to prove that a nanostructure is present (in the Pd films electrodeposited through phytantriol) is to conduct CVs in H_2SO_4 to measure the electroactive surface area. Controls can also be done to compare surface area to films deposited in the absence of phytantriol and a comparison to a high surface area Pd can be made, in this case Pd black. The resulting CVs can be seen in Figure 6-13. Five scans of each can be seen in Figure D-1, Figure D-2 and Figure D-3. Figure 6-13 compares the second scan of each.

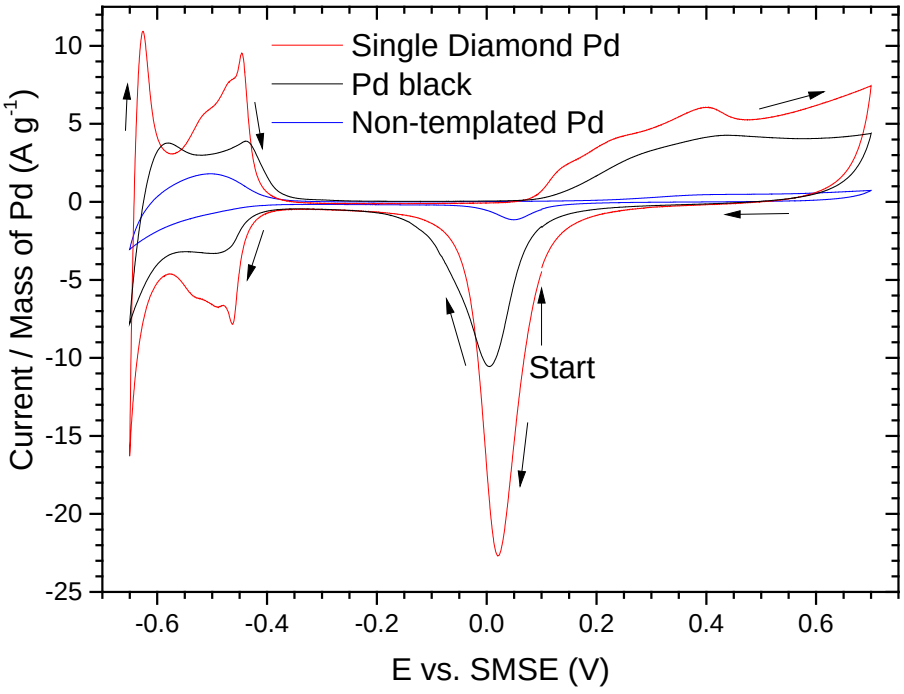

Figure 6-13 - Cyclic voltammogram of Single Diamond Pd, Pd black and non-templated Pd in 1 *M* H_2SO_4 recorded at 20 *mV* s^{-1}. The voltammogram was measured at room temperature and started at a potential of +0.1 *V vs. SMSE* where no reaction occurred and is scanned between -0.65 *V vs. SMSE* and 0.7 *V vs. SMSE*, for 5 scans. Here all the second scans are compared so full oxygen stripping can be observed. The black arrows indicate the direction of the scan. The non-templated Pd and single diamond Pd were deposited on a 2 *mm* polished gold disc electrode, from an electrolyte of 50 *mM* $(NH_4)_2PdCl_4$, 1 *M* NH_4Cl and 1 *M* HCl. The deposition potential was +0.1 *V vs. SMSE* and deposition was halted once 14.4 *mC* of charge was passed. 0.385 *mg* of Pd

black was applied onto a 2 *mm* polished gold disc electrode by pipetting on 5 *μL* of an ink consisting of 80 *mg* Pd black (Alfa Aesar, 99.9%), 40 *μL* Nafion® 117 solution (Aldrich) and 1000 *μL* deionised water and leaving in an oven at 100 °C for at least 15 minutes. Current was normalised by dividing by the mass of Pd on the electrode. For electrodeposited films this was calculated assuming 100% faradaic efficiency.

For each Pd type hydrogen sorption can be seen on the cathodic scan from -0.40 *V vs. SMSE* onwards and hydrogen desorption can be seen on the return anodic scan up to -0.30 *V vs. SMSE*. Whilst for non-templated Pd no clear hydrogen adsorption peak is seen, there are distinct hydrogen adsorption peaks for Pd black and single diamond Pd. Pd black has a single hydrogen adsorption peak at -0.50 *V vs. SMSE* that can be seen on the cathodic scan, indicating a single surface environment (which is consistent with a sphere). For single diamond Pd, however, peaks for hydrogen adsorption can be seen at -0.46 *V vs. SMSE*, -0.49 *V vs. SMSE* and -0.53 *V vs. SMSE* on the cathodic scan indicating at least 3 different surface environments. This is in line with single diamond architecture which has different surface environments. Hydrogen absorption can be seen for non-templated Pd, Pd black and single diamond Pd at -0.65 *V vs. SMSE*. Hydrogen desorption peaks can be seen for every hydrogen sorption peak on the anodic scan. The formation of a surface oxide can be seen from +0.05 *V vs. SMSE* on the anodic scan for all 3 Pds, and on the return cathodic scan the stripping of the surface oxide gives rises to peaks that can be seen between +0.4 *V vs. SMSE* and -0.3 *V vs. SMSE*.

Distinctive hydrogen adsorption peaks are a sign of nanostructured Pd, and were also observed for $H_{1\text{-}e}$ nanostructured Pd by Bartlett *et al.* [60]. The greatly enhanced peak currents seen for single diamond Pd over non-templated Pd are indicative of a greatly enhanced electroactive surface area.

Surface area was deduced using the oxygen striping peaks. The oxygen striping peaks were integrated between +0.4 *V vs. SMSE* and -0.3 *V vs. SMSE*, and a conversion factor of 424 $\mu C\ cm^{-2}$ derived by Rands and Woods [259] was used to establish the electroactive surface area. For a deposition charge of 14.3 *mC* for Pd, the surface area was shown to be 0.16457 cm^{-2} for non-templated Pd, whilst the surface area was shown to be 2.21349 cm^{-2} for Pd deposited through phytantriol. This shows a 13.5 × increase in surface area simply by using a phytantriol template. The surface area per gram for non-templated Pd was shown to be 2.11 $m^2\ g^{-1}$, whilst for Pd black the surface area per gram was 17.8 $m^2\ g^{-1}$ (which is expected as the Pd black was described as having a surface area of 20 $m^2\ g^{-1}$ when sold), and for Pd deposited through phytantriol the surface area per gram was shown to be 28.3 $m^2\ g^{-1}$. Again this shows a 13.5 × increase simply by

using a phytantriol template, whilst also interestingly showing the surface area per gram of Pd deposited through phytantriol to be 59% greater than that for Pd black.

Surface area experiments were conducted for phytantriol templated palladium at several deposition charges between 9 *mC* and 50 *mC*. From these experiments roughness factors (Rf) were determined by dividing the electrochemically determined surface area, by the underlying geometric surface area of the substrate electrode. Rf was observed to be linear with deposition charge, as shown in Figure 6-14. This linear relationship demonstrates a uniformly accessible nanostructure. From the gradient of the plot the specific electrochemical surface area to mass ratio and the surface area to volume ratio were estimated to be 30.8 ±0.4 $m^2\ g^{-1}$ and 3.66 (±0.04) × $10^6\ cm^2\ cm^{-3}$ respectively, assuming 100% faradaic efficiency. Although these are lower than 91 $m^2\ g^{-1}$ and 1.1 × $10^7\ cm^2\ cm^{-3}$ observed for $H_{1\text{-}e}$ Pd [60], here we show scalability up to at least a deposition charge density of 1.59 $C\ cm^{-2}$, whereas Bartlett *et al.* [60] only used a deposition charge density of 0.89 $C\ cm^{-2}$. Here we also use substrate electrodes with 4 × the geometric surface area. Therefore in absolute terms we demonstrate the ability to form a single diamond nanostructure using phytantriol which has an accessible Pd surface area over 7 × greater in size than was seen for a $H_{1\text{-}e}$ Pd nanostructure created using $C_{16}EO_8$ [60]. Pd catalytic activity towards fuel cells is also determined by facets, not simply surface area alone [72]. This could lead to a single diamond Pd nanostructure having greater catalytic effect per mass than that of H_{1e} Pd nanostructure.

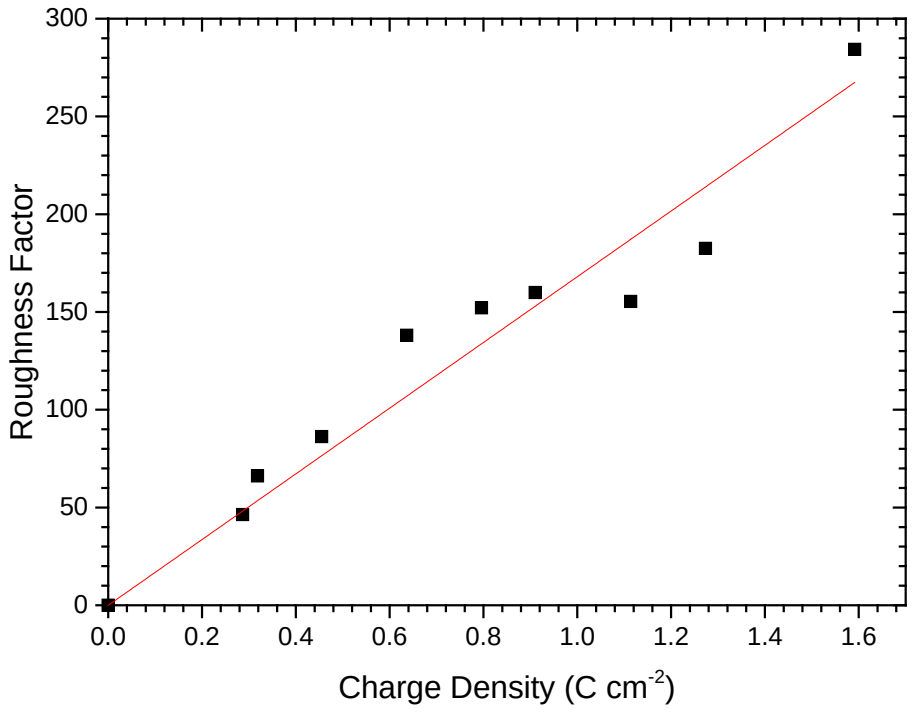

Figure 6-14 – Roughness factor was calculated by dividing the calculated surface area from CVs in 1 *M* H_2SO_4 by the surface area of the substrate electrode. Charge density was calculated by dividing the charge passed whilst electrodepositing the single diamond Pd by the surface area of the underlying electrode. The deposition substrate was a 3 *mm* diameter glassy carbon electrode.

6.2.4 Application in Fuel cells

Whilst a large surface area Pd has been established, there is not yet an indication of whether this is more effective than commercially available Pd for fuel cell applications. In this section single diamond Pd will be tested against non-templated Pd and Pd black for applications in methanol, ethanol and glycerol fuel cells.

6.2.4.1 Methanol Fuel Cells

Single diamond Pd was compared to non-templated Pd and Pd black in effectiveness to catalyse the electrooxidation of methanol by conducting cyclic voltammetry in 1 *M* methanol and 1 *M* KOH. The results are shown in Figure 6-15.

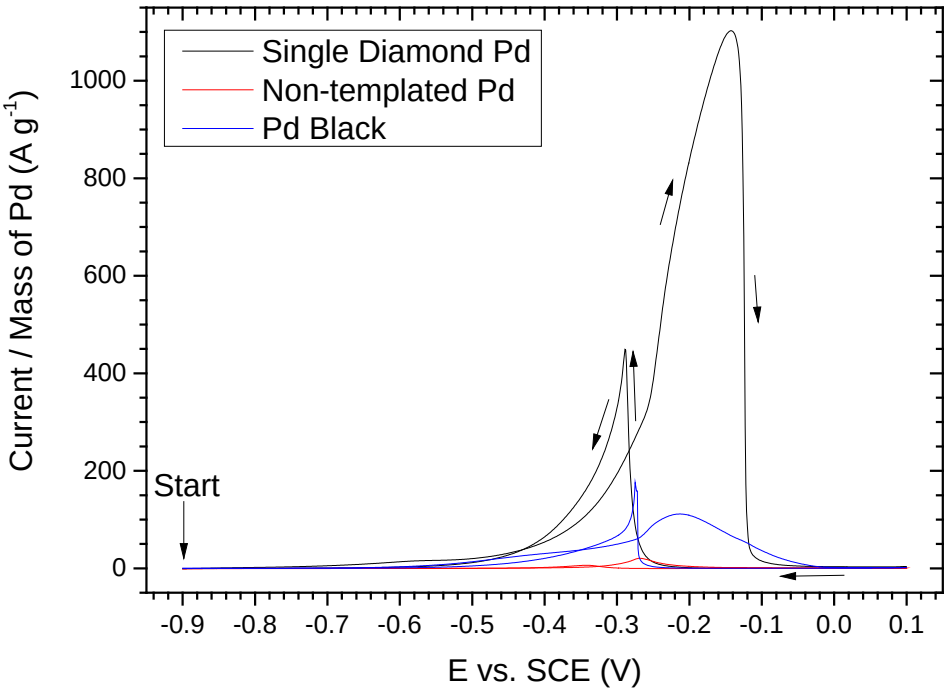

Figure 6-15 – Cyclic voltammetry of Single Diamond Pd, Pd black and non-templated Pd in 1 *M* methanol and 1 *M* KOH, recorded at 10 $mV\ s^{-1}$. The voltammogram was measured at room temperature and started at a potential of -0.90 *V vs. SCE* where no reaction occurred and is scanned between -0.90 *V vs. SCE* and +0.10 *V vs. SCE*, for 250 scans. Here the first scan is shown for comparison. The cell volume was 100 *mL* and the cell was covered to prevent evaporation. Current was normalised by dividing by the mass of Pd on the electrode. For electrodeposited films this was calculated assuming 100% faradaic efficiency.

From Figure 6-15 single Diamond Pd is shown to exhibit a peak current on the anodic scan of 1100 A g^{-1}, which is 10 × larger than 110 $A\ g^{-1}$ shown by Pd black and over 50 × larger than 21 $A\ g^{-1}$ shown by non-templated Pd. The peak current of 1100 $A\ g^{-1}$ is larger than is seen in the literature for Pd electrooxidation of methanol. Yin *et al.* [260] report a value of 210.5 $A\ g^{-1}$ for 4.6 *nm* particle size Pd and up to 950.6 $A\ g^{-1}$ with 70% Au incorporation. Yin *et al.* [260] use a scan rate of 50 $mV\ s^{-1}$ which makes the value for single diamond Pd more impressive (peak current $\alpha\ v^{0.5}$ [261], [262]). 1100 $A\ g^{-1}$ is also higher than 40 $A\ g^{-1}$ (10 $mV\ s^{-1}$) reported for Pd nanoflowers [263], higher than 680 $A\ g^{-1}$ (20 $mV\ s^{-1}$) reported for Ni at Pd on multiwall carbon nanotubes [261] and higher than that even shown for Pt in acidic conditions, 600 $A\ g^{-1}$ (50 $mV\ s^{-1}$) [264]. These results are extremely encouraging, as they show single diamond Pd is very effective at the electrooxidation of methanol.

The peak current is however strongly limited by mass transport for all three Pd catalysts in Figure 6-15. To allow for a more reasonable comparison of the mass activities, currents were extracted at -0.4 *V vs. SCE*. These currents can be seen in Table 6-1. Currents are also shown for surface specific activity where the current is normalised against surface area instead of mass. Figure D-4 shows the cyclic voltammograms normalised against surface area.

Table 6-1 – Comparison of mass activity and surface specific activity at -0.4 *V vs. SCE* in the surface kinetic limited regime from cyclic voltammetry of Single Diamond Pd, Pd black and non-templated Pd in 1 *M* methanol and 1 *M* KOH, recorded at 10 $mV\ s^{-1}$.

	Current / Mass ($A\ g^{-1}$)	Current / Surface Area ($A\ cm^{-2}$)
Single Diamond Pd	54.02774	1.75415
Non-templated Pd	0.93813	0.62183
Pd Black	30.37123	1.70625

From Table 6-1 single diamond Pd is seen to have the highest mass activity, but the surface specific activity is in line with that shown for Pd black. This means the increase in mass activity of single diamond Pd is due to only the increase in the surface area and not an increase in intrinsic surface specific activity of the Pd. These results still show however, that less mass of Pd is needed to perform the same level of methanol electrooxidation when in single diamond form compared to the Pd black form shown in this work.

The durability of the structure needs to be tested, to see if the structure is viable. This was tested in 2 ways. CVs were run for 250 scans and chronoamperometry was performed, which would test for the long term performance of the single diamond nanostructure. The 250 scans can be seen in Figure 6-16.

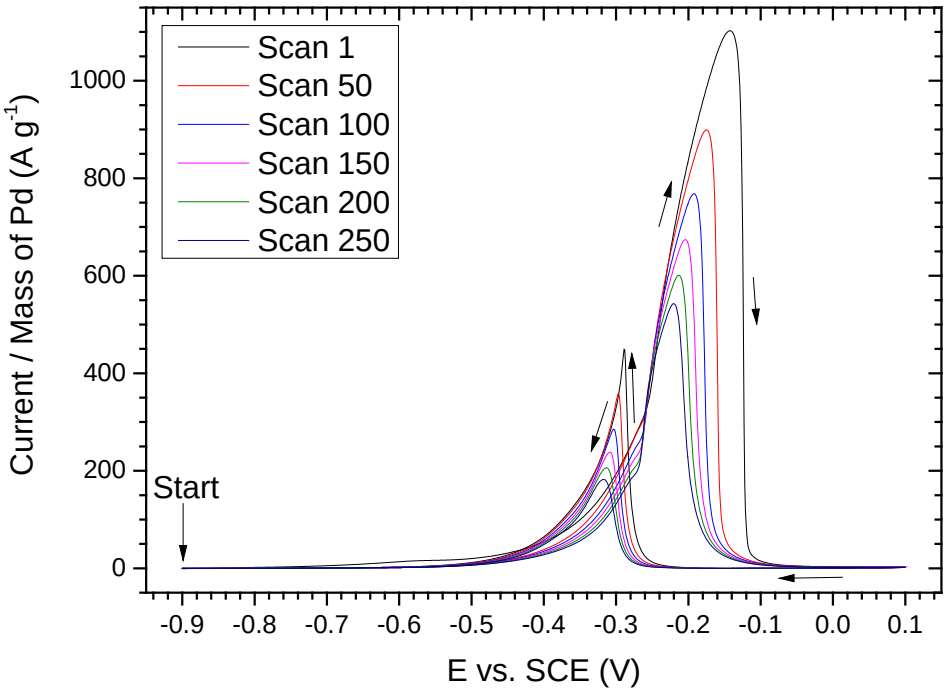

Figure 6-16 - Cyclic voltammetry of Single Diamond Pd in 1 *M* methanol and 1 *M* KOH, recorded at 10 $mV\ s^{-1}$. The voltammogram was measured at room temperature and started at a potential of -0.90 *V vs. SCE* where no reaction occurred and is scanned between -0.90 *V vs. SCE* and +0.10 *V vs. SCE*, for 250 scans. Here every 50th scan is shown for ease of viewing. The cell volume was 100 *mL* and the cell was covered to prevent evaporation. Current was normalised by dividing by the mass of Pd on the electrode. Pd mass was calculated assuming 100% faradaic efficiency during electrodeposition, with deposition charge being 20 *mC*.

Whilst the peak current consistently decays over the course of the 250 scans, the same trend is seen for Pd black (Figure D-6) and non-templated Pd (Figure D-5). The peak current after 250 scans is seen to be 544 $A\ g^{-1}$ for single diamond Pd, higher than that for Pd black (89 $A\ g^{-1}$) and for non-templated Pd (18 $A\ g^{-1}$). Therefore single diamond Pd is seen to be as durable as other Pd types studied in this work and to have a higher catalytic efficiency towards methanol electrooxidation after numerous scans. Chronoampometry (as seen in Figure 6-17) also shows a consistently higher rate of methanol electrooxidation per gram over time when using single diamond Pd compared to both non-templated Pd and Pd black. Figure D-8 shows the chronoampometry normalised against surface area.

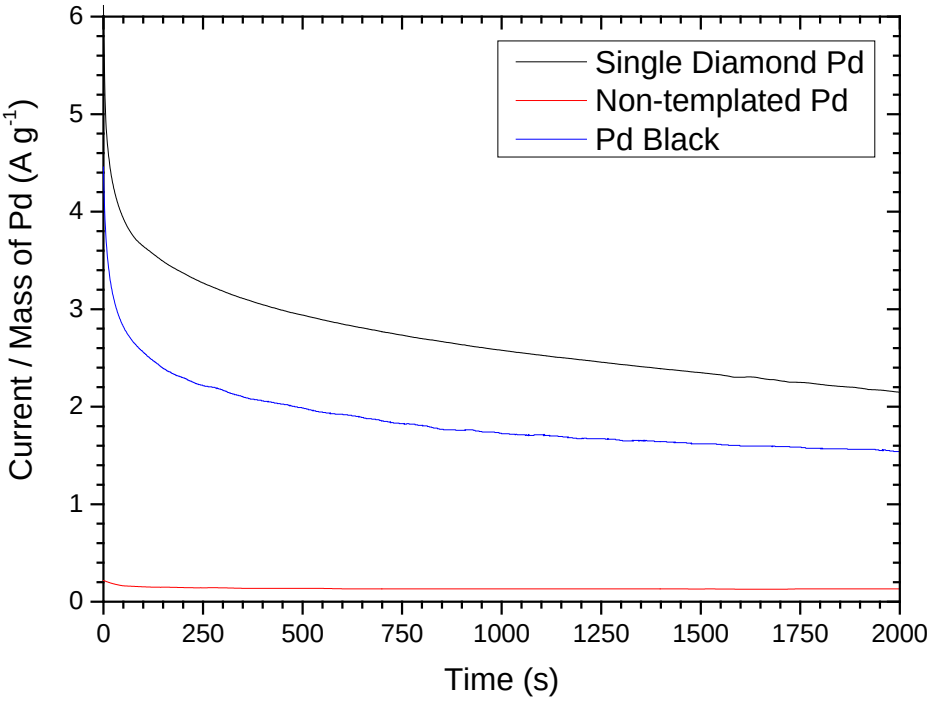

Figure 6-17 - Chronoampometry of Single Diamond Pd, Pd black and non-templated Pd in 1 *M* methanol and 1 *M* KOH, recorded at +0.30 *V vs. SCE*. The experiment was conducted at room temperature. The cell volume was 100 *mL* and the cell was covered to prevent evaporation. Current was normalised by dividing by the mass of Pd on the electrode. For electrodeposited films this was calculated assuming 100% faradaic efficiency.

6.2.4.2 Ethanol Fuel Cells

Single diamond Pd was compared to non-templated Pd and Pd black in effectiveness to catalyse the electrooxidation of ethanol by conducting cyclic voltammetry in 0.1 *M* ethanol and 0.1 *M* NaOH. The results are shown in Figure 6-15. Here a lower pH is used compared to the Methanol Fuel Cells section (6.2.4.1) because lowering the pH (by lowering the concentration of OH^-) gives

conditions that more easily facilitate the complete oxidation of ethanol to CO_2 [77], [265].

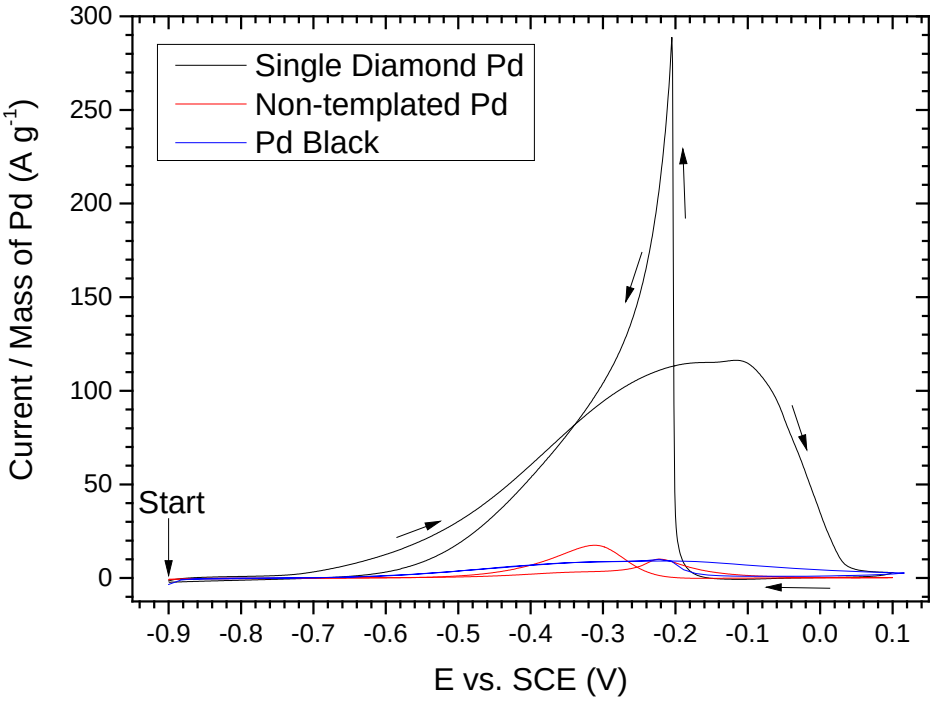

Figure 6-18 - Cyclic voltammetry of Single Diamond Pd, Pd black and non-templated Pd in 0.1 *M* ethanol and 0.1 *M* NaOH, recorded at 10 $mV\ s^{-1}$. The voltammogram was measured at room temperature and started at a potential of -0.90 *V vs. SCE* where no reaction occurred and is scanned between -0.90 *V vs. SCE* and +0.10 *V vs. SCE*, for 250 scans. Here the first scan is shown for comparison. The cell volume was 100 *mL* and the cell was covered to prevent evaporation. Current was normalised by dividing by the mass of Pd on the electrode. For electrodeposited films this was calculated assuming 100% faradaic efficiency.

From Figure 6-18 single Diamond Pd is shown to exhibit a peak current on the anodic scan of 116 $A\ g^{-1}$, which is over 11 × larger than 10 $A\ g^{-1}$ shown by Pd black and non-templated Pd. The peak current of 116 $A\ g^{-1}$ is similar to than seen for tetrahedral Pd (151 $A\ g^{-1}$) in the literature for Pd electrooxidation of ethanol [243]. These results are encouraging, as they show single diamond Pd is effective for the electrooxidation of ethanol.

The peak current is however strongly limited by mass transport for all three Pd catalysts in Figure 6-18. To allow for a more reasonable comparison of the mass activities, currents were extracted at -0.4 *V vs. SCE*. These currents can be seen in Table 6-2. Currents are also shown for surface specific activity where the current is normalised against surface area instead of mass. Figure D-8 shows the cyclic voltammograms normalised against surface area.

Table 6-2 - Comparison of mass activity and surface specific activity at -0.4 *V vs. SCE* in the surface kinetic limited regime from cyclic voltammetry of Single Diamond Pd, Pd black and non-templated Pd in 0.1 *M* ethanol and 0.1 *M* NaOH, recorded at 10 $mV\ s^{-1}$.

	Current / Mass ($A\ g^{-1}$)	Current / Surface Area ($A\ cm^{-2}$)
Single Diamond Pd	60.33125	1.95881
Non-templated Pd	2.06312	1.36753
Pd Black	7.2012	0.40456

From Table 6-2 single diamond Pd is seen to have the highest mass activity, the surface specific activity is also seen to be the highest. This means the increase in mass activity of single diamond Pd is due to an increase in the surface area and an increase in intrinsic surface specific activity of the Pd. These results show that less Pd is needed to perform the same level of ethanol electrooxidation when in single diamond form compared to the Pd black form shown in this work.

The durability of the structure needs to be tested, to see if the structure is viable. This was tested in 2 ways. CVs were run for 250 scans and chronoampometry was performed, these would test for the long term performance of the single diamond Pd nanostructure. The 250 scans can be seen in Figure 6-19.

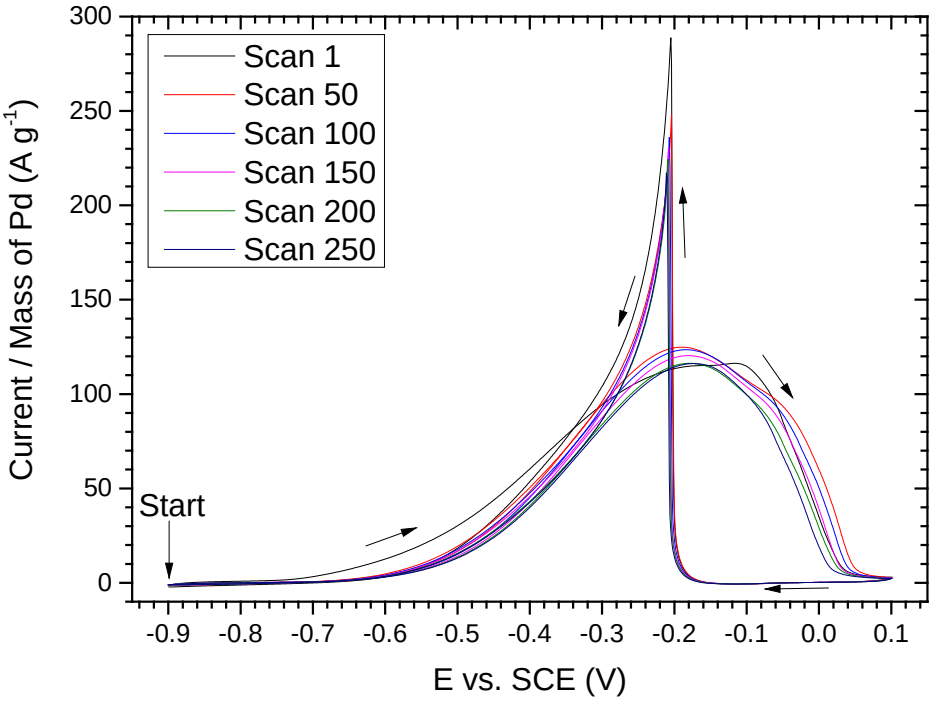

Figure 6-19 - Cyclic voltammetry of Single Diamond Pd in 0.1 *M* ethanol and 0.1 *M* NaOH, recorded at 10 $mV\ s^{-1}$. The voltammogram was measured at room temperature and started at a potential of -0.90 *V vs. SCE* where no reaction occurred and is scanned between -0.90 *V vs. SCE* and +0.10 *V vs. SCE*, for 250 scans. Here every 50th scan is shown for ease of viewing. The cell volume was 100 *mL* and the cell was covered to prevent evaporation. Current was normalised by dividing by the mass of Pd on the electrode. Pd mass was calculated assuming 100% faradaic efficiency during electrodeposition, with deposition charge being 20 *mC*.

Whilst the peak current consistently decays over the course of the 250 scans the drop is not very steep, Pd black (Figure D-9) is seen to decay far steeper after 50 scans and whilst non-templated Pd (Figure D-10) is seen to initially improve performance (most likely due to roughening of the surface) the performance is seen to consistently decay after 50 scans. The peak current after 250 scans is seen to be 116 $A\ g^{-1}$ for single diamond Pd, higher than that for Pd black (0.5 $A\ g^{-1}$) and for non-templated Pd (10 $A\ g^{-1}$). Therefore single diamond Pd is seen to be as durable as other Pd types studied in this work and to have a higher catalytic efficiency towards ethanol electrooxidation after numerous scans. Chronoampometry (as seen in Figure 6-20) shows a higher rate of ethanol electrooxidation per gram after 100 *s* when using single diamond Pd compared to both non-templated Pd and Pd black, showing single diamond Pd to be more durable than other

Pd types tested here in the time range studied (2000 *s*). Figure D-11 shows the chronoampometry normalised against surface area.

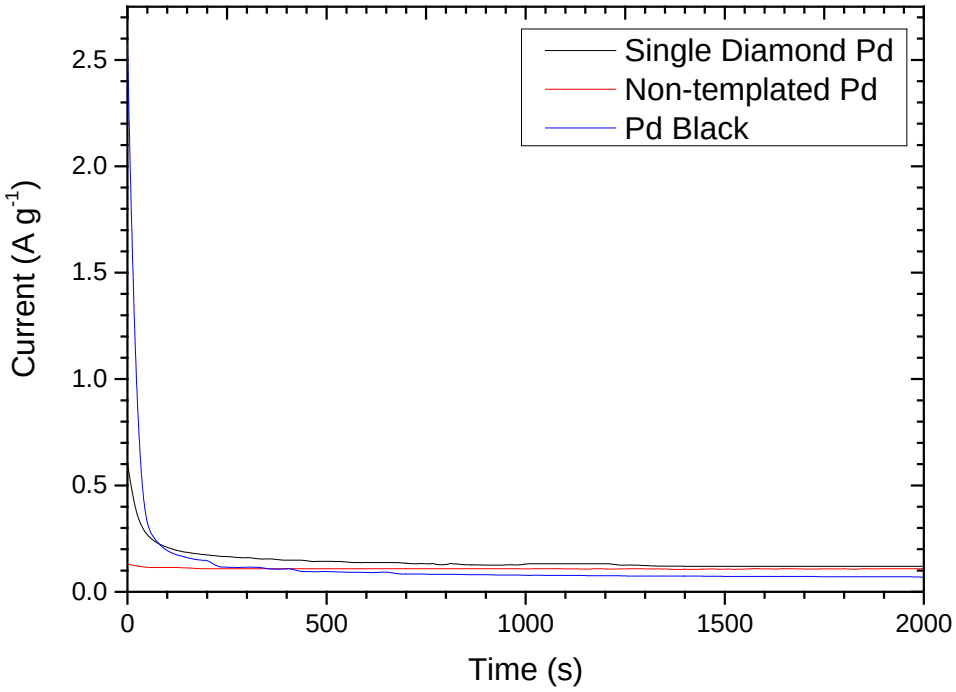

Figure 6-20 - Chronoampometry of Single Diamond Pd, Pd black and non-templated Pd in 0.1 *M* ethanol and 0.1 *M* NaOH, recorded at +0.30 *V vs. SCE*. The experiment was conducted at room temperature. The cell volume was 100 *mL* and the cell was covered to prevent evaporation. Current was normalised by dividing by the mass of Pd on the electrode. For electrodeposited films this was calculated assuming 100% faradaic efficiency.

6.2.4.3 Glycerol Fuel Cells

Single diamond Pd was compared to non-templated Pd and Pd black in effectiveness to catalyse the electrooxidation of glycerol by conducting cyclic voltammetry in 1 *M* glycerol and 1 *M* KOH. This setup is also used by Geraldes *et al.* [266]. The comparison of the first scans of the CV for single diamond Pd, non-templated Pd and Pd black can be seen in Figure 6-21.

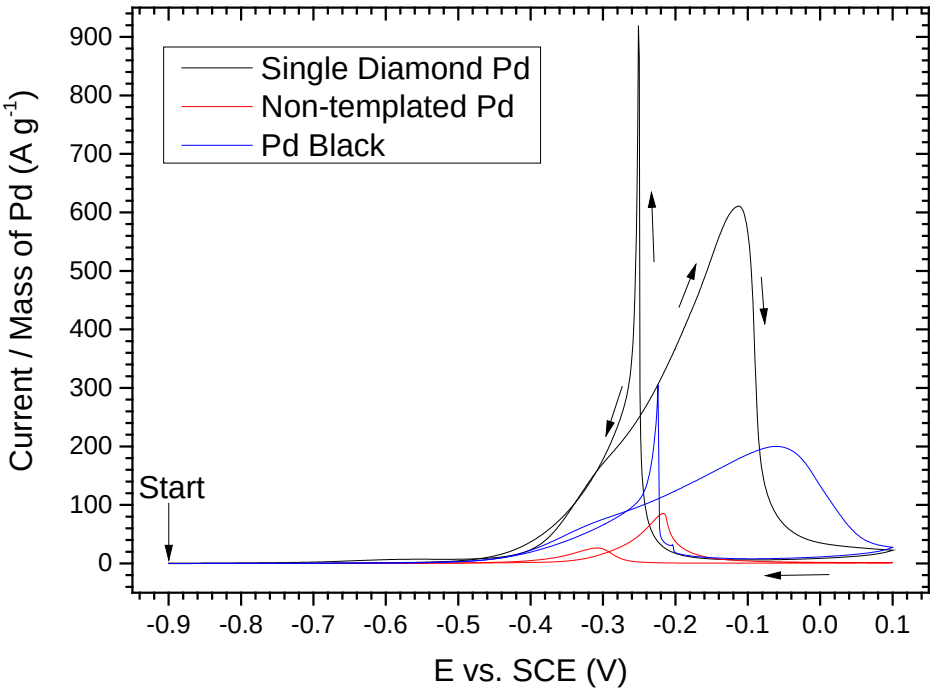

Figure 6-21 - Cyclic voltammetry of Single Diamond Pd, Pd black and non-templated Pd in 1 *M* glycerol and 1 *M* KOH, recorded at 10 $mV\ s^{-1}$. The voltammogram was measured at room temperature and started at a potential of -0.90 *V vs. SCE* where no reaction occurred and is scanned between -0.90 *V vs. SCE* and +0.10 *V vs. SCE*, for 250 scans. Here the first scan is shown for comparison. The cell volume was 100 *mL* and the cell was covered to prevent evaporation. Current was normalised by dividing by the mass of Pd on the electrode. For electrodeposited films this was calculated assuming 100% faradaic efficiency.

From Figure 6-21 single Diamond Pd is shown to exhibit a peak current on the anodic scan of 612 $A\ g^{-1}$, which is over 3 × larger than 199 $A\ g^{-1}$ shown by Pd black and over 7 × larger than 85 $A\ g^{-1}$ shown by non-templated Pd. The peak current of 612 $A\ g^{-1}$ is larger than is seen in the literature for Pd electrooxidation of glycerol. Geraldes *et al.* [266] report a value of 37 $A\ g^{-1}$ for Pd on carbon with average particle sizes of around 4.0 *nm* particle size Pd and up to 54 $A\ g^{-1}$ with 50% Au incorporation. Wang *et al.* [262] use a scan rate of 50 $mV\ s^{-1}$ and get a peak current of 257 $A\ g^{-1}$ (peak current $\alpha\ v^{0.5}$ [261], [262]), using Pd on carbonised porous anodic alumina. This is still under 2 × smaller, without factoring in the faster scan rate. These results are extremely encouraging, as they show single diamond Pd is very effective at the electrooxidation of glycerol.

The peak current is however strongly limited by mass transport for all three Pd catalysts in Figure 6-21. To allow for a more reasonable comparison of the mass activities, currents were

extracted at -0.4 *V vs. SCE*. These currents can be seen in Table 6-3. Currents are also shown for surface specific activity where the current is normalised against surface area instead of mass. Figure D-12 shows the cyclic voltammograms normalised against surface area.

Table 6-3 - Comparison of mass activity and surface specific activity at -0.4 *V vs. SCE* in the surface kinetic limited regime from cyclic voltammetry of Single Diamond Pd, Pd black and non-templated Pd in 1 *M* glycerol and 1 *M* KOH, recorded at 10 $mV\,s^{-1}$.

	Current / Mass ($A\,g^{-1}$)	Current / Surface Area ($A\,cm^{-2}$)
Single Diamond Pd	23.52166	0.76369
Non-templated Pd	1.69892	1.12612
Pd Black	22.54928	1.26681

From Table 6-3 single diamond Pd is seen to have slightly higher mass activity than Pd black, but has lower surface specific activity than both Pd black and non-templated Pd. This means the increase in mass activity of single diamond Pd is due to only the increase in the surface area and not an increase in intrinsic surface specific activity of the Pd. These results still show however, that slightly less mass of Pd is needed to perform the same level of glycerol electrooxidation when in single diamond form compared to the Pd black form shown in this work.

The durability of the structure needs to be tested, to see if the structure is viable. This was tested in 2 ways. CVs were run for 250 scans and chronoampometry was performed, this would test for the long term performance of the single diamond nanostructured Pd. The 250 scans can be seen in Figure 6-22.

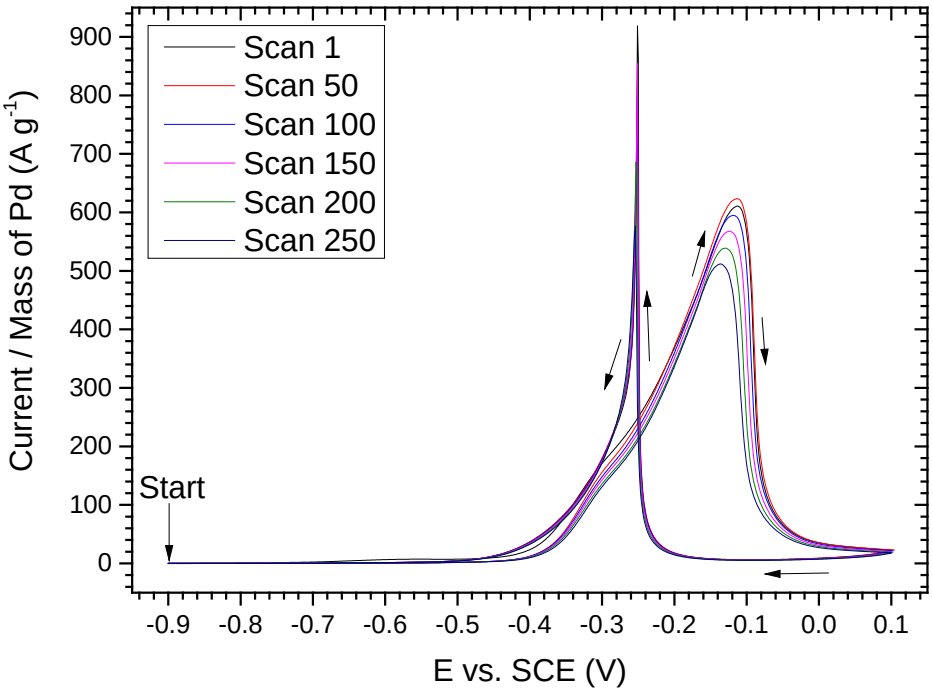

Figure 6-22 - Cyclic voltammetry of Single Diamond Pd in 1 *M* glycerol and 1 *M* KOH, recorded at 10 $mV\ s^{-1}$. The voltammogram was measured at room temperature and started at a potential of -0.90 *V vs. SCE* where no reaction occurred and is scanned between -0.90 *V vs. SCE* and +0.10 *V vs. SCE*, for 250 scans. Here every 50th scan is shown for ease of viewing. The cell volume was 100 *mL* and the cell was covered to prevent evaporation. Current was normalised by dividing by the mass of Pd on the electrode. Pd mass was calculated assuming 100% faradaic efficiency during electrodeposition, with deposition charge being 20 *mC*.

Whilst the peak current consistently decays over the course of the 250 scans for single diamond Pd (Figure 6-22), the same trend is seen for Pd black (Figure D-13). Non-templated Pd (Figure D-14) also decays, but is seen to initially drop in performance (after 50 scans) then the performance is seen to consistently marginally improve over the next 200 scans. The peak current after 250 scans is seen to be 512 $A\ g^{-1}$ for single diamond Pd, higher than that for Pd black (178 $A\ g^{-1}$) and for non-templated Pd (40 $A\ g^{-1}$). Therefore single diamond Pd is seen to be as durable as other Pd types studied in this work and to have a higher catalytic efficiency towards glycerol electrooxidation after numerous scans. Chronoampometry (as seen in Figure 6-23) shows a higher rate of glycerol electrooxidation per gram over time when using single diamond Pd compared to both non-templated Pd and Pd black, showing single diamond Pd to be more durable than other Pd types tested here in the time range studied (2000 *s*). Single diamond Pd is shown to have a current of 15

A g^{-1} after 2000 *s*, which is higher than the 11 *A* g^{-1} shown by a 50:50 mixture of Pd and Au on C after 1800 *s* shown by Geraldes *et al.* [266] (pure Pd on C produced 7 A g^{-1} after 1800 *s* in the same paper [266]). Figure D-15 shows the chronoampometry normalised against surface area.

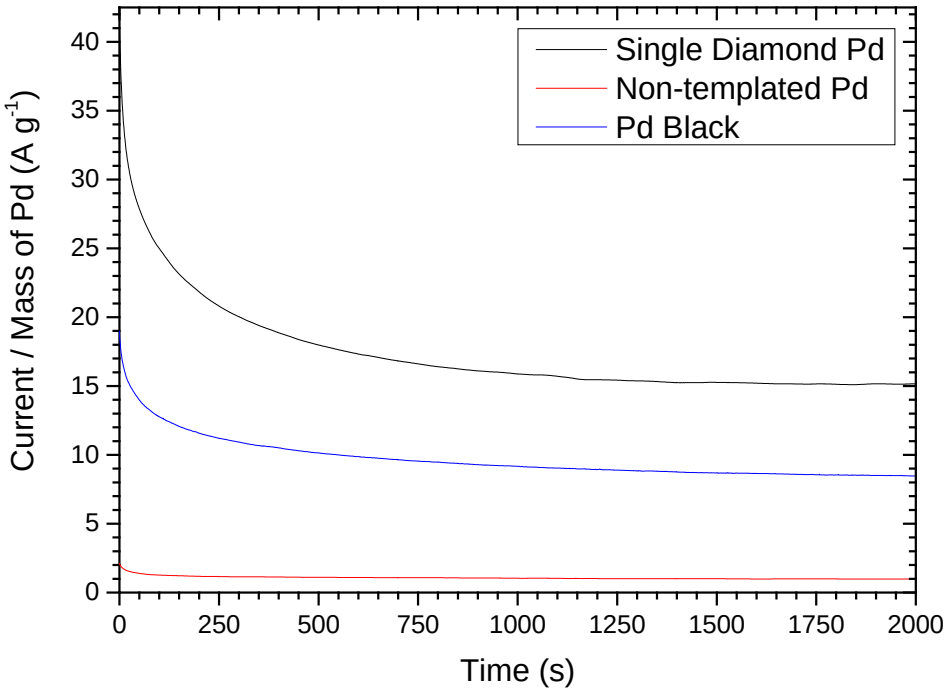

Figure 6-23 - Chronoampometry of Single Diamond Pd, Pd black and non-templated Pd in 1 *M* glycerol and 1 *M* KOH, recorded at +0.30 *V vs. SCE*. The experiment was conducted at room temperature. The cell volume was 100 *mL* and the cell was covered to prevent evaporation. Current was normalised by dividing by the mass of Pd on the electrode. For electrodeposited films this was calculated assuming 100% faradaic efficiency.

6.3 Conclusions

Prior to this project the only reported electrochemical templating using phytantriol, was for the fabrication of single diamond structured Pt [57], [95]. Whilst previous chapters have shown that phytantriol can be used to fabricate nanostructures for thermoelectric materials of bismuth telluride (Chapter 4) and bismuth sulphide (Chapter 5), there are no reports of other materials being successfully templated by phytantriol.

In this chapter the successful fabrication of a single diamond nanostructured Pd has been shown via electrodeposition through a phytantriol template. This structure was confirmed via SAXS

(Figure 6-11), and was shown to be deposited through a double diamond phytantriol template (Figure 6-10). The presence of a nanostructure was further confirmed by TEM (Figure 6-12) and CVs in 1 *M* H_2SO_4 for surface area calculations (Figure 6-15).

Single diamond Pd was deposited with deposition charges ranging between 9 *mC* and 50 *mC*. The plot was seen to be linear (Figure 6-14), demonstrating a uniformly accessible nanostructure. From the gradient of the plot specific electrochemical surface area to mass ratio and the surface area to volume ratio were estimated to be 30.8 ±0.4 $m^2\ g^{-1}$ and 3.66 (±0.04) × $10^6\ cm^2\ cm^{-3}$ respectively.

Single diamond Pd was tested as a catalyst for the electrooxidation of alcohols to assess the potential use of single diamond Pd in alkaline fuel cells. For methanol electrooxidation (Figure 6-15) single diamond Pd was shown to exhibit a peak current per mass on the anodic scan 10 × larger than that seen for Pd black and over 50 × larger than shown by non-templated Pd. The peak current of 1100 $A\ g^{-1}$ is larger than is seen in the literature for Pd [260], [261], [263] and seen for Pt [264]. The peak current is however strongly limited by mass transport so currents in the surface kinetic limited regime were compared, where single diamond Pd was seen to have the highest mass activity, but the surface specific activity was in line with that shown for Pd black meaning the increase in mass activity is due to only an increase in the surface area. For ethanol electrooxidation (Figure 6-18) single Diamond Pd was shown to exhibit a peak current per mass on the anodic scan 11 × larger than was shown by Pd black and non-templated Pd. The peak current of 116 $A\ g^{-1}$ is similar to than seen for Pd (151 $A\ g^{-1}$) in the literature [243]. Currents in the surface kinetic limited regime were compared, where single diamond Pd is seen to have the highest mass activity and surface specific activity. Here the increase in mass activity of single diamond Pd appears to be due to an increase in the surface area and an increase in intrinsic surface specific activity of the Pd towards ethanol electrooxidation. For glycerol electrooxidation (Figure 6-21) single Diamond Pd was shown to exhibit a peak current per mass on the anodic scan over 3 × larger than was shown by Pd black and over 7 × larger than was shown by non-templated Pd. The peak current of 612 $A\ g^{-1}$ is larger than is seen in the literature for Pd electrooxidation of glycerol [262], [266]. Currents in the surface kinetic limited regime were compared, where single diamond Pd was seen to have the highest mass activity, but the lowest surface specific activity meaning the increase in mass activity was due to only an increase in the surface area.

Chapter 7: Conclusions and Further Work

7.1 Conclusions

Electrodeposited bismuth telluride thin films were measured throughout the course of 12 months to access thermoelectric performance. The Seebeck coefficient was seen to slightly increase to -46.9 (±1.3) $\mu V\ K^{-1}$ (from -43.8 (±0.5) $\mu V\ K^{-1}$), whilst the electrical conductivity slightly decreased to 797 (±103) S cm^{-1}(from 820 (±72) S cm^{-1}), which lead to a slightly increased power factor of 0.175 (±0.017) $mW\ m^{-1}\ K^{-2}$ (from 0.158 (±0.008) $mW\ m^{-1}\ K^{-2}$). Electrodeposited bismuth tellurium selenide thin films were also measured throughout the course of 12 months. The Seebeck coefficient was seen to slightly increase to -56.5 (±1.4) $\mu V\ K^{-1}$(from -54.7 (±0.4) $\mu V\ K^{-1}$), whilst the electrical conductivity slightly decreased to 547 (±90) S cm^{-1} (from 580 (±101) S cm^{-1}), which lead to a slightly increased power factor of 0.175 (±0.037) $mW\ m^{-1}\ K^{-2}$ (from 0.173 (±0.023) $mW\ m^{-1}\ K^{-2}$). These results showed that electrodeposited bismuth telluride and bismuth tellurium selenide were both stable for thermoelectric applications.

Both Cu and Ag doped bismuth tellurium selenide thin films were seen to not have reproducible improvements on thermoelectric performance. Electrical conductivity was seen to exponentially decay with increasing Cu incorporation, whilst the Seebeck coefficient was seen to inconsistent. Electrical conductivity was seen to initially decrease with Ag incorporation, although did not deteriorate further upon more Ag doping. The Seebeck coefficient was seen to similarly initially decrease with Ag incorporation, although did not deteriorate further upon more Ag doping.

Phytantriol was used as a template to fabricate nanostructured bismuth telluride by electrodeposition. SAXS studies showed that the phytantriol covering the electrode formed a double diamond phase (Q_{224}) when immersed in the electrolyte with a lattice parameter of 72.4 (± 0.7) *Å*, the electrodeposited films did not show the anticipated single diamond (Q_{227}) structure [57] but a broad peak with a q value of 0.028 $Å^{-1}$ (1/d value of 0.0045 $Å^{-1}$) was observed. HIM images showed that the SAXS was indicating a disordered cubic nanostructure, with a lattice parameter of approximately 320 *Å*. A Seebeck value of -88 (±4) $\mu V\ K^{-1}$ was measured for the average stoichiometric nanostructured bismuth telluride, which is double the value recorded for electrodeposited non-templated bismuth telluride films.

Bismuth sulphide was successfully electrodeposited from an electrolyte of 100 *mM* $Bi(NO_3)$, 100 *mM* $Na_2S_2O_3$ and 200 *mM* EDTA in Milli-Q deionised water onto a Au substrate. The deposition potential was -0.4 *V vs SCE* and the deposition time was 4 *h*. This was confirmed to be bismuth sulphide by EDX and XRD. Following successful electrodeposition of bismuth sulphide,

nanostructured bismuth sulphide was formed by using phytantriol as a template. SAXS studies showed that the bismuth sulphide precursor electrolyte hydrated phytantriol to form the Q_{224} "double diamond" phase with a lattice parameter of 68.9 (± 0.9) *Å*. SAXS on bismuth sulphide films electrodeposited through the template showed a Q_{227} "single diamond" structure, confirmed by TEM. The Q_{227} structure had a lattice parameter of 139.6 (± 3.2) *Å*. These results were consistent with those seen for Pt [57], where this observation is rationalised by one of the two water channels of the Q_{224} phase being blocked to the outside aqueous region to preserve the bilayer topology [57], [182], [183], causing deposition to occur down only one water channel. These results however detail the first formation of a single diamond nanostructured semiconductor using a phytantriol template. Initial Seebeck coefficient measurements were low for both non-templated bismuth sulphide (-29.8 (±10.3) $\mu V\,K^{-1}$) and single diamond bismuth sulphide (-12.3 (±1.8) $\mu V\,K^{-1}$). Bismuth sulphide is a large band gap semiconductor however, so in theory should exhibit greatly enhanced Seebeck coefficients at elevated temperatures.

Successful fabrication of a single diamond nanostructured Pd with a lattice parameter of 140.0 (± 4.6) *Å* was also achieved via electrodeposition through a phytantriol double diamond template with a lattice parameter of 71.0 (± 0.5) *Å*. This was observed via SAXS and was further confirmed by TEM. Single diamond Pd was deposited with deposition charges ranging between 9 *mC* and 50 *mC* and was demonstrated to have a uniformly accessible nanostructure with an average specific electrochemical surface area to mass ratio and the surface area to volume ratio of 30.8 ±0.4 $m^2\,g^{-1}$ and 3.66 (±0.04) × $10^6\,cm^2\,cm^{-3}$ respectively. Single diamond Pd was tested as a catalyst for the electrooxidation of alcohols to assess the potential use of single diamond Pd in alkaline fuel cells. For methanol electrooxidation currents in the surface kinetic limited regime showed single diamond Pd to have the highest mass activity, but the surface specific activity was in line with that shown for Pd black. This showed the increase in mass activity was due only to an increase in the surface area. For ethanol electrooxidation currents in the surface kinetic limited regime showed single diamond Pd to have the highest mass activity and surface specific activity. Here the increase in mass activity of single diamond Pd appeared to be due to an increase in the surface area and an increase in intrinsic surface specific activity of the Pd towards ethanol electrooxidation. For glycerol electrooxidation currents in the surface kinetic limited regime showed single diamond Pd to have the highest mass activity, but the lowest surface specific activity meaning the increase in mass activity was due to only an increase in the surface area. The increases in mass activity seen, showed that less Pd was required in the single diamond form than in Pd black form used in this work to achieve the same levels of methanol, ethanol and glycerol electrooxidation.

7.2 Further Work

Bismuth telluride and bismuth tellurium selenide films should be electrodeposited using a SMSE reference electrode instead of a SCE reference electrode, due to the increased power from 0.13 mW m^{-1} K^{-1} to 0.33 mW m^{-1} K^{-1} being observed when all other conditions were the same for a bismuth tellurium selenide film. These films should then be studied to monitor thermoelectric performance over the course of 12 months. The lower power factor generated using the SCE reference electrode is believed to be due to Cl^- ions entering the electrolyte from the SCE reference, this hypothesis needs to be examined as K^+ ions (from the SMSE reference electrode) being incorporated in the films could not be conclusively ruled out as the cause. This could be tested by the use of a third type of reference electrode not containing Cl^- of K^+ (e.g. Mercury / Mercury Oxide), this would help further understand the underlying cause of the increase in thermoelectric performance. Various deposition potentials should be explored with a SMSE reference electrode to find the peak power factor deposition potential.

The uniformity of stoichiometry of the bismuth telluride nanowires films through the film thickness should be analysed. This could be achieved by depositing films of different thicknesses and analysing their stoichiometry. If variation in stoichiometry was observed to be an issue, a pulsed deposition method could be tested which would give time for diffusion layers to dissipate during deposition.

Due to the high oxidation of the bismuth telluride nanowires fabricated by electrodeposition through phytantriol, nanowires should be fabricated in the same manner in a glove box. This should prevent the oxidation that was observed in this work, which is believed to be the main cause for the observed low conductivity of 19.48 (±0.14) S cm^{-1}. The thermoelectric performance should then be characterised in the glove box, allowing for the electrical conductivity of pure bismuth telluride nanowires to be evaluated. These experiments should then be repeated to check for repeatability of results.

This work has shown aqueous electrodeposited bismuth sulphide films to be uneven, therefore a plating additive (such as sodium liganosulphate), should be used in an attempt to fabricate uniform electrodeposited bismuth sulphide films. The aim being able to electrodeposit a film from which an electrical conductivity measurement could be conducted. If successful, the bismuth sulphide precursor electrolyte should then be doped with a source of potassium, with the aim of generating electrodeposited sulphur deficient potassium doped bismuth sulphide films. This is because sulphur deficient potassium doped bismuth sulphide films have been showed to have enhanced thermoelectric properties compared to bismuth sulphide [199]. This doping technique

could also be applied to bismuth sulphide nanowires electrodeposited through phytantriol. The electrical conductivity of single diamond bismuth sulphide nanowires should also be measured.

Thermal conductivity should be measured for all thermoelectric material samples prepared in this work. This would allow for a ZT “figure of merit” to be established. This would allow for a better comparison of the thermoelectric performance of samples prepared in this work, to materials seen in the literature. All three thermoelectric performance parameters: electrical conductivity, Seebeck coefficient and thermal conductivity should also be measured over a range of temperatures to establish which temperature yields the maximum ZT value for each sample.

The palladium precursor electrolyte should be doped with a source of Au, with the aim of fabricating Pd-Au single diamond nanowires. This is because Pd-Au materials have been observed as efficient materials in the electrooxidation of fuel cell fuels [251], [260], [266]. The usefulness of single diamond Pd should be explored for applications beyond fuel cells for which palladium can be useful. These include electrochemical biosensors, gas sensors, electrochemical capacitors and wastewater treatment [72].

Appendices

Appendix A

A.1 Electrolyte Mixtures

Table A-1 – 100 *mL* of 7.5 *mM* Bi and 10.0 *mM* TeO_2 in 1 *M* HNO_3

Compound	Amount	Source
Bi	0.1567 *g*	Alfa Aesar (99.999%)
TeO_2	0.1596 *g*	Sigma-Aldrich (99.9995%)
HNO_3	6.37 *mL*	Fisher (70%, analytical grade)

Table A-2 - 100 *mL* of 10.0 *mM* Bi and 10.0 *mM* TeO_2 in 1 *M* HNO_3

Compound	Amount	Source
Bi	0.2089 *g*	Alfa Aesar (99.999%)
TeO_2	0.1596 *g*	Sigma-Aldrich (99.9995%)
HNO_3	6.37 *mL*	Fisher (70%, analytical grade)

Table A-3 - 100 *mL* of 12.5 *mM* Bi and 10.0 *mM* TeO_2 in 1 *M* HNO_3

Compound	Amount	Source
Bi	0.2612 *g*	Alfa Aesar (99.999%)
TeO_2	0.1596 *g*	Sigma-Aldrich (99.9995%)
HNO_3	6.37 *mL*	Fisher (70%, analytical grade)

Appendix A

Table A-4 - 100 *mL* of 15.0 *mM* Bi and 10.0 *mM* TeO_2 in 1 *M* HNO_3

Compound	Amount	Source
Bi	0.3134 *g*	Alfa Aesar (99.999%)
TeO_2	0.1596 *g*	Sigma-Aldrich (99.9995%)
HNO_3	6.37 *mL*	Fisher (70%, analytical grade)

Table A-5 - 100 *mL* of 17.0 *mM* Bi and 10.0 *mM* TeO_2 in 1 *M* HNO_3

Compound	Amount	Source
Bi	0.3552 *g*	Alfa Aesar (99.999%)
TeO_2	0.1596 *g*	Sigma-Aldrich (99.9995%)
HNO_3	6.37 *mL*	Fisher (70%, analytical grade)

Table A-6 - 100 *mL* of 8.0 *mM* Bi, 9.0 *mM* TeO_2 and 1.0 *mM* SeO_2 in 1 *M* HNO_3

Compound	Amount	Source
Bi	0.1671 *g*	Alfa Aesar (99.999%)
TeO_2	0.1596 *g*	Sigma-Aldrich (99.9995%)
SeO_2	0.0111 *g*	Across Organics (99.999%)
HNO_3	6.37 *mL*	Fisher (70%, analytical grade)

Table A-7 - 100 *mL* of 8.0 *mM* Bi, 9.0 *mM* TeO_2, 1.0 *mM* SeO_2 and 2.00 *mM* Cu in 1 *M* HNO_3

Compound	Amount	Source
Bi	0.1671 *g*	Alfa Aesar (99.999%)
TeO_2	0.1596 *g*	Sigma-Aldrich (99.9995%)
SeO_2	0.0111 *g*	Across Organics (99.999%)
$Cu(NO_3)_2.5H_2O$	0.0559 *g*	Sigma-Aldrich (99.999%)
HNO_3	6.37 *mL*	Fisher (70%, analytical grade)

Table A-8 - 100 *mL* of 8.0 *mM* Bi, 9.0 *mM* TeO_2, 1.0 *mM* SeO_2 and 1.00 *mM* Ag in 1 *M* HNO_3

Compound	Amount	Source
Bi	0.1671 *g*	Alfa Aesar (99.999%)
TeO_2	0.1596 *g*	Sigma-Aldrich (99.9995%)
SeO_2	0.0111 *g*	Across Organics (99.999%)
$Ag(NO_3)$	0.0170 *g*	Sigma-Aldrich (99.9999%)
HNO_3	6.37 *mL*	Fisher (70%, analytical grade)

Table A-9 – 100 *mL* of 100 *mM* $Bi(NO_3)_3$, 100 *mM* $Na_2S_2O_3$ and 200 *mM* EDTA in Milli-Q deionised water

Compound	Amount	Source
$Bi(NO_3)_3.5H_2O$	4.8507 *g*	Across Organics (99.999%)
$Na_2S_2O_3$	1.5811 *g*	Fischer (reagent grade)
EDTA	5.8448 *g*	Sigma-Aldrich (99.995%)

Table A-10 – 100 *mL* of 50 *mM* $(NH_4)_2PdCl_4$ and 1 *M* NH_4Cl dissolved in 1 *M* HCl

Compound	Amount	Source
$(NH_4)_2PdCl_4$	1.4216 *g*	Alfa Aesar (99.998%)
NH_4Cl	5.3490 *g*	Fischer (reagent grade)
HCl	8.25 *mL*	Fischer (reagent grade)

A.2 Film Thickness

The average thickness of a film (*d*) was estimated using the deposition charge (*Q*) by using Equation A.1 which is derived from Faraday's law assuming 100% faradaic efficiency.

$$d = \frac{Q}{nFA}\frac{M}{\rho} \quad \text{(A.1)}$$

where n is the number of electrons in the reaction (18 for bismuth telluride), *F* is Faraday's constant (96 485 C mol^{-1}), *A* is geometric surface area (1 cm^2), *M* is the molar mass (800.76 $g\ mol^{-1}$ for bismuth telluride) and ρ is density of the electrodeposit (7.7 $g\ cm^{-3}$ for bismuth telluride).

All samples were assumed to be stoichiometric bismuth telluride for thickness estimations. A profilometer found estimations were all inside the range of thicknesses measured for each sample.

Table A-11 – Estimated film thickness of bismuth telluride and bismuth tellurium selenide electrodeposited films calculated using equation A.1, along with measured thicknesses ranges from profilometry.

		Sample 1	Sample 2	Sample 3
Bismuth Telluride	Estimated Thickness	7.982 *µm*	7.988 *µm*	8.449 *µm*
	Measured Thickness	7.8 (±0.2) *µm*	7.9 (±0.3) *µm*	8.5 (±0.1) *µm*
Bismuth Tellurium Selenide	Estimated Thickness	7.034 *µm*	6.607 *µm*	7.064 *µm*
	Measured Thickness	7.2 (±0.3) *µm*	6.4 (±0.3) *µm*	7.0 (±0.1) *µm*

Table A-12 - Estimated film thickness of Cu doped bismuth tellurium selenide electrodeposited films calculated using equation A.1, along with measured thicknesses from profilometry.

$[Cu(NO_3)_2]$ (*mM*)	0.00	0.25	0.50	0.75	1.00	1.25	1.50	1.75	2.00
Estimated Thickness (*μm*)	6.523	6.326	6.216	6.206	6.041	5.530	5.020	4.490	4.400
Measured Thickness (*μm*)	6.7 (±0.3)	6.4 (±0.3)	6.2 (±0.1)	6.1 (±0.3)	6.2 (±0.3)	5.5 (±0.2)	5.0 (±0.1)	4.4 (±0.1)	4.3 (±0.3)

Table A-13 - Estimated film thickness of Ag doped bismuth tellurium selenide electrodeposited films calculated using equation A.1, along with measured thicknesses from profilometry.

$[Ag(NO_3)]$ (*mM*)	0.00	0.25	0.50	0.75	1.00
Estimated Thickness (*μm*)	8.530	8.840	8.260	8.810	9.010
Measured Thickness (*μm*)	8.6 (±0.1)	8.7 (±0.2)	8.1 (±0.2)	8.8 (±0.1)	9.2 (±0.2)

A.3 ICDD Powder Stick Patterns

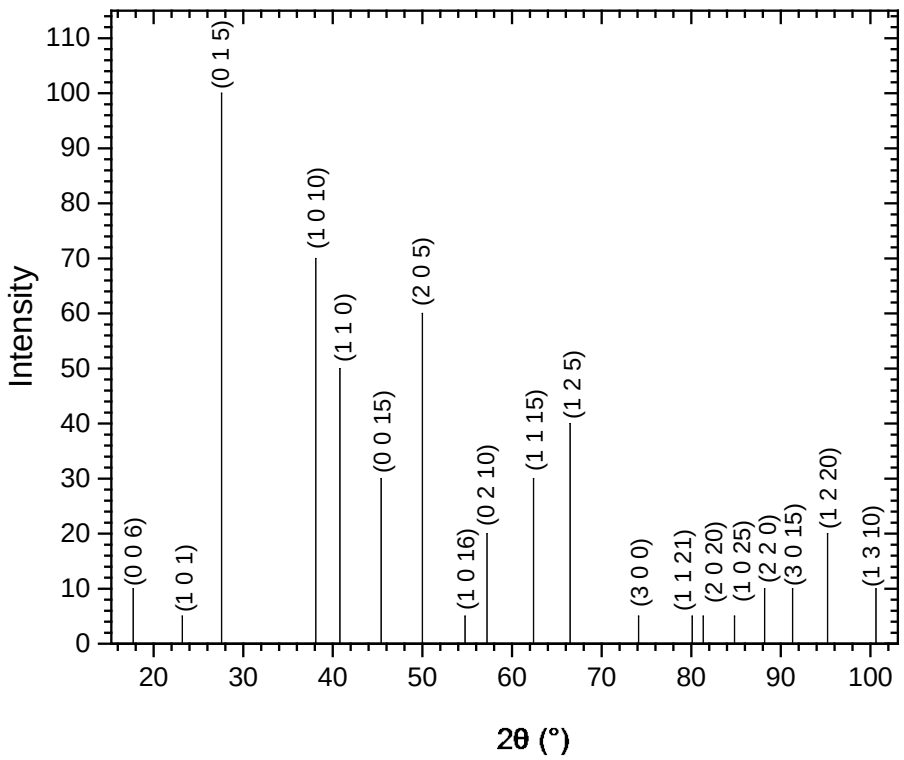

Figure A-1 – Stick powder pattern for PDF card number 00-015-0863 “Tellurobismthite”.

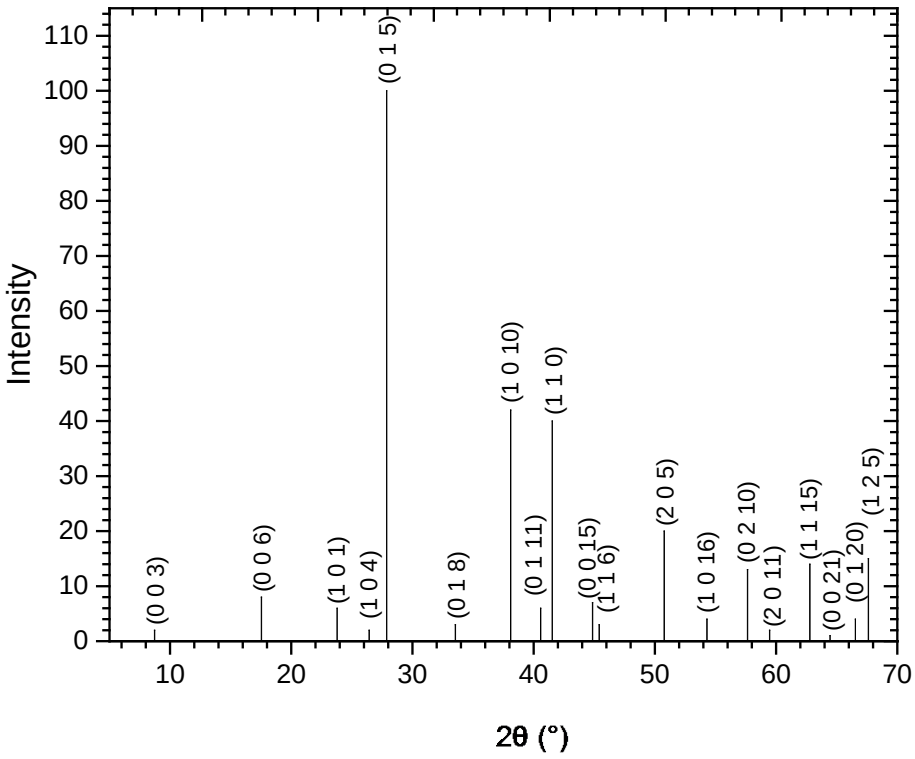

Figure A-2 - Stick powder pattern for PDF card number 00-051-0643 “Bismuth Tellurium Selenide”.

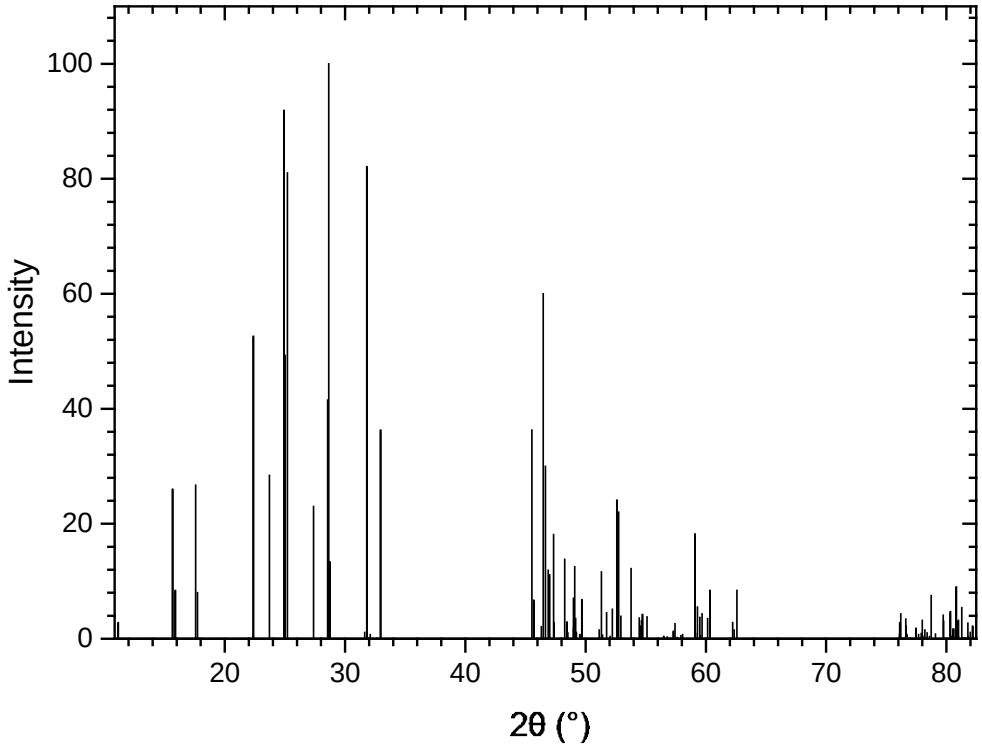

Figure A-3 - Stick powder pattern for PDF card number 9007375 “Bismuthinite”. Peaks are unlabelled due to the number of peaks, (h k l) values can be found in Table A-14.

Table A-14 – Relative intensity and h k l values for peaks in the PDF card number 9007375 “Bismuthinite”, seen in Figure A-3.

2Theta	Intensity	h k l	2Theta	Intensity	h k l	2Theta	Intensity	h k l
11.14	2.8	1 0 1	51.13	1.5	6 0 2	75.82	0	8 1 3
15.66	26	2 0 0	51.31	11.6	2 2 2	76.1	0.7	4 0 8
15.89	8.4	0 0 2	51.41	0.6	4 1 4	76.11	2.8	0 3 3
17.58	26.7	2 0 1	51.75	4.5	2 0 6	76.21	4.3	9 0 1
17.73	8	1 0 2	52.04	0.4	5 0 4	76.35	0.1	7 2 1
22.38	52.6	2 0 2	52.22	5.1	4 0 5	76.53	0.1	3 3 1
23.71	28.4	0 1 1	52.6	24.1	3 2 1	76.62	3.4	7 1 5
24.92	91.9	3 0 1	52.63	15.6	5 1 3	76.65	2.2	1 3 3

25	49.3	1 1 1	52.75	22	1 2 3	76.68	0.8	3 1 8
25.21	81	1 0 3	52.93	3.9	3 1 5	76.73	0.6	5 2 5
27.38	23	2 1 0	53.78	12.2	6 1 0	77	0.1	5 1 7
28.55	41.5	2 1 1	54.46	3.6	6 1 1	77.1	0	1 2 7
28.57	11.3	3 0 2	54.57	2.2	6 0 3	77.46	1.8	1 0 9
28.64	100	1 1 2	54.64	3.1	3 2 2	77.68	0.7	6 2 4
28.73	13.4	2 0 3	54.73	4.2	2 2 3	77.9	0.9	9 0 2
31.63	1.1	4 0 0	55.07	0	3 0 6	77.99	3.2	4 2 6
31.81	82.1	2 1 2	55.11	3.8	1 1 6	78.04	0.4	7 2 2
32.09	0.7	0 0 4	56.45	0.1	6 1 2	78.21	1.5	3 3 2
32.66	0.1	4 0 1	56.5	0.4	4 2 0	78.29	0	2 3 3
32.95	36.3	0 1 3	56.79	0.3	0 2 4	78.39	1	7 0 6
45.53	36.3	0 2 0	57.03	0.1	2 1 6	78.59	0.4	6 0 7
45.68	6.7	4 0 4	57.16	0	4 2 1	78.73	7.5	2 2 7
46.32	2.1	4 1 3	57.3	1.3	5 1 4	79.09	0.8	2 0 9
46.47	60	3 1 4	57.43	2.6	1 2 4	79.74	4.1	8 1 4
46.66	30	0 1 5	57.47	0.1	4 1 5	79.77	3	4 3 0
46.89	11.9	5 1 1	57.62	0.2	7 0 1	80.33	4.7	4 3 1
47.01	11.1	5 0 3	57.93	0.5	3 2 3	80.39	0.4	8 0 5
47.03	0.2	1 2 1	58.06	0.7	5 0 5	80.48	0.1	4 1 8
47.34	18.1	3 0 5	58.48	0	1 0 7	80.56	1.6	1 3 4
47.38	2.8	1 1 5	59.09	18.2	4 2 2	80.59	1.7	9 1 1
48.26	13.8	6 0 0	59.14	0.9	6 0 4	80.68	0.1	9 0 3
48.44	2.9	2 2 0	59.3	5.5	2 2 4	80.82	9	7 2 3
48.53	1	0 2 2	59.5	3.7	4 0 6	80.99	3.2	5 0 8
48.99	7	0 0 6	59.55	0.5	7 0 2	80.99	0.3	3 3 3

48.99	1.8	6 0 1	59.68	4.3	6 1 3	81.28	5.4	0 1 9
49.1	12.5	5 1 2	60.15	3.5	3 1 6	81.43	0.1	3 2 7
49.17	3.5	2 2 1	60.34	8.4	2 0 7	81.79	2.7	3 0 9
49.23	1.1	1 2 2	62.23	2.8	4 2 3	81.82	0.4	1 1 9
49.52	0.7	2 1 5	62.35	1.5	3 2 4	81.99	1.1	4 3 2
49.69	6.8	1 0 6	62.58	8.4	7 1 1	82.18	2.2	2 3 4

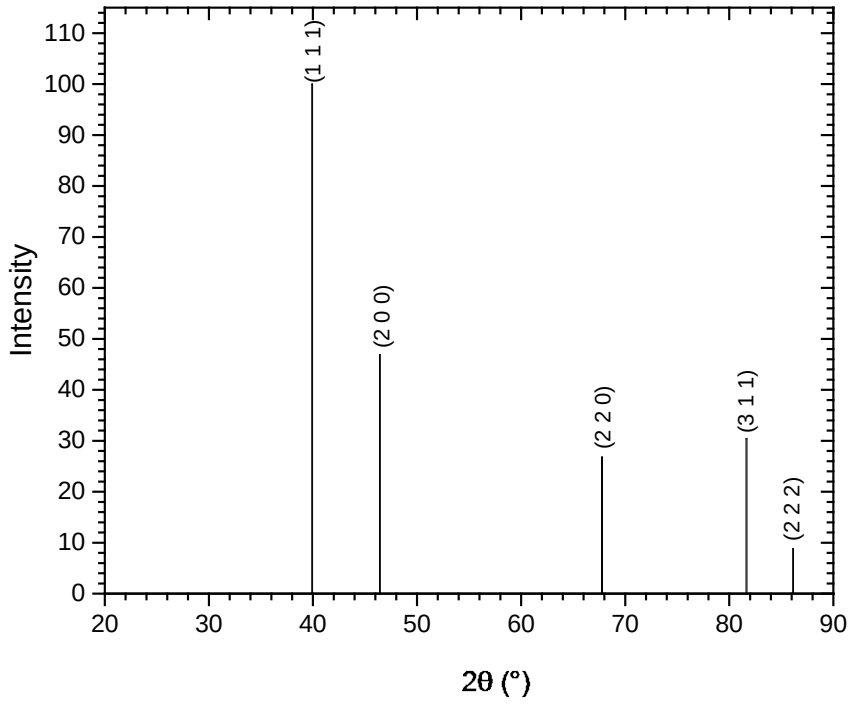

Figure A-4 - Stick powder pattern for PDF card number 1011110 “Paladium”.

Appendix B Small Angle X-ray Scattering Calculations

B.1 Bismuth Telluride

B.1.1 Phytantriol lined capillary mixed with excess bismuth telluride precursor electrolyte

(2 1 1) peak determined to have a 1/d value of 0.0341 $Å^{-1}$, therefore d spacing of the (2 1 1) planes was 29.36 *Å*. Using Equation 2.3 the lattice parameter was calculated to be 71.9 *Å*.

$$a_0 = d_{hkl} \times \sqrt{h^2 + k^2 + l^2} = 29.36 \text{ Å} \times \sqrt{6} = 71.9 \text{ Å}$$

The error was calculated using the edge of the (2 1 1) peak which had a 1/d value of 0.0344 $Å^{-1}$, giving a d spacing of 29.05 *Å*. Using Equation 2.3 the lattice parameter was calculated to be 71.2 *Å*.

$$a_0 = d_{hkl} \times \sqrt{h^2 + k^2 + l^2} = 29.05 \text{ Å} \times \sqrt{6} = 71.2 \text{ Å}$$

71.2 *Å* is 0.7 *Å* away from 71.9 *Å*, therefore the error was determined to 0.7 *Å*.

B.1.2 Phytantriol coated gold DVD placed in excess bismuth sulphide precursor electrolyte

(1 1 0) peak determined to have a 1/d value of 0.0196 $Å^{-1}$, therefore d spacing of the (1 1 0) planes was 51.20 *Å*. Using Equation 2.3 the lattice parameter was calculated to be 72.4 *Å*.

$$a_0 = d_{hkl} \times \sqrt{h^2 + k^2 + l^2} = 51.20 \text{ Å} \times \sqrt{2} = 72.4 \text{ Å}$$

The error was calculated using the edge of the (1 1 0) peak which had a 1/d value of 0.0197 $Å^{-1}$, giving a d spacing of 50.65 *Å*. Using Equation 2.3 the lattice parameter was calculated to be 71.6 *Å*.

$$a_0 = d_{hkl} \times \sqrt{h^2 + k^2 + l^2} = 50.65 \text{ Å} \times \sqrt{2} = 71.6 \text{ Å}$$

71.6 *Å* is 0.8 *Å* away from 72.4 *Å*, therefore the error was determined to 0.8 *Å*.

B.2 Bismuth Sulphide

B.2.1 Phytantriol lined capillary mixed with excess bismuth sulphide precursor electrolyte

(2 2 1) peak at 477 minutes determined to have a 1/d value of 0.0441 $Å^{-1}$, therefore d spacing of the (2 2 1) planes was 22.69 *Å*. Using Equation 2.3 the lattice parameter was calculated to be 68.9 *Å*.

$$a_0 = d_{hkl} \times \sqrt{h^2 + k^2 + l^2} = 22.97\ \text{Å} \times \sqrt{9} = 68.1\ \text{Å}$$

The error was calculated using the edge of the (2 2 1) peak at 477 minutes which had a 1/d value of 0.0442 $Å^{-1}$, giving a d spacing of 22.62 *Å*. Using Equation 2.3 the lattice parameter was calculated to be 67.9 *Å*.

$$a_0 = d_{hkl} \times \sqrt{h^2 + k^2 + l^2} = 22.62\ \text{Å} \times \sqrt{9} = 67.9\ \text{Å}$$

67.9 *Å* is 0.2 *Å* away from 68.1 *Å*, therefore the error was determined to 0.2 *Å*.

B.2.2 Phytantriol coated gold foil placed in excess bismuth sulphide precursor electrolyte

(2 1 1) peak determined to have a 1/d value of 0.0356 $Å^{-1}$, therefore d spacing of the (2 1 1) planes was 28.13 *Å*. Using Equation 2.3 the lattice parameter was calculated to be 68.9 *Å*.

$$a_0 = d_{hkl} \times \sqrt{h^2 + k^2 + l^2} = 28.13\ \text{Å} \times \sqrt{6} = 68.9\ \text{Å}$$

The error was calculated using the edge of the (2 1 1) peak which had a 1/d value of 0.0360 $Å^{-1}$, giving a d spacing of 27.76 *Å*. Using Equation 2.3 the lattice parameter was calculated to be 68.0 *Å*.

$$a_0 = d_{hkl} \times \sqrt{h^2 + k^2 + l^2} = 27.76\ \text{Å} \times \sqrt{6} = 68.0\ \text{Å}$$

68.0 *Å* is 0.9 *Å* away from 68.9 *Å*, therefore the error was determined to 0.9 *Å*.

B.2.3 Bismuth Sulphide Electrodeposited Through Phytantriol

(1 1 1) peak determined to have a 1/d value of 0.0124 $Å^{-1}$, therefore d spacing of the (1 1 1) planes was 80.60 *Å*. Using Equation 2.3 the lattice parameter was calculated to be 139.6 *Å*.

$$a_0 = d_{hkl} \times \sqrt{h^2 + k^2 + l^2} = 80.60\ \text{Å} \times \sqrt{3} = 139.6\ \text{Å}$$

The error was calculated by taking the edge of the (1 1 1) peak at half maximum which had a 1/d value of 0.0127 *Å*$^{-1}$, giving a d spacing of 78.75 *Å*. Using Equation 2.3 the lattice parameter was calculated to be 136.4 *Å*.

$$a_0 = d_{hkl} \times \sqrt{h^2 + k^2 + l^2} = 78.75\ \text{Å} \times \sqrt{3} = 136.4\ \text{Å}$$

136.4 *Å* is 3.2 *Å* away from 139.6 *Å*, therefore the error was determined to 3.2 *Å*.

B.3 Palladium

B.3.1 Phytantriol lined capillary mixed with excess palladium precursor electrolyte

(2 2 0) peak determined to have a 1/d value of 0.0398 *Å*$^{-1}$, therefore d spacing of the (2 2 0) planes was 25.11 *Å*. Using Equation 2.3 the lattice parameter was calculated to be 71.0 *Å*.

$$a_0 = d_{hkl} \times \sqrt{h^2 + k^2 + l^2} = 25.11\ \text{Å} \times \sqrt{8} = 71.0\ \text{Å}$$

The error was calculated using the edge of the (2 2 0) peak which had a 1/d value of 0.0401 *Å*$^{-1}$, giving a d spacing of 24.94 *Å*. Using Equation 2.3 the lattice parameter was calculated to be 70.5 *Å*.

$$a_0 = d_{hkl} \times \sqrt{h^2 + k^2 + l^2} = 24.94\ \text{Å} \times \sqrt{8} = 70.5\ \text{Å}$$

70.5 *Å* is 0.5 *Å* away from 71.0 *Å*, therefore the error was determined to 0.5 *Å*.

B.3.2 Phytantriol Electrodeposited Through Phytantriol

(1 1 1) peak determined to have a 1/d value of 0.0124 *Å*$^{-1}$, therefore d spacing of the (1 1 1) planes was 80.85 *Å*. Using Equation 2.3 the lattice parameter was calculated to be 140.0 *Å*.

$$a_0 = d_{hkl} \times \sqrt{h^2 + k^2 + l^2} = 80.85\ \text{Å} \times \sqrt{3} = 140.0\ \text{Å}$$

The error was calculated by taking the edge of the (1 1 1) peak at half maximum which had a 1/d value of 0.0128 *Å*$^{-1}$, giving a d spacing of 78.20 *Å*. Using Equation 2.3 the lattice parameter was calculated to be 135.4 *Å*.

$$a_0 = d_{hkl} \times \sqrt{h^2 + k^2 + l^2} = 78.20\ \text{Å} \times \sqrt{3} = 135.4\ \text{Å}$$

135.4 *Å* is 4.6 *Å* away from 140.0 *Å*, therefore the error was determined to 4.6 *Å*.

Appendix C

C.1 Cu Cyclic Voltammetry

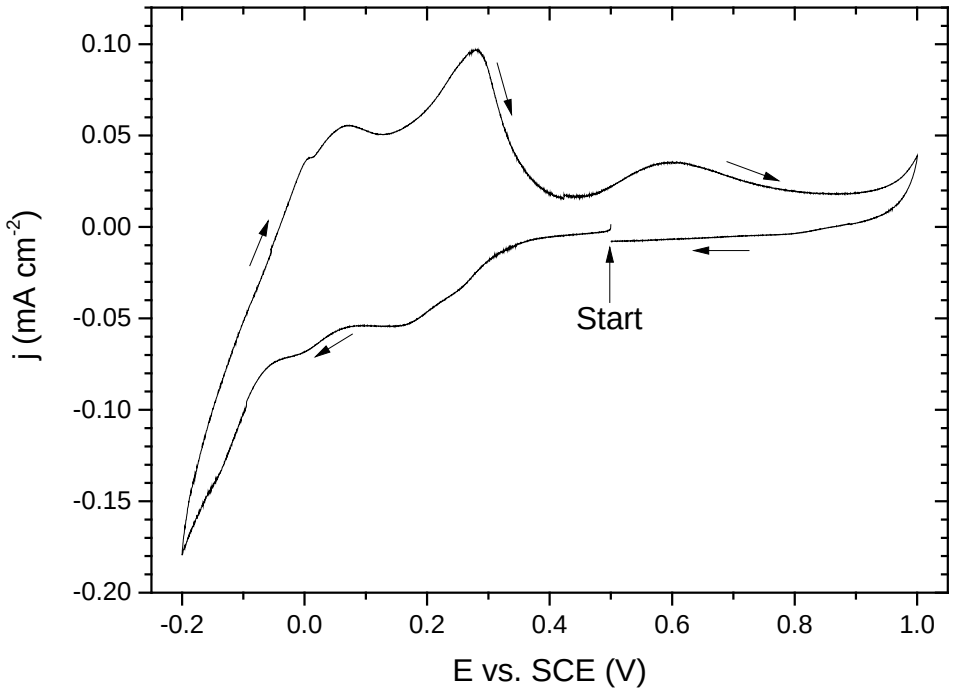

Figure C-1 - Cyclic voltammogram recorded at 20 *mV* s^{-1} in an electrolyte of 1.00 *mM* $Cu(NO_3)_2$ dissolved in 1 *M* HNO_3. The voltammogram started at a potential of +0.50 *V vs. SCE* where no reaction occurs and is scanned between -0.20 *V vs. SCE* and +1.00 *V vs. SCE*. The black arrows indicate the direction of the scan. The working electrode was a 2 *mm* gold disc electrode.

Appendix D

D.1 Pd Surface Area Cyclic Voltammetry

D.1.1 Non-Templated Pd

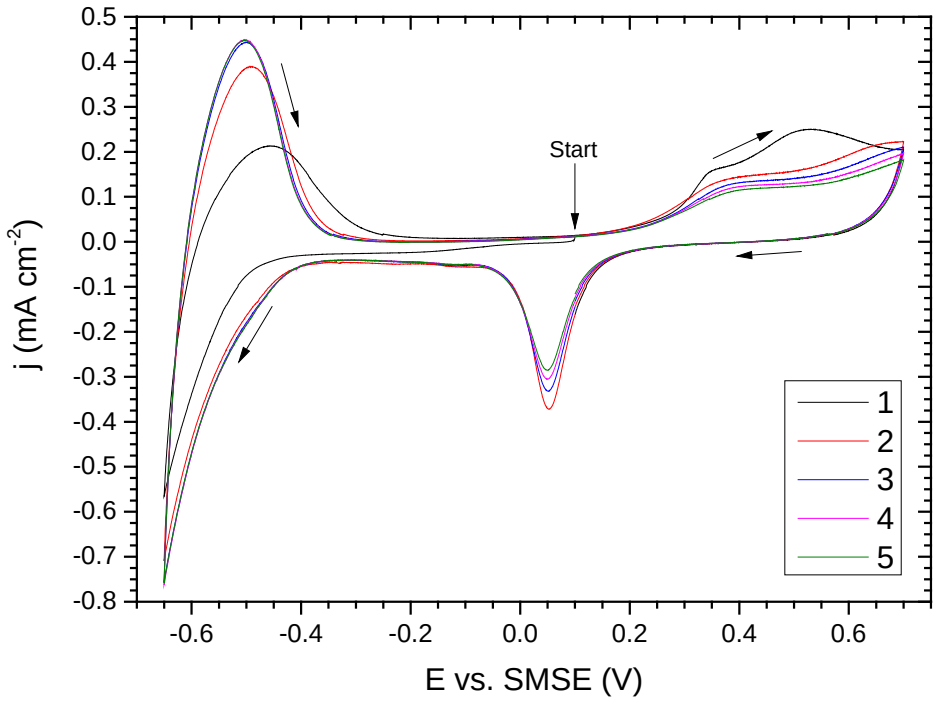

Figure D-1 – Cyclic voltammogram of non-templated Pd recorded at 20 *mV* s^{-1} in 1 *M* H_2SO_4. The voltammogram was measured at room temperature and started at a potential of +0.1 *V vs. SMSE* where no reaction occurred and is scanned between -0.65 *V vs. SMSE* and 0.7 *V vs. SMSE*, for 5 scans. The black arrows indicate the direction of the scan. The non-templated Pd was deposited on a 2 *mm* polished gold disc electrode, from an electrolyte of 50 *mM* $(NH_4)_2PdCl_4$, 1 M NH_4Cl and 1 *M* HCl. The deposition potential was +0.1 *V vs. SMSE* and deposition was halted once 14.4 *mC* of charge was passed. Current density was calculated by dividing the recorded current by the surface area of the 2 *mm* gold disc electrode.

D.1.2 Pd Black

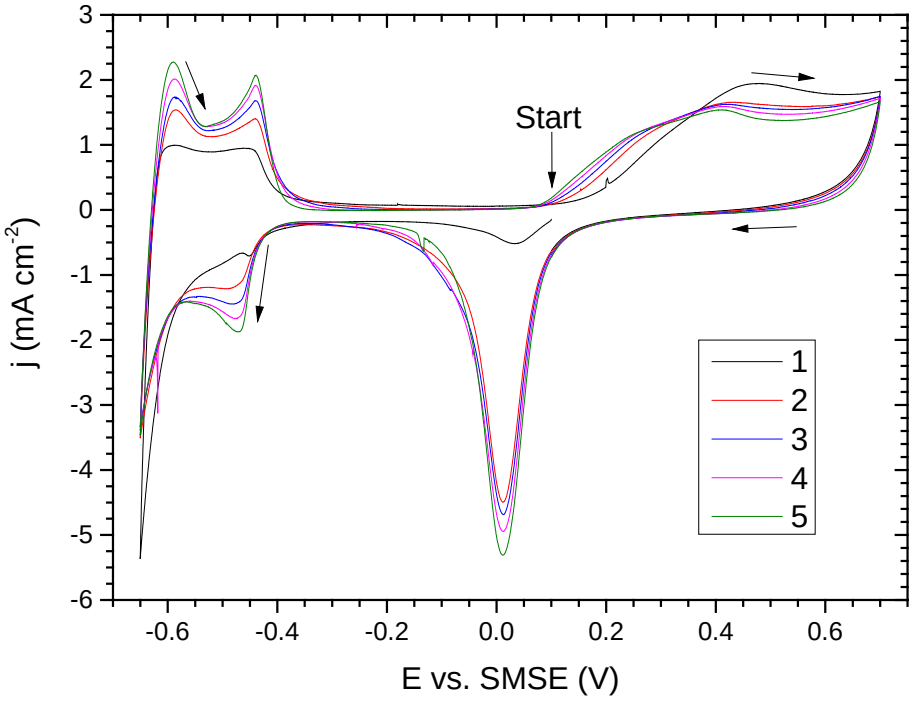

Figure D-2 - Cyclic voltammogram of Pd black recorded at 20 *mV* s^{-1} in 1 *M* H_2SO_4. The voltammogram was measured at room temperature and started at a potential of +0.1 *V vs. SMSE* where no reaction occurred and is scanned between -0.65 *V vs. SMSE* and 0.7 *V vs. SMSE*, for 5 scans. The black arrows indicate the direction of the scan. 0.385 *mg* of Pd black was applied onto a 2 *mm* polished gold disc electrode by pipetting on 5 *µL* of an ink consisting of 80 *mg* Pd black (Alfa Aesar, 99.9%), 40 *µL* Nafion® 117 solution (Aldrich) and 1000 *µL* deionised water and leaving in an oven at 100 °C for at least 15 minutes. Current density was calculated by dividing the recorded current by the surface area of the 2 *mm* gold disc electrode.

D.1.3 Single Diamond Pd

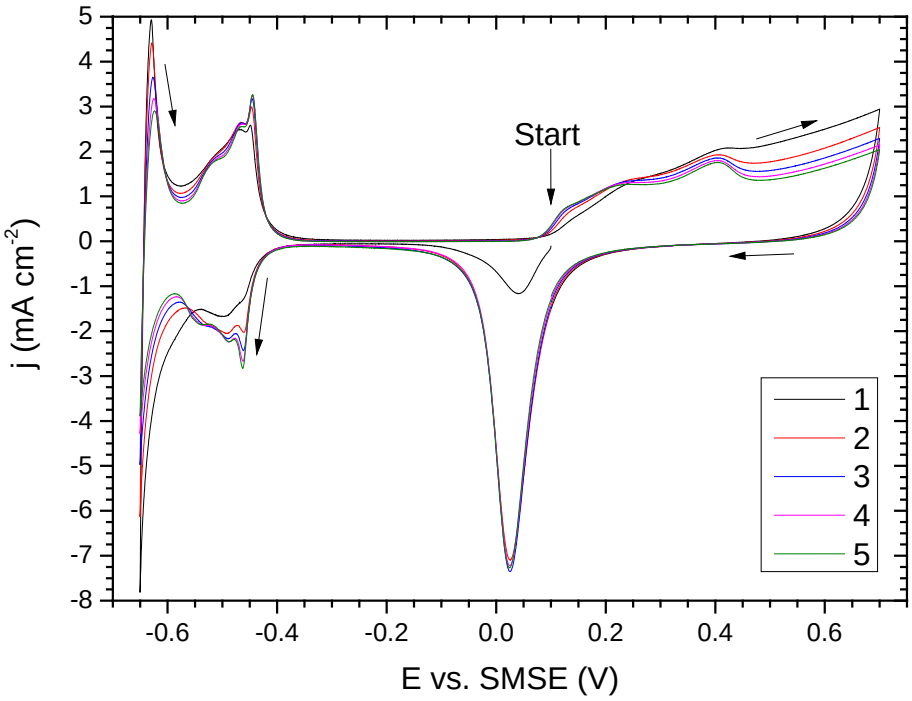

Figure D-3 - Cyclic voltammogram of Pd electrodeposited through a phytantriol template, recorded at 20 *mV* s^{-1} in 1 *M* H_2SO_4. The voltammogram was measured at room temperature and started at a potential of +0.1 *V vs. SMSE* where no reaction occurred and is scanned between -0.65 *V vs. SMSE* and +0.70 *V vs. SMSE*, for 5 scans. The black arrows indicate the direction of the scan. The Pd was deposited on a 2 *mm* polished gold disc electrode, from an electrolyte of 50 *mM* $(NH_4)_2PdCl_4$, 1 *M* NH_4Cl and 1 *M* HCl, through a phytantriol template of phytantriol. The deposition potential was +0.1 *V vs. SMSE* and deposition was halted once 14.4 *mC* of charge was passed. Current density was calculated by dividing the recorded current by the surface area of the 2 *mm* gold disc electrode.

D.2 Catalytic Efficiency of Pd

D.2.1 For Methanol

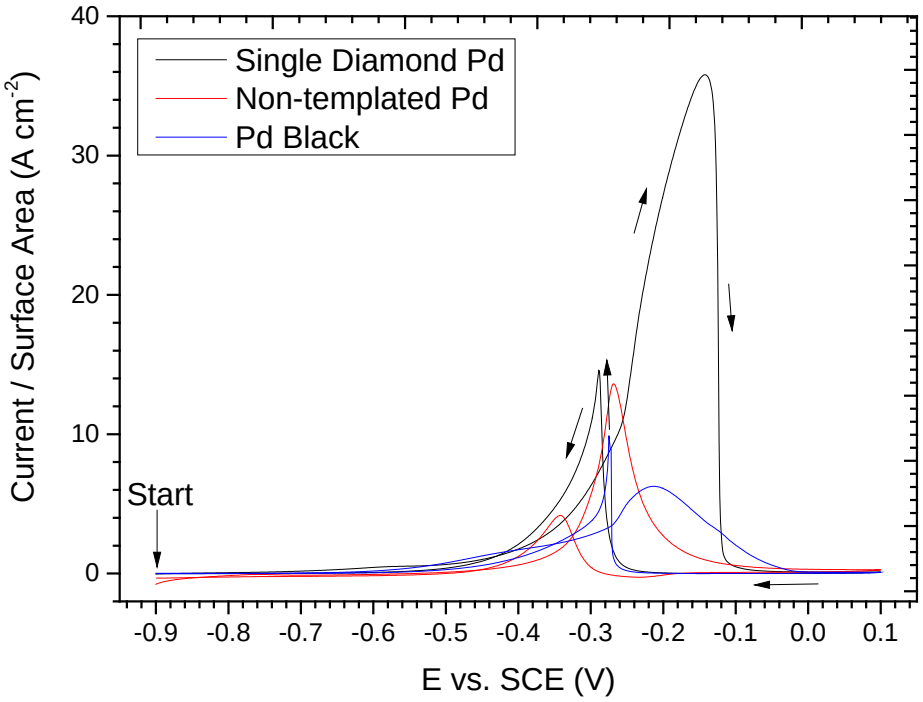

Figure D-4 - Cyclic voltammetry of Single Diamond Pd, Pd black and non-templated Pd in 1 *M* methanol and 1 *M* KOH, recorded at 10 $mV\ s^{-1}$. The voltammogram was measured at room temperature and started at a potential of -0.90 *V vs. SCE* where no reaction occurred and is scanned between -0.90 *V vs. SCE* and +0.10 *V vs. SCE*, for 250 scans. Here the first scan is shown for comparison. The cell volume was 100 *mL* and the cell was covered to prevent evaporation. Current was normalised by dividing by the surface area of Pd on the electrode.

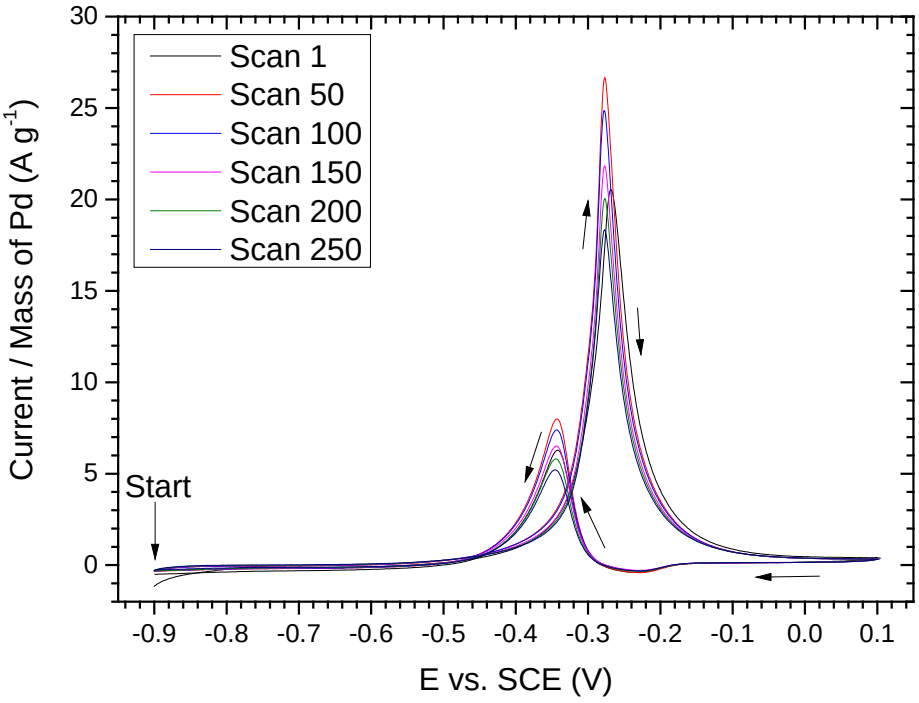

Figure D-5 - Cyclic voltammetry of non-templated Pd in 1 *M* methanol and 1 *M* KOH, recorded at 10 $mV\ s^{-1}$. The voltammogram was measured at room temperature and started at a potential of -0.90 *V vs. SCE* where no reaction occurred and is scanned between -0.90 *V vs. SCE* and +0.10 *V vs. SCE*, for 250 scans. Here every 50th scan is shown for ease of viewing. The cell volume was 100 *mL* and the cell was covered to prevent evaporation. Current was normalised by dividing by the mass of Pd on the electrode. Pd mass was calculated assuming 100% faradaic efficiency during electrodeposition, with deposition charge being 20 *mC*.

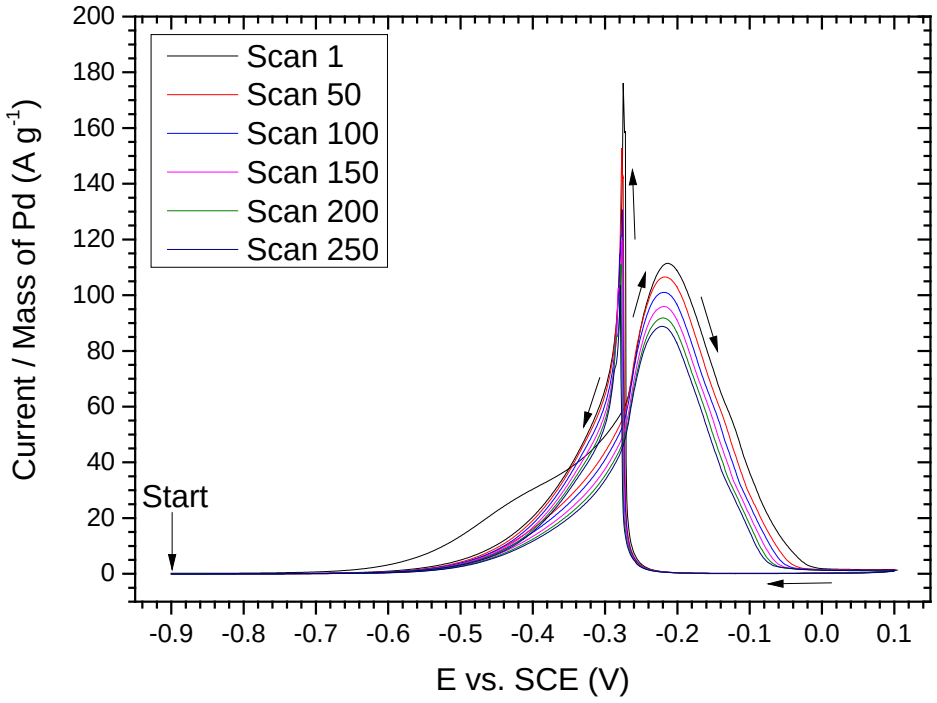

Figure D-6 - Cyclic voltammetry of Pd black in 1 *M* methanol and 1 *M* KOH, recorded at 10 $mV\,s^{-1}$. The voltammogram was measured at room temperature and started at a potential of -0.90 *V vs. SCE* where no reaction occurred and is scanned between -0.90 *V vs. SCE* and +0.10 *V vs. SCE*, for 250 scans. Here every 50th scan is shown for ease of viewing. The cell volume was 100 *mL* and the cell was covered to prevent evaporation. Current was normalised by dividing by the mass of Pd (0.385 *mg*) on the electrode. 0.385 *mg* of Pd black was applied onto a 2 *mm* polished gold disc electrode by pipetting on 5 *µL* of an ink consisting of 80 *mg* Pd black (Alfa Aesar, 99.9%), 40 *µL* Nafion® 117 solution (Aldrich) and 1000 *µL* deionised water and leaving in an oven at 100 *°C* for at least 15 minutes.

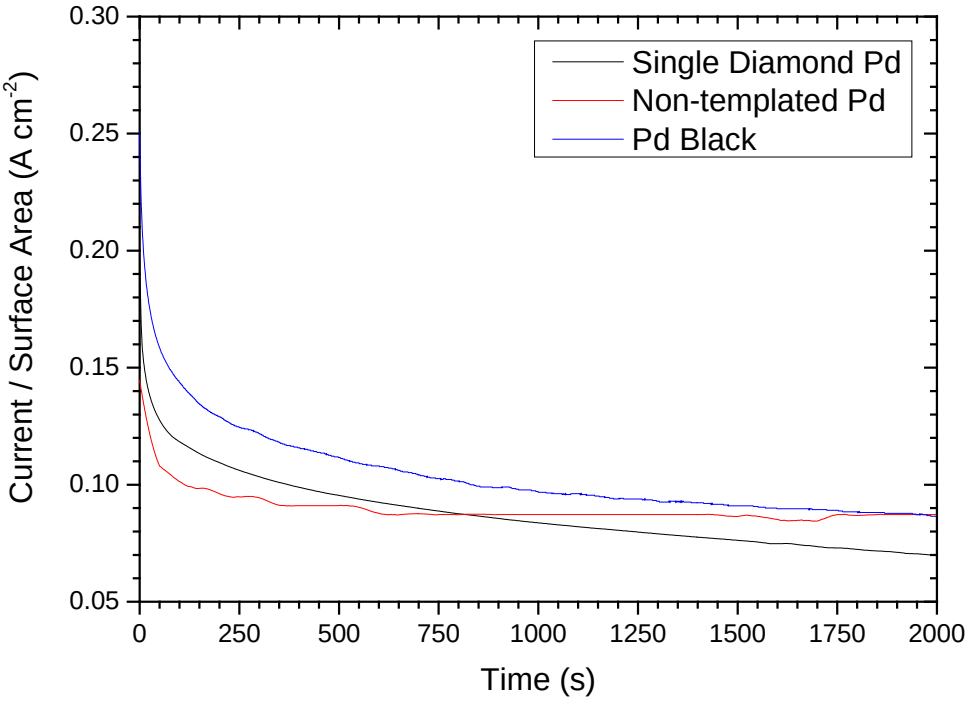

Figure D-7 - Chronoampometry of Single Diamond Pd, Pd black and non-templated Pd in 1 *M* methanol and 1 *M* KOH, recorded at +0.30 *V vs. SCE*. The experiment was conducted at room temperature. The cell volume was 100 *mL* and the cell was covered to prevent evaporation. Current was normalised by dividing by the surface area of Pd on the electrode.

D.2.2 For Ethanol

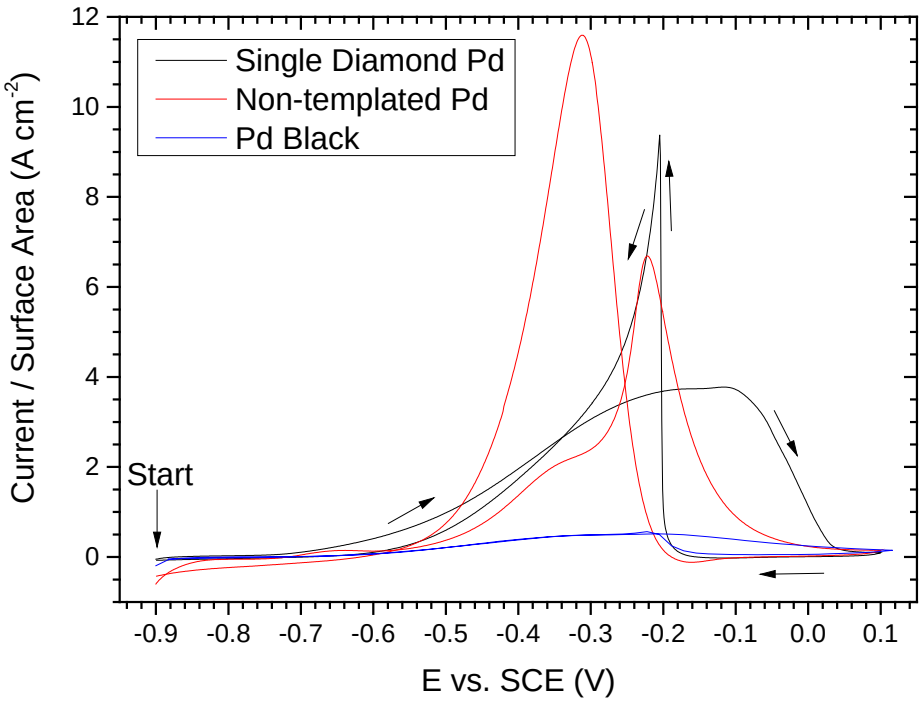

Figure D-8 - Cyclic voltammetry of Single Diamond Pd, Pd black and non-templated Pd in 0.1 *M* ethanol and 0.1 *M* NaOH, recorded at 10 $mV\,s^{-1}$. The voltammogram was measured at room temperature and started at a potential of -0.90 *V vs. SCE* where no reaction occurred and is scanned between -0.90 *V vs. SCE* and +0.10 *V vs. SCE*, for 250 scans. Here the first scan is shown for comparison. The cell volume was 100 *mL* and the cell was covered to prevent evaporation. Current was normalised by dividing by the surface area of Pd on the electrode.

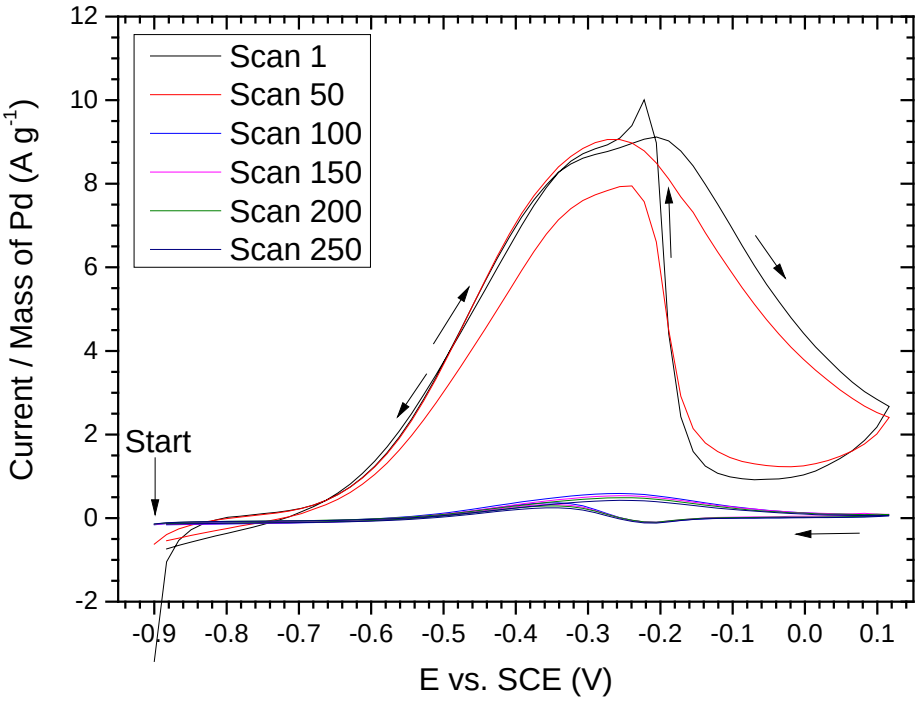

Figure D-9 - Cyclic voltammetry of Pd black in 0.1 *M* ethanol and 0.1 *M* NaOH, recorded at 10 *mV* s^{-1}. The voltammogram was measured at room temperature and started at a potential of -0.90 *V vs. SCE* where no reaction occurred and is scanned between -0.90 *V vs. SCE* and +0.10 *V vs. SCE*, for 250 scans. Here every 50th scan is shown for ease of viewing. The cell volume was 100 *mL* and the cell was covered to prevent evaporation. Current was normalised by dividing by the mass of Pd (0.385 *mg*) on the electrode. 0.385 *mg* of Pd black was applied onto a 2 *mm* polished gold disc electrode by pipetting on 5 *µL* of an ink consisting of 80 *mg* Pd black (Alfa Aesar, 99.9%), 40 *µL* Nafion® 117 solution (Aldrich) and 1000 *µL* deionised water and leaving in an oven at 100 °C for at least 15 minutes.

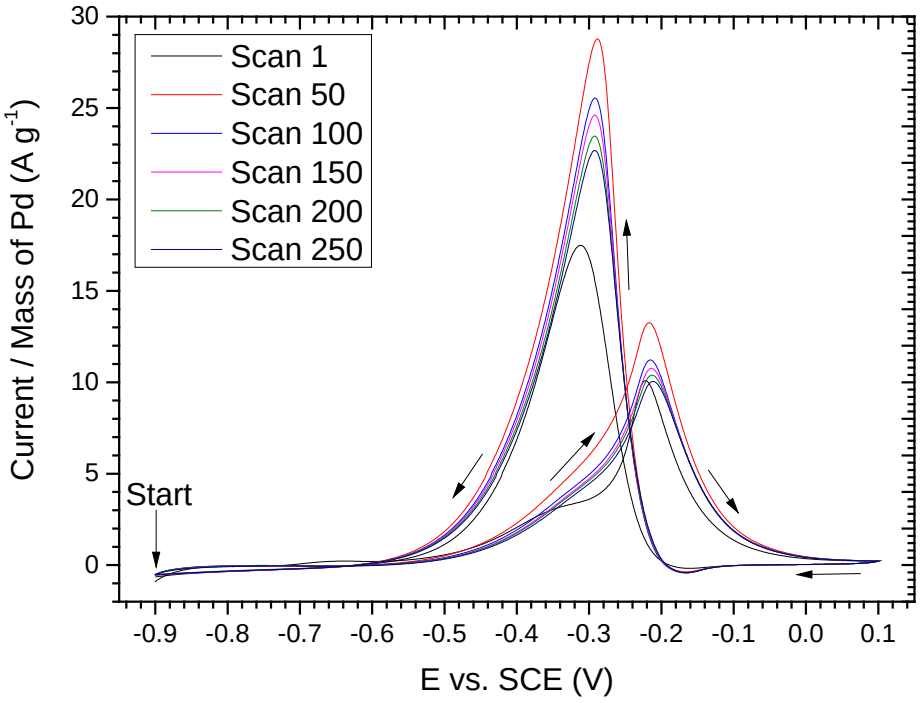

Figure D-10 - Cyclic voltammetry of non-templated Pd in 0.1 *M* ethanol and 0.1 *M* NaOH, recorded at 10 $mV\ s^{-1}$. The voltammogram was measured at room temperature and started at a potential of -0.90 *V vs. SCE* where no reaction occurred and is scanned between -0.90 *V vs. SCE* and +0.10 *V vs. SCE*, for 250 scans. Here every 50th scan is shown for ease of viewing. The cell volume was 100 *mL* and the cell was covered to prevent evaporation. Current was normalised by dividing by the mass of Pd on the electrode. Pd mass was calculated assuming 100% faradaic efficiency during electrodeposition, with deposition charge being 20 *mC*.

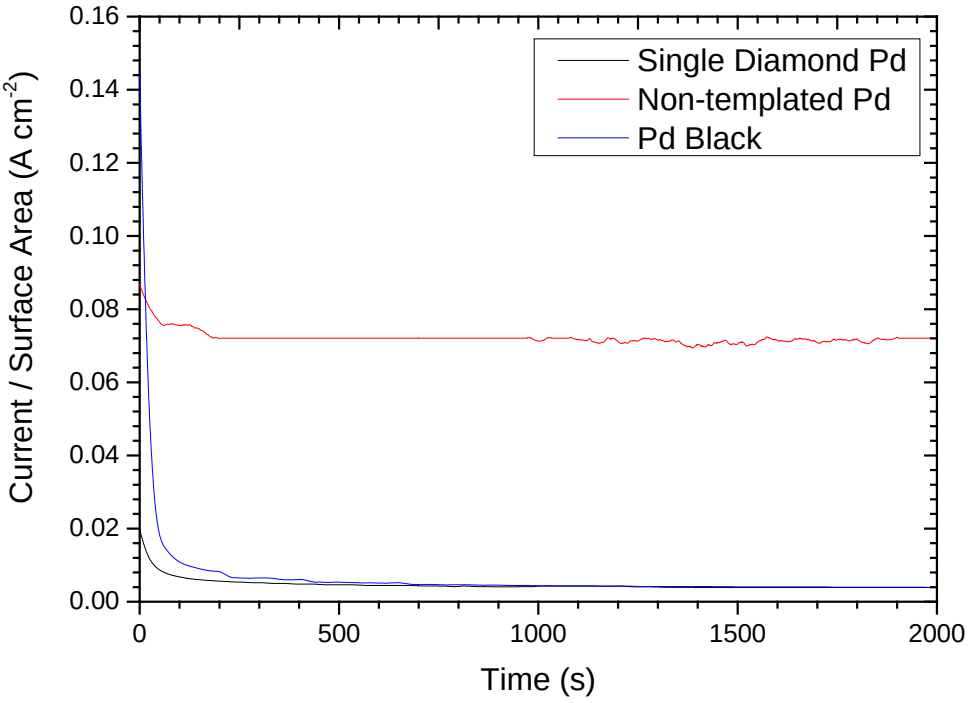

Figure D-11 - Chronoampometry of Single Diamond Pd, Pd black and non-templated Pd in 0.1 *M* ethanol and 0.1 *M* NaOH, recorded at +0.30 *V vs. SCE*. The experiment was conducted at room temperature. The cell volume was 100 *mL* and the cell was covered to prevent evaporation. Current was normalised by dividing by the surface area of Pd on the electrode.

D.2.3 For Glycerol

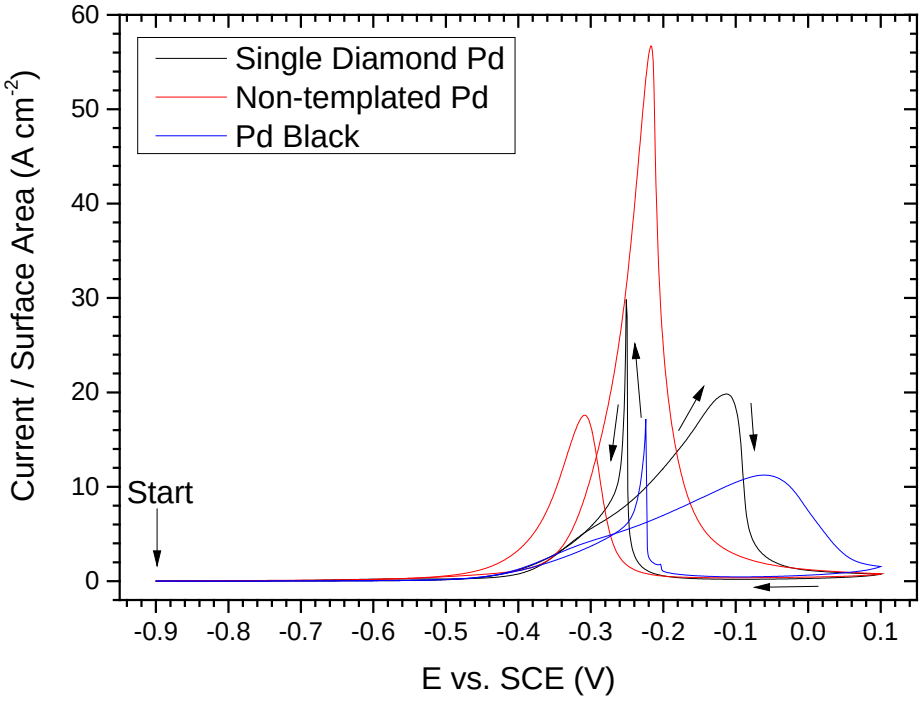

Figure D-12 - Cyclic voltammetry of Single Diamond Pd, Pd black and non-templated Pd in 1 *M* glycerol and 1 *M* KOH, recorded at 10 $mV\ s^{-1}$. The voltammogram was measured at room temperature and started at a potential of -0.90 *V vs. SCE* where no reaction occurred and is scanned between -0.90 *V vs. SCE* and +0.10 *V vs. SCE*, for 250 scans. Here the first scan is shown for comparison. The cell volume was 100 *mL* and the cell was covered to prevent evaporation. Current was normalised by dividing by the surface area of Pd on the electrode.

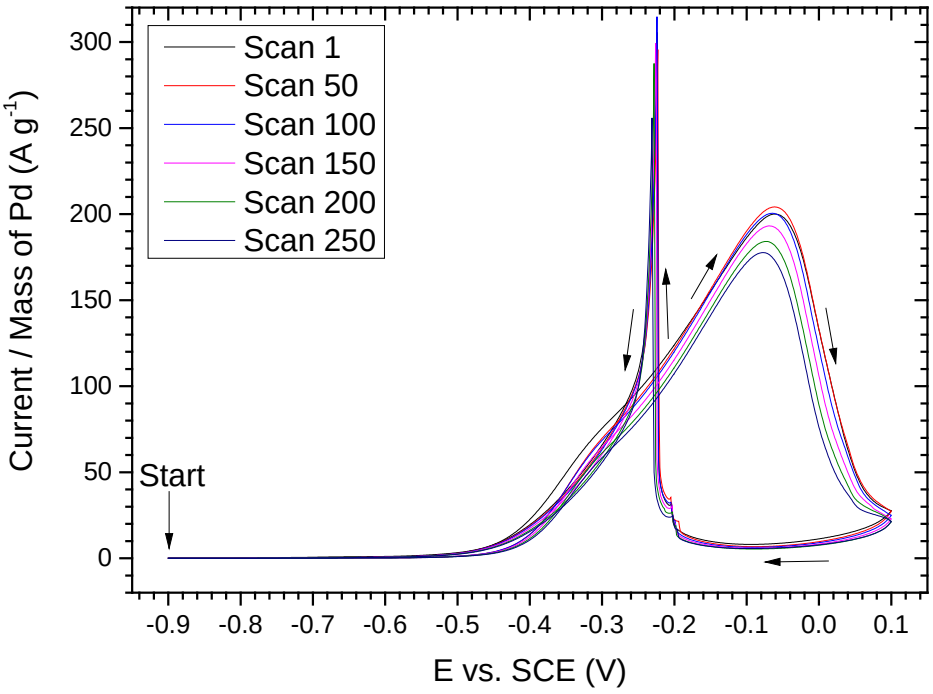

Figure D-13 - Cyclic voltammetry of Pd black in 1 *M* glycerol and 1 *M* KOH, recorded at 10 $mV\ s^{-1}$. The voltammogram was measured at room temperature and started at a potential of -0.90 *V vs. SCE* where no reaction occurred and is scanned between -0.90 *V vs. SCE* and +0.10 *V vs. SCE*, for 250 scans. Here every 50th scan is shown for ease of viewing. The cell volume was 100 *mL* and the cell was covered to prevent evaporation. Current was normalised by dividing by the mass of Pd (0.385 *mg*) on the electrode. 0.385 *mg* of Pd black was applied onto a 2 *mm* polished gold disc electrode by pipetting on 5 *µL* of an ink consisting of 80 *mg* Pd black (Alfa Aesar, 99.9%), 40 *µL* Nafion® 117 solution (Aldrich) and 1000 *µL* deionised water and leaving in an oven at 100 °C for at least 15 minutes.

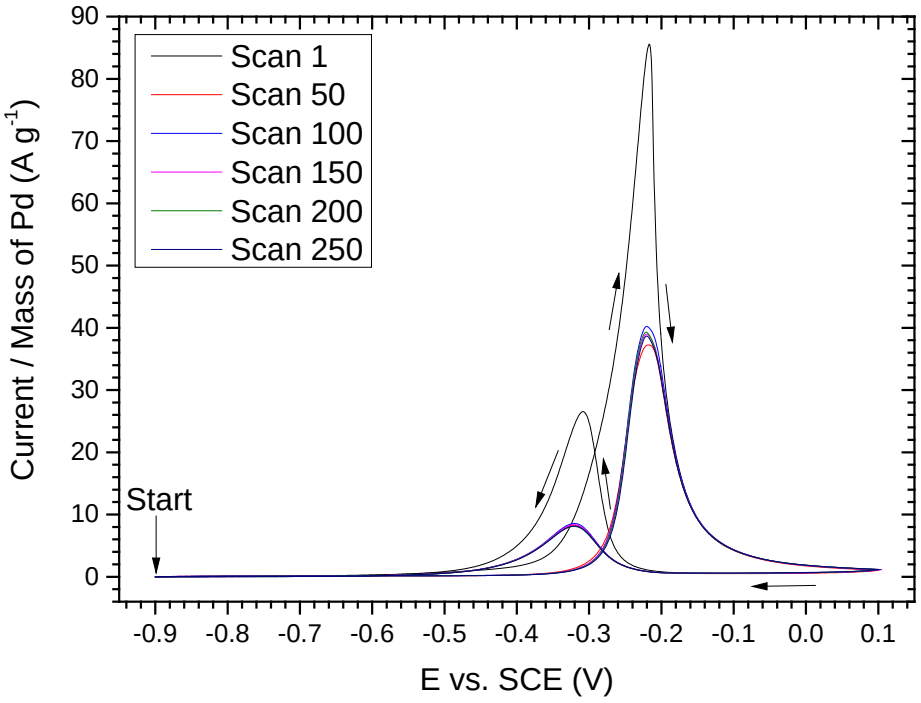

Figure D-14 - Cyclic voltammetry of non-templated Pd in 1 *M* glycerol and 1 *M* KOH, recorded at 10 $mV\ s^{-1}$. The voltammogram was measured at room temperature and started at a potential of -0.90 *V vs. SCE* where no reaction occurred and is scanned between -0.90 *V vs. SCE* and +0.10 *V vs. SCE*, for 250 scans. Here every 50th scan is shown for ease of viewing. The cell volume was 100 *mL* and the cell was covered to prevent evaporation. Current was normalised by dividing by the mass of Pd on the electrode. Pd mass was calculated assuming 100% faradaic efficiency during electrodeposition, with deposition charge being 20 *mC*.

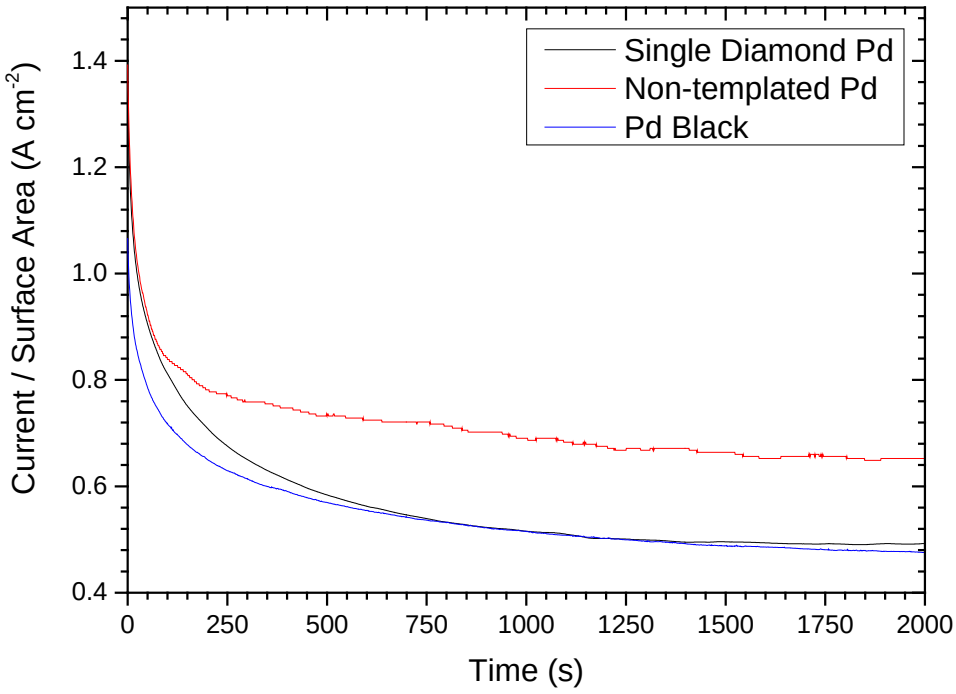

Figure D-15 - Chronoampometry of Single Diamond Pd, Pd black and non-templated Pd in 1 *M* glycerol and 1 *M* KOH, recorded at +0.30 *V vs. SCE*. The experiment was conducted at room temperature. The cell volume was 100 *mL* and the cell was covered to prevent evaporation. Current was normalised by dividing by the surface area of Pd on the electrode.

List of References

[1] L. E. Bell, “Cooling, Heating, Generating Power, and Recovering Waste Heat with Thermoelectric Systems,” *Science (80-.).*, vol. 321, no. 5895, pp. 1457–1461, Sep. 2008.

[2] J. Lesurf, “How a PN-Junction Diode works,” *University of St Andrews*. [Online]. Available: https://www.st-andrews.ac.uk/~www_pa/Scots_Guide/info/comp/passive/diode/pn_junc/pn_junc.htm. [Accessed: 22-Jan-2015].

[3] “Understanding the PN Junction.” [Online]. Available: http://www.circuitstoday.com/understanding-the-pn-junction. [Accessed: 04-Feb-2016].

[4] “The Science of Thermoelectric Materials,” *Northwestern Materials Science and Engineering*. [Online]. Available: http://thermoelectrics.matsci.northwestern.edu/thermoelectrics/. [Accessed: 05-Jan-2016].

[5] L.-P. Ma, H.-J. Bart, P. Ning, A. Zhang, G. Wu, and Z. Zengzang, “Kinetic study of three-way catalyst of automotive exhaust gas: Modeling and application,” *Chem. Eng. J.*, vol. 155, no. 1, pp. 241–247, 2009.

[6] P. Pichanusakorn and P. Bandaru, “Nanostructured thermoelectrics,” *Mater. Sci. Eng. R Reports*, vol. 67, no. 2–4, pp. 19–63, Jan. 2010.

[7] V. Zaitsev, M. Fedorov, and I. Eremin, *Thermoelectrics handbook: macro to nano*. CRC Press, Taylor & Francis, 2006.

[8] J. Fleurial, T. Caillat, B. J. Nesmith, R. C. Ewell, D. F. Woerner, G. C. Carr, and L. E. JonesJet, “Thermoelectrics: From space power systems to terrestrial waste heat recovery applications,” in *Proceedings of the Thermoelectrics Applications Workshop*, 2011.

[9] “How to charge your mobile phone using a mud oven,” *BBC News*, 2015. [Online]. Available: http://www.bbc.co.uk/news/science-environment-34905136.

[10] “GENTHERM | THRM | Thermal Systems & Climate Control.” [Online]. Available: http://www.gentherm.com/. [Accessed: 17-Oct-2016].

[11] J. W. Fairbanks, “Vehicular thermoelectrics: a new green technology,” in *Proceedings of the 2nd Thermoelectrics Applications Workshop*, 2011.

[12] T. Kuroki, K. Kabeya, K. Makino, T. Kajihara, H. Kaibe, H. Hachiuma, H. Matsuno, and A. Fujibayashi, "Thermoelectric Generation Using Waste Heat in Steel Works," *J. Electron. Mater.*, vol. 43, no. 6, pp. 2405–2410, Jun. 2014.

[13] I. Johnson, W. T. Choate, and A. Davidson, "Waste Heat Recovery. Technology and Opportunities in U.S. Industry," Mar. 2008.

[14] G. J. Snyder and E. S. Toberer, "Complex thermoelectric materials," *Nat. Mater.*, vol. 7, no. 2, pp. 105–14, Feb. 2008.

[15] D. Rowe and G. Min, "α-in σ plot as a thermoelectric material performance indicator," *J. Mater. Sci. Lett.*, vol. 14, pp. 617–619, 1995.

[16] P. Atkins and J. de Paula, *Elements of Physical Chemistry*, 5th ed. W. H. Freeman, 2009.

[17] W. Harrison, *Electronic structure and the properties of solids: the physics of the chemical bond*. 2012.

[18] H. Rosenberg, *The solid state*. Oxford University Press, 1988.

[19] B. Streetman and S. Banerjee, *Solid state electronic devices*. Pearson/Prentice Hall, 2000.

[20] A. J. Naylor, "Towards highly-efficient thermoelectric power harvesting generators." 31-Mar-2014.

[21] S. LeBlanc, "Thermoelectric generators: Linking material properties and systems engineering for waste heat recovery applications," *Sustain. Mater. Technol.*, vol. 1–2, pp. 26–35, Dec. 2014.

[22] S. Il Kim, K. H. Lee, H. A. Mun, H. S. Kim, S. W. Hwang, J. W. Roh, D. J. Yang, W. H. Shin, X. S. Li, Y. H. Lee, G. J. Snyder, and S. W. Kim, "Dense dislocation arrays embedded in grain boundaries for high-performance bulk thermoelectrics," *Science (80-.).*, vol. 348, no. 6230, 2015.

[23] D. Wu, L.-D. Zhao, X. Tong, W. Li, L. Wu, Q. Tan, Y. Pei, L. Huang, J.-F. Li, Y. Zhu, M. G. Kanatzidis, and J. He, "Superior thermoelectric performance in PbTe–PbS pseudo-binary: extremely low thermal conductivity and modulated carrier concentration," *Energy Environ. Sci.*, vol. 8, no. 7, pp. 2056–2068, 2015.

[24] "IUPAC Gold Book - clathrates." [Online]. Available: http://goldbook.iupac.org/C01097.html. [Accessed: 07-Feb-2016].

[25] J. R. Sootsman, D. Y. Chung, and M. G. Kanatzidis, “New and old concepts in thermoelectric materials.,” *Angew. Chem. Int. Ed. Engl.*, vol. 48, no. 46, pp. 8616–39, Jan. 2009.

[26] G. Nolas and J. Cohn, “Semiconducting Ge clathrates: Promising candidates for thermoelectric applications,” *Appl. Phys. Lett.*, vol. 73, no. 2, pp. 178–180, 1998.

[27] N. P. Blake, S. Latturner, J. D. Bryan, G. D. Stucky, and H. Metiu, “Band structures and thermoelectric properties of the clathrates Ba[sub 8]Ga[sub 16]Ge[sub 30], Sr[sub 8]Ga[sub 16]Ge[sub 30], Ba[sub 8]Ga[sub 16]Si[sub 30], and Ba[sub 8]In[sub 16]Sn[sub 30],” *J. Chem. Phys.*, vol. 115, no. 17, p. 8060, Nov. 2001.

[28] V. L. Kuznetsov, L. A. Kuznetsova, A. E. Kaliazin, and D. M. Rowe, “Preparation and thermoelectric properties of A[sub 8][sup II]B[sub 16][sup III]B[sub 30][sup IV] clathrate compounds,” *J. Appl. Phys.*, vol. 87, no. 11, p. 7871, 2000.

[29] J. R. Salvador, J. Y. Cho, Z. Ye, J. E. Moczygemba, A. J. Thompson, J. W. Sharp, J. D. König, R. Maloney, T. Thompson, J. Sakamoto, H. Wang, A. A. Wereszczak, and G. P. Meisner, “Thermal to Electrical Energy Conversion of Skutterudite-Based Thermoelectric Modules,” *J. Electron. Mater.*, vol. 42, no. 7, pp. 1389–1399, Oct. 2012.

[30] S. R. Culp, S. J. Poon, N. Hickman, T. M. Tritt, and J. Blumm, “Effect of substitutions on the thermoelectric figure of merit of half-Heusler phases at 800 °C,” *Appl. Phys. Lett.*, vol. 88, no. 4, p. 42106, Jan. 2006.

[31] M. I. Fedorov and V. Zaitsev, “Silicides: Promising Thermoelectric Materials,” *Mater. Matters*, vol. 6, no. 4, pp. 100–102, 2011.

[32] V. K. Zaitsev, M. I. Fedorov, E. A. Gurieva, I. S. Eremin, P. P. Konstantinov, A. Yu, A. Y. Samunin, and M. V. Vedernikov, “Highly effective Mg 2 Si 1− x Sn x thermoelectrics,” *Phys. Rev. B*, vol. 74, pp. 45207-1-45207–5, 2006.

[33] A. Nag and V. Shubha, “Oxide Thermoelectric Materials: A Structure–Property Relationship,” *J. Electron. Mater.*, vol. 43, no. 4, pp. 962–977, Feb. 2014.

[34] M. Ohtaki, K. Araki, and K. Yamamoto, “High Thermoelectric Performance of Dually Doped ZnO Ceramics,” *J. Electron. Mater.*, vol. 38, no. 7, pp. 1234–1238, Jun. 2009.

[35] “CONVERTING HEAT TO ELECTRICITY WORLDWIDE WITH TEG POWER,” 2015. [Online]. Available: http://www.tegpower.com/. [Accessed: 02-Jan-2017].

[36] D. A. WRIGHT, “Thermoelectric Properties of Bismuth Telluride and its Alloys,” *Nature*, vol.

181, no. 4612, pp. 834–834, Mar. 1958.

[37] L. D. Hicks and M. S. Dresselhaus, “Effect of quantum-well structures on the thermoelectric figure of merit,” *Phys. Rev. B*, vol. 47, no. 19, pp. 12727–12731, May 1993.

[38] L. D. Hicks and M. S. Dresselhaus, “Thermoelectric figure of merit of a one-dimensional conductor,” *Phys. Rev. B*, vol. 47, no. 24, pp. 16631–16634, Jun. 1993.

[39] F. Xiao, C. Hangarter, B. Yoo, and Y. Rheem, “Recent progress in electrodeposition of thermoelectric thin films and nanostructures,” *Electrochim. Acta*, vol. 53, no. 28, pp. 8103–8117, 2008.

[40] A. Al Bayaz, A. Giani, and A. Foucaran, “Electrical and thermoelectrical properties of Bi 2 Se 3 grown by metal organic chemical vapour deposition technique,” *Thin Solid Films*, 2003.

[41] S.-D. Kwon, B. Ju, S.-J. Yoon, and J.-S. Kim, “Fabrication of Bismuth Telluride-Based Alloy Thin Film Thermoelectric Devices Grown by Metal Organic Chemical Vapor Deposition,” *J. Electron. Mater.*, vol. 38, no. 7, pp. 920–924, Feb. 2009.

[42] Y. Kim and A. DiVenere, “Structural and thermoelectric transport properties of Sb2Te3 thin films grown by molecular beam epitaxy,” *J. Appl. Phys.*, vol. 91, no. 2, pp. 715–718, 2002.

[43] L. Plucinski, G. Mussler, J. Krumrain, A. Herdt, S. Suga, D. Grützmacher, and C. M. Schneider, “Robust surface electronic properties of topological insulators: Bi[sub 2]Te[sub 3] films grown by molecular beam epitaxy,” *Appl. Phys. Lett.*, vol. 98, no. 22, p. 222503, Jun. 2011.

[44] V. Zemskov and A. Belaya, “Growth and investigation of thermoelectric properties of Bi–Sb alloy single crystals,” *J. Cryst. Growth*, vol. 212, no. 1–2, pp. 161–166, 2000.

[45] C.-H. Kuo, C.-S. Hwang, M.-S. Jeng, W.-S. Su, Y.-W. Chou, and J.-R. Ku, “Thermoelectric transport properties of bismuth telluride bulk materials fabricated by ball milling and spark plasma sintering,” *J. Alloys Compd.*, vol. 496, no. 1–2, pp. 687–690, Apr. 2010.

[46] M. Paunovic and M. Schlesinger, *Fundamentals of electrochemical deposition*, Second Edi. John Wiley and Sons, Inc., 2006.

[47] C. Lei, K. S. Ryder, E. Koukharenko, M. Burton, and I. S. Nandhakumar, “Electrochemical deposition of bismuth telluride thick layers onto nickel,” *Electrochem. commun.*, vol. 66, pp. 1–4, May 2016.

[48] W. Glatz, L. Durrer, E. Schwyter, and C. Hierold, “Novel mixed method for the

electrochemical deposition of thick layers of Bi2+xTe3−x with controlled stoichiometry," *Electrochim. Acta*, vol. 54, no. 2, pp. 755–762, 2008.

[49] M. S. Sander, R. Gronsky, T. Sands, and A. M. Stacy, "Structure of Bismuth Telluride Nanowire Arrays Fabricated by Electrodeposition into Porous Anodic Alumina Templates," *Chem. Mater.*, vol. 15, no. 1, pp. 335–339, Jan. 2003.

[50] E. Koukharenko, N. White, X. Li, and I. Nandhakumar, "Ion-Track Etched Templates for the High Density Growth of Nanowires of Bismuth Telluride and Bismuth Antimony Telluride by Electrodeposition," *ECS Trans.*, vol. 64, no. 35, pp. 9–14, Apr. 2015.

[51] E. Koukharenko, X. Li, I. Nandhakumar, N. Frety, S. P. Beeby, D. Cox, M. J. Tudor, B. Schiedt, C. Trautmann, A. Bertsch, and N. M. White, "Towards a nanostructured thermoelectric generator using ion-track lithography," *J. Micromechanics Microengineering*, vol. 18, no. 10, p. 104015, Oct. 2008.

[52] C. Frantz, N. Stein, L. Gravier, S. Granville, and C. Boulanger, "Electrodeposition and Characterization of Bismuth Telluride Nanowires," *J. Electron. Mater.*, vol. 39, no. 9, pp. 2043–2048, Dec. 2009.

[53] P. Collings and M. Hird, *Introduction to liquid crystals: chemistry and physics*. Taylor & Francis, 1997.

[54] P. N. Bartlett, "Electrodeposition of nanostructured films using self-organizing templates," *Electrochem. Soc. Interface*, vol. 13, no. 4, pp. 28–33, Dec. 2004.

[55] X. Li, I. S. Nandhakumar, T. Gabriel, G. S. Attard, M. L. Markham, D. C. Smith, J. J. Baumberg, K. Govender, P. O'Brien, and D. Smyth-Boyle, "Electrodeposition of mesoporous CdTe films with the aid of citric acid from lyotropic liquid crystalline phases," *J. Mater. Chem.*, vol. 16, no. 31, p. 3207, Aug. 2006.

[56] G. S. Attard, P. N. Bartlett, N. R. B. Coleman, J. M. Elliott, J. R. Owen, and J. H. Wang, "Mesoporous Platinum Films from Lyotropic Liquid Crystalline Phases," *Science (80-.).*, vol. 278, no. 5339, pp. 838–840, Oct. 1997.

[57] S. Akbar, J. M. Elliott, M. Rittman, and A. M. Squires, "Facile production of ordered 3D platinum nanowire networks with 'single diamond' bicontinuous cubic morphology.," *Adv. Mater.*, vol. 25, no. 8, pp. 1160–4, Feb. 2013.

[58] A. H. Whitehead, J. M. Elliott, and J. R. Owen, "Nanostructured tin for use as a negative electrode material in Li-ion batteries," *J. Power Sources*, vol. 81–82, pp. 33–38, Sep. 1999.

[59] P. N. Bartlett, P. N. Birkin, M. A. Ghanem, P. de Groot, and M. Sawicki, “The Electrochemical Deposition of Nanostructured Cobalt Films from Lyotropic Liquid Crystalline Media,” *J. Electrochem. Soc.*, vol. 148, no. 2, p. C119, 2001.

[60] P. N. Bartlett, B. Gollas, S. Guerin, and J. Marwan, “The preparation and characterisation of H1-e palladium films with a regular hexagonal nanostructure formed by electrochemical deposition from lyotropic liquid crystalline phases,” *Phys. Chem. Chem. Phys.*, vol. 4, no. 15, pp. 3835–3842, Jul. 2002.

[61] H. Luo, J. Zhang, and Y. Yan, “Electrochemical Deposition of Mesoporous Crystalline Oxide Semiconductor Films from Lyotropic Liquid Crystalline Phases,” *Chem. Mater.*, vol. 15, no. 20, pp. 3769–3773, Oct. 2003.

[62] I. Nandhakumar, J. M. Elliott, and G. S. Attard, “Electrodeposition of Nanostructured Mesoporous Selenium Films (H $_{I}$ -eSe),” *Chem. Mater.*, vol. 13, no. 11, pp. 3840–3842, Nov. 2001.

[63] T. Gabriel, I. S. Nandhakumar, and G. S. Attard, “Electrochemical synthesis of nanostructured tellurium films,” *Electrochem. commun.*, vol. 4, no. 8, pp. 610–612, Aug. 2002.

[64] J. M. Elliott, L. M. Cabuché, and P. N. Bartlett, “Electrochemical Characterization of a Templated Insulating Polymer-Modified Electrode,” *Anal. Chem.*, vol. 73, no. 13, pp. 2855–2861, Jul. 2001.

[65] P. N. Bartlett and J. Marwan, “Electrochemical Deposition of Nanostructured (H 1 -e) Layers of Two Metals in Which Pores within the Two Layers Interconnect,” *Chem. Mater.*, vol. 15, no. 15, pp. 2962–2968, Jul. 2003.

[66] P. Bartlett and S. Guerin, “A Micromachined Calorimetric Gas Sensor: an Application of Electrodeposited Nanostructured Palladium for the Detection of Combustible Gases,” *Anal. Chem.*, vol. 75, no. 1, pp. 126–132, 2003.

[67] L. Meng, J. Jin, G. Yang, T. Lu, H. Zhang, and C. Cai, “Nonenzymatic Electrochemical Detection of Glucose Based on Palladium−Single-Walled Carbon Nanotube Hybrid Nanostructures,” *Anal. Chem.*, vol. 81, no. 17, pp. 7271–7280, Sep. 2009.

[68] M. Łukaszewski, K. Hubkowska, U. Koss, and A. Czerwiński, “Characteristic of hydrogen-saturated Pd-based alloys for the application in electrochemical capacitors,” *J. Solid State Electrochem.*, vol. 16, no. 7, pp. 2533–2539, Jul. 2012.

[69] M. Łukaszewski, A. Żurowski, and A. Czerwiński, “Hydrogen in thin Pd-based layers deposited on reticulated vitreous carbon—A new system for electrochemical capacitors,” *J. Power Sources*, vol. 185, no. 2, pp. 1598–1604, 2008.

[70] T. Hübert, L. Boon-Brett, G. Black, and U. Banach, “Hydrogen sensors – A review,” *Sensors Actuators B Chem.*, vol. 157, no. 2, pp. 329–352, 2011.

[71] T. Hübert, L. Boon-Brett, V. Palmisano, and M. A. Bader, “Developments in gas sensor technology for hydrogen safety,” *Int. J. Hydrogen Energy*, vol. 39, no. 35, pp. 20474–20483, 2014.

[72] A. Chen and C. Ostrom, “Palladium-Based Nanomaterials: Synthesis and Electrochemical Applications,” *Chem. Rev.*, vol. 115, no. 21, pp. 11999–12044, Nov. 2015.

[73] E. Antolini, “Palladium in fuel cell catalysis,” *Energy Environ. Sci.*, vol. 2, no. 9, p. 915, 2009.

[74] Y. Iwai, S. Ikemoto, K. Haramaki, R. Hattori, and S. Yonezawa, “Influence of ligands of palladium complexes on palladium/Nafion composite membranes for direct methanol fuel cells by supercritical CO2 impregnation method,” *J. Supercrit. Fluids*, vol. 94, pp. 48–58, 2014.

[75] H. S. Thiam, W. R. W. Daud, S. K. Kamarudin, A. B. Mohamad, A. A. H. Kadhum, K. S. Loh, and E. H. Majlan, “Performance of direct methanol fuel cell with a palladium–silica nanofibre/Nafion composite membrane,” *Energy Convers. Manag.*, vol. 75, pp. 718–726, 2013.

[76] C. Bianchini and P. K. Shen, “Palladium-Based Electrocatalysts for Alcohol Oxidation in Half Cells and in Direct Alcohol Fuel Cells,” *Chem. Rev.*, vol. 109, no. 9, pp. 4183–4206, Sep. 2009.

[77] U. Martinez, A. Serov, M. Padilla, and P. Atanassov, “Mechanistic Insight into Oxide-Promoted Palladium Catalysts for the Electro-Oxidation of Ethanol,” *ChemSusChem*, vol. 7, no. 8, pp. 2351–2357, Aug. 2014.

[78] V. Bambagioni, C. Bianchini, A. Marchionni, J. Filippi, F. Vizza, J. Teddy, P. Serp, and M. Zhiani, “Pd and Pt–Ru anode electrocatalysts supported on multi-walled carbon nanotubes and their use in passive and active direct alcohol fuel cells with an anion-exchange membrane (alcohol=methanol, ethanol, glycerol),” *J. Power Sources*, vol. 190, no. 2, pp. 241–251, 2009.

[79] M. Simões, S. Baranton, and C. Coutanceau, “Electro-oxidation of glycerol at Pd based

nano-catalysts for an application in alkaline fuel cells for chemicals and energy cogeneration," *Appl. Catal. B Environ.*, vol. 93, no. 3, pp. 354–362, 2010.

[80] J. Goldstein, D. Newbury, and P. Echlin, *Scanning electron microscopy and X-ray microanalysis: a text for biologists, materials scientists, and geologists*. 2012.

[81] "Geology Department Facilities." [Online]. Available: http://www.colgate.edu/academics/departments-and-programs/geology/facilities. [Accessed: 03-Jan-2017].

[82] "The Prashunt Kamat Laboratory - Physical Characterization." [Online]. Available: https://www3.nd.edu/~kamatlab/facilities_physchar.html#Pos6. [Accessed: 03-Jan-2017].

[83] S. Reed, *Electron microprobe analysis and scanning electron microscopy in geology*. 2005.

[84] L. Scipioni, "Principles and Applications of Helium Ion Microscopy | Microscopy and Analysis." [Online]. Available: http://www.microscopy-analysis.com/editorials/editorial-listings/principles-and-applications-helium-ion-microscopy. [Accessed: 16-Apr-2016].

[85] H. Guo, C. Wang, K. Miyazawa, H. Wang, H. Masuda, and D. Fujita, "Thermal decomposition of fullerene nanowhiskers protected by amorphous carbon mask," *Sci. Rep.*, vol. 6, p. 38760, Dec. 2016.

[86] K. Ohya, K. Inai, A. Nisawa, and A. Itoh, "Emission statistics of X-ray induced photoelectrons and its comparison with electron- and ion-induced electron emissions," *Nucl. Instruments Methods Phys. Res. Sect. B Beam Interact. with Mater. Atoms*, vol. 266, no. 4, pp. 541–548, Feb. 2008.

[87] R. Ramachandra, B. Griffin, and D. Joy, "A model of secondary electron imaging in the helium ion scanning microscope.," *Ultramicroscopy*, vol. 109, no. 6, pp. 748–57, May 2009.

[88] B. W. Avery, V. Shutthanandan, and W. Jiang, "Helium Ion Microscopy versus Scanning Electron Microscopy." [Online]. Available: https://www.microscopy.org/MandM/2010/arey.pdf. [Accessed: 16-Apr-2016].

[89] R. Hill and F. Rahman, "Advances in helium ion microscopy," *Nucl. Instruments Methods Phys. Res. Sect. A Accel. Spectrometers, Detect. Assoc. Equip.*, vol. 645, no. 1, pp. 96–101, 2011.

[90] "ORION NanoFab." [Online]. Available: https://www.zeiss.com/microscopy/int/products/multiple-ion-beam/orion-nanofab-for-

materials.html. [Accessed: 31-Jan-2017].

[91] "Transmission Electron Microscopy | Central Microscopy Research Facility," *The University of Iowa*. [Online]. Available: https://cmrf.research.uiowa.edu/transmission-electron-microscopy. [Accessed: 12-Feb-2017].

[92] University of Minnestoa, "CSE Characterization Facility · Electron Microscopy – FEI Tecnai T12 Overview." [Online]. Available: http://www.charfac.umn.edu/instruments/tecnai_t12_overview.html. [Accessed: 13-Feb-2017].

[93] C. Nave, "Bragg's Law," *HyperPhysics*. [Online]. Available: http://hyperphysics.phy-astr.gsu.edu/hbase/quantum/bragg.html. [Accessed: 05-Jan-2017].

[94] A. L. Patterson, "The Scherrer Formula for X-Ray Particle Size Determination," *Phys. Rev.*, vol. 56, no. 10, pp. 978–982, Nov. 1939.

[95] S. J. Richardson, M. R. Burton, P. A. Staniec, I. Nandhakumar, N. J. Terrill, J. M. Elliott, and A. M. Squires, "Aligned Platinum Nanowire Networks from Surface-Oriented Lipid Cubic Phase Templates," *Nanoscale*, vol. 8, no. 5, pp. 2850–2856, Jan. 2016.

[96] I. Yutsis, "Thermopower measurements and electron-phonon coupling in molecular devices," Tel Aviv University, 2010.

[97] M. Takahashi, M. Kojima, S. Sato, N. Ohnisi, A. Nishiwaki, K. Wakita, T. Miyuki, S. Ikeda, and Y. Muramatsu, "Electric and thermoelectric properties of electrodeposited bismuth telluride (Bi[sub 2]Te[sub 3]) films," *J. Appl. Phys.*, vol. 96, no. 10, p. 5582, 2004.

[98] M. Takahashi, K. Uosaki, H. Kita, and S. Yamaguchi, "Resistivity, carrier concentration, and carrier mobility of electrochemically deposited CdTe films," *J. Appl. Phys.*, vol. 60, no. 6, p. 2046, Sep. 1986.

[99] A. S. Baranski, M. S. Bennett, and W. R. Fawcett, "The physical properties of CdS thin films electrodeposited from aqueous diethylene glycol solutions," *J. Appl. Phys.*, vol. 54, no. 11, pp. 6390–6394, Nov. 1983.

[100] M. Takahashi, Y. Muramatsu, M. Watanabe, K. Wakita, T. Miyuki, and S. Ikeda, "Preparation and Characterization of Cu-Doped p-CdTe Films Grown by Cathodic Electrodeposition," *J. Electrochem. Soc.*, vol. 149, no. 6, p. C311, Jun. 2002.

[101] "Four Point Probes: Ecopia HMS-3000 Hall Measurement System." [Online]. Available:

http://four-point-probes.com/ecopia-hms-3000-hall-measurement-system/. [Accessed: 12-Jan-2016].

[102] "Resistivity and Hall Measurements." [Online]. Available: http://www.nist.gov/pml/div683/hall_resistivity.cfm. [Accessed: 14-Mar-2016].

[103] "The Hall Effect." [Online]. Available: http://www.nist.gov/pml/div683/hall_effect.cfm. [Accessed: 14-Mar-2016].

[104] Y. Feutelais, B. Legendre, N. Rodier, and V. Agafonov, "A study of the phases in the bismuth - tellurium system," *Mater. Res. Bull.*, vol. 28, no. 6, pp. 591–593, 1993.

[105] The Cambridge Crystallographic Data Centre, "Mercury." 2014.

[106] A. Giani, A. Boulouz, F. Pascal-Delannoy, A. Foucaran, and A. Boyer, "MOCVD growth of Bi2Te3 layers using diethyltellurium as a precursor," *Thin Solid Films*, vol. 315, no. 1, pp. 99–103, 1998.

[107] R. Venkatasubramanian, T. Colpitts, E. Watko, M. Lamvik, and N. El-Masry, "MOCVD of Bi2Te3, Sb2Te3 and their superlattice structures for thin-film thermoelectric applications," *J. Cryst. Growth*, vol. 170, no. 1, pp. 817–821, 1997.

[108] S. Cho, Y. Kim, A. DiVenere, G. K. Wong, J. B. Ketterson, and J. R. Meyer, "Antisite defects of Bi[sub 2]Te[sub 3] thin films," *Appl. Phys. Lett.*, vol. 75, no. 10, p. 1401, 1999.

[109] A. Bailini, F. Donati, M. Zamboni, V. Russo, M. Passoni, C. S. Casari, A. Li Bassi, and C. E. Bottani, "Pulsed laser deposition of Bi2Te3 thermoelectric films," *Appl. Surf. Sci.*, vol. 254, no. 4, pp. 1249–1254, 2007.

[110] H. Zou, D. . Rowe, and G. Min, "Growth of p- and n-type bismuth telluride thin films by co-evaporation," *J. Cryst. Growth*, vol. 222, no. 1, pp. 82–87, 2001.

[111] X. Wang, H. He, N. Wang, and L. Miao, "Effects of annealing temperature on thermoelectric properties of Bi2Te3 films prepared by co-sputtering," *Appl. Surf. Sci.*, vol. 276, pp. 539–542, 2013.

[112] M. Takahashi, Y. Oda, T. Ogino, and S. Furuta, "Electrodeposition of Bi-Te Alloy Films," *J. Electrochem. Soc.*, vol. 140, no. 9, pp. 2550–2553, 1993.

[113] M. Takahashi, Y. Katou, K. Nagata, and S. Furuta, "The composition and conductivity of electrodeposited Bi_Te alloy films," *Thin Solid Films*, vol. 240, no. 1–2, pp. 70–72, 1994.

[114] M. Takahashi, Y. Muramatsu, and T. Suzuki, “Preparation of Bi2Te3 films by electrodeposition from solution containing bi-ethylenediaminetetraacetic acid complex and TeO2,” *J. Electrochem. Soc.*, vol. 150, no. 3, pp. C169–C174, 2003.

[115] P. Magri, C. Boulanger, and J. Lecuire, “Synthesis, properties and performances of electrodeposited bismuth telluride films,” *J. Mater. Chem.*, vol. 6, no. 5, pp. 773–779, 1996.

[116] S. Michel, N. Stein, M. Schneider, C. Boulanger, and J-M.Lecuire, “Optimization of chemical and electrochemical parameters for the preparation of n-type Bi2Te2.7Se0.3 thin films by electrodeposition,” *J. Appl. Electrochem.*, vol. 33, no. 1, pp. 23–27, 2003.

[117] S. Michel, S. Diliberto, C. Boulanger, and B. Bolle, “Effect of electrochemical deposition conditions on the crystallographic texture of bismuth telluride alloys,” *J. Cryst. Growth*, vol. 296, no. 2, pp. 227–233, 2006.

[118] M. S. Martín-González, A. L. Prieto, R. Gronsky, T. Sands, and A. M. Stacy, “Insights into the Electrodeposition of Bi[sub 2]Te[sub 3],” *J. Electrochem. Soc.*, vol. 149, no. 11, p. C546, 2002.

[119] F. Kröger, “Cathodic deposition and characterization of metallic or semiconducting binary alloys or compounds,” *J. Electrochem. Soc.*, vol. 125, no. 12, pp. 2028–2034, 1978.

[120] C. Boulanger, “Thermoelectric Material Electroplating: a Historical Review,” *J. Electron. Mater.*, vol. 39, no. 9, pp. 1818–1827, Sep. 2010.

[121] R. Rostek, N. Stein, and C. Boulanger, “A review of electroplating for V–VI thermoelectric films: from synthesis to device integration,” *J. Mater. Res.*, vol. 30, no. 17, pp. 2518–2543, Sep. 2015.

[122] Y. Cao, Z. Zeng, Y. Liu, X. Zhang, C. Shen, X. Wang, Z. Gan, H. Wu, and Z. Hu, “Electrodeposition and Thermoelectric Characterization of (00L)-Oriented Bi2Te3 Thin Films on Silicon with Seed Layer,” *J. Electrochem. Soc.*, vol. 160, no. 11, pp. D565–D569, Oct. 2013.

[123] L. M. Goncalves, C. Couto, P. Alpuim, A. G. Rolo, F. Völklein, and J. H. Correia, “Optimization of thermoelectric properties on Bi2Te3 thin films deposited by thermal co-evaporation,” *Thin Solid Films*, vol. 518, no. 10, pp. 2816–2821, 2010.

[124] L. Qiu, J. Zhou, X. Cheng, and R. Ahuja, “Electrochemical deposition of Bi2Te3-based thin films,” *J. Phys. Chem. Solids*, vol. 71, no. 8, pp. 1131–1136, Aug. 2010.

[125] A. Zimmer, N. Stein, H. Terryn, and C. Boulanger, “Optical and thermoelectric characterizations of electroplated n-Bi2(Te0.9Se0.1)3,” *J. Phys. Chem. Solids*, vol. 68, no. 10, pp. 1902–1907, 2007.

[126] L. Bu, W. Wang, and H. Wang, “Effect of the substrate on the electrodeposition of Bi2Te3−ySey thin films,” *Mater. Res. Bull.*, vol. 43, no. 7, pp. 1808–1813, 2008.

[127] C. Schumacher, K. G. Reinsberg, R. Rostek, L. Akinsinde, S. Baessler, S. Zastrow, G. Rampelberg, P. Woias, C. Detavernier, J. A. C. Broekaert, J. Bachmann, and K. Nielsch, “Optimizations of Pulsed Plated p and n-type Bi_2Te_3-Based Ternary Compounds by Annealing in Different Ambient Atmospheres,” *Adv. Energy Mater.*, vol. 3, no. 1, pp. 95–104, Jan. 2013.

[128] H. Li, H. Jing, Y. Han, Y. Xu, G.-Q. Lu, and L. Xu, “Microstructure and transport properties of copper-doped p-type BiSbTe alloy prepared by mechanical alloying and subsequent spark plasma sintering,” *J. Alloys Compd.*, vol. 576, pp. 369–374, Nov. 2013.

[129] J. Cui, L. Mao, W. Yang, and X. Xu, “Thermoelectric properties of Cu-doped n-type (Bi 2 Te 3) 0.9–(Bi 2− xCuxSe 3) 0.1 (x= 0–0.2) alloys,” *J. Solid State Chem.*, vol. 180, no. 12, pp. 3583–3587, 2007.

[130] J. L. Cui, W. J. Xiu, L. D. Mao, P. Z. Ying, L. Jiang, and X. Qian, “Thermoelectric properties of Ag-doped n-type (Bi2Te3)0.9–(Bi2−xAgxSe3)0.1 (x=0–0.4) alloys prepared by spark plasma sintering,” *J. Solid State Chem.*, vol. 180, no. 3, pp. 1158–1162, Mar. 2007.

[131] J. Yang, R. Chen, X. Fan, S. Bao, and W. Zhu, “Thermoelectric properties of silver-doped n-type Bi2Te3-based material prepared by mechanical alloying and subsequent hot pressing,” *J. Alloys Compd.*, vol. 407, no. 1–2, pp. 330–333, Jan. 2006.

[132] M. Takashiri, K. Miyazaki, S. Tanaka, J. Kurosaki, D. Nagai, and H. Tsukamoto, “Effect of grain size on thermoelectric properties of n-type nanocrystalline bismuth-telluride based thin films,” *J. Appl. Phys.*, vol. 104, no. 8, p. 84302, 2008.

[133] D. M. Rowe, *CRC handbook of thermoelectrics*. CRC Press, 1995.

[134] J.-P. Fleurial, A. Borshchevsky, M. A. Ryan, W. M. Phillips, J. G. Snyder, T. Caillat, E. A. Kolawa, J. A. Herman, P. Mueller, and M. Nicolet, “Development of Thick-Film Thermoelectric Microcoolers Using Electrochemical Deposition,” *MRS Proc.*, vol. 545, p. 493, Jan. 1998.

[135] B. Hamdou, J. Kimling, A. Dorn, E. Pippel, R. Rostek, P. Woias, and K. Nielsch,

"Thermoelectric Characterization of Bismuth Telluride Nanowires, Synthesized Via Catalytic Growth and Post-Annealing," *Adv. Mater.*, vol. 25, no. 2, pp. 239–244, Jan. 2013.

[136] Y. Deng, C.-W. Cui, N.-L. Zhang, T.-H. Ji, Q.-L. Yang, and L. Guo, "Bi2Te3–Te nanocomposite formed by epitaxial growth of Bi2Te3 sheets on Te rod," *J. Solid State Chem.*, vol. 179, no. 5, pp. 1575–1580, 2006.

[137] H. Yu, P. C. Gibbons, and W. E. Buhro, "Bismuth, tellurium, and bismuth telluride nanowires," *J. Mater. Chem.*, vol. 14, no. 4, p. 595, Feb. 2004.

[138] G. Zhang, B. Kirk, L. A. Jauregui, H. Yang, X. Xu, Y. P. Chen, and Y. Wu, "Rational Synthesis of Ultrathin n-Type Bi_2Te_3 Nanowires with Enhanced Thermoelectric Properties," *Nano Lett.*, vol. 12, no. 1, pp. 56–60, Jan. 2012.

[139] G. Zhang, H. Fang, H. Yang, L. A. Jauregui, Y. P. Chen, and Y. Wu, "Design Principle of Telluride-Based Nanowire Heterostructures for Potential Thermoelectric Applications," *Nano Lett.*, vol. 12, no. 7, pp. 3627–3633, Jul. 2012.

[140] H. Masuda and K. Fukuda, "Ordered metal nanohole arrays made by a two-step replication of honeycomb structures of anodic alumina," *Science (80-.).*, vol. 268, no. 5216, pp. 1466–1468, 1995.

[141] O. Jessensky, F. Müller, and U. Gösele, "Self-organized formation of hexagonal pore arrays in anodic alumina," *Appl. Phys. Lett.*, vol. 72, no. 10, pp. 1173–1175, 1998.

[142] A. P. Li, F. Müller, A. Birner, K. Nielsch, and U. Gösele, "Hexagonal pore arrays with a 50–420 nm interpore distance formed by self-organization in anodic alumina," *J. Appl. Phys.*, vol. 84, no. 11, p. 6023, 1998.

[143] K. Nielsch, J. Choi, K. Schwirn, R. B. Wehrspohn, and U. Gösele, "Self-ordering Regimes of Porous Alumina: The 10 Porosity Rule," *Nano Lett.*, vol. 2, no. 7, pp. 677–680, Jul. 2002.

[144] O. Eibl, K. Nielsch, N. Peranio, and F. Volklein, Eds., *Thermoelectric Bi2Te3 nanomaterials*. Wiley, 2015.

[145] X. A. Fan, J. Y. Yang, Z. Xie, K. Li, W. Zhu, X. K. Duan, C. J. Xiao, and Q. Q. Zhang, "Bi 2 Te 3 hexagonal nanoplates and thermoelectric properties of n-type Bi 2 Te 3 nanocomposites," *J. Phys. D. Appl. Phys.*, vol. 40, no. 19, pp. 5975–5979, Oct. 2007.

[146] Y. Deng, C.-W. Nan, G.-D. Wei, L. Guo, and Y. Lin, "Organic-assisted growth of bismuth telluride nanocrystals," 2003.

[147] A. Purkayastha, Q. Yan, M. S. Raghuveer, D. D. Gandhi, H. Li, Z. W. Liu, R. V. Ramanujan, T. Borca-Tasciuc, and G. Ramanath, "Surfactant-Directed Synthesis of Branched Bismuth Telluride/Sulfide Core/Shell Nanorods," *Adv. Mater.*, vol. 20, no. 14, pp. 2679–2683, Jul. 2008.

[148] † Feng Xiao, † Bongyoung Yoo, ‡ and Kyu Hwan Lee, and † Nosang V. Myung*, "Synthesis of Bi2Te3 Nanotubes by Galvanic Displacement," 2007.

[149] W.-L. Wang, C.-C. Wan, and Y.-Y. Wang, "Investigation of Electrodeposition of Bi_2Te_3 Nanowires into Nanoporous Alumina Templates with a Rotating Electrode," *J. Phys. Chem. B*, vol. 110, no. 26, pp. 12974–12980, Jul. 2006.

[150] M. S. Sander, A. L. Prieto, R. Gronsky, T. Sands, and A. M. Stacy, "Fabrication of High-Density, High Aspect Ratio, Large-Area Bismuth Telluride Nanowire Arrays by Electrodeposition into Porous Anodic Alumina Templates," *Adv. Mater.*, vol. 14, no. 9, pp. 665–667, May 2002.

[151] L. Li, Y. Yang, X. Huang, G. Li, and L. Zhang, "Pulsed electrodeposition of single-crystalline Bi 2 Te 3 nanowire arrays," *Nanotechnology*, vol. 17, no. 6, pp. 1706–1712, Mar. 2006.

[152] S. A. Sapp, B. B. Lakshmi, and C. R. Martin, "Template Synthesis of Bismuth Telluride Nanowires," *Adv. Mater.*, vol. 11, no. 5, pp. 402–404, Mar. 1999.

[153] C. Jin, X. Xiang, C. Jia, W. Liu, W. Cai, L. Yao, and X. Li, "Electrochemical Fabrication of Large-Area, Ordered Bi_2Te_3 Nanowire Arrays," *J. Phys. Chem. B*, vol. 108, no. 6, pp. 1844–1847, Feb. 2004.

[154] M. S. Sander, R. Gronsky, T. Sands, and A. M. Stacy, "Structure of Bismuth Telluride Nanowire Arrays Fabricated by Electrodeposition into Porous Anodic Alumina Templates," *Chem. Mater.*, vol. 15, no. 1, pp. 335–339, Jan. 2003.

[155] W. Wang, Q. Huang, F. Jia, and J. Zhu, "Electrochemically assembled p-type Bi[sub 2]Te[sub 3] nanowire arrays," *J. Appl. Phys.*, vol. 96, no. 1, p. 615, 2004.

[156] J. Lee, S. Farhangfar, J. Lee, L. Cagnon, R. Scholz, U. Gösele, and K. Nielsch, "Tuning the crystallinity of thermoelectric Bi 2 Te 3 nanowire arrays grown by pulsed electrodeposition," *Nanotechnology*, vol. 19, no. 36, p. 365701, Sep. 2008.

[157] L. Trahey, C. R. Becker, and A. M. Stacy, "Electrodeposited Bismuth Telluride Nanowire Arrays with Uniform Growth Fronts," *Nano Lett.*, vol. 7, no. 8, pp. 2535–2539, Aug. 2007.

[158] A. L. Prieto, M. S. Sander, M. S. Martín-González, R. Gronsky, T. Sands, and A. M. Stacy, "Electrodeposition of Ordered Bi_2Te_3 Nanowire Arrays," *J. Am. Chem. Soc.*, vol. 123, no. 29, pp. 7160–7161, Jul. 2001.

[159] W.-J. Li, W.-L. Yu, and C.-Y. Yen, "Pulsed electrodeposition of Bi2Te3 and Bi2Te3/Te nanowire arrays from a DMSO solution," *Electrochim. Acta*, vol. 58, pp. 510–515, 2011.

[160] J. Martín, C. V Manzano, O. Caballero-Calero, and M. Martín-González, "High-aspect-ratio and highly ordered 15-nm porous alumina templates," *ACS Appl. Mater. Interfaces*, vol. 5, no. 1, pp. 72–9, Jan. 2013.

[161] L. Trahey, C. R. Becker, and A. M. Stacy, "Electrodeposited bismuth telluride nanowire arrays with uniform growth fronts.," *Nano Lett.*, vol. 7, no. 8, pp. 2535–9, Aug. 2007.

[162] F. Xiao, B. Yoo, K.-H. Lee, and N. V Myung, "Electro-transport studies of electrodeposited $(Bi_{1-x}Sb_x)_2Te_3$ nanowires," *Nanotechnology*, vol. 18, no. 33, p. 335203, Aug. 2007.

[163] C. Frantz, N. Stein, Y. Zhang, E. Bouzy, O. Picht, M. E. Toimil-Molares, and C. Boulanger, "Electrodeposition of bismuth telluride nanowires with controlled composition in polycarbonate membranes," *Electrochim. Acta*, vol. 69, pp. 30–37, 2012.

[164] O. Picht, S. Müller, I. Alber, M. Rauber, J. Lensch-Falk, D. L. Medlin, R. Neumann, and M. E. Toimil-Molares, "Tuning the Geometrical and Crystallographic Characteristics of Bi_2Te_3 Nanowires by Electrodeposition in Ion-Track Membranes," *J. Phys. Chem. C*, vol. 116, no. 9, pp. 5367–5375, Mar. 2012.

[165] S. Müller, C. Schötz, O. Picht, W. Sigle, P. Kopold, M. Rauber, I. Alber, R. Neumann, and M. E. Toimil-Molares, "Electrochemical Synthesis of $Bi_{1-x}Sb_x$ Nanowires with Simultaneous Control on Size, Composition, and Surface Roughness," *Cryst. Growth Des.*, vol. 12, no. 2, pp. 615–621, Feb. 2012.

[166] D. Pinisetty, D. Davis, E. J. Podlaha-Murphy, M. C. Murphy, A. B. Karki, D. P. Young, and R. V. Devireddy, "Characterization of electrodeposited bismuth–tellurium nanowires and nanotubes," *Acta Mater.*, vol. 59, no. 6, pp. 2455–2461, 2011.

[167] M. Cassinelli, S. Müller, Z. Aabdin, N. Peranio, O. Eibl, C. Trautmann, and M. E. Toimil-Molares, "Structural and compositional characterization of Bi1−xSbx nanowire arrays grown by pulsed deposition to improve growth uniformity," *Nucl. Instruments Methods Phys. Res. Sect. B Beam Interact. with Mater. Atoms*, vol. 365, pp. 668–674, 2015.

[168] A. I. Cooper, "Porous Materials and Supercritical Fluids," *Adv. Mater.*, vol. 15, no. 13, pp.

1049–1059, Jul. 2003.

[169] D.-A. Borca-Tasciuc and G. Chen, “Anisotropic thermal properties of nanochanneled alumina templates,” *J. Appl. Phys.*, vol. 97, no. 8, p. 84303, 2005.

[170] J. Blumm and A. Lindemann, “Characterization of the thermophysical properties of molten polymers and liquids using the flash technique,” *High Temp High Press*, 2003.

[171] GE Healthcare Life Sciences, “Track-Etched Polycarbonate Membranes.” [Online]. Available: http://www.gelifesciences.com/webapp/wcs/stores/servlet/CategoryDisplay?categoryId=11251&catalogId=10101&productId=&top=Y&storeId=12751&langId=-1. [Accessed: 20-Feb-2017].

[172] R. L. Fleisher, B. P. Price, and R. M. Walker, *Nuclear tracks in solids: principles and applications*. University of California Press, 1975.

[173] M. Rauber, “Controlled Synthesis of Nanowire Assemblies by Ion-Track Template Electrodeposition,” Technical University of Darmstadt, 2012.

[174] M. F. P. Wagner, F. Völklein, H. Reith, C. Trautmann, and M. E. Toimil-Molares, “Fabrication and thermoelectrical characterization of three-dimensional nanowire networks,” *Phys. status solidi*, vol. 213, no. 3, pp. 610–619, Mar. 2016.

[175] C. T. Kresge, M. E. Leonowicz, W. J. Roth, J. C. Vartuli, and J. S. Beck, “Ordered mesoporous molecular sieves synthesized by a liquid-crystal template mechanism,” *Nature*, vol. 359, no. 6397, pp. 710–712, Oct. 1992.

[176] J. S. Beck, J. C. Vartuli, W. J. Roth, M. E. Leonowicz, C. T. Kresge, K. D. Schmitt, C. T. W. Chu, D. H. Olson, E. W. Sheppard, S. B. McCullen, J. B. Higgins, and J. L. Schlenker, “A new family of mesoporous molecular sieves prepared with liquid crystal templates,” *J. Am. Chem. Soc.*, vol. 114, no. 27, pp. 10834–10843, Dec. 1992.

[177] G. S. Attard, J. C. Glyde, and C. G. Göltner, “Liquid-crystalline phases as templates for the synthesis of mesoporous silica,” *Nature*, vol. 378, no. 6555, pp. 366–368, Nov. 1995.

[178] G. S. Attard, J. M. Corker, C. G. Göltner, S. Henke, and R. H. Templer, “Liquid-Crystal Templates for Nanostructured Metals,” *Angew. Chemie Int. Ed. English*, vol. 36, no. 12, pp. 1315–1317, Jul. 1997.

[179] J. M. Elliott, G. S. Attard, P. N. Bartlett, N. R. B. Coleman, D. A. S. Merckel, and J. R. Owen, “Nanostructured Platinum (H I -ePt) Films: Effects of Electrodeposition Conditions on Film

Properties," *Chem. Mater.*, vol. 11, no. 12, pp. 3602–3609, Dec. 1999.

[180] J. Barauskas and T. Landh, "Phase Behavior of the Phytantriol/Water System," *Langmuir*, vol. 19, no. 23, pp. 9562–9565, 2003.

[181] G. Tiddy, "Surfactant-water liquid crystal phases," *Phys. Rep.*, vol. 57, no. 1, pp. 1–46, Jan. 1980.

[182] K. Larsson, "Aqueous dispersions of cubic lipid–water phases," *Curr. Opin. Colloid Interface Sci.*, vol. 5, no. 1, pp. 64–69, 2000.

[183] M. Rittman, M. Frischherz, F. Burgmann, G. Hartley, and A. Squires, "Direct visualisation of lipid bilayer cubic phases using Atomic Force Microscopy," vol. 6, no. 17, pp. 4058–4061, 2010.

[184] S. Akbar, "Novel synthesis of nanostructured platinum materials via true liquid crystal templating utilising phytantriol as a structure directing agent," *PhD Thesis*, no. July, 2012.

[185] I. Bejenari, V. Kantser, and A. A. Balandin, "Thermoelectric properties of electrically gated bismuth telluride nanowires," *Phys. Rev. B*, vol. 81, no. 7, p. 75316, Feb. 2010.

[186] E. van der Drift and D. J. Maas, "Helium Ion Lithography," in *Nanofabrication*, Vienna: Springer Vienna, 2012, pp. 93–116.

[187] L. Hu, T. Zhu, X. Liu, and X. Zhao, "Point Defect Engineering of High-Performance Bismuth-Telluride-Based Thermoelectric Materials," *Adv. Funct. Mater.*, vol. 24, no. 33, pp. 5211–5218, Sep. 2014.

[188] H. Peng, N. Kioussis, and G. J. Snyder, "Elemental tellurium as a chiral p -type thermoelectric material," *Phys. Rev. B*, vol. 89, no. 19, p. 195206, May 2014.

[189] O. Caballero-Calero and M. Martín-González, "Thermoelectric nanowires: A brief prospective," *Scr. Mater.*, vol. 111, pp. 54–57, 2016.

[190] J.-F. Li, W.-S. Liu, L.-D. Zhao, and M. Zhou, "High-performance nanostructured thermoelectric materials," *NPG Asia Mater.*, vol. 2, no. 4, pp. 152–158, Oct. 2010.

[191] R. Ayres and L. Ayres, *A handbook of industrial ecology*. Edward Elgar Publishing Limited, 2002.

[192] H. E. Suess and H. C. Urey, "Abundances of the Elements," *Rev. Mod. Phys.*, vol. 28, no. 1, pp. 53–74, Jan. 1956.

[193] The National Institute for Occupational Safety and Health, “Tellurium,” *Centers for Disease Control and Prevention*, 2016. [Online]. Available: https://www.cdc.gov/niosh/npg/npgd0587.html. [Accessed: 07-Feb-2016].

[194] F. K. . Lutgens and E. J. . Tarbuck, *Essentials of geology*, 7th Editio. Prentice Hall, 2000.

[195] K. Biswas, L.-D. Zhao, and M. G. Kanatzidis, “Tellurium-Free Thermoelectric: The Anisotropic n-Type Semiconductor Bi2S3,” *Adv. Energy Mater.*, vol. 2, no. 6, pp. 634–638, Jun. 2012.

[196] L.-J. Zhang, B.-P. Zhang, Z.-H. Ge, and C.-G. Han, “Fabrication and properties of Bi2S3−xSex thermoelectric polycrystals,” 2013.

[197] Z.-H. Ge, B.-P. Zhang, P.-P. Shang, and J.-F. Li, “Control of anisotropic electrical transport property of Bi2S3 thermoelectric polycrystals,” *J. Mater. Chem.*, vol. 21, no. 25, p. 9194, 2011.

[198] Z.-H. Ge, B.-P. Zhang, and J.-F. Li, “Microstructure composite-like Bi2S3 polycrystals with enhanced thermoelectric properties,” *J. Mater. Chem.*, vol. 22, no. 34, p. 17589, 2012.

[199] B. Chen, C. Uher, L. Iordanidis, and M. G. Kanatzidis, “Transport Properties of Bi_2S_3 and the Ternary Bismuth Sulfides $KBi_{6.33}S_{10}$ and $K_2Bi_8S_{13}$,” *Chem. Mater.*, vol. 9, no. 7, pp. 1655–1658, Jul. 1997.

[200] J. O. Sofo and G. D. Mahan, “Optimum band gap of a thermoelectric material,” *Phys. Rev. B*, vol. 49, no. 7, pp. 4565–4570, Feb. 1994.

[201] B. Van Zeghbroeck, “Doping dependence of the energy bandgap,” *Electrical, Computer and Energy Engineering, University of Colorado Boulder*, 2011. [Online]. Available: http://ecee.colorado.edu/~bart/book/eband6.htm. [Accessed: 07-Feb-2017].

[202] R. Caracas and X. Gonze, “First-principles study of the electronic properties of A2B3 minerals, with A=Bi,Sb and B=S,Se,” *Phys. Chem. Miner.*, vol. 32, no. 4, pp. 295–300, Jul. 2005.

[203] A. F. Wells, *Structural Inorganic Chemistry*, Fifth Edit. Oxford Science Publications, 1984.

[204] H. Mizoguchi, H. Hosono, N. Ueda, and H. Kawazoe, “Preparation and electrical properties of Bi2S3 whiskers,” *J. Appl. Phys.*, vol. 78, no. 2, p. 1376, 1995.

[205] Z.-H. Ge, B.-P. Zhang, P.-P. Shang, Y.-Q. Yu, C. Chen, and J.-F. Li, “Enhancing Thermoelectric Properties of Polycrystalline Bi2S3 by Optimizing a Ball-Milling Process,” *J. Electron. Mater.*,

vol. 40, no. 5, pp. 1087–1094, May 2011.

[206] L.-D. Zhao, B.-P. Zhang, W.-S. Liu, H.-L. Zhang, and J.-F. Li, “Enhanced thermoelectric properties of bismuth sulfide polycrystals prepared by mechanical alloying and spark plasma sintering,” *J. Solid State Chem.*, vol. 181, no. 12, pp. 3278–3282, 2008.

[207] R. Chmielowski, D. Péré, C. Bera, I. Opahle, W. Xie, S. Jacob, F. Capet, P. Roussel, A. Weidenkaff, G. K. H. Madsen, and G. Dennler, “Theoretical and experimental investigations of the thermoelectric properties of Bi2S3,” *J. Appl. Phys.*, vol. 117, no. 12, p. 125103, Mar. 2015.

[208] X. Du, F. Cai, and X. Wang, “Enhanced thermoelectric performance of chloride doped bismuth sulfide prepared by mechanical alloying and spark plasma sintering,” *J. Alloys Compd.*, vol. 587, pp. 6–9, 2014.

[209] Y. Yu, C. H. Jin, R. H. Wang, Q. Chen, and L.-M. Peng, “High-Quality Ultralong Bi_2S_3 Nanowires: Structure, Growth, and Properties,” *J. Phys. Chem. B*, vol. 109, no. 40, pp. 18772–18776, Oct. 2005.

[210] M. B. Sigman and B. A. Korgel, “Solventless Synthesis of Bi_2S_3 (Bismuthinite) Nanorods, Nanowires, and Nanofabric,” *Chem. Mater.*, vol. 17, no. 7, pp. 1655–1660, Apr. 2005.

[211] S.-C. Liufu, L.-D. Chen, Q. Yao, and C.-F. Wang, “Bismuth Sulfide Thin Films with Low Resistivity on Self-Assembled Monolayers,” *J. Phys. Chem. B*, vol. 110, no. 47, pp. 24054–24061, Nov. 2006.

[212] S.-C. Liufu, L.-D. Chen, Q. Yao, and C.-F. Wang, “Assembly of one-dimensional nanorods into Bi[sub 2]S[sub 3] films with enhanced thermoelectric transport properties,” *Appl. Phys. Lett.*, vol. 90, no. 11, p. 112106, 2007.

[213] C. D. Lokhande and C. H. Bhosale, “Electrodeposition of CdS, Bi2S3 and Cd-Bi-S thin films and their photoelectrochemical properties,” *Bull. Electrochem.*, vol. 6, no. 6, pp. 662–624, 1990.

[214] N. S. Yesugade, C. D. Lokhande, and C. H. Bhosale, “Structural and optical properties of electrodeposited Bi2S3, Sb2S3 and As2S3 thin films,” *Thin Solid Films*, vol. 263, no. 2, pp. 145–149, 1995.

[215] C. Georges, R. Tena-Zaera, S. Bastide, J. C. Rouchaud, G. Larramona, and C. Lévy-Clément, “Electrochemical Deposition of Bi[sub 2]S[sub 3] Thin Films Using Dimethylsulfoxide as a Solvent,” *J. Electrochem. Soc.*, vol. 154, no. 12, p. D669, 2007.

[216] X. S. Peng, G. W. Meng, J. Zhang, L. X. Zhao, X. F. Wang, Y. W. Wang, and L. D. Zhang, "Electrochemical fabrication of ordered Bi 2 S 3 nanowire arrays," *J. Phys. D. Appl. Phys.*, vol. 34, no. 22, pp. 3224–3228, Nov. 2001.

[217] "Precision and accuracy in EDX analysis | Scanning Electron Microscopy School," *University of Cape Town*. [Online]. Available: http://emu.uct.ac.za/training/sem-school/precision-and-accuracy-in-edx-analysis/. [Accessed: 07-Feb-2017].

[218] G. Merle, M. Wessling, and K. Nijmeijer, "Anion exchange membranes for alkaline fuel cells: A review," *J. Memb. Sci.*, vol. 377, no. 1, pp. 1–35, 2011.

[219] A. Capon and R. Parsons, "The oxidation of formic acid on noble metal electrodes: II. A comparison of the behaviour of pure electrodes," *J. Electroanal. Chem. Interfacial Electrochem.*, vol. 44, no. 2, pp. 239–254, 1973.

[220] C. Bianchini and P. K. Shen, "Palladium-Based Electrocatalysts for Alcohol Oxidation in Half Cells and in Direct Alcohol Fuel Cells," *Chem. Rev.*, vol. 109, no. 9, pp. 4183–4206, Sep. 2009.

[221] S. Rousseau, C. Coutanceau, C. Lamy, and J.-M. Léger, "Direct ethanol fuel cell (DEFC): Electrical performances and reaction products distribution under operating conditions with different platinum-based anodes," *J. Power Sources*, vol. 158, no. 1, pp. 18–24, 2006.

[222] O. Savadogo, K. Lee, K. Oishi, S. Mitsushima, N. Kamiya, and K.-I. Ota, "New palladium alloys catalyst for the oxygen reduction reaction in an acid medium," 2004.

[223] L. Gu, N. Luo, and G. H. Miley, "Cathode electrocatalyst selection and deposition for a direct borohydride/hydrogen peroxide fuel cell," *J. Power Sources*, vol. 173, no. 1, pp. 77–85, 2007.

[224] S. R. Yoon, G. H. Hwang, W. I. Cho, I.-H. Oh, S.-A. Hong, and H. Y. Ha, "Modification of polymer electrolyte membranes for DMFCs using Pd films formed by sputtering," *J. Power Sources*, vol. 106, no. 1, pp. 215–223, 2002.

[225] M. Mougenot, A. Caillard, P. Brault, S. Baranton, and C. Coutanceau, "High Performance plasma sputtered PdPt fuel cell electrodes with ultra low loading," 2011.

[226] L. E. Ocola, C. Rue, and D. Maas, "High-resolution direct-write patterning using focused ion beams," *MRS Bull.*, vol. 39, no. 4, pp. 336–341, Apr. 2014.

[227] J. A. Spencer, S. G. Rosenberg, M. Barclay, Y.-C. Wu, L. McElwee-White, and D. Howard

Fairbrother, “Understanding the electron-stimulated surface reactions of organometallic complexes to enable design of precursors for electron beam-induced deposition,” *Appl. Phys. A*, vol. 117, no. 4, pp. 1631–1644, Dec. 2014.

[228] V. A. Kochemirovsky, L. G. Menchikov, I. I. Tumkin, L. S. Logunov, and S. V Safonov, “Laser-induced chemical liquid phase deposition of copper from aqueous solutions without reducing agents,” *Quantum Electron.*, vol. 42, no. 8, pp. 693–695, Aug. 2012.

[229] G. Cristoforetti, E. Pitzalis, R. Spiniello, R. Ishak, and M. Muniz-Miranda, “Production of Palladium Nanoparticles by Pulsed Laser Ablation in Water and Their Characterization,” *J. Phys. Chem. C*, vol. 115, no. 12, pp. 5073–5083, Mar. 2011.

[230] P. Guo, Z. Wei, W. Ye, W. Qin, Q. Wang, X. Guo, C. Lu, and X. S. Zhao, “Preparation and characterization of nanostructured Pd with high electrocatalytic activity,” *Colloids Surfaces A Physicochem. Eng. Asp.*, vol. 395, pp. 75–81, 2012.

[231] L. Kuai, X. Yu, S. Wang, Y. Sang, and B. Geng, “Au–Pd Alloy and Core–Shell Nanostructures: One-Pot Coreduction Preparation, Formation Mechanism, and Electrochemical Properties,” *Langmuir*, vol. 28, no. 18, pp. 7168–7173, May 2012.

[232] Q. Yi, F. Niu, and L. Sun, “Fabrication of novel porous Pd particles and their electroactivity towards ethanol oxidation in alkaline media,” *Fuel*, vol. 90, no. 8, pp. 2617–2623, 2011.

[233] M. H. Shao, T. Huang, P. Liu, J. Zhang, K. Sasaki, and M. B. Vukmirovic, and R. R. Adzic*, “Palladium Monolayer and Palladium Alloy Electrocatalysts for Oxygen Reduction†,” 2006.

[234] Y. Lu and W. Chen, “Nanoneedle-Covered Pd−Ag Nanotubes: High Electrocatalytic Activity for Formic Acid Oxidation,” *J. Phys. Chem. C*, vol. 114, no. 49, pp. 21190–21200, Dec. 2010.

[235] R. Ojani, Z. Abkar, E. Hasheminejad, and J.-B. Raoof, “Rapid fabrication of Cu/Pd nano/micro-particles porous-structured catalyst using hydrogen bubbles dynamic template and their enhanced catalytic performance for formic acid electrooxidation,” *Int. J. Hydrogen Energy*, vol. 39, no. 15, pp. 7788–7797, 2014.

[236] R. Larsen, S. Ha, J. Zakzeski, and R. I. Masel, “Unusually active palladium-based catalysts for the electrooxidation of formic acid,” *J. Power Sources*, vol. 157, no. 1, pp. 78–84, 2006.

[237] C. Xu, L. Cheng, P. Shen, and Y. Liu, “Methanol and ethanol electrooxidation on Pt and Pd supported on carbon microspheres in alkaline media,” 2007.

[238] C.-H. Lee, S.-C. Wang, C.-J. Yuan, M.-F. Wen, and K.-S. Chang, “Comparison of

amperometric biosensors fabricated by palladium sputtering, palladium electrodeposition and Nafion/carbon nanotube casting on screen-printed carbon electrodes," *Biosens. Bioelectron.*, vol. 22, no. 6, pp. 877–884, 2007.

[239] M. Arenz, V. Stamenkovic, T. J. Schmidt, K. Wandelt, P. N. Ross, and N. M. Markovic, "The electro-oxidation of formic acid on Pt–Pd single crystal bimetallic surfaces," *Phys. Chem. Chem. Phys.*, vol. 5, no. 19, pp. 4242–4251, 2003.

[240] Q. Shi and G. Diao, "The electrocatalytical reduction of m-nitrophenol on palladium nanoparticles modified glassy carbon electrodes," *Electrochim. Acta*, vol. 58, pp. 399–405, 2011.

[241] Y. Jiang, Y. Lu, F. Li, T. Wu, L. Niu, and W. Chen, "Facile electrochemical codeposition of 'clean' graphene–Pd nanocomposite as an anode catalyst for formic acid electrooxidation," 2012.

[242] Y. Zhao, S.-J. Qin, Y. Li, F.-X. Deng, Y.-Q. Liu, and G.-B. Pan, "Electrodeposition of dendritic Pd nanoarchitectures on n-GaN(0001): nucleation and electrocatalysis for direct formic acid fuel cells," *Electrochim. Acta*, vol. 145, pp. 148–153, 2014.

[243] N. Tian, Z. Y. Zhou, N. F. Yu, L. Y. Wang, and S. G. Sun, "Direct electrodeposition of tetrahexahedral Pd nanocrystals with high-index facets and high catalytic activity for ethanol electrooxidation," *J. Am. Chem. Soc.*, vol. 132, no. 22, pp. 7580–7581, 2010.

[244] N. Tian, Z.-Y. Zhou, and S.-G. Sun, "Electrochemical preparation of Pd nanorods with high-index facets," *Chem. Commun.*, vol. 0, no. 12, p. 1502, 2009.

[245] A. Safavi, N. Maleki, F. Tajabadi, and E. Farjami, "High electrocatalytic effect of palladium nanoparticle arrays electrodeposited on carbon ionic liquid electrode," 2007.

[246] J. Liu, J. Ye, C. Xu, S. P. Jiang, and Y. Tong, "Kinetics of ethanol electrooxidation at Pd electrodeposited on Ti," 2007.

[247] W. E. Mustain and J. Prakash, "Kinetics and mechanism for the oxygen reduction reaction on polycrystalline cobalt–palladium electrocatalysts in acid media," *J. Power Sources*, vol. 170, no. 1, pp. 28–37, 2007.

[248] S. H. Lim, J. Wei, J. Lin, Q. Li, and J. KuaYou, "A glucose biosensor based on electrodeposition of palladium nanoparticles and glucose oxidase onto Nafion-solubilized carbon nanotube electrode," 2005.

[249] M. Łukaszewski and A. Czerwiński, “Selected electrochemical properties of Pd–Au alloys: hydrogen absorption and surface oxidation,” *J. Solid State Electrochem.*, vol. 12, no. 12, pp. 1589–1598, Dec. 2008.

[250] F. Sarto, E. Castagna, M. De Francesco, T. M. Dikonimos, L. Giorgi, S. Lecci, M. Sansovini, and V. Violante, “Morphology and electrochemical properties of Pd-based catalysts deposited by different thin-film techniques,” *Int. J. Hydrogen Energy*, vol. 39, no. 27, pp. 14701–14711, 2014.

[251] A. Renjith and V. Lakshminarayanan, “One step preparation of ‘ready to use’ Au@Pd nanoparticle modified surface using deep eutectic solvents and a study of its electrocatalytic properties in methanol oxidation reaction,” *J. Mater. Chem. A*, vol. 3, no. 6, pp. 3019–3028, 2015.

[252] S. Choi, H. Jeong, K. Choi, J. Y. Song, and J. Kim, “Electrodeposition of Triangular Pd Rod Nanostructures and Their Electrocatalytic and SERS Activities,” *ACS Appl. Mater. Interfaces*, vol. 6, no. 4, pp. 3002–3007, Feb. 2014.

[253] X. Lu, F. Luo, H. Song, S. Liao, and H. Li, “Pulse electrodeposition to prepare core–shell structured AuPt@Pd/C catalyst for formic acid fuel cell application,” 2014.

[254] H. Wang, C. Xu, F. Cheng, and S. Jiang, “Pd nanowire arrays as electrocatalysts for ethanol electrooxidation,” 2007.

[255] C.-H. Cui, J.-W. Yu, H.-H. Li, M.-R. Gao, H.-W. Liang, and S.-H. Yu, “Remarkable Enhancement of Electrocatalytic Activity by Tuning the Interface of Pd–Au Bimetallic Nanoparticle Tubes,” *ACS Nano*, vol. 5, no. 5, pp. 4211–4218, May 2011.

[256] F. Cheng, H. Wang, Z. Sun, M. Ning, Z. Cai, and M. Zhang, “Electrodeposited fabrication of highly ordered Pd nanowire arrays for alcohol electrooxidation,” 2008.

[257] L. Liu, S.-H. Yoo, S. A. Lee, and S. Park, “Wet-Chemical Synthesis of Palladium Nanosprings,” *Nano Lett.*, vol. 11, no. 9, pp. 3979–3982, Sep. 2011.

[258] H. Bai, M. Han, Y. Du, J. Bao, and Z. Dai, “Facile synthesis of porous tubular palladium nanostructures and their application in a nonenzymatic glucose sensor,” *Chem. Commun.*, vol. 46, no. 10, p. 1739, 2010.

[259] D. A. J. Rand and R. Woods, “The nature of adsorbed oxygen on rhodium, palladium and gold electrodes,” *J. Electroanal. Chem. Interfacial Electrochem.*, vol. 31, no. 1, pp. 29–38, Jun. 1971.

[260] Z. Yin, M. Chi, Q. Zhu, D. Ma, J. Sun, and X. Bao, “Supported bimetallic PdAu nanoparticles with superior electrocatalytic activity towards methanol oxidation,” *J. Mater. Chem. A*, vol. 1, no. 32, p. 9157, 2013.

[261] Y. Zhao, X. Yang, J. Tian, F. Wang, and L. Zhan, “Methanol electro-oxidation on Ni@Pd core-shell nanoparticles supported on multi-walled carbon nanotubes in alkaline media,” *Int. J. Hydrogen Energy*, vol. 35, no. 8, pp. 3249–3257, 2010.

[262] Z. Wang, F. Hu, and P. K. Shen, “Carbonized porous anodic alumina as electrocatalyst support for alcohol oxidation,” 2006.

[263] Z. Yin, H. Zheng, D. Ma, and X. Bao, “Porous Palladium Nanoflowers that Have Enhanced Methanol Electro-Oxidation Activity,” *J. Phys. Chem. C*, vol. 113, no. 3, pp. 1001–1005, Jan. 2009.

[264] D. Y. Chung, K.-J. Lee, and Y.-E. Sung, “Methanol Electro-Oxidation on the Pt Surface: Revisiting the Cyclic Voltammetry Interpretation,” *J. Phys. Chem. C*, vol. 120, no. 17, pp. 9028–9035, May 2016.

[265] W. Wang, Y. Yang, Y. Liu, Z. Zhang, W. Dong, and Z. Lei, “Hybrid NiCoOx adjacent to Pd nanoparticles as a synergistic electrocatalyst for ethanol oxidation,” *J. Power Sources*, vol. 273, pp. 631–637, 2015.

[266] A. N. Geraldes, D. F. Silva, J. C. M. Silva, R. F. B. Souza, E. V. Spinacé, A. Oliveira Neto, M. Linardi, and M. C. Santos, “Glycerol Electrooxidation in Alkaline Medium Using Pd/C, Au/C and PdAu/C Electrocatalysts Prepared by Electron Beam Irradiation,” *J. Braz. Chem. Soc.*, vol. 25, no. 5, pp. 831–840, 2014.